Mechanism–Based Flow Stress Model for Ti–6Al–4V

Applicable for Simulation of Additive Manufacturing and Machining

Bijish Babu

Material Mechanics

LULEÅ
UNIVERSITY
OF TECHNOLOGY

Mechanism-Based Flow Stress Model for Ti-6Al-4V

Applicable for Simulation of Additive Manufacturing and Machining

Bijish Babu

Division of Mechanics of Solid Materials
Department of Engineering Sciences and Mathematics
Luleå University of Technology
Luleå, Sweden

Doctoral Thesis in Material Mechanics

Mechanism-based flow stress model for Ti-6Al-4V, applicable for simulation of additive manufacturing and machining

©Bijish Babu (2018)

"When you can measure what you are speaking about, and express it in numbers, you know something about it."

Lord Kelvin

PREFACE

This thesis work was carried out within the research group of material mechanics at Luleå University of Technology under the supervision of Prof. Lars-Erik Lindgren. I would like to thank Prof. Lindgren for his coaching, patience, unlimited positivism and encouragement.

The current and previous colleagues within the division at LTU has been really cordial and encouraging which I very much appreciate. Andreas Lundbäck, Dan Wedberg, Paul Åkerström, Ales Svoboda, Hao Qin, Corinne Charles, Magnus Söderberg and Martin Fisk deserves a special mention.

The financial support for the work was provided in-part by EU through the project VERDI under the initiation of GKN Aerospace Sweden AB. I thank the current and previous employees of GKN, Henrik Runnemalm, Robert Pederson, Torbjörn Kvist and Henrik Tersing for their support.

During the last 5 years, I have been working at Swerea MEFOS AB, now renamed as Swerim AB. My colleagues here have been providing outstanding support and friendship during these years. To my friends in Sweden and abroad who have extended a helping hand and shared a laugh, you made this journey possible.

My parents and family have always been supportive and encouraging throughout my life. Most importantly, my wife Nerine Mary George who has been really jovial and supportive deserves a ton of appreciation. To my son Nathan, I wish you stay curious throughout your life as you are now. And to my daughter Nova who is born today, I am genuinely eager to know you.

Bijish Babu
Luleå, October 07 2018.

ABSTRACT

Ti-6Al-4V has remarkable properties such as high specific mechanical properties (viz. stiffness, strength, toughness, fatigue resistance), corrosion resistance and bio-compatibility. These properties make it attractive for applications in aerospace, chemical industry, energy production, surgical implants, etc. Many of these applications have to satisfy high requirements on mechanical properties, which are directly affected by the microstructure. Therefore, it is essential to understand and to model the microstructure evolution and related changes in properties during manufacturing as well as in-service. Furthermore, this alloy has a narrow temperature and strain rate window of workability.

This work was initiated as part of a project aimed at performing finite element simulations of a manufacturing process chain involving hot-forming, welding, machining, additive manufacturing and heat treatment of Ti-6Al-4V components within the aerospace industry. Manufacturing process chain simulations can compute the cumulative effect of the various processes by following the material state through the whole chain and give a realistic prediction of the final component's properties. Capacity to describe material behavior in a wide range of temperatures and strain rates is crucial for this task.

A material model based on the dominant deformation mechanisms of the alloy is assumed to have a more extensive range of validity compared to an empirical relationship. Explicit dislocation dynamics based models are not practically feasible for manufacturing process simulation, and therefore the concept of dislocation density, ρ (length of dislocations per unit volume) developed by (Kocks, 1966; Bergström, 1970) is followed here. This approach provides a representation of the average behavior of a large number of dislocations, grains, etc. Conrad, 1981 studied the influence of various factors like solutes, interstitials, strain, strain rate, temperature, etc., on the strength and ductility of titanium systems and proposed a binary additive relationship for its yield strength. The first component relates to long-range interactions and second short-range relates to lattice resistance for dislocation motion. For high strain rate deformation, this short-range term is extended to include the effects of a viscous drag given by phonon and electron drag (Lesuer et al., 2001). Immobilisation of dislocation by pile-ups give hardening and remobilization/annihilation by dislocation glide and climb gives restoration. Globularization is also considered to restore the material. The material model is calibrated using isothermal compression tests at a wide range of temperatures and strain rates. Compression tests performed using Gleeble thermo-mechanical simulator is used at low-strain rates and split-Hopkins pressure bar

is used at high strain rates for calibration.

During manufacturing processes like additive manufacturing or multi-pass welding that involves cyclic heating/cooling, depending on the temperature and heating/cooling rates, Ti-6Al-4V undergoes allotropic phase transformation. This transformation results in a variety of morphology that can give different mechanical properties. Based on the morphology, (Semiatin et al., 1999; Seetharaman and Semiatin, 2002; Thomas et al., 2005) identified few microstructural features that are relevant to the mechanical properties. The three separate alpha phase fractions; Widmanstatten, grain boundary, Martensite, and the beta-phase fraction are included in the current model. However, since the strengthening contributions of these individual alpha phases are not known, a linear rule of mixtures for the total alpha-beta composition is developed. This model is calibrated using continuous cooling tests performed by Malinov et al., 2001 with differential scanning calorimeter at varying cooling rates.

This mechanism-based model is formulated in such a way that it can be implemented in any standard finite element software. In the current work, this is implemented as subroutines within MSC Marc and used for simulation of hot-forming and additive manufacturing.

Thesis

This thesis is a compilation of a synopsis and following five scientific articles. The contributions of the current author towards these articles are listed after each item.

Paper A:
Henrik Tersing, John Lorentzon, Arnaud François, Andreas Lundbäck, Bijish Babu, Josue Barboza, Vladimir Bäcker, Lars-Erik Lindgren. Simulation of manufacturing chain of a titanium aerospace component with experimental validation. *Finite Elements in Analysis and Design* 51, pp. 10-21. 2012.

- Implementation of the flow stress model in MSC Marc as FORTRAN subroutines for the simulation of forming, additive manufacturing and heat treatment.
- Modeling and simulation of the hot forming process.
- Writing the respective parts of the paper.

Paper B:
Bijish Babu, Lars-Erik Lindgren. Dislocation density based model for plastic deformation and globularization of Ti-6Al-4V. *International Journal of Plasticity* 50(0), pp. 94-108. 2013.

- Planning the experimental work.
- Implementation and calibration of the flow stress model.
- Writing the paper.

Paper C:
Bijish Babu, Corinne Charles Murgau, Lars-Erik Lindgren. Physically-based constitutive model of Ti-6Al-4V for arbitrary phase composition. *Submitted to Modelling and Simulation in Materials Science and Engineering* 2018.

- Planning the experimental work.
- Implementation and calibration of the flow stress model.
- Assisting in Implementation and calibration of the microstructure model.
- Writing the paper.

Paper D:
Bijish Babu, Ales Svoboda, Ehsan Ghassemali, Lars-Erik Lindgren. Dislocation density based plasticity model applied to high strain rate deformation of Ti-6Al-4V. *To be submitted* 2018.

- Assisting in the planning of the experimental work as well as implementation and calibration of the flow stress model.
- Developing the methodology to quantify globularization.
- Writing the respective parts of the paper.

Paper E:
Bijish Babu, Andreas Lundbäck, Lars-Erik Lindgren. Simulation of additive manufacturing of Ti-6Al-4V using a coupled physically-based flow stress and metallurgical model. *To be submitted* 2018.

- Implementation of the model from paper C in MSC Marc as FORTRAN subroutines for simulation of additive manufacturing.
- Simulation of the additive manufacturing case using the co-author's FORTRAN subroutines from earlier work.
- Writing the paper.

CONTENTS

Synopsis

Introduction

"Shoot for the moon.
Even if you miss, you'll land among the stars."

Norman Vincent Peale

Ti-6Al-4V has good specific strength, toughness and corrosion resistance which makes it attractive for applications in aerospace, pressure vessels, surgical implants etc. Components for these applications have precise requirements for mechanical and physical properties (Williams and Lütjering, 2003). Besides, this alloy has a narrow temperature and strain rate window of workability (Kailas et al., 1994; Seshacharyulu et al., 2002). Optimization of the process parameters to satisfy the requirements on the component can be enabled by simulation.

The deformation mechanisms of crystalline materials involve various phenomena depending on the temperature, stress levels and strain rates. Chapter 2 explains the active deformation mechanisms in polycrystals. In Chapter 3, the various microstructural changes of Ti-6Al-4V during temperature and mechanical loading are studied. The dominant deformation mechanisms of this alloy are identified to be dislocation glide controlled by Peierls-Nabarro stress and dislocation climb controlled by lattice and core diffusion. In Chapter 4, the various flow stress models available in the literature for Ti-6Al-4V are reviewed. This is not an exhaustive list, but is selected based on the most frequently cited in literature.

Chapter 5 explains the formulation of a physically based constitutive model for Ti-6Al-4V. This model extends the dislocation density based model (Lindgren et al., 2008) by including the effects of enhanced diffusivity. A model for viscous drag to include the effects of high strain rate deformation is described here. Globularization is a dominant restoration mechanism applicable for Ti-6Al-4V which is included here.

In the solid state, the Ti-6Al-4V microstructure is composed of two main phases; the high-temperature stable β-phase and the lower temperature stable α-phase. The α-phase with a hexagonal close pack structure is present in three different forms; Widmanstatten,

grain boundary, and Martensite. A metallurgical model that computes the formation and dissolution of each of these phases is described in chapter 6.

In chapter 7, a rule of mixture methodology is proposed to compute the combined effects of α and β phases on estimating the thermal strain and material yield. One of the main challenges in developing a physically-based model for plastic flow is the many different parameters that need to be calibrated. Some of these parameters are temperature dependent which adds to the problem. In chapter 8 a Matlab™ based toolbox is described which facilitates preparation of the test data, interaction with the model and calibration of model parameters.

Chapter 9 shows three manufacturing simulation cases where hot forming, welding, additive manufacturing, and heat treatment processes are simulated using a general purpose finite element software (MSC.Marc) utilizing the physically based model described here. Chapter 10 gives the conclusions and way forward for future research.

1.1   Background

This work was initiated as part of a project aimed to perform finite element simulations of a manufacturing chain involving hot-forming, welding, additive manufacturing, machining and heat treatment of Ti-6Al-4V components. Manufacturing chain simulations can compute the cumulative effect of the various processes by following the material state through the whole chain and give a realistic prediction of the final component. Capacity to describe material behavior in a wide range of temperatures and strain rates is crucial for this task. The hypothesis in the current work is that such a model should be based on the physics of the material behavior.

1.2   The Scope of this work

The scope can be phrased as the following question.

What constitutive model, including its parameters, is required to describe the plastic behavior of Ti-6Al-4V when simulating a manufacturing chain?

In this thesis, the dominant deformation mechanisms of the alloy are identified from the existing published literature. A suitable physically based model is chosen and calibrated with one-dimensional compression tests performed at temperatures between 20 - 1100℃ and strain rates between 10^{-3} - $9{\times}10^3\mathrm{s}^{-1}$. The flow stress is computed based on the evolution of internal state variables; dislocation density and vacancy concentration. The isotropic hardening model used here ignores the anisotropy of the material. This model could predict stress relaxation with an accuracy adequate for simulating heat treatment. A novel method based on EBSD to estimate the extent of globularization is developed as a part of this thesis work.

Deformation Mechanisms of Polycrystals

"Crystals are like people:
it is the defects in them which tend to make them
interesting!"

Colin Humphreys

On application of an external force, crystalline materials undergo deformation. This shape change is reversible or elastic if the applied force produces a small deformation ($\varepsilon < 10^{-4}$). During elastic deformation, the atoms will be displaced from their average positions, but will not change their relative positions. The theoretical shear strength (resistance to moving a plane of atoms past another) of a single crystal is approximately $10^{-2}G$ as opposed to $(10^{-4}\text{-}10^{-8})G$ for measured resolved shear strength, where G is the shear modulus (Hull and Bacon, 2001). This is because deformation is facilitated by the introduction of dislocations and imperfections in the crystal lattice. Propagation of dislocations requires lower energy than breaking of atomic bonds along a plane of atoms. Dislocations travel in a preferred direction depending on the crystal orientation and applied force. It is the formation, evolution, and interaction of the lattice imperfections that constitute the various deformation mechanisms. Figure 2.1 shows the impeding of dislocation motion by (a) interstitials and other point defects, (b) precipitates, (c) other dislocations, and (d) grain boundaries & other planar defects.
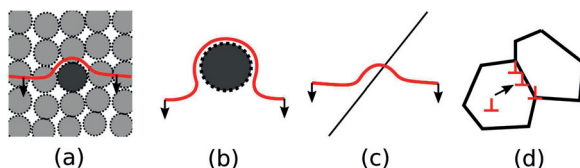

(a)   (b)   (c)   (d)

Figure 2.1: Interaction of dislocations with other defects.

2.1 Crystalline defects

Defects in crystals can be classified based on their spatial dimensions as the point, line, planar, and bulk.

2.1.1 Point defects

Vacancies and interstitials shown in figure 2.2 are common defects in crystal lattices. These point defects will introduce strains in the lattice. A vacancy is produced when an atom jumps from a lattice position. If it moves to an interstitial site, a self-interstitial is created. Both these defects generate equal lattice strain energies. A substitutional impurity is produced when an external atom occupies the lattice position of the material. Its strain energy is the lowest if the atoms are nearly the same size. Atoms of an external material residing in the interstitial location of a crystal produce an interstitial impurity. They are usually smaller in size as compared to the lattice atoms and therefore posses lowest strain energy.
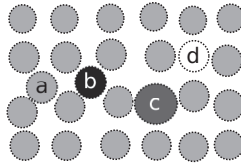
Figure 2.2: a) Self-interstitial, b) Interstitial impurity, c) Substitutional, and d) Vacancy.

2.1.2 Line defects

Edge dislocations are crystalline imperfections constituted by an extra half plane of atoms. The terminating line of the extra plane locates the region of severe lattice strain. On application of an external shear force, this plane progressively makes and breaks bonds with the atoms in the lattice. A screw dislocation is an imperfection where one part of the plane moves toward the right and other part moves to the left thereby moving the dislocation normal to the direction of application of force. Figure 2.3 shows the motion of edge and screw dislocations.

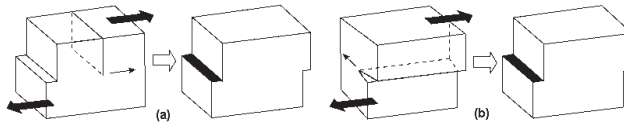Figure 2.3: a) Edge dislocation and b) Screw dislocation.

Jogs and kinks are defects in a dislocation which occur frequently in the lattice and strongly affect its mobility. Figure 2.4 shows the jogs and kinks in both edge and screw dislocations. They are defined as steps in a dislocation line of atomic dimensions present in all kinds of dislocations which are formed by a thermally activated mechanism. Kinks

fall in the glide plane whereas jogs do not. Both of them can be formed by the intersection of dislocations. The movement of a jog is made possible by addition and emission of interstitial atoms and absorption of vacancies.
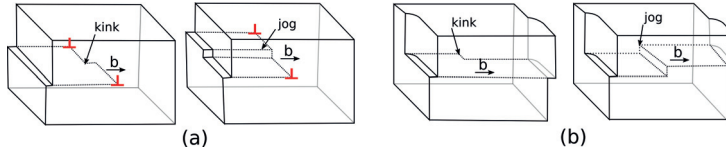

Figure 2.4: Jog & Kink in (a) edge dislocation, and screw dislocation.

2.1.3 Planar defects

Planar boundaries are formed in a lattice due to changes in orientation. They are classified based on the misorientations as, low angle grain boundary (LAGB) and high angle grain boundary (HAGB). Tilt and twist boundaries belong to the LAGB group with an angle of misorientation lower than 11°C whereas grain and phase boundaries belong to HAGB with a misorientation greater than 15°C (Humphreys and Hatherly, 2004), see figure 2.5. Twinning is a low-temperature deformation mechanism where a lattice volume upon shear would transform itself into an orientation with mirror symmetry relative to the parent lattice. Twins formed during recrystallization or grain growth are known as annealing twins. Tilt boundaries are formed when dislocations of the same polarity get aligned. This produces a low energy orientation and splits the parent grain lattice to subgrains. Twist boundaries are similar to tilt boundaries but are twisted in a direction normal to the boundary plane. In reality, tilt and twist boundaries are mixed up. Two different phases or lattice with different orientations that share an interface plane and are oriented with a high angle between them produce a phase or grain boundary.
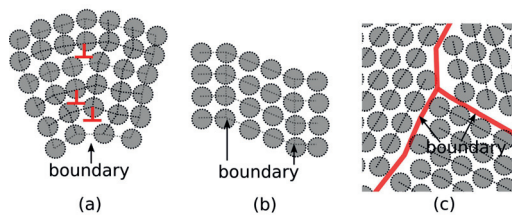

Figure 2.5: a)Tilt Boundary, b)Twin boundary and c) Grain boundary.

2.1.4 Bulk defects

Three-dimensional defects formed by a cluster of interstitial atoms are called precipitates. Depending on its coherency with the matrix material, precipitates can introduce lattice strains and also hinder dislocation movement. Cracks, pores, and voids are also bulk
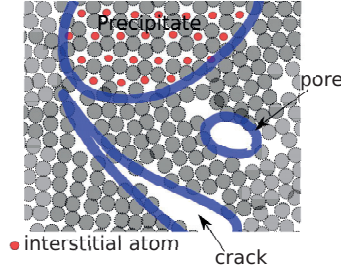
Figure 2.6: Bulk defects.

defects that are formed in a lattice which often reduces the strength of the material. pores and voids can be considered as a cluster of vacancies, see figure 2.6.

2.2 Plasticity

Plastic flow of a material is governed by the motion of dislocations. This is a kinetic process which involves gliding of atomic planes, the diffusive flow of atoms, vacancies and interstitials, the climb of dislocations normal to glide plane, grain boundary sliding, twinning, etc. These mechanisms vary and overlap with the magnitude of stress, strain rate, temperature and microstructure of the material. However, dislocation glide is the dominating factor for plasticity at temperatures less than $0.4T_{Melt}$.

2.2.1 Hardening process

Moving dislocations when confronted with obstacles produce pileups resulting in a reversed stress which oppose the applied shear stress. This is manifested in the stress-strain curve as hardening behavior. The force necessary for plastic flow is the difference between shear stress and the back stress. All crystalline imperfections act as obstacles to dislocation motion with varying degrees and further escalates the defect formation. Therefore, the plastic flow of a material can be controlled by regulating the dislocation motion which can be achieved by introducing or removing crystalline defects. The yield strength of a material depends on long range and short range obstacles created by the imperfections written as (Hertzberg, 1995).

$$\sigma_y = \sigma_{short} + \sigma_{long} + \sigma_{very-long} \tag{2.1}$$

Here, σ_{short} is due to the short range interactions of dislocations to overcome the lattice resistance field of the order less than 10Å. This is strongly temperature sensitive and has additional contributions from point defects. σ_{long} is the athermal component that is due to long-range interactions of dislocations with substructures of the order $(10^2 - 10^3\text{Å})$. $\sigma_{very-long}$ is due to structural size obstacles like planar defects of the order greater than 10^4Å.

2.2.2 Restoration processes

Plastic deformation changes the microstructure of the material by introducing defects in the lattice. This corresponds to the energy stored ($\approx$10%) by the material as strain energy due to lattice distortions which is the difference between work done for deformation and adiabatic heating (Reed-Hill and Abbaschian, 1991). Every material can store a limited amount of lattice strain energy which reduces with increasing temperature. When in excess, this energy is released and produces a lattice with lesser defects which is called restoration. During this process, the dislocations which are pinned by obstacles are assisted thermally or by the stored energy to remobilize themselves reducing the flow strength of the material. Recovery and recrystallization are competing restoration mechanisms driven by the stored energy of the crystal and each of them consists of a series of events. Recovery process shown schematically in
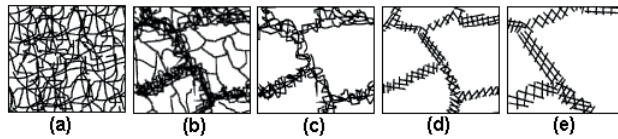

Figure 2.7: a) Pileups, b) Cell formation, c) Annihilation, d) Subgrain formation and e) Grain growth.

figure 2.7 involves the formation of cells, the annihilation of dislocations, the formation of subgrains and the grain growth occurring with some overlap (Humphreys and Hatherly, 2004). Cells are regions of low dislocation density (channels) surrounded by regions with a high density of dislocations with alternating polarity (walls). Subgrains are similar to cells except that the walls contain dislocations with same polarity and are neatly arranged. Recovery during deformation is known as dynamic recovery (DRy) and after deformation is static recovery (SRy). Recovery produces subtle changes in the microstructure that cannot be observed by an optical microscope, but brings in large changes in mechanical property; *viz* yield strength, hardness etc. This can be quantitatively measured by using differential scanning calorimetry (DSC) or hardness measurements (Woldt and Jensen, 1995; Knudsen et al., 2008). The rearrangement of dislocations to form low energy structures is called polygonization or cell formation. Based on the Read-Schockley equation (Read and Shockley, 1950), energy of a tilt boundary increases with increasing misorientation and energy per dislocation decreases with increasing misorientation. This indicates that a fewer highly mis-oriented boundaries are favored after recovery. The glide and climb of dislocations allow dislocations to move and reorganize. This also results in the annihilation of dislocations with opposite polarity.

Glide

Thermally activated glide or cross-slip has been accounted for as a recovery mechanism (Friedel, 1964). During cross-slip, dislocations move along the plane driven by applied

stress or stored energy. Dislocations try to rearrange themselves and possibly annihilate or exit through the free surface in order to produce a low energy state by distorting the lattice. Figure 2.8 shows the glide of an edge dislocation. Various obstacles like precipitates, solutes, immobile dislocations etc are responsible for inducing a glide resistance which may vanish or rearrange during restoration processes (Kocks et al., 1975).
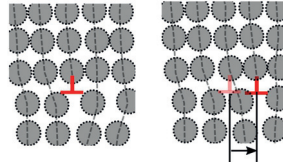
Figure 2.8: Edge dislocation gliding in the lattice.

Climb

The climb is a thermally activated mechanism driven by vacancy motion due to lattice diffusion and jogs which enables dislocations to circumvent obstacles (see figure 2.9). At elevated temperatures, the activation energy for formation and motion of vacancy otherwise known as activation energy for self diffusion is the controlling factor. At low temperatures, the activation energy for formation of jog contributes to the activation energy for self diffusion. In some cases, the diffusion along dislocations (core diffusion) can be the controlling factor for the climb as the activation energy for core diffusion is lower than for self diffusion (Prinz et al., 1982; Cahn and Peter, 1996b; Humphreys and Hatherly, 2004).
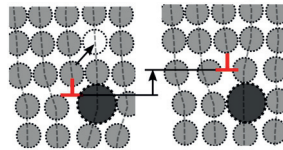
Figure 2.9: Edge dislocation climbing past an obstacle.

Recrystallization

Recrystallization (Rx) is the nucleation and growth of new grains with fewer defects at regions of high energy gradient. These grains will consume the deformed microstructure as it grows. During deformation, the amount of stored energy is increased by the presence of multiple phases and precipitates where large particles will act as sites of nucleation. They can also hinder grain growth by pinning the grain boundaries (Humphreys and Hatherly, 2004). Rx occurs in different time scales. A low temperature deformed material subjected to an elevated temperature can result in Rx known as static recrystallization

(SRx). Dynamic recrystallization (DRx) can be considered as the SRx occurring in the timescale of deformation (Barnett et al., 2000).
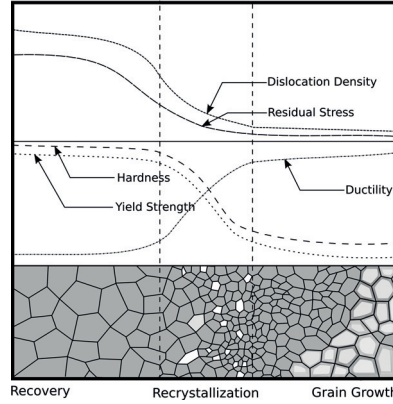
Figure 2.10: Restoration processes.

Some materials can store a high amount of energy even at elevated temperatures. This is primarily due to the slow recovery process which favors DRx. For DRx to occur, the driving force or defect energy present in the deformed microstructure must be high enough. This requires the temperature to be sufficiently low to ensure storing of adequate energy and high enough to provide the needed activation energy. During Rx, the density of dislocations and thereby the fraction of LAGB is reduced by a diffusion process. The mechanism of grain boundary migration in LAGB is by the climb of individual dislocations, whereas in HAGB, it is one of the atomic jumps across boundaries. In the intermediate ranges, its more difficult and vague (Humphreys and Hatherly, 2004). Figure 2.10 shows the response of the material to various restoration processes. The hardness, yield strength and, dislocation density drop suddenly at the same rate during recrystallization while the residual stress undergoes a more gradual reduction during recovery and gets saturated during recrystallization. The ductility of the material increases during recrystallization and gets saturated during grain growth.

2.3 Creep

Most materials at an elevated temperature when applied with a constant stress, undergo a transient response with a reducing strain rate ($\dot{\varepsilon}$) towards a constant value which lasts for a long time (hours to years). Later the $\dot{\varepsilon}$ increases rapidly leading to rupture. These three regions shown in figure 2.11 can be attributed to different deformation mechanisms. Primary creep is due to substructure changes and leads to dislocation hardening. The stable secondary creep is due to the dynamic balance between hardening and restoration. However, the final unstable tertiary creep can be due to metallurgical instabilities like corrosion, granular shear, granular fracture, cavitation, necking, dissolution of precipitates etc. A material which undergoes creep
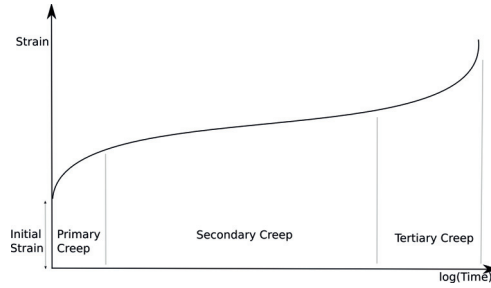
Figure 2.11: Creep curve.

might also exhibit strain recovery and stress relaxation as shown in figure 2.12 (Stouffer and Dame, 1996). On removal of creep stress, the material undergoes instantaneous elastic recovery followed by a slow recovery phase. The driving force for this process is the stored energy during creep deformation. Stress relaxation is the decay of stress with time while a material is held at a constant nonzero strain. Depending on the stress and temperature, the possible creep mechanisms can be dislocation creep, dislocation glide, bulk diffusion, grain boundary diffusion, granular shear, granular fracture, etc.
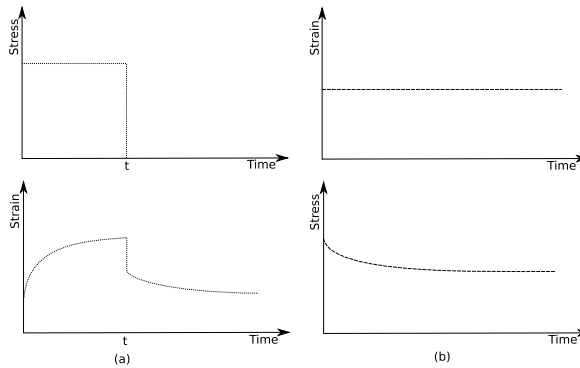
Figure 2.12: a) Creep followed by recovery and b) Stress relaxation test.

2.3.1   Dislocation creep

The motion of dislocations during creep is believed to be controlled by self diffusion because of the similarity in the activation energy. Vacancies assist the motion of dislocations to overcome obstacles on their slip planes. It requires the combined effect of a group of vacancies for a dislocation line to climb. The probability of climb at an elevated temperature is increased largely because of the high equilibrium vacancy concentration.

When the vacancies get closer to dislocation core, they replace atoms in the core and dislocations move perpendicular to the glide plane on to the nearest neighboring plane

(Gottstein, 2004). In many materials, the climb of dislocations is controlled by core or pipe diffusion rather than by lattice diffusion (Humphreys and Hatherly, 2004).

2.3.2   Nabarro-Herring and Coble creep

At high temperature and low stress, creep occurs not by motion of dislocations, but by the transport of matter through volume diffusion as shown in figure 2.13(a). This is driven by the chemical potential of atoms which depend on the elastic stress state leading to the motion of atoms from a compressed region to a dilated region. The strain rate is equivalent to the diffusive motion of the atoms which is proportional to the applied stress.
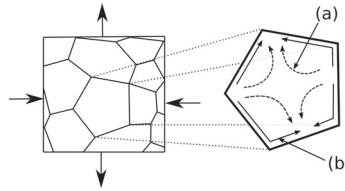
Figure 2.13: a) Nabarro-Herring creep and b) Coble creep.

At a lower temperature, fine-grained materials allow transport of material along its grain boundaries as shown in figure 2.13(b). This flow which is limited to grain boundary can be much higher than the volume diffusion.

Both Nabarro-Herring and Coble creep occur in polycrystals. But it is less prominent in metals as compared to ceramics because the dislocation creep is the dominant mechanism in metals. Grain boundary strengthening can deteriorate creep resistance of a material because it enhances the diffusivity.

2.3.3   Granular shear and Granular fracture

The motion of grain boundaries relative to each other as shown in figure 2.14 is known as grain boundary shear. The direction of shear is the boundary lying along the direction of critical resolved shear stress. This is also known as grain boundary sliding and can lead to a spasmodic and irregular flow of material.
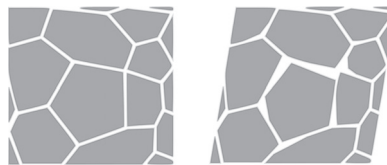
Figure 2.14: Motion of grain boundaries along its boundaries.

At temperatures below $0.5T_{Melt}$, metals may fail by granular fracture. Fracture occurs when the stress concentration exceeds the cohesive strength of the grain boundaries.This often results in the formation of cavities in the corners of grains or pores along the grain

boundaries. Depending on the stress, temperature and time, the mechanism of fracture changes from transgranular to intergranular fracture (Bendick, 1991). Transgranular fracture is shown in figure 2.15 (a) usually occurs at low temperatures and high stress whereas Intergranular fracture shown in figure 2.15 (b) occurs at higher temperature and stress. Plastic flow, grain boundary sliding, and grain boundary migration can act as a hindrance for granular fracture.
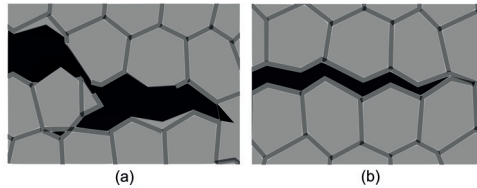
Figure 2.15: a) Transgranular Fracture b) Intergranular Fracture.

CHAPTER 3

Ti-6Al-4V Microstructure and Properties

"Look deep into nature,
and then you will understand everything better."

Albert Einstein

Ti-6Al-4V is a two-phase $(\alpha + \beta)$ alloy with a variety of possible microstructures. The proportion of Al and V gives attractive mechanical properties to the material. Ti-6Al-4V contains 6wt% Al stabilizing the α-phase which has HCP structure and 4wt% V stabilizing the β-phase which has BCC structure. The two phases have different properties given by their structures, with α exhibiting greater strength yet lower ductility and formability (Tiley, 2002). The microstructure at equilibrium and in room temperature consists mainly of α-phase ($\approx$95%) with some retained β-phase. The various physical properties of this alloy are dependent on factors such as thermo-mechanical processing, chemical composition, and interstitial impurities, mainly oxygen (Odenberger, 2005). Commercial purity (CP) Ti-6Al-4V contains (0.15-0.18) wt% oxygen whereas extra low interstitial (ELI) Ti-6Al-4V contains (0.1-0.13) wt% oxygen. ELI Ti-6Al-4V has lower room temperature strength than CP Ti-6Al-4V whereas the latter has lower elongation and fatigue life (Tiley, 2002). Low-temperature plasticity in α-Ti is extremely sensitive to the concentration of the interstitial impurities. The chemical composition of the material used in this work is shown in

Table 3.1: Chemical composition given in wt%. Remaining is Ti.

Alloy:	Al	V	O	Fe	C	H	N
1	6.19	3.98	0.162	0.21	0.01	0.0082	0.0062
2	6.02	4.07	0.152	0.0.15	0.003	0.0012	0.01

table 3.1. Two different materials were used for the work performed in this thesis. The material used in modeling of low strain rate behavior is denoted as Alloy 1 and the

material used in high strain rate modeling is denoted as Alloy 2. Though both materials fall under the same specification, their heat treatment regimes differ substantially.

The common heat treatments employed for Ti-6Al-4V are mill annealing, duplex annealing and solution treatment (Donachie, 1988). Mill annealing is achieved by keeping the specimen at $720\,^{\circ}$C for about an hour, followed by slow cooling. This will result in a microstructure of globular β in an α matrix which is soft and machinable. β-annealing or duplex annealing is achieved by 30min annealing at $1030\,^{\circ}$C, followed by air cooling and 2h aging at $730\,^{\circ}$C. Solution treating or $\alpha+\beta$ field annealing consist of keeping the material at $950\,^{\circ}$C for 10min followed by 4h annealing around $600\,^{\circ}$C and air cooling. Table 3.2 shows the variation of mechanical properties with heat treatment. If properly processed, this alloy can have better strength than α or β alloys (Donachie, 1988).

Table 3.2: Effect of processing on material property.

Heat treatment:	Yield strength (MPa)	Elongation (%)
Mill Annealed	945	10
Duplex Annealed	917	18
Solution Treated	1103	13

Alloy 1 was supplied as 12mm thick plates by ATI Allvac®, USA. It is checked for defects using ultrasonic technique and has undergone annealing heat treatment for 6h at 790℃. The material is free from the hard and brittle α-case (oxygen rich surface layer). Cylindrical specimens machined from the plates were used in the experiments. The axis of the specimens is oriented in the transverse direction of rolling. Alloy 2 was supplied as 8mm rolled rods by Harald Pihl AB, Sweden. It has been verified defect free and has undergone annealing heat treatment for 1.5h at 700℃ followed by air cooling and center-less grinding.

The morphology of Ti-6Al-4V can be classified as lamellar, equiaxed and a mixture of both. The lamellar structure can be controlled by heat treatment. The cooling rate from above the β-transus temperature determines the size of the lamellas. Higher cooling rate implies finer lamellas. The equiaxed microstructures can be obtained by extensive mechanical working in the $(\alpha + \beta)$ phase region during which, the lamellar α breaks up into equiaxed α. The bimodal type of microstructure is obtained by annealing for 1hr at $995\,^{\circ}$C followed by cooling and aging at $600\,^{\circ}$C. The result is a structure consisting of isolated primary α grains in a transformed β matrix (Westman, 2003).

3.1   Phase evolution

The temperature at which α changes to β (β-transus) depends on the composition of Al and V (see figure 3.1). The β-transus is also sensitive to interstitial impurity; for example, higher amount of oxygen will raise β transus , whereas higher amounts of Fe will lower it (Prasad et al., 2001). Depending on the processing conditions, this alloy can form two
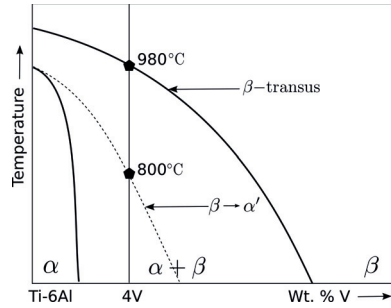
Figure 3.1: Ternary phase diagram.

stable phases (α and β), two metastable phases ($\alpha\prime$ and $\alpha\prime\prime$) and the intermetallic phase α_2

3.1.1 The primary phases (α, β)

When cooled from β-transus temperature (980 °C), the HCP α-phase starts to form as plates with basal plane parallel to a special plane in β-phase. The growth is fast along the plates as compared to the perpendicular direction. Later, this develops to parallel α plates with β trapped between them. Also, the plates formed parallel to one plane of β will meet plates formed with another plane which is demonstrated schematically in figure 3.2. This process is referred to as 'sympathetic nucleation and growth' which results in a structure commonly known as 'Widmanstätten' (Williams and Lütjering, 2003). The
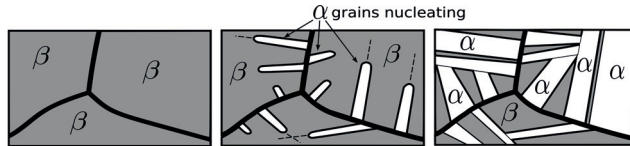
Figure 3.2: Formation of the Widmanstätten structure.

kinetics of beta to alpha transformation has been studied by Malinov et al., 2001a using DSC at continuous cooling conditions with constant cooling rates. Figure 3.3 shows the fraction of α phase formed during cooling from 1000 °C at varying rates. The V-enriched BCC β-phase is present between 5% to 10% in Ti-6Al-4V at room temperature and it plays a minor role in strengthening because of its small proportion. As discussed by Picu and Majorell, 2002, the mechanical behavior changes remarkably only when the amount of β becomes larger than 50%. The microstructure is composed entirely of β above 980 °C.

3.1.2 The metastable phases ($\alpha\prime$, $\alpha\prime\prime$)

The physical and mechanical properties of Ti-6Al-4V are very much influenced by the presence of metastable phases which are formed during rapid cooling. One such phase is
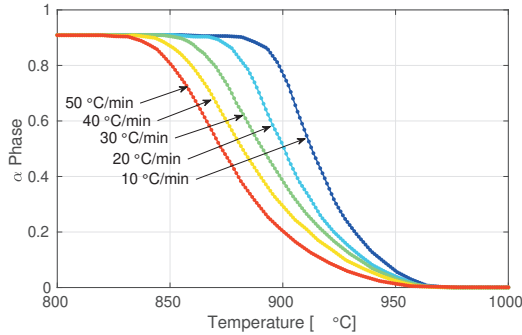
Figure 3.3: α phase fraction evolving with temperature.

the acicular $\alpha\prime$ (see figure 3.1 for its formation temperature) which has HCP structure and due to its rapid nucleation and growth contains a higher dislocation density compared to the primary α grains. Hence, the deformation mechanisms in $\alpha\prime$ are similar to those in α, with the main difference being a higher dislocation density in the undeformed state and a smaller plate thickness. Both the smaller grain size and the higher dislocation density suggest that $\alpha\prime$ is harder than the α. Also, this phase can undergo more strain hardening than α phase. Massive $\alpha\prime$ is very similar to acicular $\alpha\prime$ but is formed at lower cooling rates. Another metastable phase in Ti-6Al-4V is the $\alpha\prime\prime$ with a rhombic structure instead of hexagonal (Moiseyev, 2005). This can be considered as an intermediate between HCP and BCC with the mechanical properties close to that of the α phase.

3.1.3 The intermetallic phase (α_2)

During heating of Ti-6Al-4V above 500 °C, alloy element partitioning takes place leaving a larger % fraction of elements like Al, O, and Sn available for enriching the alpha phase. This leads to the precipitation of the coherent Ti$_3$-Al particles which is also known as α_2 phase. These particles can be sheared by dislocations and also can have an extensive pileup of dislocations against boundaries (Williams and Lütjering, 2003). Ti$_3$-Al particles grow in ellipsoidal shape with its long axis parallel to the c-axis of the hexagonal lattice. The presence of O and Sn can further enhance the precipitation of this intermetallic phase.

3.2 Plastic flow

Plastic flow of Ti-6Al-4V subjected to a wide range of temperatures and strain rates have been reported in the literature (Semiatin and Bieler, 2001; Park et al., 2002; Bruschi et al., 2004; Khan et al., 2007; Li, 2000; Nemat-Nasser et al., 2001; Prasad and Seshacharyulu, 1998; Semiatin et al., 1999a; Semiatin et al., 1998; Ding and Guo, 2004; Ding et al., 2002; Johnson et al., 2003a; Johnson et al., 2003b; Kailas et al., 1994; Vanderhasten et al., 2007;

Mosher and Dawson, 1996; Sheppard and Norley, 1988; Barnett et al., 2000; Montheillet, 2002; Fujii and Suzuki, 1990; Nicolaou et al., 2005; Khan and Yu, 2012; Khan et al., 2012; Tabei et al., 2017). The flow curves obtained from compression testing in the range of

(a) $\dot{\varepsilon} = 0.001 s^{-1}$.
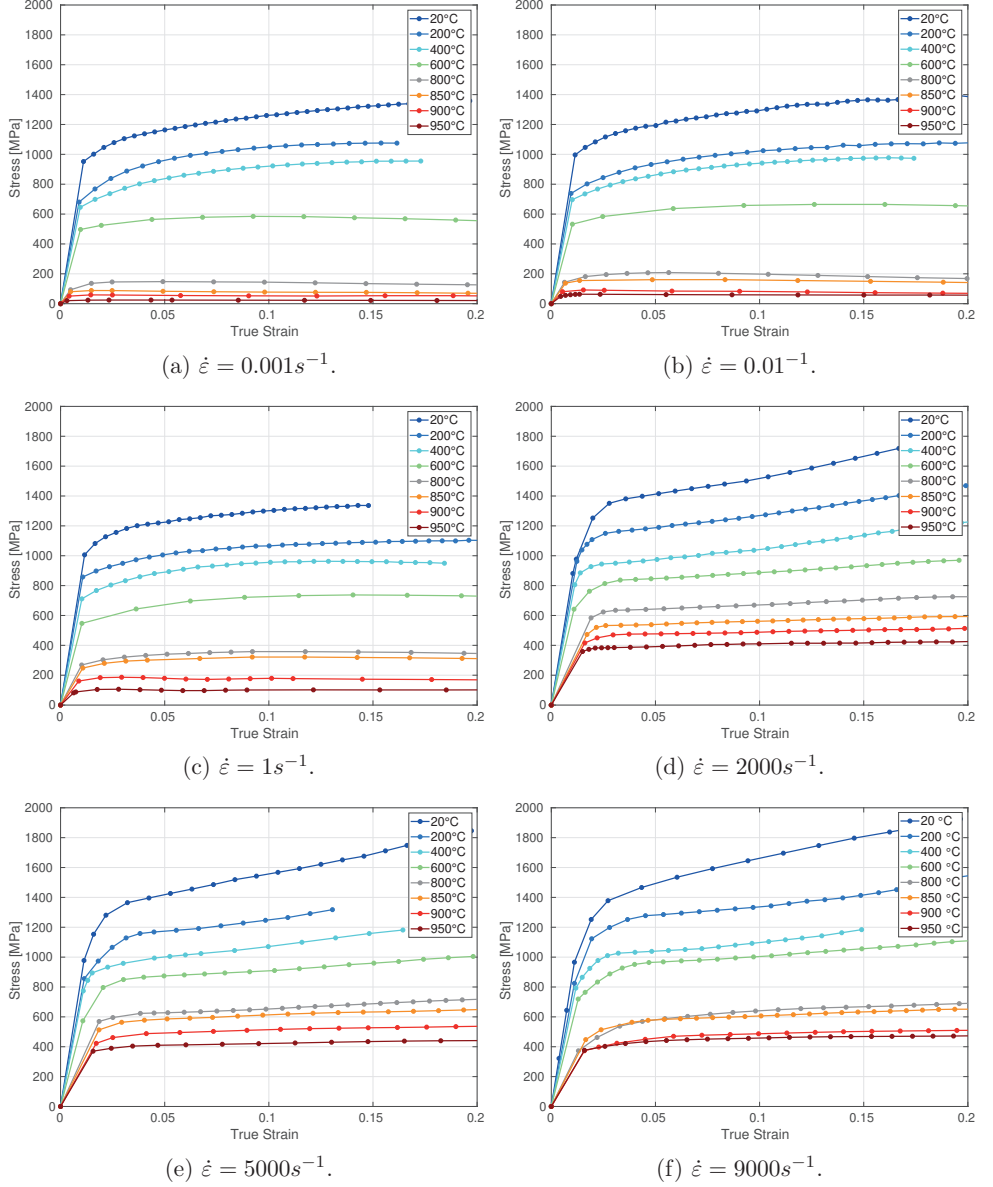
(b) $\dot{\varepsilon} = 0.01^{-1}$.

(c) $\dot{\varepsilon} = 1 s^{-1}$.

(d) $\dot{\varepsilon} = 2000 s^{-1}$.

(e) $\dot{\varepsilon} = 5000 s^{-1}$.

(f) $\dot{\varepsilon} = 9000 s^{-1}$.

Figure 3.4: Stress vs Strain curves.

temperatures from $20\,^{\circ}\mathrm{C}$ to $950\,^{\circ}\mathrm{C}$ and strain rates from $10^{-3}\mathrm{s}^{-1}$ to $9000\mathrm{s}^{-1}$ are given in figures 3.4a to 3.4f. See Babu and Lindgren, 2013 for the complete set of curves from the low strain rate tests. The compression tests performed at low strain rates between $20\,^{\circ}\mathrm{C}$ to $500\,^{\circ}\mathrm{C}$ resulted in hardening followed by fracture and at temperatures between $600\,^{\circ}\mathrm{C}$ to $900\,^{\circ}\mathrm{C}$ resulted in flow softening after the initial hardening. It can be noted that at temperatures nearing to $1000\,^{\circ}\mathrm{C}$, the material behavior is close to elastic-perfectly plastic. During high strain rate deformation, all the curves demonstrated hardening at a reducing rate with temperature. Since the flow curves are smooth and do not exhibit serrations, the presence of dynamic strain aging can be ruled out.

3.2.1 Strain rate sensitivity

At temperatures below room temperature, the temperature sensitivity is dependent on the Al concentration. This effect can be modeled by considering the Peierls stress to be dependent on the Al concentration, or by defining an equivalent Peierls stress. Additionally, the activation energy for self-diffusion of Ti in the α-phase is similar to that for self-diffusion of substitutional Al in Ti-6Al-4V. From this, it can be concluded that deformation in this temperature regime is controlled by the thermal activation of dislocations over short-range obstacles (Chichili et al., 1998).
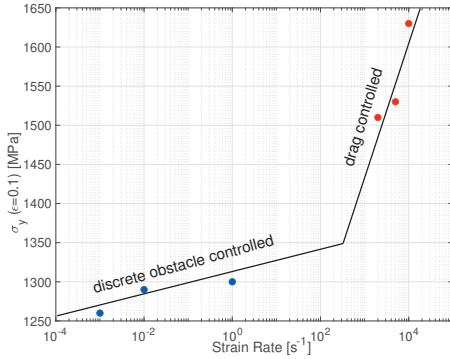
Figure 3.5: Stress vs Strain Rate at $20\,^{\circ}\mathrm{C}$.

Figure 3.6: $\sigma_y(T, \dot{\varepsilon}, \varepsilon = 0.1)$.

Stress vs strain rate at a strain of 10% is given in figure 3.5. At about a strain rate of $10^3 s^{-1}$, the material exhibits a dramatic increase in strength with deformation rate. This can be attributed to a change in deformation mechanism from obstacle controlled plasticity to dislocation drag controlled plasticity (Lesuer, 2000). From figure 3.6, it can be seen that the material is almost strain rate insensitive at lower temperature and sensitivity increases rapidly towards the β-transus temperature. According to Majorell et al., 2002, the increase in strain rate sensitivity in the high-temperature range can be attributed to its large grain size. Grain boundary sliding close to the β-transus can also lead to the increase in strain rate sensitivity. Nemat-Nasser et al., 2001 studied the dependence of flow stress on temperature and strain rate for various strains and material microstructure. The flow stress is more sensitive to temperature than to strain rate.
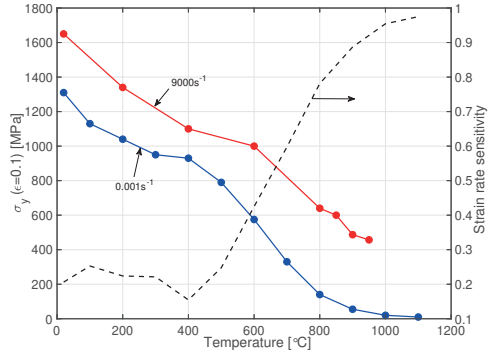
Based on this results and other supporting literature, they have identified the thermally activated mechanisms for dislocation motion.

3.2.2 Hall-Petch relation

The HCP structure has limited independent slip systems and this lead to high grain boundary strengthening. The Hall-Petch relation is valid also in two-phase $\alpha+\beta$ titanium alloys with Widmanstatten or colony alpha microstructures. Since the α phase is much stronger compared to β, it can be assumed that the phenomena related to grain boundary strengthening is occurring only inside the α phase and the β phase can be considered as a grain boundary (Semiatin and Bieler, 2001). The flow stress of Ti-6Al-4V is independent of colony size at temperatures between 815 °C and 955 °C. This suggests that plastic flow is controlled by glide and climb of dislocations at these temperatures.

3.2.3 Flow softening

Flow softening (reduction of resistance to plastic flow) is observed during low strain rate compression tests at temperatures between 500 °C and 800 °C in Ti-6Al-4V (see figure 3.7). This can be attributed to adiabatic heating, dynamic microstructural changes, localization etc. Deformation heating can be ruled out in this case because of the low strain rates applied. Microstructural changes include a change in volume fraction of the phases, morphology change, substructure change, recrystallization, etc. Localization denotes shear band formation and damage.

Figure 3.7: Flow softening.

Recrystallization

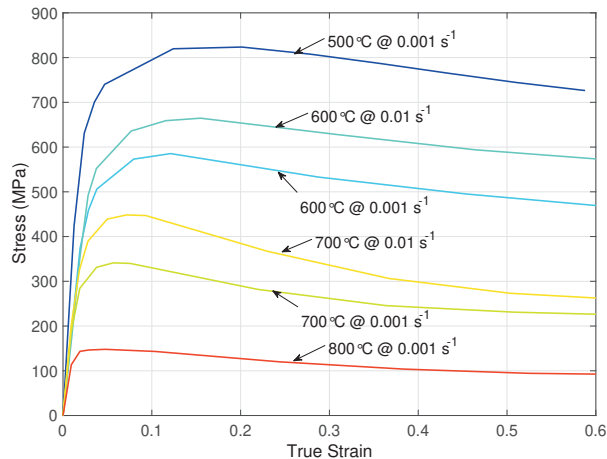The deformation characteristics of Ti-6Al-4V during torsion in the temperature range (800-1150) °C have been studied by Sheppard and Norley, 1988. Based on optical and electron microscopy studies, they have established that dynamic recovery is the operative deformation mechanisms in the β-region, while DRx predominates in the $\alpha + \beta$ region. Majorell et al., 2002 observed no significant recrystallization in Ti-6Al-4V during forging in the $\alpha + \beta$ domain, particularly when the forging operation is followed by quenching. Limited recrystallization is observed even inside deformed adiabatic shear bands where the total strain, the strain rate, and temperature are much higher than usually encountered in a homogeneous test.

Deformation of Ti-6Al-4V at a strain rate of $5 \cdot 10^{-4}\text{s}^{-1}$ from room temperature to 1050 °C has been studied by Vanderhasten et al., 2007. Using microstructural, EBSD and mechanical investigations, they observed that from 650 °C to 750 °C, grain boundary sliding is the dominant mechanism. Between 750 °C and 950 °C, DRx and grain growth occur that result in superplasticity and at higher temperatures, it is only grain growth.

Globularisation

Grain growth is usually observed during superplastic deformation of this material. In specimens with larger grains tested under conditions described by Picu and Majorell, 2002, superplasticity does not occur and a negligible amount of grain growth is observed. Grain boundary sliding occurs in all specimens at high temperatures. This phenomenon is reflected in the much larger activation energy of the deformation than that for self-diffusion (Meier and Mukherjee, 1990). Sargent et al., 2008 have observed that, in Ti-6Al-4V, static and dynamic coarsening occur at elevated temperatures (650-815℃) and dynamic coarsening occurs at a faster rate as compared to the static. The deformation energy stored as dislocations and the supplied thermal energy provide the driving force for this grain growth. Coarsening also results in the grain becoming more globular; hence, it is called globularization. During coarsening, grain boundaries move through the lattice and annihilate the dislocations, thereby resulting in a reduction of the dislocation density (Jessell et al., 2003). Thus, globularization reduces the flow stress of the material. The mechanisms of globularisation are studied by Stefansson et al., 2002 and they identified that recovery induced substructure in α-phase and α-β interface energy can affect the rate of globularisation. This phenomenon was modeled using analytical and numerical techniques by Semiatin et al., 2005. Stefansson and Semiatin, 2003 observed that during deformation and shortly afterwards, globularization is driven by dislocation substructure resulting in boundary splitting and edge spheroidization. This is followed by a second stage characterized by grain coarsening. This is similar to the two-stage process of dynamic and static recrystallization. Bai et al., 2012, based on experimental evidence, demonstrated the mechanism of globularization and how it leads to flow softening.

During deformation, the lamellar microstructure is fragmented by the formation of kinks (Park et al., 2008b; Mironov et al., 2009). Globularization occurs at this kinked alpha plates where some grains grow and become globular subsequently reducing the
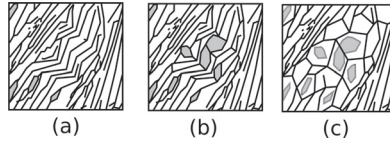
Figure 3.8: Schematic diagram of globularization: (a) Lamella kinking (b) Fragmentation (c) Grain growth.

aspect ratios. These phenomena are shown in the schematic diagram described in figure 3.8. Quantification of globularization has been attempted by many authors (Shell and Semiatin, 1999; Semiatin et al., 1999b; Poths et al., 2004; Kedia et al., 2018). These works have been based on analyzing the images using ImageJ software (Schneider et al., 2012) and estimating the globularization by measuring the aspect ratios of the lamellae. Grains with aspect ratios less than 2.0 are accounted as fully globularized.

3.2.4 Localization

Concentration of defects in regions of highest principal strain leads to localization. The specimens fractured catastrophically during the compression tests at temperatures between $20\,°C$ to $500\,°C$, and at strain rates between $10^{-3}s^{-1}$ to $1s^{-1}$. This can be attributed to shear banding and cavity nucleation which is common for most metals deformed at low temperature. During high strain rate loading between 2×10^3 to 9×10^3 s^{-1}, all test specimens showed effects of localization to a varying extent.

Shear banding

Kailas et al., 1994 have studied the failure mechanism of Ti-6Al-4V at low temperatures and strain rates. They have attributed this to adiabatic shear banding and classified the instabilities as 'geometric' as opposed to 'intrinsic' and therefore independent of the dynamic constitutive behavior. Fujii and Suzuki, 1990 have observed strain localization at soft β regions close to grain boundary α which is formed at the roots of α side plates near the grain boundary alpha. This is assisted by the presence of β stabilizing elements.

Cavitation

Nicolaou et al., 2005 observed that during torsional loading of Ti-6Al-4V specimens with colony microstructure, cavities appeared along prior-β grain boundaries and triple points. The concentration of cavities was higher along the boundaries perpendicular to the direction of the loading. The cavities grew in an elliptical manner and there were evidence of dynamic globularisation of colony microstructure in the vicinity of the cavity. The effect of local crystallographic texture on the size of cavities formed during hot tension tests for colony microstructure was studied by Thomas et al., 2005. Cavity growth was found to be most rapid at a location where (20-40)% of the area surrounding the cavity also had colonies with soft orientations.

Semiatin et al., 1998 studied the kinetics of cavitation during hot tension tests of Ti-6Al-4V at strain rates from 10^{-2}s^{-1} to 3s^{-1}. The cavity growth rate was measured to be exponentially increasing with strain. But at a temperature close to β-transus, the alloy exhibited ductile rupture with no evidence of cavitation. With decreasing temperature, the cavities grew at the expense of ductility.

3.3 Thermo-physical properties

Thermo-physical properties like elastic modulus, Poisson's ratio, thermal strain, density, heat capacity, thermal conductivity etc for Ti-6Al-4V have been measured by many which is provided in figures (3.9 to 3.12).

3.3.1 Elastic modulus and Poisson's ratio

The Young's modulus obtained from isothermal tension tests are given in figure 3.9. Figure 3.9 also shows the temperature dependent Young's modulus and Poisson's ratio of the alloy obtained from the literature (Fukuhara and Sanpei, 1993) along with own measurements of elastic modulus.

3.3.2 Density

The density of Ti-6Al-4V from Mills, 2002 is given in figure 3.10. This is based on the room temperature data of density and thermal expansion coefficient. Mills, 2002 has shown that this is in good agreement with measurements in the liquid phase.
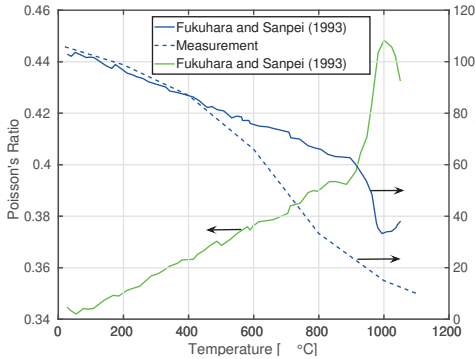

Figure 3.9: E-modulus and Poissons Ratio.
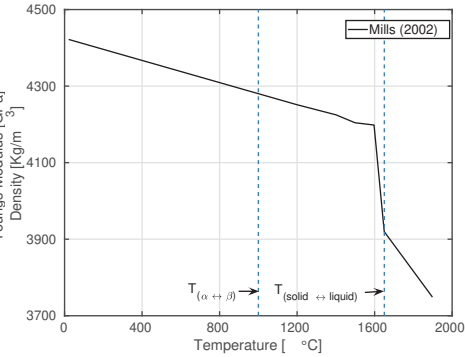

Figure 3.10: Density.

3.3.3 Heat capacity

The specific heat capacity of Ti-6Al-4V is given in figure 3.11 with data from Bros et al., 1994; Boivineau et al., 2006; Pederson, 2004. The measurements of Boivineau et al.,

2006 and Pederson, 2004 performed using a Differential Scanning Calorimeter (DSC) are in good agreement and gives the latent heat of phase transformation ($\alpha \to \beta$) to be 62kJ/Kg and 64kJ/Kg respectively (computed between $935-1000\,°C$). The latent heat of fusion is measured by Boivineau et al., 2006 to be (290 ± 5)kJ/Kg.
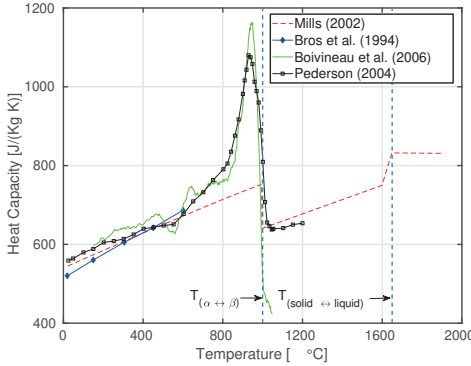
Figure 3.11: Specific Heat Capacity.
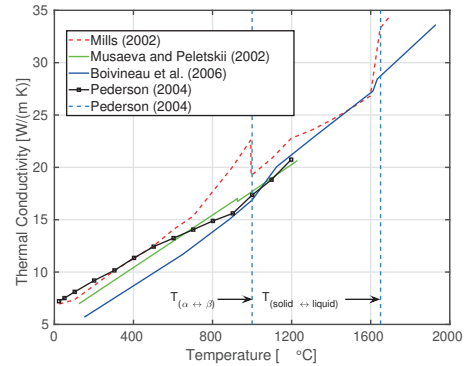
Figure 3.12: Thermal Conductivity.

3.3.4   Thermal conductivity

The thermal conductivity of Ti-6Al-4V is given in figure 3.12 with data from Mills, 2002; Musaeva and Peletskii, 2002; Pederson, 2004; Boivineau et al., 2006. Boivineau et al., 2006 measured the thermal conductivity from electrical resistivity based on the Wiedemann–Franz law (Franz and Wiedemann, 1853) whereas Pederson, 2004 used a laser flash technique.

3.3.5   Thermal dilatation

Pederson, 2004; Elmer et al., 2005; Swarnakar et al., 2011 have performed X-Ray diffraction measurements to study the volumetric expansion of unit cells of α and β phases during heating (see figure 3.13 for data from Elmer et al., 2005). Figure 3.13 also shows the total linear thermal strain measured using a differential expansion dilatometer. This data is used to develop a model for arbitrary phase composition using the rule of mixtures.

3.3.6   Diffusivity

The mechanism of diffusion in Ti systems is less understood and the published diffusion data shows large scatter which is attributed to the variation in measurement techniques (Liu and Welsch, 1988; Mishin and Herzig, 2000). Figure 3.14 shows measurement of the self diffusion in α and β Ti by Mishin and Herzig, 2000 and the measurement by Semiatin et al., 2003 for Al diffusion in β phase of Ti-6Al-4V. Lattice diffusion is responsible for dislocation climb at high temperatures. However, at intermediate temperatures, diffusion
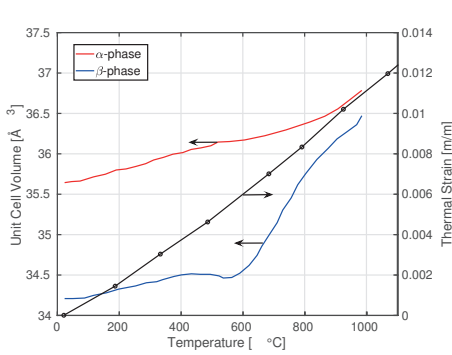
Figure 3.13: Volume expansion and ε_{th}.
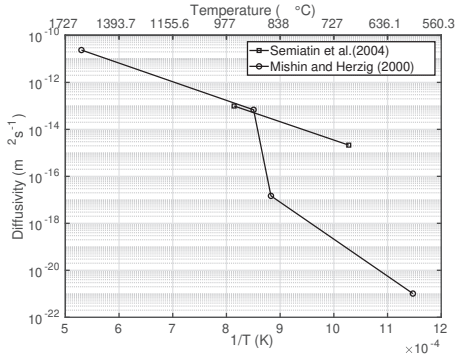
Figure 3.14: Measurements of diffusion.

along dislocation lines referred to as core or pipe diffusion has a larger effect on the climb (Prinz et al., 1982). It has been reported that dislocations in the Ti-6Al-4V act as high diffusivity paths leading to an enhanced diffusion (Park et al., 2008a). While studying the static grain growth of fine-grained Ti-6Al-4V ($g < 2\mu m$), Johnson et al., 1998 has concluded that grain boundary and pipe diffusion are the controlling mechanisms at temperatures less than $0.5T_{melt}$.

3.4   Creep

Barboza et al., 2006 studied the creep behavior of the Ti–6Al–4V with a Widmanstätten microstructure under constant tensile loads. They have observed that the creep strain rate of Ti–6Al–4V alloy is lower than that of elemental Ti. The creep resistance of Ti–6Al–4V has been attributed to α-β interfaces acting as obstacles to dislocation motion and to the large grain size. The increase of grain size reduces the grain boundary sliding, number of sources for dislocations and the rate of oxygen diffusion along grain boundaries. The increase in tertiary creep rate is related to nucleation and coalescence of microvoids which result in necking. The activation energy for creep in β-Ti is close to that for self-diffusion and therefore can be assumed to be a diffusive transport mechanism (Frost and Ashby, 1982).

The creep failure mechanisms of Ti–6Al–4V alloy in various heat treating conditions have been investigated by Seco and Irisarri, 2001. Mill annealed specimens showed the lowest creep resistance and its metallographic analysis revealed that the temperature-activated dislocation climb is the mechanism responsible for the failure. The observed voids were generated by plastic deformation, rather than by creep cavitations. β-annealed specimens demonstrated the highest creep resistance. The fracture surfaces of these broken specimens exhibited an intergranular morphology that was attributed to grain boundary sliding along the former beta grains. $\alpha+\beta$ field annealed samples underwent diffusional creep by nucleation and coalescence of the creep cavities generated at the alpha–beta interfaces and the triple points.

3.5 Dominant deformation mechanisms

The scope of this work is limited to the strain rates between 10^{-3}s^{-1} to 10^4s^{-1} and temperature between $20\,^{\circ}\text{C}$ to $1100\,^{\circ}\text{C}$. Here, at the lower temperature, interstitial solutes concentration (C_s) control the plastic flow whereas, at a higher temperature, it is the concentration of interstitial impurities (C_i) that has control (Conrad, 1981). Studying the effect of strain (ε), strain rate ($\dot{\varepsilon}$), temperature (T) and grain size (g) on Ti systems, Conrad arrived at the following additive strengthening relationship.

$$\sigma_y = \sigma_G(G, \varepsilon, g, C_s) + \sigma^*(T, \dot{\varepsilon}, C_i) \tag{3.1}$$

Here, first component varies with temperature through the temperature dependence of the shear modulus (G). The second component is strain rate dependent and has short range influence. The underlying mechanism of plastic flow is identified as dislocation motion by glide and climb which is assisted by diffusion (Conrad, 1981).

At strain rates greater than 10^3s^{-1}, the interaction of moving dislocations with phonons and electrons can provide additional strengthening (Frost and Ashby, 1982). This viscous drag component can be written as $\sigma_{drag}(G, \dot{\varepsilon})$, which can be considered as a third component to equation 3.1

Models for Plastic Flow of Ti-6Al-4V

"Essentially, all models are wrong,
but some are useful."

George Box

Engineering or empirical models are determined by means of fitting model equations and parameters with experimental data without considering the physical processes causing the observed behavior. This kind of modeling approach is more common in engineering applications and therefore got the name (Domkin, 2005).

Physically based material models, on the other hand, are models where knowledge about the underlying physical process, dislocation processes etc, is used to formulate the constitutive equations. Naturally, the division between these kinds of models is somewhat arbitrary. Both types of models can be considered "engineering". Developing a physically based model requires more experiments and analysis in different scales as compared to empirical models.

Despite their good fit to the measured stress-strain curves within a certain range of strains, strain rates, and temperatures, empirical relations have little predictive power beyond that range of deformation conditions and material microstructure used for their calibration. The tabulated data approach has the same limitations as extrapolation is not recommended outside the range of the experimental data.

4.1 Empirical models

Empirical models like Johnson-Cook, modified KHL, Sellars-Tegart and polynomial models are used to simulate the mechanical constitutive behavior of Ti-6Al-4V by different researchers.

4.1.1 Johnson-Cook model

Johnson and Cook, 1985 model has been widely used to model the high strain rate deformation of metals. The yield stress can be written as

$$\sigma_y = (A + B\bar{\varepsilon}^{p^n})(1 + C\ln\dot{\varepsilon}')(1 - (T')^m) \tag{4.1}$$

where, A is the quasi-static yield strength of the material, $\bar{\varepsilon}^p$ is the equivalent plastic strain, and $\dot{\varepsilon}' = \dot{\bar{\varepsilon}}^p/\dot{\varepsilon}^{ref}$ is non-dimensionalised plastic strain rate. T' is the non-dimensional temperature calculated by

$$T' = \frac{T - T_{room}}{T_{melt} - T_{room}} \tag{4.2}$$

The temperature change from adiabatic heating can be computed by

$$\Delta T = \frac{\alpha}{\rho C} \int \sigma d\varepsilon \tag{4.3}$$

where, α is the percentage of plastic work converted to heat, ρ is the mass density of the material and C is the specific heat of the material. Fracture is computed using cumulative damage law (Lesuer, 2000)

$$D = \Sigma\frac{\Delta\varepsilon^p}{\varepsilon_f} \tag{4.4}$$

where the failure strain is computed as

$$\varepsilon_f = [D_1 + D_2\exp D_3\sigma'][1 + D_4\ln\dot{\varepsilon}'][1 + D_5 T'] \tag{4.5}$$

Here $\Delta\varepsilon^p$ is the increment of plastic strain in a load increment, σ' is the mean stress normalized by the effective stress and D_1, D_2, D_3, D_4, D_5 are constants. Failure occurs when $D = 1$. The parameters of the model are given in table 4.1.

Table 4.1: Material parameters estimated.

Reference	A	B	n	C	m	D_1	D_2	D_3	D_4	D_5
	MPa	MPa	10^{-2}	10^{-4}	10^{-1}	10^{-2}	10^{-1}	10^{-1}	10^{-3}	10^{-2}
Westman, 2003	Not Published									
Lee and Lin, 1997	724.7	683.1	47	350	10					
Meyer and Kleponis, 2001	896	656	50	128	8					
Lesuer, 2000	862	331	34	120	8	-9	2.5	-5	-14	387
Lesuer, 2000	1098	1092	93	140	11	-9	2.5	-5	-14	387

A modified version of the Johnson-Cook model is used for Ti-6Al-4V by Seo et al., 2005 and is found to be a good representation of the material behavior at high strain rates.The main advantages of this model are its ease of calibration and implementation and its robustness. Therefore it is very commonly used in Finite Element simulations of machining. According to Meyer and Kleponis, 2001, the strain rate hardening of Ti-6Al-4V is poorly described by this model. Tabei et al., 2017 described the inconsistencies and inaccuracies of the JC model.

4.1.2 Modified-KHL model

Khan et al., 2004 has developed a model for the high strain rate deformation of Ti-6Al-4V. According to this model, yield stress can be written as

$$\sigma_y = \left[A + B \left(1 - \frac{ln\dot{\bar{\varepsilon}}^p}{D_p^o} \right)^{n1} \bar{\varepsilon}^{p^{n_o}} \right] \left(\frac{\dot{\bar{\varepsilon}}^p}{\dot{\varepsilon}^*} \right)^C \left(\frac{T_m - T}{T_m - T_{ref}} \right)^m \tag{4.6}$$

where, $\bar{\varepsilon}^p$ is the equivalent plastic strain, T_m, T_{ref}, T are the melting, reference and, current temperature, $D_p^o = 10^6$ is the upper-bound of plastic strain rate, $\dot{\varepsilon}^*$ is the plastic strain rate at which certain parameters are identified. $\dot{\bar{\varepsilon}}^p$ is the current plastic strain rate and A, B, n_1, n_o, C and, m are the material parameters to be estimated. The parameters of the model are given in table 4.2.

Table 4.2: Parameters estimated by Khan et al., 2004

A	B	n_1	n_o	C	m
1069	874.8	0.5456	0.4987	0.02204	1.3916

4.1.3 Sellars-Tegart model

A rate dependent model for plastic flow can be written as

$$\dot{\bar{\varepsilon}}^p = AF e^{\frac{-Q}{RT}} \tag{4.7}$$

$$F = \begin{cases} \sigma_y^n & \text{if } \alpha\sigma_y < 0.8 \\ e^{\beta\sigma_y} & \text{if } \alpha\sigma_y > 1.2 \\ (sin(\alpha\sigma_y))^n & \text{for all } \sigma_y \end{cases} \tag{4.8}$$

where σ_y is the yield stress, Q is the activation energy, R is the gas constant and T is the absolute temperature in kelvin. Lee and Lin, 1997 has chosen $F = (sin(\alpha\sigma_y))^n$. Other parameters of the model are given in table 4.3.

Table 4.3: Material parameters estimated.

Reference	α	n	A
Lee and Lin, 1997	0.0012	38.01	$A(\dot{\bar{\varepsilon}}^p)$

4.1.4 Polynomial relation model

Westman, 2003 used a polynomial model to compute the flow stress as below

$$\sigma_y = A(B + C\bar{\varepsilon}^{p^{1/n}}) \tag{4.9}$$

$$A = a_0 + a_1 T + a_2 T^2 + a_3 T^3 \tag{4.10}$$

$$n = n_0 + n_1 T \tag{4.11}$$

Where, T is the temperature and $B, C, a_0, a_1, a_2, a_3, n_0, n_1$ are material parameters which were not published.

4.2   Physically-based models

The physically based models used in literature can be divided into explicit physical models and implicit physical models.   Explicit physical models contain physical parameters computed from evolution equations and are coupled to the constitutive model. In the implicit model, the form of the constitutive equation is determined based on knowledge about the physical process. Though this approach is phenomenological, it has a strong hold on the underlying physics observed during experiments..   This approach is referred to as "model-based-phenomenology" (Frost and Ashby, 1982).

4.2.1   Armstrong-Zerilli (AZ) model

AZ model (Zerilli and Armstrong, 1998) has been used by Macdougall and Harding, 1999; Meyer and Kleponis, 2001 to model flow stress behavior of Ti-6Al-4V. According to AZ model, the yield strength can be written as

$$\sigma_y = C_0 + C_1 e^{(-C_3 T + C_4 \ln \dot{\bar{\varepsilon}}^p)} + C_5 \bar{\varepsilon}^{p^n} \tag{4.12}$$

where T is the absolute temperature, $\bar{\varepsilon}^p$ is the equivalent plastic strain, $\dot{\bar{\varepsilon}}^p$ is the equivalent plastic strain rate and C_0, C_1, C_3, C_4 are material parameters to be estimated. C_5 and n are the same as B and n in the Johnson-Cook model. The parameters of the model are given in table 4.4.   This model is not recommended for temperatures above one half

Table 4.4: Parameters Estimated by Meyer and Kleponis, 2001

C_1	C_2	C_3	C_4	C_5	n
740	240	0.0024	0.00043	656	0.5

of the melting point. Meyer and Kleponis, 2001 reported that this model gave better predictions as compared to the Johnson-Cook model

4.2.2   Meyers model

The flow stress of Ti has been modeled by Meyers et al., 2002 as

$$\sigma_y = \sigma_G + C_1 \left(\frac{\dot{\bar{\varepsilon}}^p}{\dot{\bar{\varepsilon}}^{ref}} \right)^{C_3 T} + \frac{C_2}{e^{-C_4 T}} \bar{\varepsilon}^{p^n} + \frac{k_s}{\sqrt{d}} \tag{4.13}$$

where σ_G is the athermal component of stress, n is the work hardening, d is the grain size and k_s is the slip term in the Hall-Petch relation. $e^{-c_4 T}$ term will reduce work hardening with the increase of temperature. C_1, C_2, C_3, C_4, k_s are material parameters which were not published.

4.2.3   Majorell model

The total stress $\sigma_y = \sigma^* + \sigma_G$ where σ^* is the thermally activated component of stress and σ_G is the athermal component of stress. The thermally activated component of stress

for each phase can be written as

$$
\sigma_\alpha^* = \tau^0(C_{O_{eq}}) \left[1 - \left(\frac{kT}{\Delta G_{O_{eq}}} \ln \frac{\dot{\varepsilon}_0}{\dot{\bar{\varepsilon}}^p} \right)^{\frac{1}{q_{O_{eq}}}} \right]^{\frac{1}{p_{O_{eq}}}}
$$

$$
+ \tau^0(C_{Al}) \left[1 - \left(\frac{kT}{\Delta G_{Al}} \ln \frac{\dot{\varepsilon}_0}{\dot{\bar{\varepsilon}}^p} \right)^{\frac{1}{q_{Al}}} \right]^{\frac{1}{p_{Al}}} \tag{4.14}
$$

$$
\sigma_\beta^* = \tau_\beta^0 \left[1 - \left(\frac{kT}{\Delta G_\beta} \ln \frac{\dot{\varepsilon}_{0_\beta}}{\dot{\bar{\varepsilon}}^p} \right) \right]^{\frac{1}{p_\beta}} \tag{4.15}
$$

The parameters of the model are given in table 4.5.

Table 4.5: Material parameters estimated by Picu and Majorell, 2002.

$\tau^0(C_{O_{eq}})$	$\tau^0(C_{Al})$	τ_β^0	$G_{O_{eq}}$	G_β	$\dot{\varepsilon}_0$	$\dot{\varepsilon}_{0_\beta}$	$p_{O_{eq}}$	$q_{O_{eq}}$	p_{Al}	q_{Al}	p_β
1050	1080	1200	150	200	10^7	$2 \cdot 10^{13}$	0.45	1.7	0.7	2.7	0.4

$$
\Delta G_{Al} = \begin{cases} 400 & \text{if } T < 800\text{K} \\ 400 - 350\dfrac{2}{\pi}\tan^{-1}\left(\dfrac{T-800}{130}\right) & \text{if } T > 800\text{K} \end{cases} \tag{4.16}
$$

The athermal component can be written as,

$$
\sigma_{G_\alpha} = \zeta G b \sqrt{\rho} + \frac{k}{\sqrt{d}} \tag{4.17}
$$

where ζ and k are material parameters, $G = 49.02 - \frac{5.821}{e^{181/T}-1}$ is the temperature dependant shear modulus, b is the burgers vector and d is the grain size. The evolution of dislocation density is computed as

$$
\frac{d\rho}{d\bar{\varepsilon}^p} = \frac{d\rho}{d\bar{\varepsilon}^p}\Big|_{pr} + \frac{d\rho}{d\bar{\varepsilon}^p}\Big|_{re} \tag{4.18}
$$

$$
\frac{d\rho}{d\bar{\varepsilon}^p}\Big|_{pr} = a_1\sqrt{\rho} \tag{4.19}
$$

$$
\frac{d\rho}{d\bar{\varepsilon}^p}\Big|_{re} = -a_2\frac{\dot{\varepsilon}_0^{ath}}{\dot{\bar{\varepsilon}}^p}\rho\left(1 - e^{-0.7R_c^4\rho^2}\right)e^{-Q/kT} \tag{4.20}
$$

where $\dfrac{d\rho}{d\bar{\varepsilon}^p}\Big|_{pr}$ is the storage term and $\dfrac{d\rho}{d\bar{\varepsilon}^p}\Big|_{re}$ is the recovery term. $\dot{\varepsilon}_0^{ath} = 1/\Delta t$ and $\dot{\bar{\varepsilon}}^p$ are the reference and applied strain rate, Q is the activation energy of cross slip and recombination, R_c is the cut off radius for dislocations to climb or annihilate and a_2 is a proportionality constant.

Total stress in alpha and beta phases is given by

$$
\sigma_y = (1 - X_\beta)^{0.8}\left(\sigma_\alpha^* + \sigma_{G_\alpha}\right) + X_\beta^{0.8}\sigma_\beta^* \tag{4.21}
$$

where $X_\beta = (T/1270)^{10}$ is the temperature dependent fraction of β phase.

4.2.4   Nemat-Nasser model

The flow strength is written as

$$\sigma_y\left(\dot{\bar{\varepsilon}}^p, \bar{\varepsilon}^p, T\right) = \tau^0 \left\{1 - \left[\frac{kT}{G_0}\left(\ln\frac{\dot{\bar{\varepsilon}}^p f(\bar{\varepsilon}^p, T)}{\dot{\varepsilon}_0}\right)\right]^{1/q}\right\}^{1/p}$$

$$+ \quad \tau_a^0 \bar{\varepsilon}^{p^n} + f(\bar{\varepsilon}^p, T) \tag{4.22}$$

$$f = 1 + a_0\left[1 - \left(\frac{T}{T_m}\right)^2\right]\bar{\varepsilon}^{p^{1/2}} \tag{4.23}$$

where $\bar{\varepsilon}^p$ and $\dot{\bar{\varepsilon}}^p$ is the effective plastic strain and strain rate, T and T_m are the absolute and melting temperature respectively, τ^0 is the empirically determined effective stress, G_0 is the energy barrier of dislocations, $\dot{\varepsilon}_0$ is the reference strain rate, $\tau_a^0 \bar{\varepsilon}^{p^n}$ is the athermal part of the flow stress and a_0 depends on average initial dislocation spacing. This model was fit to Ti-6Al-4V with different microstructures produced with different manufacturing techniques. The material parameters of the model are given in the table 4.6.

Table 4.6: Material Parameters Estimated by Nemat-Nasser et al., 2001

Material	p	q	k/G_0	$\dot{\varepsilon}_0$	a_0	τ^0	τ_a^0	n
			$10^{-5}\mathrm{K}^{-1}$	$10^{10}\mathrm{s}^{-1}$				
Commercial[1]	1	2	6.2	1.32	2.4	1560	685	0.05
RS-HIP[2]	1	2	6.2	1.32	2.4	1620	680	0.04
RS-MIL-HIP[3]	1	2	6.2	1.32	2.4	1900	710	0.03

[1]Commercial purity Ti-6Al-4V

[2]Hot Isostatic Pressed Ti-6Al-4V

[3]Hot Isostatic Pressed material made with milled powder Ti-6Al-4V

Dislocation Density Based Model

The plastic behavior of Ti-6Al-4V is complicated as it involves varying phases and morphologies as explained in chapter 3. A constitutive model which should account for these phenomena should be based on the physics of material behavior.

5.1 Formulation of the model

The flow stress model is formulated on a homogeneous representative volume element and, it provides a bridge between various sub-micro scale phenomena and macro scale continuum mechanics. Properties of dislocations are related to macroscopic plasticity. Plastic strain is associated with the motion of dislocations, while hardening or softening is associated with the interaction of dislocations. With the increase of dislocation density, the dislocations themselves get entangled and prevent further motion which results in isotropic hardening. Due to the lattice distortion around the dislocations, elastic energy is stored in the material which also hinders the movement of the dislocations contributing to isotropic hardening. However, the internal stresses can also support dislocation movement in the opposite direction resulting in the so-called "Bauschinger effect" or kinematic hardening. Recovery and recrystallization are two competing restoration mechanisms and they balance the strain hardening. In order to compute the evolution of the material state, dislocation density and vacancy concentration are used as internal state variables in this model.
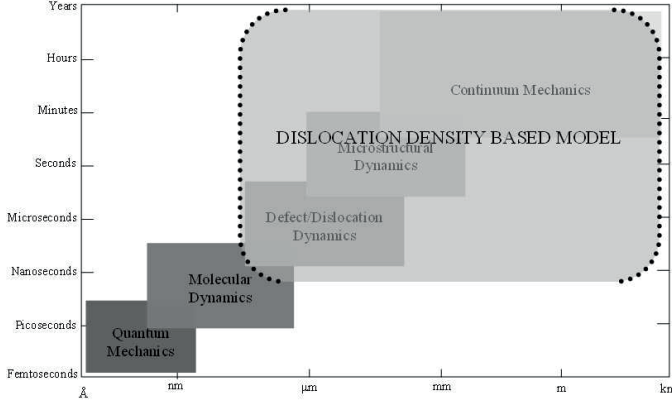
Figure 5.1: Length and time scales of deformation.

5.1.1   Bridging scales

The proposed model has the capability to connect to the microstructure of the material. This model is formulated on a homogeneous representative volume element and it provides a bridge between sub-micro scale phenomena and macron scale continuum mechanics (see figure 5.1). The flow of data from different scales is shown in figure 5.2.
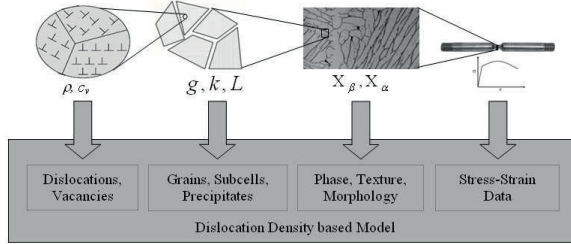
Figure 5.2: Data Flow in dislocation density based model.

5.2   Flow stress

The flow stress is split into three parts (Seeger, 1956; Bergström, 1969; Kocks, 1976; Lesuer et al., 2001; Babu and Lindgren, 2013)

$$\sigma_y = \sigma_G + \sigma^* + \sigma^{drag} \tag{5.1}$$

where, σ_G is the athermal stress contribution from the long-range interactions of the dislocation substructure. The second term σ^*, is the friction stress needed to move dislocations through the lattice and to pass short-range obstacles. Thermal vibrations can assist dislocations to overcome these obstacles. This formulation is very much in

accordance to the material behavior demonstrated by Conrad, 1981 in equation (3.1). At very high strain rates ($> 10^3 s^{-1}$), deformation rate of Ti-6Al-4V is controlled by the phonon and electron drag on moving dislocations (Lesuer, 2000). The viscous drag component of stress σ^{drag} can be computed based on a formulation proposed by Ferguson et al., 1967 and later developed by Frost and Ashby, 1982.

Long range flow stress contribution

In an isotropic and homogeneous lattice, stress field surrounding a screw dislocation can be written as

$$\tau = \frac{Gb}{2\pi r} \tag{5.2}$$

where, G is the shear modulus, b is the Burgers vector and r is the radius of the Burgers circuit.

If we assume that the number of dislocations intersecting a unit area is ρ, then the mean distance between dislocations is $\sqrt{\rho}^{-1}$. Drawing from this relation, the long-range term of equation (5.1) is derived by Seeger, 1956 as,

$$\sigma_G = m\alpha Gb\sqrt{\rho_i} \tag{5.3}$$

where m is the Taylor orientation factor translating the effect of the resolved shear stress in different slip systems into effective stress and strain quantities. Furthermore, α is a proportionality factor and ρ_i is the immobile dislocation density. The shear modulus can be computed from the Youngs modulus (E) and Poisson ratio (ν) as,

$$G = \frac{E}{2(1+\nu)} \tag{5.4}$$

Short range flow stress contribution

The strength of obstacles, which a dislocation encounters during motion determines the dependence of flow strength on applied strain rate. The dislocation velocity is related to plastic strain rate via the Orowan equation (Orowan, 1948)

$$\dot{\varepsilon}^p = \frac{\rho_m b\bar{\nu}}{m} \tag{5.5}$$

where $\bar{\nu}$ is the average velocity of mobile dislocations (ρ_m). This velocity is related to the time taken by a dislocation to pass an obstacle most of which is the waiting time. The velocity is written according to Frost and Ashby, 1982 as,

$$\bar{\nu} = \Lambda \nu_a e^{-\Delta G/kT} \tag{5.6}$$

where Λ is the mean free path, ν_a is the attempt frequency, ΔG is the activation energy, k is the Boltzmann constant and T is the temperature in kelvin. Here, $e^{-\Delta G/kT}$ can be considered as the probability that the activation energy is available.
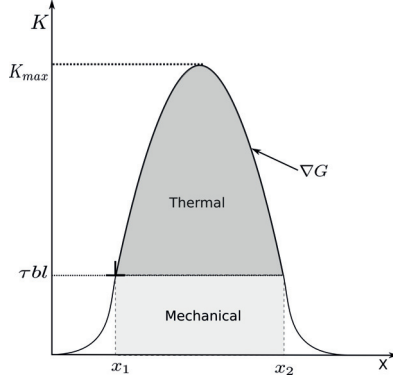
$$\dot{\bar{\varepsilon}}^p = f e^{-\Delta G/kT} \tag{5.7}$$

Figure 5.3: Obstacle Resistance

The form of the function f and ΔG depends on the applied stress, strength of obstacles etc. The stress available to move a dislocation past an obstacle is the difference between applied stress and the long-range flow stress component. Since the effective stress in the plasticity model is equal to the flow stress, $f = f(\bar{\sigma} - \sigma_G) = f(\sigma^*)$.

If obstacles of strength K as shown in figure 5.3 are arranged in a lattice with the mean spacing l, under the influence of a resolved shear stress τ, the net applied forward force is τbl. If the dislocation moves from x_1 to x_2 the net energy required is the area under the curve and part of it is supplied as the mechanical work $\tau bl(x_2 - x_1)$. The remaining energy ΔG is the free energy of activation which can be written according to Kocks et al., 1975 as

$$\Delta G = \Delta F \left[1 - \left(\frac{\sigma^*}{\sigma_{ath}} \right)^p \right]^q \tag{5.8}$$

$$0 \leq p \leq 1$$

$$1 \leq q \leq 2$$

Here, $\Delta F = \Delta f_0 G b^3$ is the activation energy necessary to overcome lattice resistance in the absence of any external force and $\sigma_{ath} = \tau_0 G$ is the shear strength in the absence of thermal energy. The parameters p and q determine the shape of the barrier either sinusoidal or hyperbolic or somewhere in between. Some guidelines for selection of Δf_0 and τ_0 are given in Table 5.1. Here l is the mean spacing of the obstacles; either precipitates or solutes. The strain rate dependent part of the yield stress from equation (5.1) can be derived according to the Kocks-Mecking formulation (Kocks et al., 1975; Mecking and Kocks, 1981) as

$$\sigma^* = \tau_0 G \left[1 - \left[\frac{kT}{\Delta f_0 G b^3} \ln \left(\frac{\dot{\varepsilon}^{ref}}{\dot{\bar{\varepsilon}}^p} \right) \right]^{1/q} \right]^{1/p} \tag{5.9}$$

Here $\dot{\varepsilon}^{ref}$ is the reference strain rate.

Table 5.1: Activation energy factor and shear strength of different obstacles from Frost and Ashby, 1982

Obstacle Strength	Δf_0	τ_0	Example
Strong	2	$> \dfrac{b}{l}$	Strong precipitates
Medium	$0.2 - 1.0$	$\approx \dfrac{b}{l}$	Weak precipitates
Weak	< 0.2	$\ll \dfrac{b}{l}$	Lattice Resistance,

Figure 5.4 shows the short range stress component in equation 5.9 plotted as a function of strain rate and temperature.
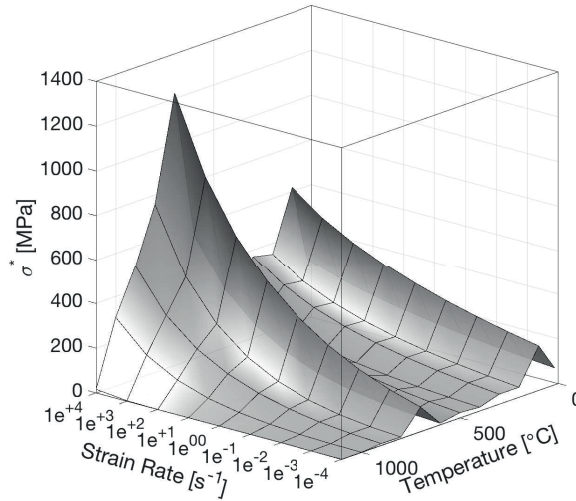
Figure 5.4: Short Range Stress

Viscous drag contribution:

At strain rates greater than 10^3s^{-1}, the interaction of moving dislocations with phonons and electrons can limit dislocation velocity. The strength of interaction is measured by the drag coefficient B with $\frac{Ns}{m^2}$ as its unit. As the temperature increases, phonon density rises and B increases linearly with temperature.

$$B = B_e + B_p \frac{T}{300} \tag{5.10}$$

where B_e is the electron drag coefficient and B_p is the phonon drag coefficient at temperature $300K$; (Frost and Ashby, 1982). Average dislocation velocity can be defined as

$$v = \frac{\sigma_{drag} b}{B} \tag{5.11}$$

Introducing the Orowan equation and combining with equation 5.11, (Frost and Ashby, 1982) proposed a rate equation where the drag coefficients characterize the opposing forces.

$$\dot{\bar{\varepsilon}} = \frac{\rho_m b^2 G \dfrac{1}{B_p}}{\dfrac{B_e}{B_p} + \dfrac{T}{300}} \left(\frac{\sigma_{drag}}{G} \right) \tag{5.12}$$

Rewriting equation 5.12, stress component σ_{drag} accounting for electron and phonon drag is derived as,

$$\sigma^{drag} = G \left(\frac{\dfrac{B_e}{B_p} + \dfrac{T}{300}}{C_{drag}} \right) \dot{\bar{\varepsilon}}^p \tag{5.13}$$

where C_{drag} and $\frac{Be}{Bp}$ are calibration parameters. Figure 5.5 shows the viscous drag stress component given in equation 5.13 plotted as a function of strain rate and temperature.
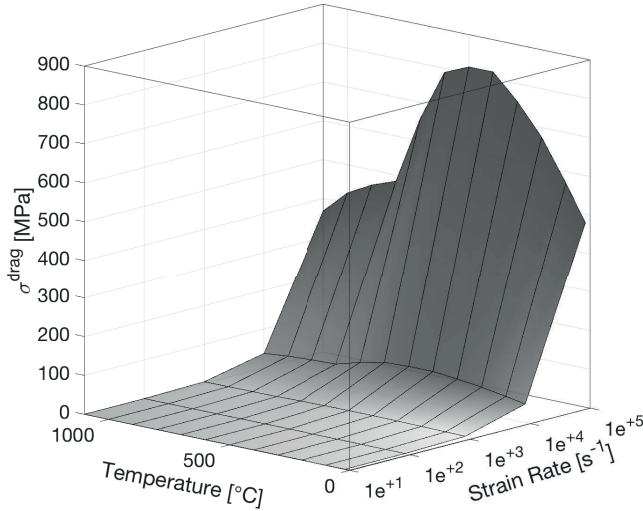

Figure 5.5: Drag Stress

5.2.1 Evolution of immobile dislocation density

The basic components for the yield stress in equation (5.1) are obtained from equations (5.3 and 5.9). However, the evolution of ρ_i in equation (5.3) needs to be computed. The model for the evolution of the immobile dislocation density has two parts; hardening and restoration.

$$\dot{\rho}_i = \dot{\rho}_i^{(+)} - \dot{\rho}_i^{(-)} \tag{5.14}$$

Hardening process

It is assumed that mobile dislocations move, on average, a distance Λ (mean free path), before they are immobilized or annihilated. According to the Orowan equation, density of mobile dislocations and their average velocity are proportional to the plastic strain rate. It is reasonable to assume that an increase in immobile dislocation density also follow the same relation. This leads to

$$\dot{\rho}_i^{(+)} = \frac{m}{b}\frac{1}{\Lambda}\dot{\bar{\varepsilon}}^p \tag{5.15}$$

where m is the Taylor orientation factor. The mean free path can be computed from the grain size (g) and dislocation subcell or subgrain diameter (s) as,

$$\frac{1}{\Lambda} = \left(\frac{1}{g} + \frac{1}{s} + others\right) \tag{5.16}$$

where *others* denote contributions from obstacles like precipitates, interstitial elements, martensite lathes etc. The effect of grain size on flow stress known as Petch-Hall relation, is accounted via this term. Models for recrystallization, grain growth, precipitation, dissolution etc can be included here (Babu, 2007).

The formation and evolution of subcells has been modeled using a relation proposed by Holt, 1970 with s_∞ as the minimum subcell size.

$$s = K_c\frac{1}{\sqrt{\rho_i}} + s_\infty \tag{5.17}$$

Restoration processes

The motion of vacancies is related to the recovery of dislocations. This usually occurs at elevated temperatures and therefore is a thermally activated reorganization process. Creation of vacancy increases entropy but consumes energy and its concentration increases with temperature and deformation. In high stacking fault materials, recovery process might balance the effects of strain hardening leading to a constant flow stress.

Recovery by Glide:
Kocks et al., 1975 has derived an equation for the evolution of mobile dislocation density which can be written as

$$\dot{\rho}_m = \rho_m\bar{\nu}\left(\frac{1}{\Lambda_{back}} - \frac{1}{\Lambda}\right) \tag{5.18}$$

where, Λ_{back} is the distance traveled by a previously emitted dislocation and $\bar{\nu}$ is the spatial average velocity of mobile dislocations. Based on the formulation by Bergström, 1983, the immobile dislocation density is proportional to the plastic strain rate.

$$\dot{\rho}_i^{(-)} = \Omega \rho_i \dot{\bar{\varepsilon}}^p \tag{5.19}$$

where Ω is a function dependent on temperature. This is analogous to Kocks formulation as ρ_i and $\dot{\bar{\varepsilon}}^p$ are proportional to ρ_m and $\bar{\nu}$ respectively.

Recovery by Climb:

In addition to dislocations, vacancies are also created during plastic deformation (Friedel, 1964). This has significant effect on diffusion controlled processes such as climb and dynamic strain aging. Militzer et al., 1994 proposed a model based on Sandstrom and Lagneborg, 1975 and Mecking and Estrin, 1980. With a modification of the diffusivity according to Babu and Lindgren, 2013, this can be written as

$$\dot{\rho}_i^{(climb)} = 2c_\gamma D_{app} \frac{Gb^3}{kT} \left(\rho_i^2 - \rho_{eq}^2 \right) \tag{5.20}$$

where, c_γ is a material coefficient, and ρ_{eq} is the equilibrium value of the dislocation density. Here D_{app} is the apparent diffusivity which includes the diffusivity of $\alpha - \beta$ phases weighted by their fractions in addition to pipe diffusion which is given in equation 5.37

Recovery by Globularisation:

The effect of globularization on the reduction of flow stress is included only when the stored deformation energy is above a critical value.

$$\text{if} \quad \rho_i \geq \rho_{cr}$$
$$\dot{\rho}_i^{(-)} = \psi \dot{X}_g \left(\rho_i - \rho_{eq} \right); \quad \text{until } \rho_i \leq \rho_{eq}$$
$$\text{else}$$
$$\dot{\rho}_i^{(-)} = 0 \tag{5.21}$$

Here, ρ_{cr} is the critical dislocation density above which globularization is initiated, ρ_{eq} is the equilibrium value of dislocation density, $\dot{X}_g$ is the globularization rate and ψ is a calibration constant. The mechanism of globularization can be modeled as a two-stage process of dynamic and static recrystallization described by Thomas and Semiatin, 2006.

$$X_g \;=\; X_d + (1 - X_d) X_s \tag{5.22}$$

Here, the volume fractions X_g, X_d and X_s denote total globularized, its dynamic component and the static component, respectively. Assuming that grain growth and static recrystallization have the same driving force, the static globularization rate can be written as (Pietrzyk and Jedrzejewski, 2001; Montheillet and Jonas, 2009),

$$\dot{X}_s \;=\; M \frac{\dot{g}}{g} \quad \text{where} \quad \dot{g} = \frac{K}{ng^{(n-1)}} \tag{5.23}$$

where, M is a material parameter. The rate of dynamic globularization is modeled based on Thomas and Semiatin, 2006 as,

$$\dot{X}_d = \frac{Bk_p\dot{\bar{\varepsilon}}_p}{\bar{\varepsilon}_p^{1-k_p}e^{B\bar{\varepsilon}_p^{k_p}}} \tag{5.24}$$

where, B and k_p are material parameters.

5.2.2 Evolution of excess vacancy concentration

The concentration of vacancies attain equilibrium if left undisturbed in isothermal conditions. When subjected to deformation or temperature change, the material generates excess vacancies. The model considered here is only concerned with mono-vacancies. The equilibrium concentration of vacancies at a given temperature according to Cahn and Peter, 1996a; Reed-Hill and Abbaschian, 1991 is

$$c_v^{eq} = e^{\frac{\Delta S_{vf}}{k}}e^{-\frac{Q_{vf}}{kT}} \tag{5.25}$$

where, ΔS_{vf} is the increase in entropy while creating a vacancy and Q_{vf} is the activation energy for vacancy formation.

Vacancy creation and annihilation

Militzer et al., 1994 proposed a model for excess vacancy concentration with the generation and annihilation components as

$$\dot{c_v}^{ex} = \dot{c}_v - \dot{c}_v^{eq} = \left[\chi\frac{\sigma b}{Q_{vf}} + \zeta\frac{c_j}{4b^2}\right]\frac{\Omega_0}{b}\dot{\bar{\varepsilon}} - D_{vm}\left[\frac{1}{s^2} + \frac{1}{g^2}\right](c_v - c_v^{eq}) \tag{5.26}$$

Here, $\chi = 0.1$ is the fraction of mechanical energy spent on vacancy generation, Ω_0 is the atomic volume and ζ is the neutralization effect by vacancy emitting and absorbing jogs which is computed as below.

$$\zeta = \begin{cases} 0.5 - \zeta_0 c_j & \text{if } c_j \leq 0.5/\zeta_0 \\ 0 & \text{if } c_j > 0.5/\zeta_0 \end{cases}$$
$$\zeta_0 = 10 \tag{5.27}$$

The concentration of jogs is given as

$$c_j = e^{-\frac{Q_{jf}}{kT}}; \quad Q_{jf} = \frac{Gb^3}{4\pi(1-\nu)} \tag{5.28}$$

where Q_{jf} is the activation energy of jog formation.

Assuming that only long-range stress contributes to vacancy formation and introducing mean free path, equation (5.26) becomes,

$$\dot{c_v}^{ex} = \left[\chi\frac{m\alpha Gb^2}{Q_{vf}} + \zeta\frac{c_j}{4b^2}\right]\frac{\Omega_0}{b}\dot{\bar{\varepsilon}} - D_{vm}\left[\frac{1}{s^2} + \frac{1}{g^2}\right](c_v - c_v^{eq}) \tag{5.29}$$

Vacancy creation from temperature change

Additionally, excess vacancy concentration can be driven by temperature change as

$$\dot{c_v}^{ex} = c_v^{eq} \left(\frac{Q_{vf}}{kT^2} \right) \dot{T} \tag{5.30}$$

5.2.3   Model for self diffusion

Diffusion occurs by the motion of defects like vacancies and interstitial atoms and by the atomic exchange. But vacancy motion is the predominant diffusion mechanism due to the lower activation energy of vacancy formation (Friedel, 1964). The self diffusion coefficient can be written according to
Reed-Hill and Abbaschian, 1991 as

$$D_l = a^2 \nu e^{\frac{\Delta S_{vm} + \Delta S_{vf}}{k}} e^{-\frac{Q_{vm} + Q_{vf}}{kT}} = D_{l0} e^{-\frac{Q_v}{kT}} \tag{5.31}$$

where, a is the lattice constant, ν is the lattice vibration frequency, ΔS_{vm} is the entropy increase due to the motion of a vacancy, Q_{vm} is the energy barrier to be overcome for vacancy motion and D_{l0} is the activity factor of lattice diffusion.

Vacancy migration leads to vacancy annihilation and it follows an Arrhenius type relation as below.

$$D_{vm} = a^2 \nu e^{\frac{\Delta S_{vm}}{k}} e^{-\frac{Q_{vm}}{kT}} \tag{5.32}$$

Introducing the equilibrium concentration of vacancy from equation (5.25), self diffusivity can be written as

$$D_l = c_v^{eq} D_{vm} \tag{5.33}$$

Thus the self-diffusivity is the product of vacancy diffusivity and its equilibrium concentration. This can be rewritten generically for any concentration of vacancy as

$$D_l^* = \frac{c_v}{c_v^{eq}} D_l \tag{5.34}$$

Lattice diffusivity of α and β phases differ in many orders of magnitude which results in a jump at the β-transus temperature (Mishin and Herzig, 2000). This transition is modeled by scaling the diffusivity with the volume fraction of each phases X_α and X_β.

$$D_l = \frac{c_v}{c_v^{eq}} [D_\alpha \cdot X_\alpha + D_\beta \cdot X_\beta] \tag{5.35}$$

Reed-Hill and Abbaschian, 1991 proposed an Arrhenius type equation for grain boundary diffusion similar to equation (5.32). The effect of grain boundary diffusion can be neglected in the proposed model because of the large grain size of the material considered. Since the basic mechanisms of grain boundary and dislocation core (pipe) diffusion are the same (Shewmon, 1963), a similar formulation is employed here for pipe diffusion.

$$D_p = D_{p0} e^{-\frac{Q_p}{kT}} \tag{5.36}$$

where, D_{p0} is the frequency factor and Q_p is the activation energy.

The total diffusive flux in the material is enhanced by the short circuit diffusion which is dependant on the relative cross-sectional area of pipe and matrix as shown schematically in figure 5.6. According to the model proposed by Porter and Easterling, 1992; Militzer
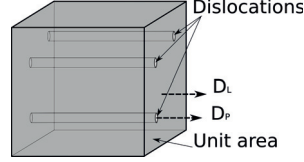

Figure 5.6: Pipe diffusion

et al., 1994, the apparent diffusivity can be written as

$$D_{app} = D_l + ND_p \tag{5.37}$$

where, N is the cross-sectional area of pipes per unit area of matrix.

$$N = \frac{n_a^p n_\rho}{N_a^l} \tag{5.38}$$

where, n_a^p is the number of atoms that can fill the cross-sectional area of a dislocation, n_ρ is the number of dislocations intersecting a unit area and N_a^l is the number of atoms per unit area of lattice. Figure 5.7 shows the apparent diffusivity of Ti-6Al-4V for different values of dislocation density which correspond to annealed and deformed material. Enhanced diffusivity due to pipe diffusion has a significant effect at low temperature ($< 0.5T_{melt}$). At high temperature, it is the lattice diffusivity which has significance. The activity factor of pipe diffusion (D_{p0}) is assumed to be of the same order as that of lattice diffusion.
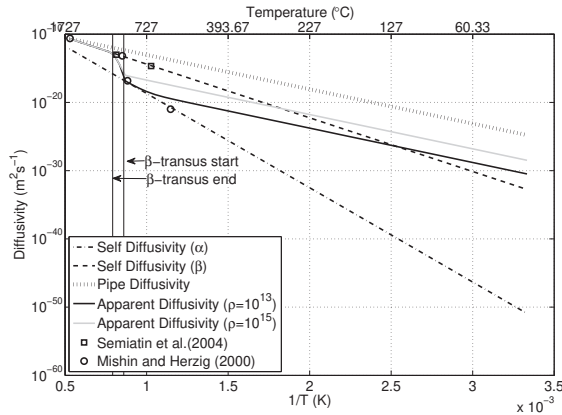

Figure 5.7: Self diffusion

5.3   Stress-update

To compute the flow stress evolution for arbitrary paths, a radial return algorithm can be used (Simo and Taylor, 1986; Simo and Hughes, 1998). This requires hardening modulus and updated internal variables for each time increment. In the proposed model, $\sigma_y = \sigma_y(\bar{\varepsilon}^p, \rho_i, c_v)$ where ρ_i and c_v are described by a coupled set of differential equations. These internal variables can be written in vector form as $\mathbf{q}^T = [q_1, q_2] = [\rho_i, c_v]$. An implicit iterative procedure is used in every time increment to calculate its evolution as given below.

$$\mathbf{H}^T = [H_1, H_2] = 0 \tag{5.39}$$

$$H_1 = \Delta q_1 - \left[\frac{m}{b\Lambda}\Delta\bar{\varepsilon}^p - \Omega q_1 \Delta\bar{\varepsilon}^p - 2c_\gamma \left(\frac{D_v^*}{c_v^{eq}} q_2 + \frac{n_a^p}{N_a^l} q_1 D_p \right) \frac{Gb^3}{kT} \left(q_1^2 - \rho_{eq}^2 \right) \Delta t \right.$$
$$\left. -\psi \Delta X_g \left(q_1 - \rho_{eq} \right) \right] \tag{5.40}$$

$$H_2 = \Delta q_2 - \left[\chi \frac{\Omega_0 m\alpha Gb}{Q_{vf}} \sqrt{q_1}\Delta\bar{\varepsilon}^p + \zeta \frac{c_j \Omega_0}{4b^3}\Delta\bar{\varepsilon}^p - D_{vm} \left[\frac{1}{s^2} + \frac{1}{g^2} \right] \left(q_2 - c_v^{eq} \right) \Delta t \right.$$
$$\left. + c_v^{eq} \left(\frac{Q_{vf}}{kT^2} \right) \Delta T \right] \tag{5.41}$$

The iterative change in $\mathbf{q}$ can be written as

$$d\mathbf{q} = - \left[\frac{\partial \mathbf{H}_{(i)}}{\partial \mathbf{q}} \right]^{-1} \mathbf{H}_{(i)} \tag{5.42}$$

where, i is the iteration counter. The value of the state variables can be updated as

$$\mathbf{q}_{(i+1)} = \mathbf{q}_{(i)} + d\mathbf{q} \tag{5.43}$$

The hardening modulus needed in the radial return algorithm is

$$H' = \frac{d\sigma_y(\mathbf{q})}{d\bar{\varepsilon}^p} = \frac{\partial\sigma_y}{\partial\mathbf{q}} \frac{\partial\mathbf{q}}{\partial\bar{\varepsilon}^p}$$
$$= \frac{\partial\sigma_G}{\partial\rho_i} \left[\frac{\partial\rho_i}{\partial\bar{\varepsilon}^p} + \frac{\partial\rho_i}{\partial c_v} \frac{\partial c_v}{\partial\bar{\varepsilon}^p} \right] + \frac{\partial\sigma^*}{\partial\bar{\varepsilon}^p} + \frac{\partial\sigma^{drag}}{\partial\bar{\varepsilon}^p} \tag{5.44}$$

CHAPTER 6

Metallurgical Model

"The Sigmoid Curve sums up the story of life itself.
We start slowly, experimentally and falteringly,
we wax and then we wane."

Charles Handy

There are relatively few published papers about microstructure models for Ti-6Al-4V. Using resistivity measurements and differential scanning calorimetry (DSC), Malinov et al., 2001a; Malinov et al., 2001b quantified the $\beta \rightarrow \alpha$ isothermal transformation of the alloy and modeled the phenomenon. Katzarov et al., 2002 using FEM, modeled the morphology changes of the alloy during transformation. Kelly, 2004; Kelly et al., 2005 developed a FEM based themo-microstructural model for the metal deposition process. This was later extended to thermo-mechanical-microstructural domains by Crespo et al., 2009; Longuet et al., 2009. Charles Murgau et al., 2012 compared many available models and evaluated their applicability in simulation of the metal deposition. Lately Mi et al., 2014 developed a fully coupled thermo-microstructural FE model for welding of Ti-6Al-4V using the JMAK formulation for phase transformation.

6.1   Model for phase evolution

The liquid–solid phase changes are not modeled in detail. Instead, a simplified model for the transition between the liquid and solid state is implemented to take care of temperatures above the melting temperature T_{melt} . In the liquid state, each of the solid phases is consequently set to zero. In the solid state, Ti–6Al–4V microstructure is composed of two main phases; the high-temperature stable β-phase and the lower temperature stable α-phase. Depending on the formation conditions, a variety of α/β morphologies can be obtained by heat treatment giving varying mechanical properties. Lütjering, 1998; Williams and Lütjering, 2003 explored the relationship between processing, microstructure, and mechanical properties. Based on the literature (Semiatin et al., 1999b; Semiatin et al., 1999a; Seetharaman and Semiatin, 2002; Thomas et al., 2005) few microstructural features have been identified to be relevant with respect to the mechanical properties. The three separate α-phase fractions; Widmanstatten (X_{α_w}), grain boundary ($X_{\alpha_{gb}}$), acicualr and massive Martensite (X_{α_m}) and the β-phase fraction (X_β) are included in the current model. Though in the current flow stress model, the individual α-phase fractions are not included separately, it is possible to incorporate them when more details about their respective strengthening mechanisms are known.

6.1.1   Phase transformations

Depending on the temperature, heating/cooling rates, Ti-6Al-4V undergoes an allotropic transformation. The mathematical model for transformation is described schematically
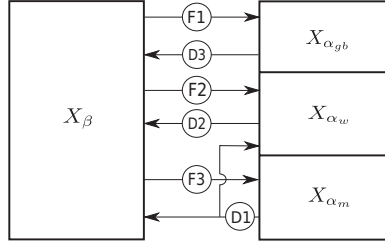

Figure 6.1: The Mechanism of phase change.

in figure 6.1. The transformations denoted by F1, F2, and F3 represent the formation of α_{gb},α_w and α_m phases respectively and D3, D2, and D1 shows the dissolution of the same phases. If the current volume fraction of β phase is more than β_{eq}, the excess β phase transforms to α phase. Here α_{gb} formation which occurs in high temperature is most preferred followed by the α_w. The remaining excess β fraction is transformed to α_m if the temperature is lower than T_m, the martensite start temperature. Conversely, if the current volume fraction of β is lower than β_{eq}, the excess α phase is converted to β. Primary, the α_m phase dissolves to β and α_w phases in the same proportion as the α_{eq} and β_{eq}. The remaining excess α_w and α_{gb} transform to β in that order.

6.1.2 Adaptation of the JMAK model for diffusional transformation

The JMAK- Model (Johnson and Mehl, 1939; Avrami, 1939; Kolmogorov, 1937) originally formulated for nucleation and growth during isothermal situations can be adapted to model any diffusional transformations. Employing the additivity principle, and using sufficiently small time steps ensures that any arbitrary temperature changes be computed. JMAK model assumes that a single phase X_1 which is 100% in volume from the start will transform to 100% of second phase X_2 in infinite time. However, in the case of Ti-6Al-4V, this is not the case as it is an $\alpha - \beta$ dual phase alloy below β-transus temperature. Hence, in order to accommodate incomplete transformation, the product fraction is normalized with the equilibrium volume. Conversely, the starting volume of a phase can also be less than 100% which is circumvented by assuming that the available phase volume is the total phase fraction. Another complication is the existence of simultaneous transformation of various α phases (α_w, α_{gb}, α_m) to β phase and back. This can be modeled by calculating each transformation in a sequential fashion within the time increment as shown in figure 6.1.

6.1.3 Equilibrium phase fraction

Charles Murgau et al., 2012 compared various measurements for equilibrium phase fraction of β^{eq}-phase ($X_{\beta^{eq}}$) available in the literature and identified that the data showed scatter. Compared to the measurements of phase fractions during cooling by Malinov et al., 2001a, the literature data showed an opposite trend. Therefore, in this work, $X_{\beta^{eq}}$ is computed by calibrating the model given by the equation 6.1 and plotted in figure 6.2 were T is the temperature in degree Celsius.

$$
\begin{aligned}
X_\beta^{eq} &= 1 - 0.89\, e^{-\left(\frac{T^*+1.83}{1.73}\right)^2} + 0.28\, e^{-\left(\frac{T^*+0.59}{0.67}\right)^2} \\
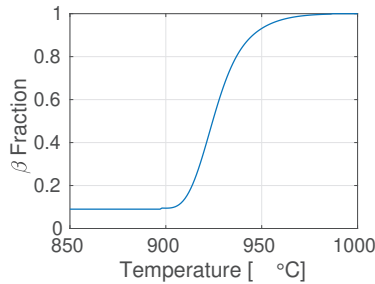T^* &= (T - 973)/24
\end{aligned}
\tag{6.1}
$$

Figure 6.2: Equilibrium β-phase fraction

6.1.4   Formation of α phase

During cooling from β-phase, α_{gb} and α_w phases are formed by a diffusional transformation. According to the incremental formulation of JMAK model described by Charles Murgau et al., 2012, the formation of α_{gb} and α_w can be modeled by the set of equations in rows F1 and F2 respectively of table 6.1. Martensite phase is formed at cooling rates above 410℃/s by a diffusion-less transformation. While cooling at rates above 20°C/s and up to 410°C/s, massive α transformation has been observed to occur simultaneously with the martensite formation (Ahmed and Rack, 1998; Lu et al., 2016). Owing to the similitude in crystal structure between massive-α and martensite-α, they are not differentitated here except that above 410℃/s, 100% α_m is allowed to form. An incremental formulation of Koistinen-Marburger equation described by Charles Murgau et al., 2012 is used here (see equation set in row F3 of table 6.1).
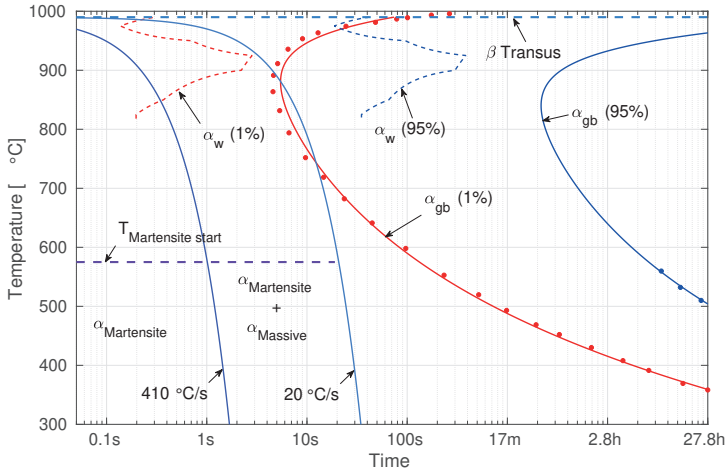

Figure 6.3: TTT Diagram.

The start(1%) shown in red and end(95%) shown in blue of phase transformation described in table 6.1 is given in figure 6.3. The dots for α_{gb} are data taken from JMatPro software. The martensite formation zone below the start temperature and above 410℃/s, as well as martensite and massive α mixed zone between 20°C/s - 410°C/s are also shown in figure 6.3. The α_w start and end curves are obtained after calibrating the model with data for the total fraction of alpha from Malinov et al., 2001a.

6.1.5   Dissolution of α phase

The α_m phase formed by instantaneous transformation is unstable and therefore undergoes a diffusional transformation to α_w and β phases based on its current equilibrium composition. The incremental formulation of classical JMAK model by Charles Murgau et al., 2012 and its parameters are given in row D1 of table 6.2. During heating or reaching non-equilibrium phase composition, α_w and α_{gb} can transform to

F1	$^{n+1}X_{\alpha_{gb}}=\left(1-e^{-k_{gb}\left(t_{gb}^{*}+\Delta t\right)^{N_{gb}}}\right)\left(^{n}X_{\beta}+^{n}X_{\alpha w}+^{n}X_{\alpha_{gb}}\right)^{n+1}X_{\alpha}^{eq}-^{n}X_{\alpha w}$
	$t_{gb}^{*}=\sqrt[N_{gb}]{-ln\left(1-\dfrac{\left(^{n}X_{\alpha w}+^{n}X_{\alpha_{gb}}\right)/^{n+1}X_{\alpha}^{eq}}{^{n}X_{\beta}+^{n}X_{\alpha w}+^{n}X_{\alpha_{gb}}}\right)\Big/ k_{gb}}$
	$t_{gb}^{1\%}=61.5e^{(-3.97e^{-3}T)}+10^{-13}e^{(2.43e^{-2}T)}$
	$t_{gb}^{95\%}=t_{gb}^{1\%}+2.20$
	$N_{gb}=\log_{10}\left(\dfrac{\ln(1-0.01)}{\ln(1-0.95)}\right)\Big/\log_{10}\left(\dfrac{t_{gb}^{1\%}}{t_{gb}^{95\%}}\right)$
	$k_{gb}=-\dfrac{\ln(1-0.01)}{(t_{gb}^{1\%})^{N_{gb}}}$

F2	$^{n+1}X_{\alpha w}=\left(1-e^{-k_{w}(t_{w}^{*}+\Delta t)^{N_{w}}}\right)\left(^{n}X_{\beta}+^{n}X_{\alpha w}+^{n}X_{\alpha_{gb}}\right)^{n+1}X_{\alpha}^{eq}-^{n}X_{\alpha_{gb}}$
	$t_{w}^{*}=\sqrt[N_{w}]{-ln\left(1-\dfrac{\left(^{n}X_{\alpha w}+^{n}X_{\alpha_{gb}}\right)/^{n+1}X_{\alpha}^{eq}}{^{n}X_{\beta}+^{n}X_{\alpha w}+^{n}X_{\alpha_{gb}}}\right)\Big/ k_{w}}$

T[°C]	0	825	850	875	900	925	950	975	1000	1900
N_w	1.10	1.10	1.10	1.13	1.16	1.16	1.16	1.16	1.16	1.16
$k_w\ [10^{-2}]$	6.00	6.00	3.00	1.70	0.40	0.30	0.15	10.0	0.00	0.00

F3	$^{n+1}X_{\alpha_m}=\begin{cases}\left(1-e^{-b_{km}}\left(T_{ms}-T\right)\right)\left(^{n}X_{\beta}+^{n}X_{\alpha_m}\right); if\left(\dot{T}>410°C/s\right)\\ \left(1-e^{-b_{km}}\left(T_{ms}-T\right)\right)\left(^{n}X_{\beta}+^{n}X_{\alpha_m}-^{n+1}X_{\alpha}^{eq}\right); if\left(20°C/s>\dot{T}>410°C/s\right)\end{cases}$
	$b_{km}=5.0e^{-3};\ T_{ms}=851.0°C$

Table 6.1: Models and parameters for α-phase formation.

β-phase controlled by a the diffusion of vanadium at the $\alpha-\beta$ interface. A parabolic equation developed by Kelly, 2004; Kelly et al., 2005 derived in its incremental form by Charles Murgau et al., 2012 is used here (see rows D2 and D3 of table 6.2).

D1	$^{n+1}X_{\alpha_m}=\left(^{n+1}X_{\alpha_m}^{eq}-e^{-k_m(t_m^{*}+\Delta t)^{N_m}}\right)\left(^{n}X_{\beta}+^{n}X_{\alpha_m}-^{n+1}X_{\alpha_m}^{eq}\right)$
	$t_{m}^{*}=\sqrt[N_{m}]{-ln\left(\dfrac{\left(^{n}X_{\alpha}-^{n+1}X_{\alpha_m}^{eq}\right)}{^{n}X_{\beta}+^{n}X_{\alpha_m}-^{n+1}X_{\alpha_m}^{eq}}\right)/k_m}$
	$^{n+1}X_{\alpha w}=^{n}X_{\alpha w}+\Delta^{n}X_{\alpha_m}(1-^{n+1}X_{\beta}^{eq})$
	$^{n+1}X_{\beta}=^{n}X_{\beta}+\Delta^{n}X_{\alpha_m}\ ^{n+1}X_{\beta}^{eq}$

T [°C]	0	400	500	700	800	1900
N_m	1.019	1.019	1.015	1.025	1.031	1.031
k_m	0.667	0.667	1.106	1.252	1.326	1.326

D2 D3	$^{n+1}(X_{\alpha w}+X_{\alpha_{gb}})=\begin{cases}^{n+1}X_{\alpha}^{eq}f_{diss}(T)\sqrt{\Delta t+t^{*}}; if\left(0<(\Delta t+t^{*})<t_{crit}\right)\\ ^{n+1}X_{\alpha}^{eq}; if\left(\Delta t+t^{*}>t_{crit}\right)\end{cases}$
	$t^{*}=\left(\dfrac{^{n}X_{\beta}}{^{n+1}X_{\beta}^{eq}f_{diss}(T)}\right)^{2}$
	$f_{diss}(T)=2.2e^{-31}T^{9.89}$
	$t_{crit}=\sqrt{f_{diss}(T)}$

Table 6.2: Models and parameters for α-phase dissolution.

CHAPTER 7

Coupling of Flow-Stress & Metallurgical Models

"Great things are done by a series of small things brought together."

Vincent van Gogh

The Young's modulus can be written according to Fan, 1993; Lee and Welsch, 1990 as a linear rule of mixtures (ROM). However, since the elastic modulus of the individual phases is not available at elevated temperatures, the effective modulus is used here. Figure 7.1 shows the model by Wachtman et al., 1961 fitted to the measurements. Based on the Wachtman model, Young's Modulus can be written as

$$E = E_0 - B(T + 273.15)e^{(-T_0/(T+273.15))} \tag{7.1}$$

where T is the temperature in degree Celsius, $E_0 = 107 GPa$ is the modulus of elasticity at $0K$, $B = 0.2$ is the calibration parameter and $T_0 = 1300K$ is the temperature at which $E - T$ relationship becomes linear. Here, a cut-off is applied at a temperature of 1050℃.

Since the data for individual phases are not available, the Poisson's ratio is assumed to be constant for both phases. A linear model fitted to the measurement by Fukuhara and Sanpei, 1993 is also shown in figure 7.1. The model for Poisson's ratio can be written as

$$\mu = 0.34 + 6.34 \cdot 10^{-5}T \tag{7.2}$$

where T is the temperature in degree Celsius.

Swarnakar et al., 2011 using X-Ray diffraction measured the volumetric expansion of unit cells of α and β phases during heating (see figure 7.2). Based on this, the average coefficient of thermal expansion (CTE) of the phase mixture can be calculated using the ROM as in equation 7.3, where α_α and α_β give the CTE of α and β phases respectively. However, since the elastic properties of the α and β phases differ, a linear ROM is not suitable here (Ho and Taylor, 1998). There exist many models based on the elastic
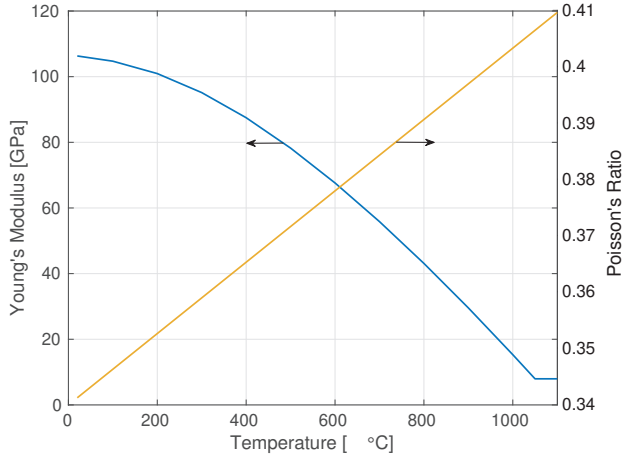
Figure 7.1: Youngs Modulus and Poisson's Ratio.

properties of the individual components applicable in this situation. However, this data is not available for the two phases at elevated temperatures. Hence, a modification of thermal strain, $\varepsilon^{adj}(T)$, which is a calibration parameter is introduced here. The linear thermal strain can be computed using equation 7.4 which is plotted in figure 7.2 and is compared with measurement data from Babu and Lindgren, 2013.

Figure 7.2: Thermal Expansion and Strain.

$$\alpha_{avg} = X_\alpha \alpha_\alpha + X_\beta \alpha_\beta \tag{7.3}$$

$$\varepsilon^{th} = \alpha_{avg} \Delta T - \varepsilon^{adj} \tag{7.4}$$

$$\varepsilon^{adj} = 1.0e^{-8}T^2 - 8.4e^{-6}T + 3.0e^{-4} \tag{7.5}$$

Since the strengthening contributions of these individual alpha phases are not known, a linear ROM for the total alpha-beta composition is developed. The yield strength of the phase mixture can be written as
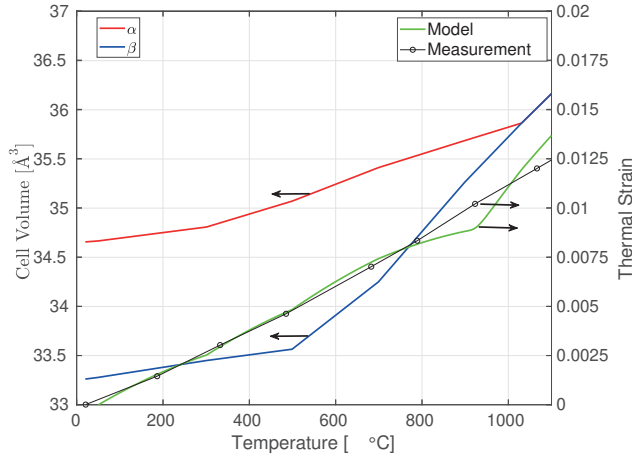
$$\sigma_y = X_\alpha \sigma_y^\alpha + X_\beta \sigma_y^\beta \tag{7.6}$$

Assuming the ad-hoc iso-work principle (Bouaziz and Buessler, 2002), the distribution of the plastic strain between the phases can be obtained. According to Bouaziz and Buessler, 2004, this can be written as,

$$\sigma_y^\alpha \dot{\bar{\varepsilon}}_\alpha = \sigma_y^\beta \dot{\bar{\varepsilon}}_\beta \tag{7.7}$$

$$\dot{\bar{\varepsilon}}^p = X_\alpha \dot{\bar{\varepsilon}}_\alpha + X_\beta \dot{\bar{\varepsilon}}_\beta \tag{7.8}$$

This ensures that the β phase with lower yield strength will get a larger share of plastic strain as compared to the stronger α phase

CHAPTER 8

Model Calibration

"An approximate answer to the right problem
is worth a good deal more than
an exact answer to an approximate problem."

John Tukey

Inverse theory deals with a large class of problems which is usually found when looking for the causes of an observed physical phenomenon. Inverse problems can be generally formulated as equation 8.1. Two problems are called inverse to each other if the formulation of one problem involves the solution of the other one (Capasso and Périaux, 2005).

$$\sigma_y = F(p) \tag{8.1}$$

were p is the set of parameters to be determined. These type of problems are common in science and technology, *viz.* measurement of temperature by recording the electric potential and measurement of strain by recording the electrical resistivity. If a problem has a unique and stable solution, it is called well-posed. Commonly, inverse problems are not well-posed because stability criteria is not satisfied. Non-linear inverse problems can also be written according to 8.1. But here F is a non-linear operator and cannot be separated to represent a linear mapping of the model parameters. Example of these problems includes weather prediction, medical imaging, non-destructive testing, etc.

8.1   Problem formulation

The parameters for a flow stress model can be identified by comparing the flow strength measurement with computed flow stress. The experimental results from a compression or tension machine include stress, strain, time and temperature denoted by σ_i^j, ϵ_i^j, t_i^j and T_i^j respectively for each experiment j and each measurement point i. The model for flow stress can be written as

$$\sigma_y = F\left(\epsilon, \dot{\epsilon}, T, p\right) \tag{8.2}$$

The parameters p can be calibrated by matching the measurements with the model. The error/cost function can be formulated as

$$\min \sum_{i=1}^{m} \sum_{j=1}^{n} w_i^j |\sigma_i^j - \sigma_y| \qquad \text{subject to} \quad lb \leq p \leq ub \tag{8.3}$$

where $0 \leq w_i \leq 1$ is the weight factor, n is the number of experiments, m is the number of measurement points for each measurement and [*lb*, *ub*] are the upper and lower bounds. The cost function is dependent on the experiment and flow strength model considered here.
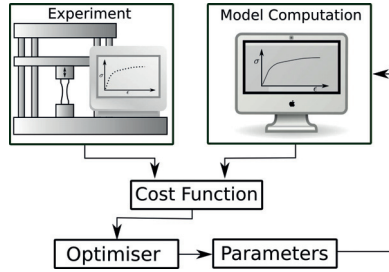
Figure 8.1: Optimisation Process.

Though the inverse problem formulation is straightforward, the non-uniqueness of the solution, dependency on initial values, and the multiple definitions of error functions pose a serious challenge to the modeler. The numerous parameters necessary for the mechanism-based flow stress model along with a vast set of material tests (multiple temperatures, strain rates, etc.) required to trigger the dominant deformation mechanisms of the alloy aggravates the problem. This necessitates the development of an easy to use and interactive software tool that allows the storage of test data, it's processing, calibration of model parameters and data visualization.

8.2   Generic Model Platform (GMoP)

A Matlab™ based platform for calibration has been developed which has several additional purposes. It consists of three modules, *viz.* pre-processor, optimizer, and post-processer. Though, this chapter describes the tool in the context of constitutive

models, it is not limited. GMoP has been used to calibrate many other models like
Frolich's B-H relation, TTT curves, etc.

8.2.1   Pre-processor

The pre-processor can import and process measurement data (time, strain, stress,
temperature etc). Smoothing, reducing and truncating the data are the most commonly
used features. The original and processed data is saved in a database together with
existing model parameters.
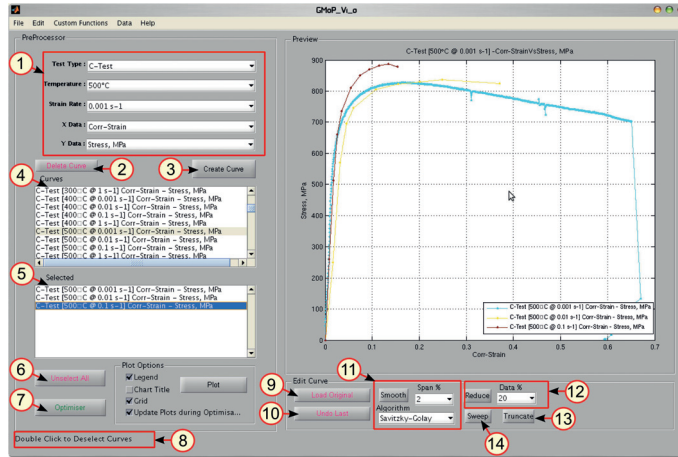
Figure 8.2: Pre-Processor.

8.2.2   Optimizer

The optimiser module makes it possible to interact with the calibration process. Here,
the parameters can be set to be fixed or free for calibration as well as upper and lower
bounds of each parameter can be defined. After the calibration process is finished, the
parameters can be exported to an ASCII file for inclusion in FORTRAN subroutines.

8.2.3   Post-processor

The post-processor module can plot the different state variables of the model for
evaluation. The actually used model is implemented in a separate Matlab™ code.
There, the model parameter space is defined and the stress-strain algorithm is
implemented. The general format of stored test data makes it possible to use the same
kind of algorithm needed in user routines for finite element codes. Therefore, the
implementation of a new model in a high-level language like Matlab™ makes
prototyping, validation and verification of convergence properties convenient.

Table 8.1: Pre-Processor Functionality

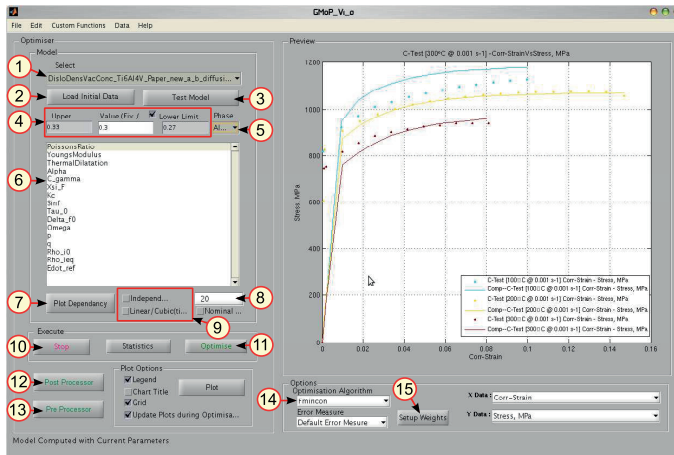| #	Details
1	**Selecting a curve from the database:** The test type (compression, tension, creep, etc), temperature, strain rate, and the different measurement points (stress, strain, temperature, force, phase fractions, etc) can be assigned to the x and y-axis.
2	**Deleting a curve:** This function deletes a saved curve.
3	**Creating a curve:** The choice of a particular curve / dataset is saved.
4	**Curve list:** The saved curves are displayed here. Double clicking / return will select the curves.
5	**Selected curves:** The curves selected for optimisation are displayed here. Double clicking / return will unselect the curves.
6	**Unselect curves:** All the selected curves can be unselected at once.
7	**Optimizer:** Activate the optimizer module.
8	**Status message:** Current status and messages to the user are displayed in this location.
9	**Load original data:** The raw data imported to the toolbox is stored in the database which can be loaded here.
10	**Undo the last step:** This will undo all the data editing done in the last step.
11	**Smooth data:** The given data can be can be processed to remove noise using various algorithms that are given in the dropbox along with its span.
12	**Reduce data:** A specified % of the raw data can be reduced to simplify the optimisation process.
13	**Truncate data:** Part of the measured data might be useless owing to sensor error or specimen failure. This can be removed from the database using this function.
14	**Sweep data:** Here, multiple points lying very close with respect to measured time can be removed.

Figure 8.3: Optimiser.

Table 8.2: Menu-bar Functionality

#	Details
1	**File→Open:** Open an existing database.
2	**File→Save:** Save the current data to a database.
3	**File→Merge:** The opened database can be merged with another database.
4	**File→Preferences:** Enter Preferences for the platform.
5	**Edit→Remove Point:** Remove a single point.
6	**Edit→Sweep:** Same as in table 8.1 (#14).
7	**Edit→Display Points:** Display points using different markers.
8	**Edit→Adjust -ve Points:** Move the strain measurements with -ve values to zero.
9	**Edit→Adjust +ve Points:** Move the strain measurements with +ve values to zero.
10	**Edit→Move First Point to [0,0]:** The first measurement point can be moved to $(0,0)$.
11	**Data→Read txt Data:** Import measurement data in csv (ascii text) format.
12	**Data→Read xls Data:** Import measurement data in Microsoft Excel™(xls) format. This is limited to Microsoft Windows™OS.
13	**Data→Dump Results:** Dump the current parameters to a file.
14	**Data→Remove Dependencies:** Remove all the dependencies of a model.
15	**Data→Export:** Export the stress-strain data from the database.

Table 8.3: Optimiser Functionality

#	Details
1	**Selecting a model from database:** The models stored in [˜\optimiser\models\] is displayed and can be selected here.
2	**Load initial data:** This function loads the initial data from the selected model file.
3	**Test model:** The selected model can be tested with the currently loaded parameters.
4	**Change Limits & parameters:** The chosen parameter at selected phase and temperature can be changed.
5	**Select Phase:** Change the selected phase.
6	**Parameter List:** View all the parameters of the model.
7	**Plot Parameters:** Make a separate plot of the parameters are a function of temperature.
8	**Select Temperature:** Select a temperature.
9	**Parameter properties:** Make parameter temperature independant or not and change interpolation from linear to cubic.
10	**Stop:** Stop Optimisation.
11	**Optimise:** Start Optimisation.
12	**Pre-Processor:** Back to Pre-Processor.
13	**Post-Processor:** Go to Post-Processor.
14	**Optimisation Algorithm:** Select Optimisation algorithm [Fmincon / Genetic Algorithm].
15	**Weights:** Apply Weights to parts of data.

8.3 Calibration of the model

Deformation tests were performed at varying strain rates and temperature for the calibration and the validation of the flow stress model described in previous chapters. The testing methodology was selected based on the range of strain rates of interest. Some samples were also characterized using electron backscattered diffraction (EBSD) technique.

8.3.1 Characterization and calibration

For low strain rate tests, in the range between 10^{-3} and $1s^{-1}$ addressed in appended paper B, C, and, D, Gleeble™ thermo-mechanical simulator is used to perform compression tests on cylindrical specimens. The dimensions of the specimens were chosen to produce a reliable force response from the equipment. Electrical resistivity heating was performed on these samples utilizing a thermocouple attached to the middle of the specimen for closed-loop control of temperature. The initial temperature of these tests was between 20 and 1100°C. However, during compression tests, the deformation energy is converted to heat and increases the specimen temperature which is measured by the thermocouple. The applied force, anvil displacement, and diameter of the specimen are also measured and recorded during the tests. Based on this, the true stress and strains can be computed by assuming constant volume during plastic deformation. As described in paper C,
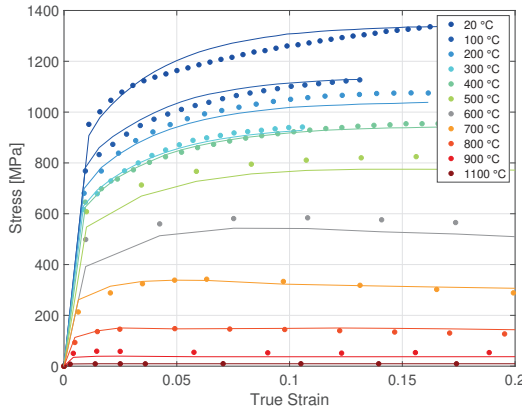
Figure 8.4: Stress vs strain at low strain rate.

deformation while cooling was also performed in a Gleeble™ simulator for validating the coupled flow stress and metallurgical model. The calibrated parameters of the model are obtained after the optimization using GMoP. Some of the parameters used in the model are available from measurements outside the domain of classical mechanical testing. Since some of these parameters are not available for this specific alloy, the data for pure Ti has been used. The temperature dependent and independent parameters are listed in separate

tables in paper B and, C along with the comparison of the flow stress measurements and the model predictions in paper B. See figure 8.4 for the measurements (dots) vs predictions (lines) of the flow stress curves at 10^{-3}s^{-1}.

The Split-Hopkinson pressure bar (SHPB) method is commonly used when determining the inelastic response of materials at high strain rates. SHPB technique is based on longitudinal elastic stress wave propagation through bars where a mechanical impact initiates stress waves. Characteristics of SHPB testing are that the impact velocity of the striker and the length of specimens affect both strain and strain rates. In paper D, the SHPB tests were performed on cylindrical specimens with 8mm diameter and 4mm height. The tested strain rates were between $2 \cdot 10^3$ and $9 \cdot 10^3 \text{s}^{-1}$ and start temperature was between 20 and 950℃. Tests at elevated initial temperature were performed using a moving arm loaded with the specimen. The arm was pushed into a stand-alone furnace. After the desired temperature was reached, the specimen was placed between the incident and the transmitting bars, but still without any contact to prevent thermal gradients in the specimen. Just before the stress wave reached the interface between the incident bar and the specimen, the transmitting bar was pushed towards the specimen establishing contact. During deformation, the temperature of the specimen was further increased due to dissipative work and is computed according to Apostol et al., 2003. The complete parameter set of the model obtained after calibration are listed in separate tables in paper D along with the comparison of the flow stress measurements and the model predictions. See figure 8.5 for the measurements (dots) vs predictions (lines) of the flow stress curves at $9 \cdot 10^3 \text{s}^{-1}$
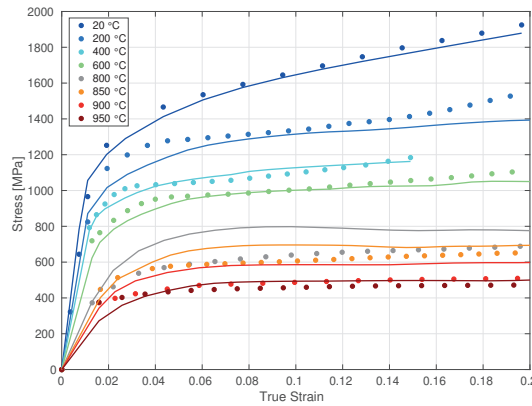
Figure 8.5: Stress vs strain at high strain rate.

In paper D, the microstructural characterization was carried out for the specimens that were deformed at $2 \cdot 10^3 \text{s}^{-1}$. They were cut into halves along the specimen's axis. The location selected for scanning was at the middle of the specimen based on the assumption that the amount of deformation was comparable between test specimens and is homogeneous. A field emission SEM (JSM7001F), equipped with an EBSD detector combined with the TSL (OIMA, v. 8.0) analysis software was used for microstructural

investigations. A small beam diameter was aligned and selected in the SEM, which is accelerated at 15kV to resolve small features even at highly deformed areas. A high-speed Hikari camera was used for pattern acquisition at binning of 4x4, which provided a proper successful indexing rate and indexing speed. Data were recorded at $0.09\mu m$ step size. Applying the high angle grain boundary (HAGB) misorientation threshold of 15°, grain boundaries are identified as shown in figure 8.6a. Circles are inscribed within the grains starting from the largest diameter and progressively reducing diameter in steps (See figure 8.6b). Area fraction (AF) is the ratio of total area covered by circles to the total area of the scanned region as shown in figure 8.6c and equation 8.4. The computed AF for different samples are given in figure 8.7 as a continuous line.
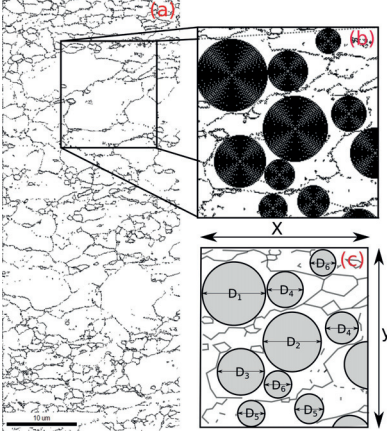
Figure 8.6: (a)HAGB of the annealed sample, (b) Inscribed circles, (c) Schematic diagram for computing the area fraction.

Figure 8.7: AF and Relative globularization fraction.

$$AF = \frac{0.25\pi}{x \cdot y} \sum_{i=1}^{n} D_i^2 \qquad (8.4)$$

Assuming that the sample deformed at 20℃ has undergone no globularization and the annealed sample is fully globularized, the relative globularization fraction is estimated based on the area fraction. This is shown in figure 8.7 as dots whereas the dotted lines show model predictions.

CHAPTER 9

Simulation of Processes

"Maybe we're in a simulation, maybe we're not,
but if we are, hey, it's not so bad"

David Chalmers

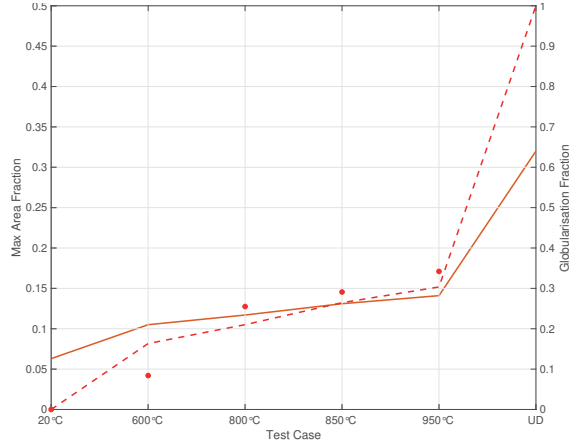The manufacturing of industrial components usually involves a chain of processes. Performing simulations of this chain and comparing the results to mechanical and geometric requirements of the component is the key to predicting its manufacturability. As a part of this thesis work, three manufacturing cases were simulated that used dislocation density based flow stress models. The manufacturing cases considered here included four different processes; forming, welding, additive manufacturing and heat treatment.

Metal forming refers to the manufacturing of thin sheet metal parts which involves stretching, drawing and bending of a sheet of metal into the desired shape. The most important part in forming is the tool design. FE simulations are often used to design the optimum tooling and process parameters for forming. This approach known as 'simulation-driven design', allows the creation of precise geometries with the near net shape of the component.

Welding is a joining process which is often done by melting the workpieces locally and adding molten filler material which when cools down, provides a strong bond. Simulation of the welding process is a multi-physics problem involving heat transfer, mechanical loads, phase transformation, arc physics, fluid flow etc. But some of these couplings are weak and can be ignored (Lindgren, 2007). The heat source parameters determine the penetration and shape of the HAZ.

Additive manufacturing (AM) process uses powder or wire for the addition of material with a heat source such as a laser, electron beam or electric arc. The deposition path is generated from a CAD geometry and is pre-programmed in a CNC machine which makes the process very flexible and suitable for low volume production eliminating the need for tooling and dies. This also enables the production of complicated geometries that are traditionally difficult to produce with the conventional

manufacturing processes. Powder bed fusion (PBF) is the technique of building a thin layer over layer by melting fine metal powder. Directed energy deposition (DED), on the other hand, is used usually for building features on large existing parts as well as for repairing damaged ones. PBF typically adds layers that are thinner than DED and therefore can create high-resolution structures whereas DED produces components at a higher built rate. The primary challenge of DED is that the higher energy input from the heat source may lead to substantial distortion and higher residual stresses.

Deformation introduces defects in crystal lattice which is reckoned as residual stress. Stress relief heat treatment (HT) is the process of subjecting a component to an elevated temperature in a furnace for a certain time in order to restore the lattice thereby relieving the residual stresses. The material model used in this simulation is capable of computing stress relaxation through the thermally activated recovery of dislocations by climb and globularization. The holding time in the furnace should be sufficient to remove the critical stresses in the component but not excessive to allow grain growth. The heating and cooling rates are also crucial as it might introduce new stresses in the component due to the temperature gradients (Alberg, 2005).

9.1   Case 1: Manufacturing process chain (Paper A)

This case involved the manufacturing of an aerospace sub-component using a range of processes like forming, AM, machining, welding, roller burnishing, and heat treatment (Tersing et al., 2012), see figure 9.1. The primary challenge involved in this work was that the simulations were performed by multiple people using a range of software at different companies utilizing their own material models. The results (final geometry, effective plastic strains, and residual stress tensors) after simulation of each process is the only information that is transferred to the next actor in the chain. In some cases, this also required a switch between rate dependent to rate independent formulation and vice versa. This experience emphasized the significance of using a single material model throughout the process chain.
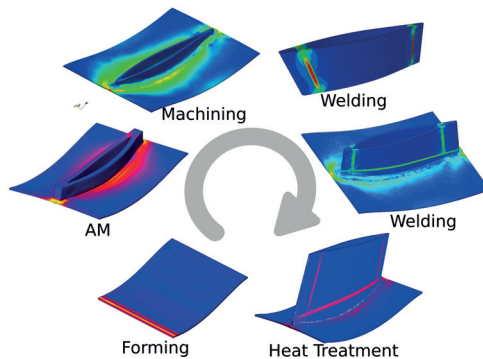

Figure 9.1: Chain of manufacturing processes

9.2   Case 2: Forming, AM, heat-treatment (Paper A)

In case 1, forming, AM and HT processes were performed using the dislocation density model described in paper B and implemented in MSC Marc software. A sheet metal with 2mm thickness is used in forming. The profile of the top and bottom die is obtained by an iterative design procedure to obtain optimal geometry of the final component. The tool is modeled by open surfaces which defines the area of contact of the dies. The sheet metal and tool is held at 800°C from the start to end of forming and is cooled to room temperature by convection during the cooling cycle after forming and tool release. The logic for AM is described in detail in Lundbäck and Lindgren, 2011. The final component produced by a chain of processes was later heated and cooled with natural convection up-to a temperature of 560℃ for two hours. See figure 9.2 for the equivalent von Mises stress contours of the component at various stages.
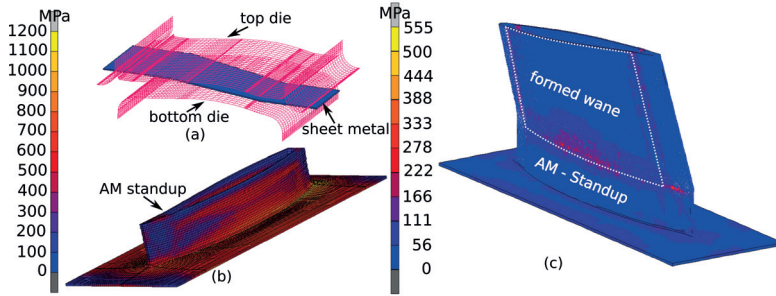

Figure 9.2: Residual Stress (a) before forming, (b) after AM, (c) after HT

9.3   Case 3: Forming, welding, heat-treatment

Babu and Lundbäck, 2009 demonstrates the simulation of the manufacturing process of an industrial component using FEM involving hot forming, TIG welding, and stress relief heat treatment performed in the same order (article not appended as part of this thesis).   Dislocation density based material model described in Babu, 2008 and implemented in MSC Marc is used to perform all the simulations. Mapping the residual state (internal state variables and stress state) on to the successive mesh is a crucial part in the simulation of process chains. This is done by exporting and importing the necessary variables using user routines.

The forming tool is assumed to be rigid and therefore modeled using analytical surfaces. In order to reduce the spring back, the plate and die are preheated to 700 °C and therefore the process is assumed to be isothermal. The friction between the tool and the plate is modeled using the Coulomb model. The heat source used for welding is TIG (Tungsten Inert Gas) and is modeled using the analytical equation of double ellipsoid where the geometric parameters are obtained from experiments (Lundbäck, 2003). A staggered thermo-mechanical simulation approach is used in solving this problem where mechanical

analysis lags one step with the thermal analysis. The addition of filler material is modelled by the activation of elements. The filler elements are thermally activated at a distance ahead of the heat source. But these elements are activated mechanically only after it cools down to a temperature lower than its melting temperature, thus resulting in a staggered activation. During the heat treatment, it is assumed that the component has uniform temperature distribution during the holding process and therefore the fluid physics inside the furnace is ignored.
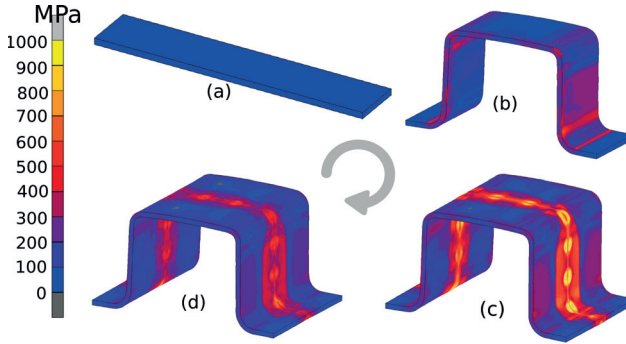

Figure 9.3: Residual stress (a) plate, (b) after forming, (c) after welding, (d) after heat treatment

The plate shown in figure 9.3a is modeled using 8-node hex elements with 4 elements through the thickness that is retained throughout the chain. Figure 9.3 (b to d) shows the snapshot of residual stresses after each process. While releasing from the die after forming, the component springs back around 2mm. Welding is performed in two steps with 12 tack welds in the first step followed by butt welding in 3 sequences in the second step. After each process, the model is released from the fixture boundary conditions which ensures the static equilibrium of the transferred results. The stress patterns originated from the tack welding is evident as distinct spots along the weld line in figure 9.3c which is scaled down by heat treatment (see figure 9.3d). This case demonstrates the possibility of using a single material model in simulations involving a wide range of temperatures and strain rates that activates various deformation mechanisms.

9.4   Case 4: Additive manufacturing (Paper E)

In this case, a DED process described in Denlinger et al., 2015 is simulated using MSC Marc utilizing the logic for modeling of AM process explained in Lundbäck and Lindgren, 2011. A coupled thermo-mechanical-metallurgical model described in paper C is also implemented as subroutines. See figure 9.4 for the residual stress in the sectioned component after the process and cooling to room temperature.
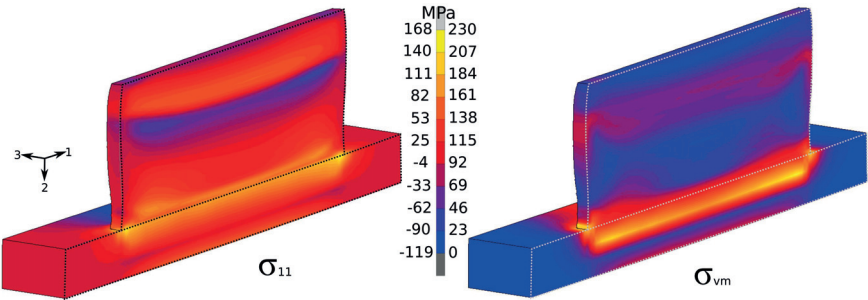
Figure 9.4: Residual stress after AM

CHAPTER 10

Conclusions and Future Work

"The truth of a theory can never be proven,
for one never knows if future experience
will contradict its conclusions."

Albert Einstein

The scope of current work has been to develop a model to describe the deformation behavior of Ti-6Al-4V to simulate a manufacturing process chain such as the one described in paper A that involves changes in microstructure and associated material properties. Empirical models do not possess a broad descriptive capacity corresponding to varying loading conditions and changing microstructure. They are therefore not suitable when simulating manufacturing processes. A constitutive model based on the physics of the material behavior has been developed and calibrated in the current work. This model can give predictions with adequate accuracy for simulations of various manufacturing processes like hot forming, welding, additive manufacturing, heat treatment, etc. and can be implemented in most commercial finite element packages. It has been formulated as a classic deviatoric plasticity model using the von Mises yield criterion and the associated flow rule. A rate-dependent yield surface has been used as the model also describes rate- dependent behavior. Therefore, the logic for stress update described in paper B, C, and D is directly applicable for large-scale simulations. Since the proposed flow stress model follows a clear physical framework based on deformation mechanisms, new sub-models can be added with relative ease. This is evident from the extension of the model for low strain rate deformation with equilibrium phase composition in paper B to arbitrary phase composition in paper C and also extending it to include the effects of dislocation drag in paper D.

The current study concludes that,

- Simulating a chain of manufacturing processes requires the use of a single flow stress model for all the processes.

- A mechanism-based flow stress model for Ti-6Al-4V has been developed

- A set of experiments that activate the dominant deformation mechanisms have been performed and simultaneously included in the model calibration together with literature data for some physical properties.

- The flow stress model has been demonstrated with the simulation of hot forming, thermo-mechanical welding, AM and heat treatment processes.

Future work:

The items listed below are some research ideas to be pursued in the future.

- Though the flow stress model has been calibrated for high strain rate deformation, it has not been demonstrated in a simulation of processes involving a high rate of deformation, viz: machining.

- The anisotropic behavior of the material and the tension-compression asymmetry shown by Ti-6Al-4V needs to be addressed.

- The capacity of the model to simulate stress-relaxation is demonstrated in paper B. However, stress-relaxation tests could be used to improve the model for static restoration described by the model. Paper E also indicates that this part may not be sufficiently accurate.

References

Ahmed, T. and H.J. Rack (1998). Phase transformations during cooling in [alpha]+[beta] titanium alloys. *Materials Science and Engineering A* 243.1-2, pp. 206–211.

Alberg, H. (2005). "Simulation of Welding and Heat Treatment: Modelling and Validation". PhD thesis. Luleå University of Technology.

Apostol, M., T. Vuoristo, and V.-T. Kuokkala (2003). "High temperature high strain rate testing with a compressive SHPB". *Journal de Physique IV (Proceedings)*. Vol. 110. EDP sciences, pp. 459–464.

Avrami, M. (1939). Kinetics of Phase Change. I General Theory. *The Journal of Chemical Physics* 7.12, pp. 1103–1112.

Babu, B. (2007). "Dislocation density based constitutive model for Ti-6Al-4V : including recovery and recrystallisation". *Computational plasticity : Fundamentals and Applications*. Ed. by E. Onate, R. Owen, and B. Suarez. Vol. 2. 9, pp. 631–634.

Babu, B. (Nov. 2008). *Physically based model for plasticity and creep of Ti-6Al-4V*. Luleå, Sweden: Luleå University of Technology.

Babu, B. and L.-E. Lindgren (2013). Dislocation density based model for plastic deformation and globularization of Ti-6Al-4V. *International Journal of Plasticity* 50.0, pp. 94–108.

Babu, B. and A. Lundbäck (Sept. 2009). "Physically based constitutive model for Ti-6Al-4V used in the simulation of manufacturing chain". *Computational Plasticity X : fundamentals and applications*. Ed. by E. Onate, D. Owen, and B. Suarez. International Conference on Computational Plasticity. Barcelona: International Center for Numerical Methods in Engineering.

Bai, Q., J. Lin, T. Dean, D. Balint, T. Gao, and Z. Zhang (2012). Modelling of dominant softening mechanisms for Ti-6Al-4V in steady state hot forming conditions. *Materials Science and Engineering: A* 0, pp. 352–358.

Barboza, M.J.R., E.A.C. Perez, M.M. Medeiros, D.A.P. Reis, M.C.A. Nono, F.P. Neto, and C.R.M. Silva (2006). Creep behavior of Ti-6Al-4V and a comparison with titanium matrix composites. *Materials Science and Engineering: A* 428.1-2, p. 319.

Barnett, M.R., G.L. Kelly, and P.D. Hodgson (2000). Predicting the critical strain for dynamic recrystallization using the kinetics of static recrystallization. *Scripta Materialia* 43.4, p. 365.

Bendick, W. (1991). Analysis of material exhaustion and damage by creep. *International Journal of Pressure Vessels and Piping* 47.1, pp. 57–78.

Bergström, Y. (1969). Dislocation model for the stress-strain behaviour of polycrystalline alpha-iron with special emphasis on the variation of the densities of mobile and immobile dislocations. *Materials Science & Engineering* 5, pp. 193–200.

Bergström, Y. (1983). The plastic deformation of metals - A dislocation model and its applicability. *Reviews on Powder Metallurgy and Physical Ceramics* 2/3, pp. 79–265.

Boivineau, M., C. Cagran, D. Doytier, V. Eyraud, M. Nadal, B. Wilthan, and G. Pottlacher (2006). Thermophysical Properties of Solid and Liquid Ti-6Al-4V (TA6V) Alloy. *International Journal of Thermophysics* 27 (2), pp. 507–529.

Bouaziz, O. and P. Buessler (2002). Mechanical behaviour of multiphase materials: an intermediate mixture law without fitting parameter. *Revue de Métallurgie–International Journal of Metallurgy* 99.1, pp. 71–77.

Bouaziz, O. and P. Buessler (2004). Iso-work Increment Assumption for Heterogeneous Material Behaviour Modelling. *Advanced Engineering Materials* 6.1-2, pp. 79–83.

Bros, H., M. Michel, and R. Castanet (1994). Enthalpy and heat capacity of titanium based alloys. *Journal of Thermal Analysis and Calorimetry* 41 (1), pp. 7–24.

Bruschi, S., S. Poggio, F. Quadrini, and M.E. Tata (2004). Workability of Ti-6Al-4V alloy at high temperatures and strain rates. *Materials Letters* 58.27-28, p. 3622.

Cahn, R.W. and H. Peter (1996a). *Physical Metallurgy.* 4th ed. Vol. 1. Amsterdam, NL: North-Holland Publishers.

Cahn, R.W. and H. Peter (1996b). *Physical Metallurgy.* 4th ed. Vol. 3. Amsterdam, NL: North-Holland Publishers.

Capasso, V. and J. Périaux (2005). *Multidisciplinary Methods for Analysis Optimization and Control of Complex Systems.* Vol. 6. Mathematics in Industry. Springer.

Charles Murgau, C., R. Pederson, and L. Lindgren (2012). A model for Ti–6Al–4V microstructure evolution for arbitrary temperature changes. *Modelling and Simulation in Materials Science and Engineering* 20.5, p. 055006.

Chichili, D.R., K.T. Ramesh, and K.J. Hemker (1998). The high-strain-rate response of alpha-titanium: Experiments, deformation mechanisms and modeling. *Acta Materialia* 46.3, p. 1025.

Conrad, H. (1981). Effect of interstitial solutes on the strength and ductility of titanium. *Progress in Materials Science* 26.2-4, pp. 123–403.

Crespo, A., A. Deus, and R. Vilar (2009). "Modeling of phase transformations and internal stresses in laser powder deposition". *XVII International Symposium on Gas Flow, Chemical Lasers, and High-Power Lasers.* Vol. 7131. International Society for Optics and Photonics, p. 713120.

Denlinger, E.R., J.C. Heigel, P. Michaleris, and T. Palmer (2015). Effect of inter-layer dwell time on distortion and residual stress in additive manufacturing of titanium and nickel alloys. *Journal of Materials Processing Technology* 215, pp. 123–131.

Ding, R. and Z.X. Guo (2004). Microstructural evolution of a Ti-6Al-4V alloy during [beta]-phase processing: experimental and simulative investigations. *Multiscale Materials Modelling* 365.1-2, p. 172.

Ding, R., Z.X. Guo, and A. Wilson (2002). Microstructural evolution of a Ti-6Al-4V alloy during thermomechanical processing. *Materials Science and Engineering A* 327.2, p. 233.

Domkin, K. (2005). "Constitutive models based on dislocation density: formulation and implementation into finite element codes". PhD thesis. Luleå Technical Univeristy.

Donachie, J.M.J. (1988). *Titanium - A Technical Guide*. ASM International.

Elmer, J.W., T.A. Palmer, S.S. Babu, and E.D. Specht (2005). In situ observations of lattice expansion and transformation rates of [alpha] and [beta] phases in Ti-6Al-4V. *Materials Science and Engineering A* 391.1-2, p. 104.

Fan, Z. (1993). On the young's moduli of Ti-6Al-4V alloys. *Scripta Metallurgica et Materialia* 29.11, pp. 1427–1432.

Ferguson, W., A. Kumar, and J. Dorn (1967). Dislocation damping in aluminum at high strain rates. *Journal of Applied Physics* 38.4, pp. 1863–1869.

Franz, R. and G. Wiedemann (1853). Ueber die Wärme-Leitungsfähigkeit der Metalle. *Annalen der Physik* 165.8, pp. 497–531.

Friedel, J. (1964). *Dislocations*. Vol. 3. International Series of Monographs on Solid State Physics. Pergamon Press.

Frost, H.J. and M.F. Ashby (1982). *Deformation-Mechanism Maps: The Plasticity and Creep of Metals and Ceramics*. Paperback.

Fujii, H. and H.G. Suzuki (1990). A model for ductility loss at intermediate temperatures in an alpha+beta titanium alloy. *Scripta Metallurgica et Materialia* 24.10, pp. 1843–1846.

Fukuhara, M. and A. Sanpei (1993). Elastic moduli and internal frictions of Inconel 718 and Ti-6Al-4V as a function of temperature. *Journal of Materials Science Letters* 12 (14), pp. 1122–1124.

Gottstein, G. (2004). *Physical Foundations of Material Science*. Springer-Verlag.

Hertzberg, R.W. (1995). *Deformation and Fracture Mechanics of Engineering Materials*. 4th ed. Wiley.

Ho, C.Y. and R.E. Taylor (1998). *Thermal expansion of solids*. Materials Park, OH: ASM International.

Holt, D.L. (1970). Dislocation cell formation in metals. *Journal of applied physics* 41.8, p. 3197.

Hull, D. and D.J. Bacon (2001). *Introduction to Dislocations*. Butterworth-Heinemann.

Humphreys, F.J. and M. Hatherly (2004). *Recrystallization and Related Annealing Phenomena*. 2nd ed. Kidlington, Oxford: Elsivier.

Jessell, M.W., O. Kostenko, and B. Jamtveit (2003). The preservation potential of microstructures during static grain growth. *Journal of Metamorphic Geology* 21.5, pp. 481–491.

Johnson, A.J.W., C.W. Bull, K.S. Kumar, and C.L. Briant (2003a). The influence of microstructure and strain rate on the compressive deformation behavior of Ti-6Al-4V. *Metallurgical and Materials Transactions* 34A.2, pp. 295–306.

Johnson, A.J.W., K.S. Kumar, and C.L. Briant (2003b). Deformation mechanisms in Ti-6l-4V/TiC composites. *Metallurgical and Materials Transactions* 34A.9, pp. 1869–1877.

Johnson, C.H., S.K. Richter, C.H. Hamilton, and J.J. Hoyt (1998). Static grain growth in a microduplex Ti-6Al-4V alloy. *Acta Materialia* 47.1, pp. 23–29.

Johnson, G.R. and W.H. Cook (1985). Fracture characteristics of three metals subjected to various strains, strain rates, temperatures and pressures. *Engineering Fracture Mechanics* 21.1, pp. 31–48.

Johnson, W. and R. Mehl (1939). Reaction Kinetics in Processes of Nucleation and Growth. *Trans. Soc. Pet. Eng.* 135, p. 416.

Kailas, S.V., Y.V.R.K. Prasad, and S.K. Biswas (1994). Flow Instabilities and Fracture in Ti-6Al-4V Deformed in Compression at 298-673K. *Metallurgical and Materials Transactions A* 25A.10, pp. 2173–2179.

Katzarov, I., S. Malinov, and W. Sha (2002). Finite element modeling of the morphology of (beta) to (alpha) phase transformation in Ti-6AI-4V alloy. *Metallurgical and Materials Transactions A* 33A.4, p. 1027.

Kedia, B., I. Balasundar, and T. Raghu (2018). Globularisation of α Lamellae in Titanium Alloy: Effect of Strain, Strain Path and Starting Microstructure. *Transactions of the Indian Institute of Metals* 71.7, pp. 1791–1801.

Kelly, S.M. (2004). "Thermal and Microstructure Modeling of Metal Deposition Processes with Application to Ti-6Al-4V". PhD Thesis. Virginia Polytechnic Institute and State University.

Kelly, S.M., S.S. Babu, S.A. David, T. Zacharia, and S.L. Kampe (2005). "A microstructure model for laser processing of Ti-6Al-4V". *24th International Congress on Applications of Lasers and Electro-Optics, ICALEO 2005*. 24th International Congress on Applications of Lasers and Electro-Optics, ICALEO 2005 - Congress Proceedings. Miami, FL, United States: Laser Institute of America, Orlando, FL 32826, United States, pp. 489–496.

Khan, A.S., R. Kazmi, B. Farrokh, and M. Zupan (2007). Effect of oxygen content and microstructure on the thermo-mechanical response of three Ti-6Al-4V alloys: Experiments and modeling over a wide range of strain-rates and temperatures. *nternational Journal of Plasticity* 23.7, pp. 1105–1125.

Khan, A.S., Y.S. Suh, and R. Kazmi (2004). Quasi-static and dynamic loading responses and constitutive modeling of titanium alloys. 20.12, p. 2233.

Khan, A.S. and S. Yu (2012). Deformation induced anisotropic responses of Ti-6Al-4V alloy. Part I: Experiments. *International Journal of Plasticity* 38.0, pp. 1–13.

Khan, A.S., S. Yu, and H. Liu (2012). Deformation induced anisotropic responses of Ti-6Al-4V alloy Part II: A strain rate and temperature dependent anisotropic yield criterion. *International Journal of Plasticity* 38.0, pp. 14–26.

Knudsen, T., W.Q. Cao, A. Godfrey, Q. Liu, and N. Hansen (2008). Stored Energy in Nickel Cold Rolled to Large Strains, Measured by Calorimetry and Evaluated from the Microstructure. *Metallurgical and Materials Transactions A* 39.2, pp. 430–440.

Kocks, U.F., A.S. Argon, and M.F. Ashby (1975). *Thermodynamics and Kinetics of Slip*. Ed. by C. Bruce, J.W. Christian, and T.B. Massalski. Vol. 19. Progress in Material Science. Pergamon Press.

Kocks, U. (1976). Laws for Work-Hardening and Low-Temperature Creep. *Journal of Engineering Materials and Technology, Transactions of the ASME* 98 Ser H.1, pp. 76–85.

Kolmogorov, A. (1937). A statistical theory for the recrystallisation of metals, Akad Nauk SSSR, Izv. *Izv. Akad. Nauk. SSSR* 3.

Lee, W.-S. and M.-T. Lin (1997). The effects of strain rate and temperature on the compressive deformation behaviour of Ti-6Al-4V alloy. 71.2, p. 235.

Lee, Y. and G. Welsch (1990). Young's modulus and damping of Ti6Al4V alloy as a function of heat treatment and oxygen concentration. *Materials Science and Engineering A* 128.1, pp. 77–89.

Lesuer, D.R. (2000). *Experimental Investigations of Material Models for Ti-6Al-4V Titanium and 2024-T3 Aluminum.*

Lesuer, D.R., G. Kay, and M. LeBlanc (2001). *Modeling large-strain, high-rate deformation in metals.* Tech. rep. Lawrence Livermore National Lab., CA (US).

Li, L.X.P.D.S. (2000). Development of constitute equations for Ti-6Al-4V alloy under hot-working condition. *Acta Metallurgica Sinica (English Letters)* 13.1, pp. 263–269.

Lindgren, L.-E. (July 2007). *Computational welding mechanics.* 1st ed. Woodhead Publishing Limited.

Lindgren, L.-E., K. Domkin, and H. Sofia (June 2008). Dislocations, vacancies and solute diffusion in physical based plasticity model for AISI 316L. *Mechanics of Materials* 40.11, pp. 907–919.

Liu, Z. and G. Welsch (1988). Literature Survey on Diffusivities of Oxygen, Aluminum, and Vanadium in Alpha Titanium, Beta Titanium, and in Rutile. *Metallurgical and Materials Transactions A* 19.4, pp. 1121–1125.

Longuet, A., Y. Robert, E. Aeby-Gautier, B. Appolaire, J. Mariage, C. Colin, and G. Cailletaud (2009). A multiphase mechanical model for Ti–6Al–4V: Application to the modeling of laser assisted processing. *Computational Materials Science* 46.3, pp. 761–766.

Lu, S., M. Qian, H. Tang, M. Yan, J. Wang, and D. StJohn (2016). Massive transformation in Ti–6Al–4V additively manufactured by selective electron beam melting. *Acta Materialia* 104, pp. 303–311.

Lundbäck, A. (2003). "Finite Element Modelling and Simulation of Welding of Aerospace Components". PhD thesis. Luleå University of Technology.

Lundbäck, A. and L.-E. Lindgren (2011). Modelling of metal deposition. *Finite Elements in Analysis and Design* 47.10, pp. 1169–1177.

Lütjering, G. (1998). Influence of processing on microstructure and mechanical properties of $(\alpha + \beta)$ titanium alloys. *Materials Science and Engineering: A* 243.1–2, pp. 32–45.

Macdougall, D. and J. Harding (1999). A constitutive relation and failure criterion for Ti6Al4V alloy at impact rates of strain. *Journal of the Mechanics and Physics of Solids* 47.5, pp. 1157–1185.

Majorell, A., S. Srivatsa, and R.C. Picu (2002). Mechanical behavior of Ti-6Al-4V at high and moderate temperatures–Part I: Experimental results. *Materials Science and Engineering A* 326.2, pp. 297–305.

Malinov, S., Z.X. Guo, W. Sha, and A. Wilson (2001a). Differential scanning calorimetry study and computer modeling of beta to alpha phase transformation in a Ti-6Al-4V alloy. *Metallurgical and Materials Transactions: A* 32A.4, p. 879.

Malinov, S., P.E. Markovsky, W. Sha, and Z.X. Guo (2001b). Resistivity study and computer modelling of the isothermal transformation kinetics of Ti-6Al-4V and Ti-6Al-2Sn-4Zr-2Mo-0.08Si alloys. *Journal of Alloys and Compounds* 314.1-2, p. 181.

Mecking, H. and Y. Estrin (1980). The effect of vacancy generation on plastic deformation. *Scripta Metallurgica* 14.7, p. 815.

Mecking, H. and U. Kocks (1981). Kinetics of flow and strain-hardening. *Acta Metallurgica* 29.11, pp. 1865–1875.

Meier, M. and A.K. Mukherjee (1990). The strain hardening behavior of superplastic Ti-6Al-4V. *Scripta Metallurgica et Materialia* 24.2, p. 331.

Meyer, J.H.W. and D.S. Kleponis (2001). Modeling the high strain rate behavior of titanium undergoing ballistic impact and penetration. *International Journal of Impact Engineering* 26.1-10, pp. 509–521.

Meyers, M.A., D. Benson, O. Vöhringer, Q.X.B. Kad, and H.-H. Fu (2002). Constitutive description of dynamic deformation: physically-based mechanisms. *Materials Science and Engineering A* 322.1-2, pp. 194–216.

Mi, G., Y. Wei, X. Zhan, C. Gu, and F. Yu (2014). A coupled thermal and metallurgical model for welding simulation of Ti–6Al–4V alloy. *Journal of Materials Processing Technology* 214.11, pp. 2434–2443.

Militzer, M., W.P. Sun, and J.J. Jonas (1994). Modelling the effect of deformation-induced vacancies on segregation and precipitation. *Acta Metallurgica et Materialia* 42.1, p. 133.

Mills, K.C. (2002). *Recommended Values of Thermophysical Properties for Selected Commercial Alloys.* Woodhead Publishing.

Mironov, S., M. Murzinova, S. Zherebtsov, G. Salishchev, and S. Semiatin (2009). Microstructure evolution during warm working of Ti-6Al-4V with a colony-alpha microstructure. *Acta Materialia* 57.8, pp. 2470–2481.

Mishin, Y. and C. Herzig (Feb. 2000). Diffusion in the Ti-Al system. *Acta Materialia* 48.3, pp. 589–623.

Moiseyev, V.N. (July 2005). *Titanium Alloys: Russian Aircraft and Aerospace Applications.* Vol. 5. Advances in Metallic Alloys. CRC Press.

Montheillet, F. (2002). Dynamic recrystallization: classical concepts and new aspects. *Revue de Metallurgie* 99.9, pp. 767–76.

Montheillet, F. and J.J. Jonas (2009). "Fundamentals of Modeling for Metals Processing". Ed. by D.U. Furrer and S.L. Semiatin. Vol. 22A. ASM Handbook. Materials Park, Ohio 44073-0002: ASM International. Chap. 17: Models of Recrystallization, pp. 220–231.

Mosher, D.A. and P.R. Dawson (1996). A state variable constitutive model for superplastic Ti-6Al-4V based on grain size. *Journal Of Engineering Materials And Technology-Transactions Of The Asme* 118.2, pp. 162–168.

Musaeva, Z.A. and V.E. Peletskii (2002). Experimental Investigation of the Thermal Conductivity of VT6 Alloy. *High Temperature* 40 (6), pp. 838–842.

Nemat-Nasser, S., W.-G. Guo, V.F. Nesterenko, S.S. Indrakanti, and Y.-B. Gu (2001). Dynamic response of conventional and hot isostatically pressed Ti-6Al-4V alloys: experiments and modeling. *Mechanics of Materials* 33.8, pp. 425–439.

Nicolaou, P.D., J.D. Miller, and S.L. Semiatin (2005). Cavitation during Hot-Torsion Testing of Ti-6Al-4V. *Metallurgical and Materials Transactions A* 36.12, p. 3461.

Odenberger, E.-L. (2005). "Material characterisation for analyses of titanium sheet metal forming". PhD thesis. Luleå Technical University.

Orowan, E. (1948). *Symposium on Internal Stresses in Metals and Alloys*. London: Institute of Metals, p. 451.

Park, C.H., Y.G. Ko, J.-W. Park, and Y.G. Ko (May 2008a). Enhanced Superplasticity Utilizing Dynamic Globularization of Ti-6Al-4V Alloy. *Materials Science and Engineering: A*.

Park, C.H., K.-T. Park, D.H. Shin, and C.S. Lee (2008b). Microstructural Mechanisms during Dynamic Globularization of Ti-6Al-4V Alloy. *Materials Transactions* 49.10, pp. 2196–2200.

Park, N.-K., J.-T. Yeom, and Y.-S. Na (2002). Characterization of deformation stability in hot forging of conventional Ti-6Al-4V using processing maps. *Journal of Materials Processing Technology* 130-131, p. 540.

Pederson, R. (2004). "The microstructures of Ti-6Al-4V and Ti-6Al-2Sn-4Zr-6Mo and their relationship to processing and properties". PhD thesis. Luleå Technical Univeristy.

Picu, R.C. and A. Majorell (2002). Mechanical behavior of Ti-6Al-4V at high and moderate temperatures–Part II: constitutive modeling. *Materials Science and Engineering A* 326.2, pp. 306–316.

Pietrzyk, M. and J. Jedrzejewski (2001). Identification of Parameters in the History Dependent Constitutive Model for Steels. *CIRP Annals - Manufacturing Technology* 50.1, pp. 161–164.

Porter, D.A. and K.E. Easterling (1992). *Phase Transformations in Metals and Alloys*. 2nd ed. CRC Press.

Poths, R.M., B. Wynne, W. Rainforth, J. Beynon, G. Angella, and S. Semiatin (2004). Effect of strain reversal on the dynamic spheroidization of Ti-6Al-4V during hot deformation. *Metallurgical and Materials Transactions A* 35.9, pp. 2993–3001.

Prasad, Y.V.R.K. and T. Seshacharyulu (1998). Processing maps for hot working of titanium alloys. *Materials Science and Engineering A* 243.1-2, pp. 82–88.

Prasad, Y.V.R.K., T. Seshacharyulu, S.C. Medeiros, and W.G. Frazier (2001). A Study of Beta Processing of Ti-6Al-4V: Is it Trivial? *Journal of Engineering Materials and Technology* 123.3, pp. 355–360.

Prinz, F., A.S. Argon, and W.C. Moffatt (1982). Recovery of dislocation structures in plastically deformed copper and nickel single crystals. *Acta Metallurgica* 30.4, pp. 821–830.

Read, W.T. and W. Shockley (May 1950). Dislocation Models of Crystal Grain Boundaries. *Phys. Rev.* 78.3, pp. 275–289.

Reed-Hill, R.E. and R. Abbaschian (1991). *Physical Metallurgy Principles*. 3rd ed. PWS Publishing Company.

Sandstrom, R. and R. Lagneborg (1975). A model for hot working occurring by recrystallization. *Acta Metallurgica* 23.3, p. 387.

Sargent, G., A. Zane, P. Fagin, A. Ghosh, and S. Semiatin (2008). Low-Temperature Coarsening and Plastic Flow Behavior of an Alpha/Beta Titanium Billet Material with an Ultrafine Microstructure. *Metallurgical and Materials Transactions A* 39 (12), pp. 2949–2964.

Schneider, C.A., W.S. Rasband, and K.W. Eliceiri (2012). NIH Image to ImageJ: 25 years of image analysis. *Nature methods* 9.7, p. 671.

Seco, F.J. and A.M. Irisarri (2001). Creep failure mechanisms of a Ti-6Al-4V thick plate. *Fatigue & Fracture of Engineering Materials and Structures* 24.11, p. 741.

Seeger, A. (1956). "The mechanism of Glide and Work Hardening in FCC and HCP Metals". *Dislocations and Mechanical Properties of Crystals*. Ed. by J. Fisher, W.G. Johnston, R. Thomson, and T.J. Vreeland, pp. 243–329.

Seetharaman, V. and S.L. Semiatin (2002). Effect of the lamellar grain size on plastic flow behavior and microstructure evolution during hot working of a gamma titanium aluminide alloy. *Metallurgical and Materials Transactions A* 33A.12, p. 3817.

Semiatin, S.L. and T.R. Bieler (2001). The effect of alpha platelet thickness on plastic flow during hot working of Ti-6Al-4V with a transformed microstructure. *Acta Materialia* 49.17, p. 3565.

Semiatin, S.L., V. Seetharaman, and A.K. Ghosh (1999a). Plastic flow, microstructure evolution, and defect formation during primary hot working of titanium and titanium aluminide alloys with lamellar colony microstructures. *Philosophical Transactions: Mathematical, Physical and Engineering Sciences* 357, pp. 1487–1512.

Semiatin, S.L., V. Seetharaman, and I. Weiss (1999b). Flow behavior and globularization kinetics during hot working of Ti-6Al-4V with a colony alpha microstructure. *Materials Science and Engineering A* 263.2, p. 257.

Semiatin, S.L., V. Seetharaman, and I. Weiss (1998). Hot workability of titanium and titanium aluminide alloys–an overview. *Materials Science and Engineering A* 243.1-2, pp. 1–24.

Semiatin, S.L., N. Stefansson, and R.D. Doherty (2005). Prediction of the Kinetics of Static Globularization of Ti-6Al-4V. *Metallurgical and Materials Transactions* 36A.5, pp. 1372–1376.

Semiatin, S., S. Knisley, P. Fagin, D. Barker, and F. Zhang (2003). Microstructure evolution during alpha-beta heat treatment of Ti-6Al-4V. *Metallurgical and Materials Transactions A* 34.10, pp. 2377–2386.

Seo, S., O. Min, and H. Yang (2005). Constitutive equation for Ti-6Al-4V at high temperatures measured using the SHPB technique. 31.6, p. 735.

Seshacharyulu, T., S.C. Medeiros, W.G. Frazier, and Y.V.R.K. Prasad (2002). Microstructural mechanisms during hot working of commercial grade Ti-6Al-4V with lamellar starting structure. 325.1-2, p. 112.

Shell, E. and S.L. Semiatin (1999). Effect of initial microstructure on plastic flow and dynamic globularization during hot working of Ti-6Al-4V. *Metallurgical and Materials Transactions A* 30.12, pp. 3219–3229.

Sheppard, J. and J. Norley (1988). Deformation Characteristics of Ti-6Al-4V. *Material Science and Technology* 4.10, pp. 903–908.

Shewmon, P.G. (1963). *Diffusion in solids.* McGraw-Hill series in materials science and engineering. McGraw-Hill.

Simo, J.C. and R.L. Taylor (1986). A return mapping algorithm for plane stress elastoplasticity. *International Journal for Numerical Methods in Engineering* 22.3, pp. 649–670.

Simo, J. and T.J.R. Hughes (1998). *Computational Inelasticity.* 1st ed. Vol. 7. Interdisciplinary Applied Mathematics. Springer.

Stefansson, N. and S.L. Semiatin (2003). Mechanisms of globularization of Ti-6Al-4V during static heat treatment. *Metallurgical and Materials Transactions* 34A.3, pp. 691–698.

Stefansson, N., S.L. Semiatin, and D. Eylon (2002). The kinetics of static globularization of Ti-6Al-4V. *Metallurgical and Materials Transactions* 33A.11, pp. 3527–3534.

Stouffer, D.C. and L.T. Dame (Feb. 1996). *Inelastic Deformation of Metals: Models, Mechanical Properties, and Metallurgy.* John Wiley & Sons, Inc.

Swarnakar, A.K., O.V. der Biest, and B. Baufeld (2011). Thermal expansion and lattice parameters of shaped metal deposited Ti–6Al–4V. *Journal of Alloys and Compounds* 509.6, pp. 2723–2728.

Tabei, A., F. Abed, G. Voyiadjis, and H. Garmestani (2017). Constitutive modeling of Ti-6Al-4V at a wide range of temperatures and strain rates. *European Journal of Mechanics-A/Solids* 63, pp. 128–135.

Tersing, H., J. Lorentzon, A. Francois, A. Lundbäck, B. Babu, J. Barboza, V. Bäcker, and L.-E. Lindgren (2012). Simulation of manufacturing chain of a titanium aerospace component with experimental validation. *Finite Elements in Analysis and Design* 51.0, pp. 10–21.

Thomas, J.-P. and S.L. Semiatin (Sept. 2006). *Mesoscale Modeling of the Recrystallization of Waspaloy and Application to the Simulation of the Ingot-Cogging Process.* Tech. rep. AFRL-ML-WP-TP-2006-483. Air Force Research Laboratory, Air Force Materiel Command, Wright-Patterson AFB, OH 45433-7750: Materials and Manufacturing Directorate.

Thomas, R.B., P.D. Nicolaou, and S.L. Semiatin (2005). An Experimental and Theoretical Investigation of the Effect of Local Colony Orientations and Misorientation on Cavitation during Hot Working of Ti-6Al-4V. *Metallurgical and Materials Transactions A* 36A.1, p. 129.

Tiley, J.S. (2002). "Modeling of Microstructure Property Relationships in Ti-6Al-4V". PhD thesis. Ohio State University.

Vanderhasten, M., L. Rabet, and B. Verlinden (2007). Deformation Mechanisms of Ti-6Al-4V During Tensile Behavior at Low Strain Rate. *Journal of Materials Engineering and Performance* 16.2, p. 208.

Wachtman, J.B., W.E. Tefft, D.G. Lam, and C.S. Apstein (June 1961). Exponential Temperature Dependence of Young's Modulus for Several Oxides. *Phys. Rev.* 122 (6), pp. 1754–1759.

Westman, E.-L. (2003). "Development of an inverse modelling programming system for evaluation of Ti-6Al-4V Gleeble experiments". Master's Thesis. Luleå University of Technology.

Williams, J.C. and G. Lütjering (2003). *Titanium*. Springer - Verlag.

Woldt, E. and D.J. Jensen (1995). Recrystallization kinetics in copper: Comparison between techniques. *Metallurgical and Materials Transactions A* 26.7, pp. 1717–1724.

Zerilli, F.J. and R.W. Armstrong (1998). "Dislocation mechanics based constitutive equation incorporating dynamic recovery and applied to thermomechanical shear instability". *The tenth American Physical Society topical conference on shock compression of condensed matter*. Vol. 429. Amherst, Massachusetts (USA): AIP, p. 215.

Appended Papers

Simulation of manufacturing chain of a titanium aerospace component with experimental validation

Authors:
Henrik Tersing, John Lorentzon, Arnaud François, Andreas Lundbäck, Bijish Babu, Josue Barboza, Vladimir Bäcker, Lars-Erik Lindgren.

Simulation of manufacturing chain of a titanium aerospace component with experimental validation

H. Tersing [a], J. Lorentzon [a], A. Francois [b], A. Lundbäck [c], B. Babu [c], J. Barboza [b], V. Bäcker [d], L.-E. Lindgren [c],*

[a] Volvo Aero Corporation, 46181 Trollhättan, Sweden
[b] Cenaero, Rue des Frères Wright 29, 6041 Gosselies, Belgium
[c] Luleå University of Technology, 97187 Luleå, Sweden
[d] Laboratory for Machine Tools and Production Engineering (WZL) of RWTH Aachen University, Chair of Manufacturing Technology, 52056 Aachen, Germany

ARTICLE INFO

ABSTRACT

Manufacturing of advanced components like aeroengine parts is performed in a global network. Different manufacturers deliver individual components to the engine and even different manufacturing steps for a given component may be performed at different companies. Furthermore, quality is of utmost importance in this context. Simulations are increasingly used to assure the latter. The current paper describes the simulation of a chain of manufacturing processes for an aeroengine component. Different partners have performed the simulations of the different steps using a variety of finite element codes. The results are discussed in the paper and particularly the lessons learned regarding the modelling process.

© 2011 Elsevier B.V. All rights reserved.

1. Introduction

Design and manufacturing of high quality components like aerospace components includes rigorous design rules as well as qualification procedures. These procedures include several tests of performance and particularly lifetime. The qualification thus includes both the actual design of the component as well as its manufacturing route. Therefore a change in the manufacturing route may require a new qualification even if the actual component design is not changed. This is because the manufacturing chain affects not only geometric tolerances but also internal stress and defect state of the component. The vision is to be able to qualify a component based on its design together for a given state of residual stresses and defects due to the manufacturing. Then it would be sufficient to show that a change in the manufacturing route does not increase these variables. Thereby, the cost for improving the manufacturing route is lowered.

The current paper describes developments done to partly address the issue above. It is concerned with simulating a manufacturing chain typical of an aerospace component. The focus is on deformations and stresses of the component, as the used models do not predict defects. The work has been done within the 6th Framework programme; project Virtual Engineering for Robust Manufacturing with Design Integration (VERDI).

A component with features of a real aerospace component has been manufactured. This manufacturing chain includes forming, machining, welding, metal deposition, and heat treatment. The chain has been simulated with different models and finite element software. Mapping of results between different models has therefore been necessary. The work illustrates the state of the art of the simulation of a manufacturing chain. Earlier work has usually focussed on one manufacturing step and sometimes two steps, like a combination of welding and heat treatment [1]. Hyun and Lindgren [2] simulated three steps but this was a fictive case and did not include any experiments. Babu and Lundbäck [3] presented a three-step simulation of a Ti–6Al–4V plate as a prelude to the current work. The used approach is described in the paper and some results are discussed and also lessons learned for future developments.

2. Manufacturing of geometrical simplified aeroengine component

The main purpose of the simplified geometrical aeroengine component, further called sub-component, is to validate the simulation tools. Therefore designs and operation sequences are not identical to components in production. Rather, the component has been designed to meet the requirements from a process simulation perspective. The material in the sub-component is the titanium alloy Ti–6Al–4V.

* Corresponding author. Tel.: +46 920 491306.
E-mail address: lars-erik.lindgren@ltu.se (L.-E. Lindgren).

The sub-component design, Fig. 1, is a geometrically simplified part of the inner flow path and vane of the structure to the left in the figure. This is a mock-up resembling a casing of an aero-engine. The sub-component is shown to the right in Fig. 1 and it is the lower part of a 36°-sector, middle in Fig. 1, which makes up the full component. The design is manufactured by five parts; a flat bottom sheet, a stand up, a leading edge, a trailing edge and two vane sheets. The leading and trailing edge are milled from a bar, the vane sheets are manufactured by hot sheet metal forming, the stand up is build by metal deposition and then a plane is milled at top of the metal deposited material to match the lower edge of the vane sheets, left part of Fig. 2. The parts are then welded together as shown in Fig. 3, followed by a stress relief heat treatment. Finally, roller burnishing is applied as in Fig. 4.

The milling and the roller burnishing steps also include micro–macro simulations in order to understand the effects of the near-surface residual stress profile on the global deformation.

The roller burnishing process was applied on the critical surface surrounding the welding line between the metal deposition area and the vane area in order to create compressive residual stresses for improved fatigue strength. The roller burnishing area covers the welding line with a width of 8 mm and the influenced area with a total width of 28 mm, see Fig. 5. The process was performed using a three-axis milling machine. A conventional roller burnishing tool was used with a ball diameter of 13 mm. In order to prevent the deformation of the complete sub-component due to the applied rolling pressure, the lower sub-component's side was supported during this step.
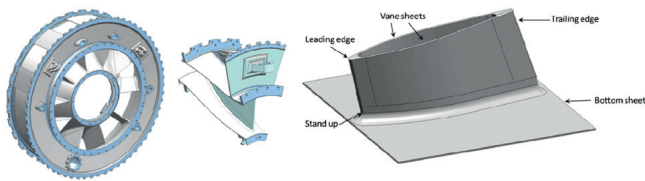

Fig. 1. Final assembly of ten 36°-sectors into an aero-engine component (left). A 36°-sector (mid) and the studied sub-component (right).
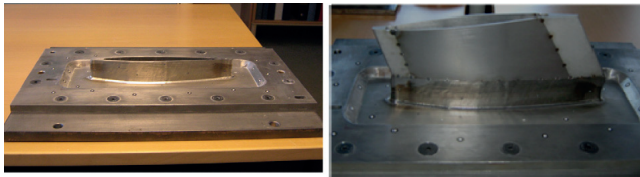

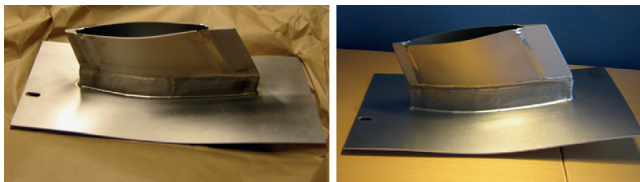**Fig. 2.** Metal deposited stand up after machining (left) and the sub-component tack welded (right).

Fig. 3. Sub-component welded and released from the fixture (left) and after heat treatment (right).
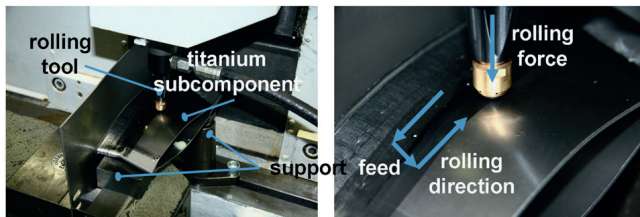

Fig. 4. Roller burnishing experimental set-up.

The following list and flow chart in Fig. 6 summarise the fabrication sequence used to make the sub-component, both in reality and in the virtual manufacturing chain.

- Metal deposit the stand-up; height 50 mm.
- Mill the top face of metal deposited stand-up.
- Hot form vane using 2 mm sheet.
- Weld the trailing edge and formed vane sheet together.
- Weld the leading edge and formed vane sheet together.
- Weld the vane to the stand-up.
- Stress relief heat the assembly.
- Roller burnish at one of the stand-up to the vane weld.

Some manufacturing steps were not simulated:

- The manufacturing of the sheets for the vane and bottom plates was not simulated. The forming of the vane sheet started with a plane sheet without any residual stresses. The same holds for the simulation of the metal deposition on the bottom plate.
- The manufacturing of the trailing and leading edge, e.g. rolling of the bar and their machining were not simulated.
- Tack welding of vane to stand-up was not simulated. Links were used to imitate the connecting of the stand-up with the vane before welding started.

The simulations were validated using the ATOS optical 3D scanner for geometry measurement. Some of the results from ATOS are shown in this paper as well as stress measurements due to the roller burnishing process.

3. Simulation of manufacturing chain

Simulation of entire manufacturing chains using different FE-solvers and meshes requires the transfer of data between the various process models. One tool was developed for reading and
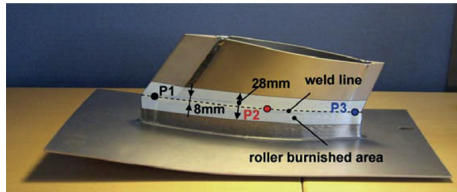

Fig. 5. Roller burnishing strategy.

writing of files of formats for different finite element codes. This tool communicated with a mapping tools that did the actual data transfer. One mapping tool is a general mapping whereas another one was tailored to map surface information from a detailed local model to a global model. The latter was used in the case of the roller burnishing simulation that is split into a 2D local model with a fine mesh and a 3D global model with a coarser mesh.

3.1. Conversion between different file formats

In the VERDI project, software to handling the data transfer between the different FE-software was created. It is called Finite Element Data Exchange System (FEDES) and can transfer Finite Element data (stresses, strains, displacements, state variables, etc.) between different FE-solvers (Abaqus, Ansys, MSC.Marc, Deform, Vulcan and Morfeo). FEDES can write the result also in two neutral formats. XML structured format is used for storage and visualisation purposes. This format can be visualised with external viewer. The second neutral format is created to link FEDES with the mapping tool described below.

3.2. Mapping of results between models

A mapping tool was used for transferring information between finite element models of the different steps. The models had different number and sizes of element as well as different types of elements.

The mapping method is based on the interpolation technique used in finite element formulations. Values to be sent to the receiving (new) model were obtained by

$$v_{new} = \mathbf{N}_{old}(\xi_{old}(\mathbf{x}_{new}))\mathbf{v}_{old} \tag{1}$$

where $\mathbf{N}_{old}$ is the shape function of the element in the sending (old) model evaluated at the local coordinate, ξ_{old}. This element was found by a search procedure locating which element the point $\mathbf{x}_{new}$ is inside and also determining which local coordinate ξ_{old} it corresponds to. $\mathbf{v}_{old}$ is the vector with nodal values of the sending elements. Thus they are interpolated to the receiving point using the finite element interpolating (shape) functions.

Two types of information are transferred between the meshes, nodal data and integration point data. The latter need an additional step before applying Eq. (1). The existing integration point data of the old element must be extrapolated to its nodes. They are extrapolated differently depending on type of element and number of integration points. Two options exist before applying Eq. (1). Either the extrapolated nodal values are only created from the actual element to containing $\mathbf{x}_{new}$ or a similar extrapolating process is performed for all surrounding elements and averaged (smoothed) nodal values are created and placed in $\mathbf{v}_{old}$. The latter option was used in all cases in the current work.
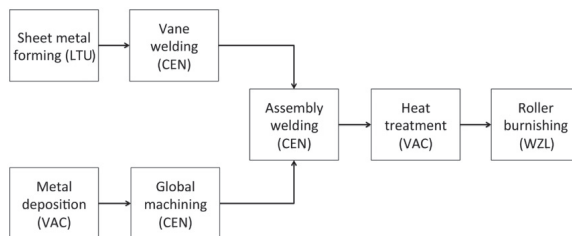

Fig. 6. Process flowchart. The abbreviations in each box denote which one of the authors that performed the simulation. LTU is Luleå University of Technology, CEN is Cenaero, VAC is Volvo Aero Corporation and WZL is Laboratory for Machine tools and Production Engineering.

3.3. Local to global mapping of results between models

The mapping described in the aforementioned section was adapted in order to transfer information from a 2D local model to
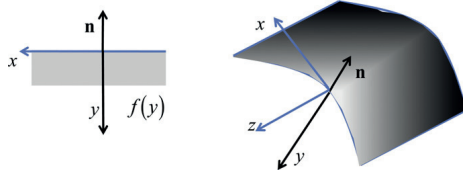

Fig. 7. 2D local geometry (left) used to map data, $f(y)$, from the local (small) model to large, global model. The latter can be in 3D and a local surface coordinate system is reconstructed (right) in order to receive this data.
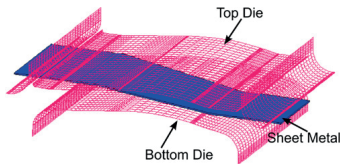

Fig. 8. Isometric view of simplified tool and sheet metal.

Fig. 9. Final geometry of the vane after releasing from the tool. Then the contact conditions are not applied so the tool surfaces (thin lines) and plate overlap.
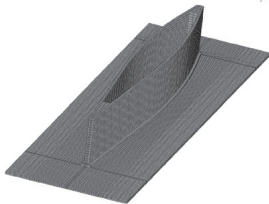

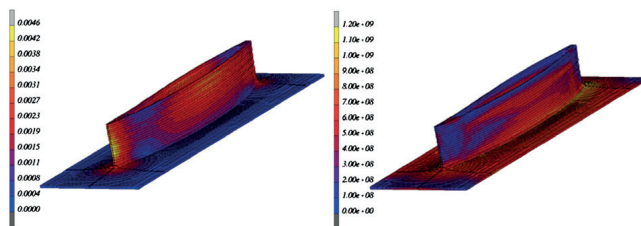**Fig. 10.** Model after metal deposition that creates the stand-up.

a 3D global model in thin surface layer of the latter. In fact, for reasons of accuracy and robustness of the computations, some local models are in 2D and the results of this model have to be transferred to a global model in 3D.

The 2D local model is in xy plane, see left part of Fig. 7, with the y-axis in the depth direction. The latter means that it is opposite to the surface normal, **n**. The first step of the local to global mapping method involves extracting data from the 2D model along this y-axis. The information to be transferred is extracted in the form of curves where the values are functions of the depth only in the local model, $f(y)$. A corresponding local coordinate system with the y-axis directed to the interior of the 3D surface is set up, see right part in Fig. 7. Thereafter the corresponding depth coordinates of points located in a predefined thin surface layer of the global model are identified. Finally, the values to be assigned are obtained from the created transfer curves.

The order of magnitude of the mesh size (or the number of integration points) in the surface layer of the global model must be the same as in the local model in order to avoid loss of information.

3.4. Simulation of forming

The vane consists of two formed sheets welded together. They are joined at two of their edges together with bars making up the leading and trailing edges of the vane. The sheets are hot formed as shown in Fig. 8 and explained below. The welding is described in Section 3.7.

The finite element code MSC.Marc using the updated Lagrangian formulation was used to model this manufacturing step. The work piece is a sheet metal made of Ti–6Al–4V with thickness of 2.04 mm and is meshed with linear hexahedral eight node elements with four elements across the thickness. The mesh has 26,455 nodes and 20,460 elements. In order to avoid problems with shear locking and volumetric locking, two modified integration schemes, assumed strain and constant dilatation are used. Assumed strain formulation is a hybrid element with additional degrees of freedom, which will reduce the shear locking. Constant dilatation is a selective reduced integration technique, which will prevent volumetric locking.

The profile of the top and bottom die is obtained by an iterative design procedure until the wanted geometry of the final component after unloading is obtained. The tools are modelled by rigid surfaces. The die and sheet metal have a prescribed temperature of 800 °C during forming. During release and cooling, necessary boundary conditions are provided to avoid rigid body motion. The motion of the tool during pressing is achieved by prescribing the displacement of the top die with the bottom die kept fixed and the velocity of the tool is 2.8 m/s. A special algorithm in Marc for contact release was applied for the unloading step.

Fig. 11. Residual deformation[m] after metal deposition (left). Residual von Mises effective stresses [Pa] after metal deposition (right).

Friction is modelled by using Coulomb friction model. The arctangent model is used to model the friction force, which gives a continuous function in terms of relative sliding velocity. The relative velocity threshold used in this simulation is 0.01 with a friction coefficient of 0.1.

The work piece is held at 800 °C from the start to end of forming and is cooled to room temperature by convection during the cooling cycle after forming and tool release. A dislocation density based material model is used to account for the mechanical constitutive behaviour of Ti–6Al–4V. Detailed descriptions of the model and its parameters are available in [4]. It is based on the developments in Lindgren et al. [5].

The solver is a multifrontal sparse solver working on ten processors with 2046 elements each and took 5.43 h to solve on 2.8 GHz CPUs. The results of the simulation are stored for the last time step and are passed to the welding of the vane sheet to the trailing and leading edge. The final geometry after forming is shown in Fig. 9.
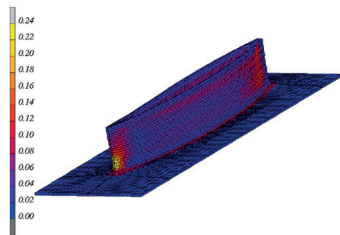

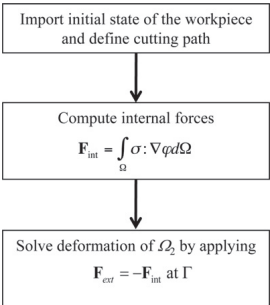**Fig. 12.** Effective plastic strains [dimensionless] after the completed process and cooling to room temperature.

Fig. 13. Computational strategy.

3.5. Simulation of metal deposition

The simulation of the metal deposition was performed on a 2 mm thick sheet. The logic for metal deposition is based on the method presented in [6] and its implementation is described in detail in [7,8]. The same material model as used in the previous forming step was used here. The mesh consists of eight-noded hexahedral elements, where the initial mesh had 14,112 elements and final mesh had 20,386 elements (Fig. 10). The analysis was carried out using MSC.Marc and using the same assumptions as in the forming simulation regarding large deformations, strains and plastic incompressibility. The staggered approach was used to solve the coupled thermo-mechanical problem and constant temperature was used in each element in the mechanical step [9]. The residual deformation, von Mises stress and effective plastic strain from the metal deposition are shown in Figs. 11 and 12.

3.6. Simulation of machining

The aim of the machining simulation is to compute the spring back and the stress re-equilibrium occurring during the machining of the stand-up onto which a vane will be welded. First, an innovative strategy for the global machining problem using the level set technique is presented. Its application to simulate the machining process of the deposited metal follows.

For the sake of simplicity, we assume that a single layer of material is removed. Let Γ denote the cutting path. Let $\Omega = \Omega_1 \cup \Omega_2$ denotes the workpiece to be machined, where Ω_1 is the

Table 1
number of vertices and cells of both meshes.

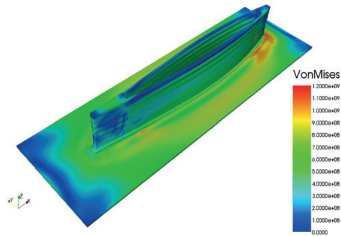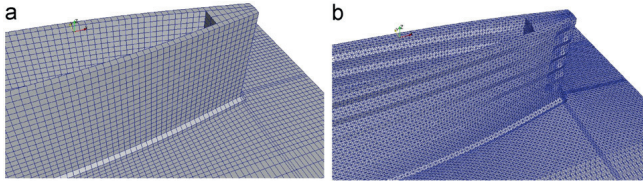|	Hexahedral deposited model mesh (8 Gauss points)	Tetrahedral global machining model (1 Gauss point)
Number of vertices	25,434	244,869
Number of cells	13,330	114,321

Fig. 15. Imported von Mises stresses [Pa].

Fig. 14. Hexahedral metal deposition model (a), tetrahedral global machining model with the update of the vertex positions (b).

domain to be removed and Ω_2 is the remaining volume. Γ defines the intersection between Ω_1 and Ω_2 ($\Gamma = \Omega_1 \cap \Omega_2$) and is modelled as a level-set defined by the signed distance function Φ, see [10].

The strategy to solve the global machining problem may be divided in three major steps, Fig. 13. First the state variables resulting from the previous process are imported. Thereafter, the computation of internal forces due to the initial residual stresses is performed and finally solving equilibrium on the remaining domain Ω_2. The latter is performed with the application of the reaction forces on the iso-zero level-set Γ coming from Ω_1. These reaction forces are opposite to the internal forces due to the existing stress state.

Using the residual stress resulting from the previous process, the internal forces are computed by the following equation:

$$F = \frac{1}{2} \int_{\Omega} \sigma : \nabla \varphi \, d\Omega \qquad (2)$$

where σ is the stress tensor, $\nabla \varphi$ the gradient of the shape function φ used for the discretisation of the displacement field.

Once computed, the opposite of the internal forces are used as a boundary condition on the iso-zero level-set Γ, on top of the clamping and other fixations, in a static solution. Solving the equilibrium equation gives the distortions due to initial residual stresses from the previous manufacturing process. Fixations are set in all directions along each side of the plate. The material behaviour was assumed to be elastic during this deformation. The Young's modulus and the Poisson's are set to 200 GPa and 0.3, respectively. Additionally, small strains and displacements are assumed.

This computation strategy used to simulate the global machining is implemented in the Morfeo software developed by Cenaero and is used to simulate the machining of the upper surface of the deposited metal.

The final state from the metal deposition process is used as initial condition. Before the simulation of the machining process, using the metal deposition process results, the following tasks were executed, see Fig. 14:

- The eight-node-hexahedral metal deposition mesh elements are transformed to four-node-tetrahedral elements.
- The mesh is refined and results are transferred from the eight-node-hexahedral elements mesh to a refined four-node-tetrahedral elements mesh.

The following table shows the number of vertices and cells for each process (Table 1).

The imported variables are stresses and displacements and the mesh vertices are updated according to the displacement field, Fig. 15. After the update of the mesh vertices the displacement field is set to zero.

Fig. 16 illustrates the cutting path represented by a level-set: machining of the upper side of inner ring. The position of the level-set is 38 mm high form the plate.

The results obtained from the global machining simulation are illustrated in Figs. 17 and 18.

3.7. Simulation of welding

The simulation of the welding process was done in the fourth simulation step. The initial state variables and geometries resulting from the previous manufacturing processes are taken into account.

First, a geometry model of the assembly was reconstructed using the final shapes resulting from the sheet forming and machining simulations of the metal deposited stand up. For this operation, the geometry model of each part is built from the deformed mesh using external NURBS surfaces, as illustrated in Fig. 19 for the stand up component. Then, appropriate rotations and translations are applied to the different components to position them in the assembly. The solid geometry model of the assembly is shown in Fig. 20. From the geometry of the assembly a finite element mesh is created. The mesh used for the welding simulation is shown Fig. 20 and consists of 39,808 nodes and 160,619 elements (tetrahedra) with mesh refinements in the weld zones.

Then, the final states from the sheet forming and stand up machining processes were imported as initial conditions in the welding simulation, using appropriate rotations and translations during the mapping (Fig. 21). The imported variables, residual stresses and equivalent plastic strains are illustrated in Fig. 22.

The simulation of the welding process was done using the Morfeo finite element software. A non-linear elasto-plastic material law, with thermally dependant parameters is used. A welding velocity of 1.2 mm/s and a power of 540 W are used in the welding process. The heat source parameters in the numerical
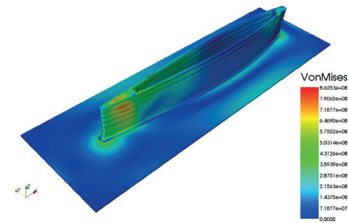
Fig. 17. Von Mises stress [Pa].
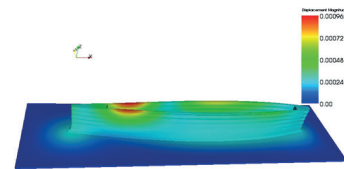
Fig. 18. Magnitude of displacement [m] due to machining.
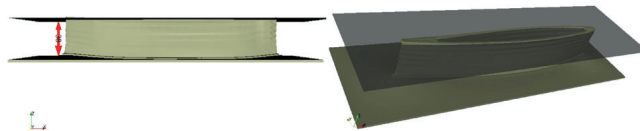
Fig. 16. Definition of the top cutting path (the surface).
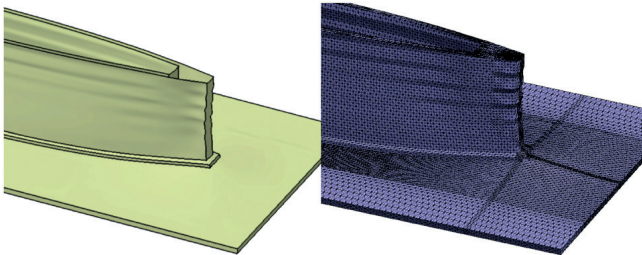
Fig. 19. Reconstructed surface geometry (left) and mesh of the assembly (right).
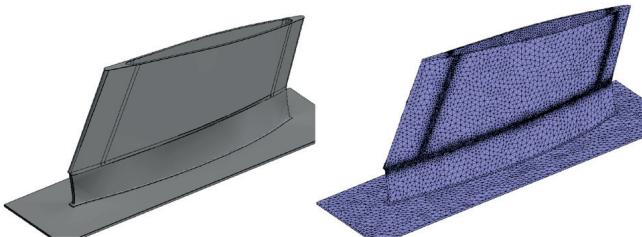
Fig. 20. Reconstructed geometry (left) and mesh of the assembly (right).
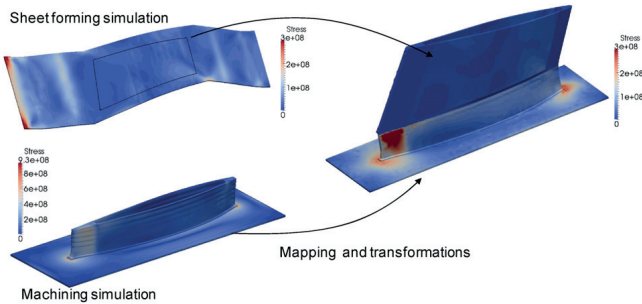
Fig. 21. Importing the initial states from the sheet forming and the stand up machining processes.
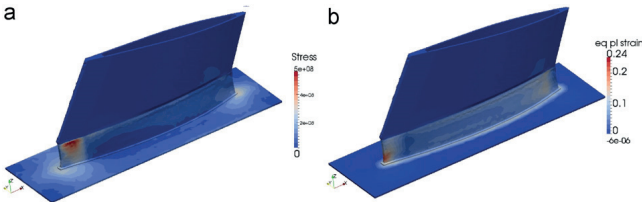
Fig. 22. Initial conditions for welding: residual stresses [Pa] (left) and equivalent plastic strains [dimensionless] (right).

model were fitted in order to match the measured width of the welds. The welding path is made of six welds and the sequence is assumed continuous, without any cooling transition between the welds. The tack welding used to fix the different parts together was not taken into account in the welding simulation.

The clamping system is applied along each side of the bottom plate with an imposed temperature of 20 °C and constrained displacements. A heat loss by convection is also taken into account (20.0 W/m^{2}K). The time step parameters used in the welding simulation are summarised in Table 2. The total simulation time, using parallel computation with 32 CPUs, was 3:10 h.

Fig. 23 shows the temperature distribution during the welding of the vane with the stand up. The residual distortions, stresses and equivalent plastic strains computed after complete cooling and removal of the clamping conditions are illustrated in Figs. 23 and 24.

3.8. Simulation of heat treatment

The simulation of the heat treatment after welding was done using MSC.Marc. The assumptions concerning large strains etc were the same as for the sheet metal forming and metal deposition simulations. The preceding process to the heat treatment process was the welding of a stand-up and a vane.

Table 2
Time step parameters used in the welding simulation.

Simulation parameters	Welding phase	Cooling phase
Time	698.0 s	2700 s
Time step (Δt)	2.0 s	Variable
Number of time steps	350	80

In the stress relief heat treatment the initial state (stresses and state variables) is extracted from the preceding process that in turn includes effect of all previous steps. The same mesh as in the welding assembly was used and thus no mapping was needed. FEDES, see Section 3.1, was used to move data from Morfeo to MSC.Marc. The heat treatment mesh consists of 160,619 four-node-tetrahedral elements and 39,808 nodes.

The final state from the welding process, see previous section, is used as initial condition for the heat treatment simulation. The initial temperature in the stress relief was 20 °C. The model was fixed in one corner to avoid rigid-body-rotation but allowing free volumetric expansion. The component was heated and cooled with natural convection using a heat transfer coefficient of 12 W/m^{2}K. The heat treatment temperature was 560 °C and hold time at that temperature was two hours.
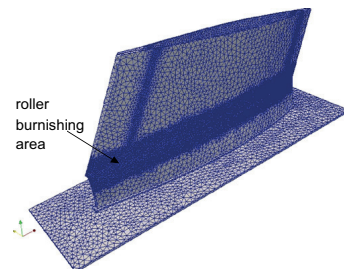

Fig. 25. Mesh refinement in the roller burnishing zone.
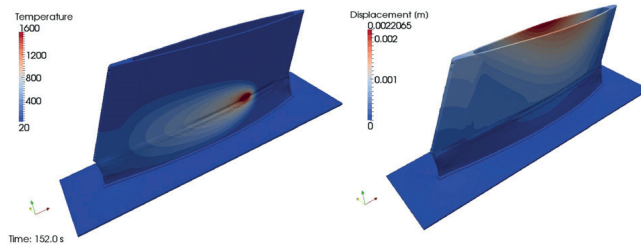

Fig. 23. Temperature distribution [°C] during welding (left) and residual displacements [m] after cooling and release (right).
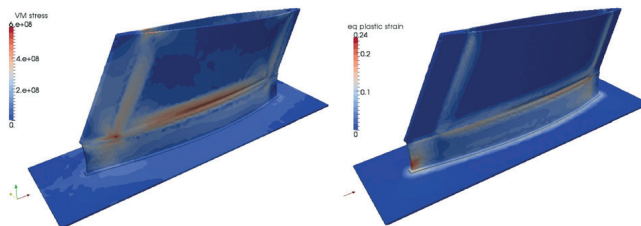

Fig. 24. Residual Von Mises stresses [Pa] (left) and equivalent plastic strain [dimensionless] computed at the end of the welding process.
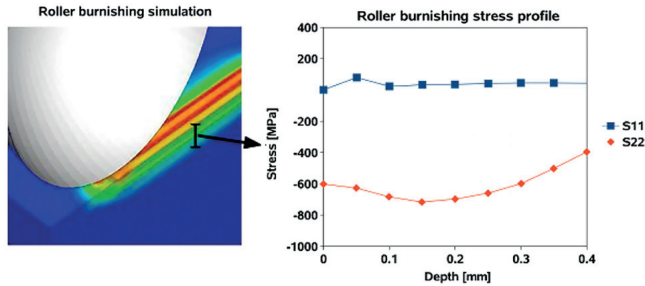
Fig. 26. Roller burnishing (left) and stress profiles (right) as function of depth.
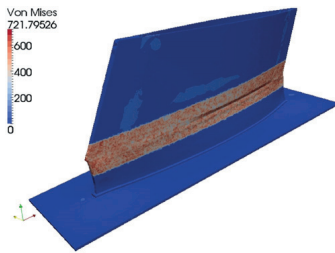

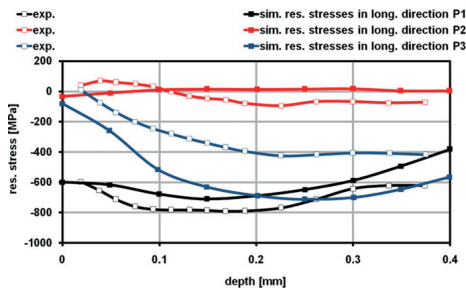**Fig. 27.** Roller burnishing stresses [MPa] imported in the sub-component.

Fig. 28. Measured and computed stress profiles. Locations P1, P2 and P3 are shown in Fig. 5.

3.9. Simulation of roller burnishing

A numerical model to simulate the roller burnishing (RB) process at the local scale has been implemented using Abaqus finite element software. The effects of the roller burnishing tool on the material are taken into account using local models with fine meshes. A detailed description of the simulation model development and its validation can be found in [11,12]. Since the application of this approach is not feasable for large scale components in a reasonable computing time, state variables resulting from the local roller burnishing are mapped into the global model on the sub-component as discussed in Section 3.3. To avoid an accuracy loss during the mapping between local and global models, the mesh used in the heat treatment simulation

has been refined in the RB zone in order to capture the RB stress profile. The mapping was limited to a given depth (0.4 mm). Fig. 25 illustrates the mesh used to import the RB stress profile made of 361,663 elements (tetrahedra) and 82,541 nodes. In this example, an isotropic mesh refinement has been used.

The stress profile curves resulting from the local roller burnishing model are shown in Fig. 26 (S11 and S22 are the stress components, respectively, normal and parallel to the surface). First, the residual states from the heat treatment simulation are imported. Then, the residual stresses resulting from the local roller burnishing simulation were imported to the sub-component and the result is shown in Fig. 27.

A comparison between measured and computed stress profiles is given in Fig. 28.

3.10. Effect of residual states from manufacturing process

The residual state from the last step of the manufacturing process is obtained using the above described steps. Two different residual states are considered for hot-spot analysis. One is the state after heat treatment and the other is the residual state after roller burnishing. The residual stress tensor and equivalent plastic strain are used as initial conditions using user routines for MSC.Marc. Figs. 29 and 30 show the different residual states imported to the component for in-service loading. They are then initial states for the component loaded with in-service loadings and subjected to hot-spot analysis. The hot-spot analysis is not included in the current paper.

4. Validation of geometry

Most measurements for validation of the complete chain were based on geometry. An example of validation of stresses is shown in Fig. 28 for the roller burnishing process.

Computed deformations and the (optical) measured geometry are compared. The latter were obtained using the ATOS system. To compare the results, the deformation result (the last increment) from all simulations is converted to STL-format and imported into ATOS together with the corresponding optical measurement. Measurements were made after each process step, although not shown in the paper due to space limitations. The figures below show the distance between a point on the real object to the 'corresponding' point on the model. An optimisation is initially done to translate and rotate the measured shape so it matches the computed shape as closely as possible. Thereafter corresponding points can be determined and the distance between them. This matching had to be done anew after each
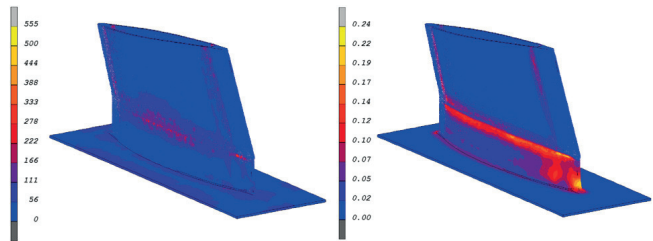
Fig. 29. Von Mises effective stress [MPa] (left) and effective plastic strain [dimensionless] (right) after heat treatment (State 1).
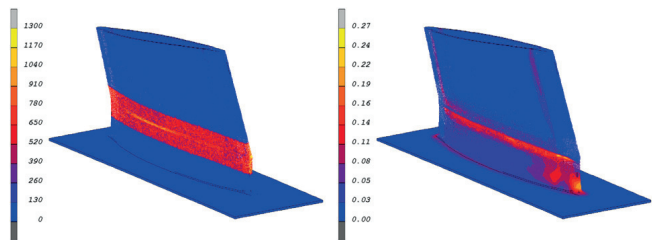

Fig. 30. Von Mises effective stress [MPa] (left) and effective plastic strain [dimensionless] (right) after roller burnishing.
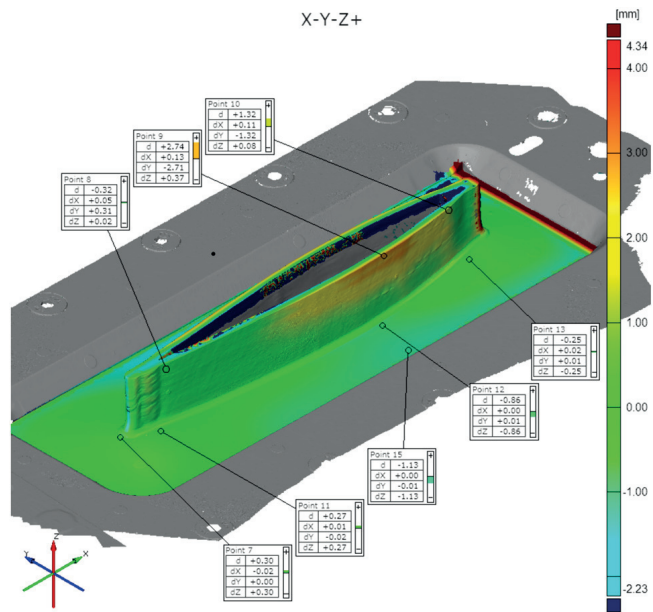

Fig. 31. Discrepancy between measured and computed geometry after machining.
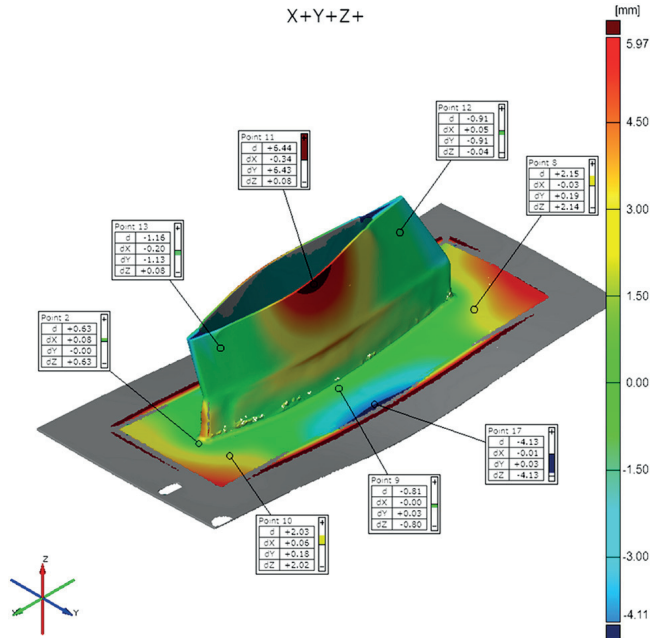
Fig. 32. Discrepancy between measured and computed geometry after heat treatment.

simulation step when comparing measured and computed shapes. The differences are smaller during the first steps, not shown here, and increases to a maximum 5–6 mm at end of the chain.

The comparison of geometry after machining and optical measured geometry by ATOS is presented in Fig. 31. The larger discrepancy at edge of plate is due that the fixture (the grey part in the figure) was imaged by ATOS and mistakenly compared with the model due to a length difference in the bottom plate. The other larger discrepancy at the front end of the vane is due to simplified welding model. This model does not account for flow of molten metal. It is only treated as a soft solid in the computational weld mechanics model, see [9]. Therefore, the computed shape is less rounded than the real shape. The maximum difference is 4.3 mm in this region but more typically it is around ± 1.5 mm.

The comparison after the heat treatment simulation results and optical measurements is presented in Fig. 32. The results show that the FE-model has not captured the tendency correctly at the vane top mid section and at the bottom plate mid section. The maximum deviation has now increased to nearly 6 mm.

5. Discussions and conclusions

Simulation of a chain of manufacturing steps has been demonstrated. The accuracy of the individual steps has been evaluated in different contexts. Validation of the model for metal deposition is presented in [8]. The simulation model is similar as the welding model, except for the element activation technique used in the

metal deposition simulation, see [8]. The roller burnishing validation is given in [11,12]. The accuracy with respect to geometry, excluding the specific issues discussed in previous chapter, is around ± 1.5 mm. This is not sufficient accurate when considering geometric tolerances required for this kind of aeroengine part.

The more challenging processes to model are machining, welding and heat treatment. They require material models that are valid over large temperature and strain rate ranges. The mapping of results between the different process models was limited to geometrical information as well as stresses and plastic strains. The mapping introduces some approximations. However, even if this would be perfect, a mismatch between the models may exist. This would be the case if the process models use different constitutive equations. Then a given stress and plastic strain state will correspond to different flow stress distribution depending on the used plasticity model. Thus a consistency between the material modelling must be assured between each step. Different material models were used in the current work. This also underlines the need for a capable material model that is valid over a large range of temperatures, strains and strain rates together with varying microstructure.

It is clear from the results in Figs. 29 and 30 that the residual stresses due to the manufacturing are considerable. Current procedures for estimating in-service life in hot-spot analysis do not take them into account explicitly. In order to make use of results like those in the present paper it is necessary to have better test data. Lifing model must be calibrated using data from test specimens with known residual stresses and defects, not only stresses due to externally applied loads. When this is available, then a change of manufacturing route for an aeroengine

component can be permitted if the obtained combination of residual stresses and defects are more favourable than for the already qualified component.

Acknowledgements

References

[1] H. Alberg, Simulation of welding and heat treatment. Modelling and validation, Department of Applied Physics and Mechanical Engineering, Luleå: Luleå University of Technology, 2005.

[2] S. Hyun, L.-E. Lindgren, Simulating a chain of manufacturing processes using a geometry-based finite element code with adaptive meshing, Finite Elem. Anal. Des. 40 (2004) 511–528.

[3] B. Babu, A. Lundbäck, Physically based constitutive model for Ti–6Al–4V used in the simulation of manufacturing chain, in: E. Onate, D.R.J. Owen (Eds.), X International Conference of Computational Plasticity, COMPLAS X, CIMNE, Barcelona, Spain, 2009, p. 4.

[4] B. Babu, Physically Based Model for Plasticity and Creep of Ti–6Al–4V, Dept. of Applied Physics and Mechanical Engineering, Luleå: Luleå University of Technology, 2008, p. 94.

[5] L.-E. Lindgren, K. Domkin, S. Hansson, Dislocations, vacancies and solute diffusion in physical based plasticity model for AISI 316L, Mech. Mater. 40 (2008) 907–919.

[6] L.-E. Lindgren, E. Hedblom, Modelling of addition of filler material in large deformation analysis of multipass welding, Commun. Numer. Methods Eng. 17 (2001) 647–657.

[7] A. Lundbäck, Modelling and Simulation of Welding and Metal Deposition, Department of Applied Physics, Mechanical and Materials Engineering, Luleå: Luleå University of Technology, 2010.

[8] A Lundbäck, Modelling of metal deposition, Finite Elem. Anal. Des. 47 (2011).

[9] L-E Lindgren, Computational Welding Mechanics. Thermomechanical and Microstructural Simulations, Woodhead Publishing, 2007.

[10] S Osher, R Fedkiw, Level Set Methods and Dynamic Implicit Surfaces, Springer, New-York, 2003.

[11] F Klocke, V Bäcker, H Wegner, B Feldhaus, H-U Baron, R Hessert, Influence of process and geometry parameters on the surface layer state after roller burnishing of IN718, Prod. Eng. 3 (2009) 391–399.

[12] F Klocke, V Bäcker, A Timmer, H Wegner, Innovative FE-analysis of the roller burnishing process for different geometries, in: E. Onate, D.R.J. Owen, B. Suarez (Eds.), Computational Plasticity X, Fundamentals and Applications, 2009.

Dislocation density based model for plastic deformation and globularization of Ti-6Al-4V

Authors:
Bijish Babu, Lars-Erik Lindgren.

Dislocation density based model for plastic deformation and globularization of Ti-6Al-4V

Bijish Babu *, Lars-Erik Lindgren

Mechanics of Solid Materials, Luleå University of Technology, SE-971 87 Luleå, Sweden

ARTICLE INFO

ABSTRACT

Although Ti-6Al-4V has numerous salient properties, its usage for certain applications is limited due to the challenges faced during manufacturing. Understanding the dominant deformation mechanisms and numerically modeling the process is the key to overcoming this hurdle. This paper investigates plastic deformation of the alloy at strain rates from 0.001 s^{-1} to 1 s^{-1} and temperatures between 20 °C and 1100 °C. Pertinent deformation mechanisms of the material when subjected to thermo-mechanical processing are discussed. A physically founded constitutive model based on the evolution of immobile dislocation density and excess vacancy concentration is developed. Parameters of the model are obtained by calibration using isothermal compression tests. This model is capable of describing plastic flow of the alloy in a wide range of temperature and strain rates by including the dominant deformation mechanisms like dislocation pile-up, dislocation glide, thermally activated dislocation climb, globularization, etc. The phenomena of flow softening and stress relaxation, crucial for the simulation of hot forming and heat treatment of Ti-6Al-4V, can also be accurately reproduced using this model.

© 2013 Elsevier Ltd. All rights reserved.

1. Introduction

Ti-6Al-4V has good specific strength, toughness and corrosion resistance, which makes it attractive for applications in aerospace, pressure vessels, surgical implants, etc. Components for these applications have precise requirements on mechanical and physical properties (James and Lutjering, 2003). Furthermore, this alloy has a narrow temperature and strain rate window of workability (Kailas et al., 1994; Seshacharyulu et al., 2002). Optimization of the process parameters to satisfy the requirements on the component can be enabled by simulation. This work is part of a project aimed at performing finite element simulations of a manufacturing process chain involving hot-forming, welding, machining, metal deposition and heat treatment of Ti-6Al-4V components (Babu and Lundbäck, 2009; Tersing et al., 2012).

Manufacturing process chain simulations can compute the cumulative effect of the various processes by following the material state through the whole chain and give a realistic prediction of the final component. Capacity to describe material behavior in a wide range of temperatures and strain rates is crucial for this task. Such a model should be based on the dominant deformation mechanisms of the material.

Many different approaches were followed by researchers in formulating a physically based model for metal plasticity. Since the discrete dislocation modeling approach is computationally too expensive for the manufacturing process simulation, averaged dislocation density models are only discussed here. Initial attempts to develop dislocation density based models for metal plasticity were made by Kocks (1966), Bergström (1970), Bergström and Roberts (1973), Roberts and Bergström

---

* Corresponding author. Tel.: +46 (0) 70 419 78 17; fax: +46 920 492228.
E-mail addresses: bijish.babu@ltu.se (B. Babu), lars-erik.lindgren@ltu.se (L.-E. Lindgren).
URL: http://www.ltu.se/research/subjects/Materialmekanik (B. Babu).

(1973), Kocks et al. (1975), Mecking and Estrin (1980), etc. These initial attempts to model basic material physics were later developed to include more detailed and complex mechanisms. Bergström (1983) partitioned dislocation density into mobile and immobile. Another approach followed by Estrin et al. (1998) is to split dislocations into low dislocation density channels and high dislocation density walls with separate evolution equations. Feaugas (1999), Feaugas and Gaudin (2001) extended this to account for kinematic hardening by separating the immobile dislocation density to walls and channels. Barlat et al. (2011) used a similar framework with forest and reverse dislocation densities to describe the Bauschinger effect. Statistically Stored Dislocations (SSD) and Geometrically Necessary Dislocations (GND) used by Arsenlis et al. (2004) and Cheong et al. (2005) are fundamentally similar to Estrin's model (Estrin et al., 1998).

Another approach is to partition dislocation densities into separate quantities for each active slip system useful for crystal plasticity models. For NiAl crystals, Busso and McClintock (1996) described the microstructure and flow characteristics during deformation based on the density and polarity of the dislocation structure. Peeters et al. (2001) proposed a model for bcc crystals which accounts for dislocation ensembles represented by three directionally sensitive dislocation densities generated during changing strain paths. For HCP crystals, Beyerlein and Tomé (2008) introduced separate hardening laws for each slip and twinning mode which are sensitive to temperature and rate.

Various approaches were employed by researchers to model the constitutive behavior of Ti-6Al-4V. Combining the Cingara model during hardening and JMAK model during softening, Shafaat et al. (2011) proposed an empirical flow stress model for Ti-6Al-4V. A similar approach was followed by Karpat (2011) by mixing a modified Johnson–Cook model for hardening and a hyperbolic model for softening which is used during machining simulation of Ti-6Al-4V. A simulated microstructure-based probabilistic framework has been used by Przybyla and McDowell (2011) for Ti-6Al-4V to model fatigue crack formation. Khan and Yu (2012), Khan et al. (2012) developed an anisotropic yield criterion for Ti-6Al-4V based on the KHL model. Dislocation density based models have been used by Nemat-Nasser et al. (1999) for commercially pure Titanium and Picu and Majorell (2002) and Gao et al. (2011) for Ti-6Al-4V. None of them has included the effects of vacancy evolution and globularization (grain coarsening).

This paper extends the model used by Lindgren et al. (2008) by including the effects of enhanced diffusivity. Further, a model for globularization that is responsible for flow-softening and stress relaxation is added. Isothermal test data is used in this paper to calibrate the model and therefore, the phase changes of the alloy are ignored.

Chaboche (2008) presented a review of the plastic and viscoplastic models, and Horstemeyer and Bammann (2010) showed the evolution and history of the internal state variable theory in plasticity. These two references show categorically where the current model stands in the family of the established constitutive theories. The constitutive model developed here for computing the yield strength can be used along with the Finite Element Method to solve thermo-mechanical problems of any dimension. The model is calibrated using compression tests and it is assumed that the material behavior is isotropic in order to generalize to a multiaxial context as needed in the manufacturing simulations.

2. Material and deformation mechanisms

Ti-6Al-4V is a two-phase alloy containing 6 wt% Al which stabilizes the α phase (HCP) and 4 wt% V which stabilizes the β phase (BCC). The proportion of these alloying elements gives attractive mechanical properties to the material. The presence of Al inhibits twinning, even though it is a common deformation mechanism for HCP materials (Majorell et al., 2002). The two phases in the alloy have different properties given by their structures, with α exhibiting greater strength yet lower ductility and formability compared to β phase (Tiley, 2002). The microstructure at equilibrium in room temperature consists mainly of α phase ($\approx 95\%$) with some retained β phase. At around 890 °C, the α phase transforms to β. This temperature (β-transus) depends on the composition of Al and V. Plastic deformation occurs in α phase primarly through dislocation slip with a-type burgers vector. These dislocations are emitted from $\alpha - \beta$ interfaces and glide in basal planes rather than on prismatic planes because of its compatiblity with the HCP-BCC interface (Salem and Semiatin, 2009).

The material used in this work was supplied as 12 mm thick plates by ATI Allvac®, USA. It has been checked for defects using ultrasonic technique and has undergone annealing heat treatment for 6 h at 790 °C. The material is free from the hard and brittle α-case (oxygen-rich surface layer). Microscopic examination of the received material revealed a bi-modal structure with primary alpha surrounded by transformed beta (Widmanstätten structure). When heated to elevated temperature followed by slow cooling, both globular and lamellar grains demonstrated coarsening.

Cylindrical specimens machined from the plates were used in the experiments. The axis of the specimens is oriented in the transverse direction of rolling. Mechanical properties of Ti-6Al-4V depend on different parameters like thermo-mechanical processing, chemical composition, interstitial impurities, etc. The chemical composition of the material is shown in Table 1.

Table 1
Chemical composition given in wt.%. Remaining is Ti.

Al	V	O	Fe	C	Si	Mn	H
6.19	3.98	0.162	0.21	0.01	<0.01	<0.01	0.0082

Conrad (1981) studied the influence of various factors like solutes, interstitials, strain, strain rate, temperature, etc., on the strength and ductility of titanium systems and proposed a binary additive relationship for its yield strength. He identified the underlying mechanism of plastic flow to be glide and climb, which is assisted by diffusion. The mechanism of diffusion in Ti systems is less understood. The published diffusion data shows large scatter, which is attributed to the variation in measurement techniques (Liu and Welsch, 1988; Mishin and Herzig, 2000). Semiatin et al. (2003) measured the diffusivity of Al and V in β-Ti between 700 and 950 °C. It has been reported that dislocations in Ti-6Al-4V act as high-diffusivity paths leading to an enhanced diffusion (Park et al., 2008a). Globularization of Ti-6Al-4V alloy at elevated temperature is reported by many authors (Stefansson and Semiatin, 2003; Semiatin et al., 2005; Yeom et al., 2007; Zhao et al., 2007; Sargent et al., 2008; Park et al., 2008b). Bai et al., 2012, based on experimental evidence, demonstrated the mechanism of globularization and how it leads to flow softening. This can also result in stress relaxation.

3. Formulation of the flow stress model

The flow stress model is formulated on a material volume which represents the average behavior of a large number of grains, dislocations, etc. This approach provides a bridge between various sub-micro scale phenomena and macro-scale continuum mechanics.

Plastic strain is related to motion of dislocations, while hardening or softening is associated with interaction of dislocations. With the increase of dislocation density, the dislocations themselves get entangled and prevent further motion, which results in isotropic hardening. Recovery and recrystallization are two competing restoration mechanisms and they counteract the strain hardening. In order to compute evolution of the material state, dislocation density and vacancy concentration are used as internal state variables in this model.

3.1. Flow stress

An incompressible von Mises model for plasticity is used here. Plastic deformation is assumed to be isotropic, although some anisotropic behavior is observed. The flow stress is assumed to consist of two parts (Seeger, 1956; Bergström, 1969; Kocks, 1976),

$$\sigma_y = \sigma_G + \sigma^* \tag{1}$$

where, σ_G is the athermal stress contribution from the long-range interactions of the dislocation substructure. The second term σ^*, is the friction stress needed to move dislocations through the lattice and to pass short-range obstacles. Thermal vibrations can assist dislocations to overcome these obstacles. Many non-linear variants of Eq. (1) to model the precipitate hardening are available in the literature (Nembach and Neite, 1985). However, linear superposition is chosen here based on the behavior of Titanium alloys identified by Conrad (1981).

3.1.1. Long-range stress component:
The long-range term from Eq. (1) is derived by Seeger (1956) as,

$$\sigma_G = m\alpha Gb\sqrt{\rho_i} \tag{2}$$

where m is the Taylor orientation factor translating the effect of the resolved shear stress in different slip systems into effective stress and strain quantities. Furthermore, α is a proportionality factor, b is the Burger's vector and ρ_i is the immobile dislocation density. The shear modulus (G) can be computed from the Young's modulus (E) and Poisson ratio (v) as,

$$G = \frac{E}{2(1+v)} \tag{3}$$

3.1.2. Short-range stress component:
The dislocation velocity is related to plastic strain rate via the Orowan equation (Orowan, 1948)

$$\dot{\varepsilon}^p = \frac{\rho_m b \bar{v}}{m} \tag{4}$$

where $\bar{v}$ is the average velocity of the mobile dislocations, ρ_m is the mobile dislocation density and $\dot{\varepsilon}^p$ is the plastic strain rate. This velocity is related to the time taken by a dislocation to pass an obstacle, most of which is the waiting time. The velocity is written according to Frost and Ashby (1982) as,

$$\bar{v} = \lambda v_a e^{-\Delta G/kT} \tag{5}$$

where λ is the average obstacle spacing, v_a is the attempt frequency, ΔG is the activation energy, k is the Boltzmann constant and T is the temperature in Kelvin. Here, $e^{-\Delta G/kT}$ can be considered as the probability that the activation energy is supplied locally. Substituting for velocity, Eq. (4) can be written as,

$$\dot{\varepsilon}^p = f e^{-\Delta G/kT} \tag{6}$$

where the form of the function f and ΔG depend on the applied stress, strength of obstacles, etc., (Frost and Ashby, 1982). The stress available to move a dislocation past an obstacle is the difference between applied stress and the long-range flow stress component. Since the equivalent stress during plastic deformation is equal to the flow stress, $f = f(\bar{\sigma} - \sigma_G) = f(\sigma^*)$. The activation energy for dislocation motion can be written according to Kocks et al. (1975) as,

$$\Delta G = \Delta F \left[1 - \left(\frac{\sigma^*}{\sigma_{ath}} \right)^p \right]^q, \quad 0 \leqslant p \leqslant 1, \; 1 \leqslant q \leqslant 2 \tag{7}$$

Here, $\Delta F = \Delta f_0 G b^3$ is the activation energy necessary to overcome short-range obstacles and $\sigma_{ath} = \tau_0 G$ is the shear strength in the absence of thermal energy. Some guidelines for selection of Δf_0 and τ_0 are given in Table 2. Based on the above formulation, the strain rate dependent part of the yield stress in Eq. (1) can be derived according to the Kocks–Mecking formulation (Kocks et al., 1975; Mecking and Kocks, 1981) as,

$$\sigma^* = \tau_0 G \left[1 - \left[\frac{kT}{\Delta f_0 G b^3} \ln \left(\frac{\dot{\varepsilon}^{ref}}{\dot{\varepsilon}^p} \right) \right]^{1/q} \right]^{1/p} \tag{8}$$

Here, $\dot{\varepsilon}^{ref}$ is the reference strain rate.

3.2. Evolution of immobile dislocation density

The basic components for the yield stress in Eq. (1) are obtained from Eqs. (2) and (8). However, the evolution of ρ_i in Eq. (2) needs to be computed. The model for evolution of the immobile dislocation density has two parts: hardening and restoration.

$$\dot{\rho}_i = \dot{\rho}_i^{(+)} - \dot{\rho}_i^{(-)} \tag{9}$$

3.2.1. Hardening process

It is assumed that mobile dislocations move, on average, a distance Λ (mean free path), before they are immobilized or annihilated. According to the Orowan equation (Orowan, 1948), density of mobile dislocations and their average velocity are proportional to the plastic strain rate. It is reasonable to assume that increase in immobile dislocation density also follows the same relation (Mecking and Kocks, 1981). This leads to,

$$\dot{\rho}_i^{(+)} = \frac{m}{b} \frac{1}{\Lambda} \dot{\varepsilon}^p \tag{10}$$

where m is the Taylor orientation factor. The mean free path can be computed from the grain size (g) and dislocation subcell or subgrain diameter (s) as,

$$\frac{1}{\Lambda} = \left(\frac{1}{g} + \frac{1}{s} + others \right) \tag{11}$$

where *others* denote contributions from obstacles like precipitates, interstitial elements, martensite lathes, etc. Models for recrystallization, grain growth, precipitation, dissolution, etc., can be included here (Fisk, 2011).

The formation and evolution of subcells has been modeled using a relation proposed by Holt (1970).

$$s = K_c \frac{1}{\sqrt{\rho_i}} \tag{12}$$

The model for grain growth based on isothermal measurements can be written according to Porter and Easterling (1992) and Sargent et al. (2008) as,

$$g^n - g_0^n = Kt \tag{13}$$

Here, g_0 is the original grain size, t is the time elapsed and K is the calibration parameter.

Table 2
Activation energy factor and shear strength of different obstacles from Frost and Ashby, 1982 (l is the mean spacing of the obstacles).

Obstacle strength	Δf_0	τ_0	Example
Strong	2	$> \frac{b}{l}$	Strong precipitates
Medium	$0.2 - 1.0$	$\approx \frac{b}{l}$	Weak precipitates
Weak	< 0.2	$\ll \frac{b}{l}$	Lattice Resistance,

3.2.2. Restoration processes

Annihilation and remobilization of dislocations are thermally activated reorganization processes that lead to restoration of the deformed lattice (Roberts and Bergström, 1973). In high-stacking fault materials, recovery process might balance the effects of strain hardening leading to a constant flow stress.

The model for recovery by glide can be written based on the formulation by Bergström (1983) as,

$$\dot{\rho}_i^{(-)} = \Omega \rho_i \dot{\bar{\varepsilon}}^p \tag{14}$$

where Ω is a function dependent on temperature. This is analogous to the model by Kocks et al. (1975) as ρ_i and $\dot{\bar{\varepsilon}}^p$ are proportional to ρ_m and $\bar{v}$, respectively.

The motion of dislocations perpendicular to its glide plane is called climb, which reduces the density of the immobile dislocations. In addition to dislocations, vacancies are also created during plastic deformation (Friedel, 1964). This has significant effect on diffusion controlled processes such as climb and dynamic strain aging. Militzer et al. (1994) proposed a model for climb based on Sandstrom and Lagneborg (1975) and Mecking and Estrin (1980). According to Lindgren et al. (2008), the recovery due to climb is enhanced by the increase in diffusivity from excess vacancy concentration. This is written as

$$\dot{\rho}_i^{(-)} = 2c_\gamma D_{app} \frac{Gb^3}{kT} \left(\rho_i^2 - \rho_{eq}^2 \right) \tag{15}$$

where c_γ is a material coefficient and D_{app} is the apparent diffusivity of the material. Lindgren et al. (2008) used the lattice diffusion enhanced by excess vacancies given in equation (24) as D_{app}. It is further developed in this work to include the effects of phase transformation and pipe diffusion (see Eq. 27).

Sargent et al., 2008 have observed that, in Ti-6Al-4V, static and dynamic coarsening occur at elevated temperatures (650–815 °C) and dynamic coarsening occurs at a faster rate as compared to the static. The deformation energy stored as dislocations and the supplied thermal energy provide the driving force for this grain growth. Coarsening also results in the grain becoming more globular; hence, it is called globularization. During coarsening, grain boundaries move through the lattice and annihilate the dislocations, thereby resulting in a reduction of the dislocation density (Jessell et al., 2003). Thus, globularization reduces the flow stress of the material. A model for the evolution of dislocation density during recrystallization is proposed by Pietrzyk and Jedrzejewski (2001), Montheillet and Jonas (2009). Since the underlying mechanisms of recrystallization and globularization are similar, this model can be adapted here as shown below.

$$\text{if} \quad \rho_i \geqslant \rho_{cr}$$
$$\dot{\rho}_i^{(-)} = \psi \dot{X}_g \left(\rho_i - \rho_{eq} \right); \quad \text{until} \quad \rho_i \leqslant \rho_{eq} \tag{16}$$
$$\text{else}$$
$$\dot{\rho}_i^{(-)} = 0 \tag{17}$$

Here, ρ_{cr} is the critical dislocation density above which globularization is initiated, ρ_{eq} is the equilibrium value of dislocation density, $\dot{X}_g$ is the globularization rate and ψ is a calibration constant. According to this model, the effect of grain growth on the reduction of flow stress is included only when the stored deformation energy is sufficiently high. This is expressed through the criterion $\rho_i \geqslant \rho_{cr}$.

The mechanism of globularization of Ti-6Al-4V has been studied by Stefansson and Semiatin (2003). They observed that during deformation and shortly after wards, globularization is driven by dislocation substructure resulting in boundary splitting and edge spheroidization. This is followed by a second stage characterized by grain coarsening. This is similar to the two-stage process of dynamic and static recrystallization modeled by Thomas and Semiatin (2006). Based on their formulation, globularization is modeled as,

$$X_g = X_d + (1 - X_d)X_s \tag{18}$$

Here, the volume fractions X_g, X_d and X_s denote total globularized, its dynamic component and static component, respectively. Pietrzyk and Jedrzejewski (2001) proposed a model for static recrystallization. Also, a model for grain growth during recrystallization is proposed by Montheillet and Jonas (2009). Assuming that grain growth and static recrystallization have the same driving force, static globularization rate can be written as,

$$\dot{X}_s = M \frac{\dot{g}}{g} \tag{19}$$

where, M is a material parameter. The rate of dynamic globularization is modeled based on Thomas and Semiatin (2006) as,

$$\dot{X}_d = \frac{-Bk\dot{\bar{\varepsilon}}^p}{(\bar{\varepsilon}^p)^{k+1} e^{B(\bar{\varepsilon}^p)^{-k}}} \tag{20}$$

where, B and k are material parameters. Eqs. (18)–(20) for computing the globularization fraction are used only when condition $\rho_i \geqslant \rho_{cr}$ for Eq. (16) is satisfied.

3.3. Self diffusion enhanced by excess vacancies and dislocations

Diffusion occurs by the motion of defects like vacancies and interstitial atoms and by atomic exchange. But vacancy motion is the predominant diffusion mechanism, due to the lower activation energy of vacancy migration (Friedel, 1964). The self diffusion coefficient can be written according to Reed-Hill and Abbaschian (1991) as,

$$D_v = a^2 v e^{\frac{\Delta S_{vm} + \Delta S_{vf}}{k}} e^{-\frac{Q_{vm} + Q_{vf}}{kT}} = D_{l0} e^{-\frac{Q_g}{kT}} \tag{21}$$

where, a is the lattice constant, v is the lattice vibration frequency, ΔS_{vm} is the entropy increase due to the motion of a vacancy, Q_{vm} is the energy barrier to be overcome for vacancy motion and D_{l0} is the activity factor of lattice diffusion.

Vacancy migration leads to vacancy annihilation and it follows an Arrhenius-type relation as below.

$$D_{vm} = a^2 v e^{\frac{\Delta S_{vm}}{k}} e^{-\frac{Q_{vm}}{kT}} \tag{22}$$

Introducing the equilibrium concentration of vacancy from Eq. (28), self-diffusivity can be written as,

$$D_v = c_v^{eq} D_{vm} \tag{23}$$

Thus the self-diffusivity is the product of vacancy diffusivity and its equilibrium concentration. This can be rewritten generically for any concentration of vacancy as,

$$D_l^* = \frac{c_v}{c_v^{eq}} D_v \tag{24}$$

Lattice diffusivity of α and β phases differ by many order of magnitude, which results in a jump at the β-transus temperature (Mishin and Herzig, 2000). This transition is modeled by scaling the diffusivity with the volume fraction of each phase.

$$D_l = \frac{c_v}{c_v^{eq}} \left[D_\alpha \cdot (1-f)^w + D_\beta \cdot f^w \right] = \frac{c_v}{c_v^{eq}} D_v^* \tag{25}$$

where $f = f(T)$ is the volume fraction of β phase. The effect of phase change on vacancy concentration is ignored here.

Lattice diffusion is responsible for climb at high temperatures. However, at intermediate temperatures, diffusion along dislocation lines, referred to as core or pipe diffusion, has a larger effect on climb (Prinz et al., 1982). While studying the static grain growth of fine-grained Ti-6Al-4V, Johnson et al. (1998) concluded that grain boundary and pipe diffusion are the controlling mechanisms at temperatures less than $0.5 T_{melt}$. The effect of grain boundary diffusion can be neglected in the proposed model because of the larger grain size of the material considered. Reed-Hill and Abbaschian (1991) proposed an Arrhenius-type equation for grain boundary diffusion similar to Eq. (22). Since the basic mechanisms of grain boundary and dislocation core diffusion are the same (Shewmon, 1963), a similar formulation can be employed here.

$$D_p = D_{p0} e^{-\frac{Q_p}{kT}} \tag{26}$$

where, D_{p0} is the frequency factor and Q_p is the activation energy.

The total diffusive flux in the material is enhanced by the short circuit diffusion, which is dependent on the relative cross sectional area of pipe and matrix, parameter N in Eq. (27). According to the model proposed by Porter and Easterling (1992), Militzer et al. (1994), the apparent diffusivity can be written as

$$D_{app} = D_l + N D_p$$
$$N = \frac{n_a^p n_\rho}{N_a^l} \tag{27}$$

where, n_a^p is the number of atoms that can fill the cross-sectional area of a dislocation, n_ρ is the number of dislocations intersecting a unit area $(= \rho_i)$ and N_a^l is the number of atoms per unit area of lattice.

3.4. Evolution of excess vacancy concentration

When subjected to deformation or temperature change, materials generate excess vacancies. Creation of vacancy increases entropy, but consumes energy, and its concentration increases with temperature and deformation. The concentration of vacancies attain equilibrium if left undisturbed in isothermal conditions. The model considered here is only concerned with mono-vacancies. The equilibrium concentration of vacancies at a given temperature, according to Reed-Hill and Abbaschian (1991), Cahn and Peter (1996), is

$$c_v^{eq} = e^{\frac{\Delta S_{vf}}{k}} e^{-\frac{Q_{vf}}{kT}} \tag{28}$$

where, ΔS_{vf} is the increase in entropy while creating a vacancy and Q_{vf} is the activation energy for vacancy formation.

Militzer et al. (1994) proposed a model for excess vacancy concentration with generation and annihilation components as

$$\dot{c}_v^{ex} = \dot{c}_v - \dot{c}_v^{eq} = \left[\chi \frac{\sigma b}{Q_{vf}} + \zeta \frac{c_j}{4b^2} \right] \frac{\Omega_0}{b} \dot{\varepsilon} - D_{vm} \left[\frac{1}{s^2} + \frac{1}{g^2} \right] (c_v - c_v^{eq}) \tag{29}$$

Here, $\chi = 0.1$ is the fraction of mechanical energy spent on vacancy generation, Ω_0 is the atomic volume and ζ is the neutralization effect by vacancy emitting and absorbing jogs, as computed as below.

$$\zeta = \begin{cases} 0.5 - \zeta_0 c_j & \text{if } c_j \leqslant 0.5/\zeta_0, \\ 0 & \text{if } c_j > 0.5/\zeta_0, \end{cases} \quad \zeta_0 = 10 \tag{30}$$

The concentration of jogs is given as

$$c_j = e^{-\frac{Q_{jf}}{kT}}; \quad Q_{jf} = \frac{Gb^3}{4\pi(1-v)}$$

where Q_{jf} is the activation energy of jog formation.

Assuming that only long-range stress contributes to vacancy formation and adding the contribution from temperature change, Eq. (29) becomes

$$\dot{c}_v^{ex} = \left[\chi \frac{m\alpha Gb^2\sqrt{\rho_i}}{Q_{vf}} + \zeta \frac{c_j}{4b^2} \right] \frac{\Omega_0}{b} \dot{\bar{\varepsilon}} - D_{vm} \left[\frac{1}{s^2} + \frac{1}{g^2} \right] (c_v - c_v^{eq}) + c_v^{eq} \left(\frac{Q_{vf}}{kT^2} \right) \dot{T} \tag{31}$$

4. Stress-update

To compute the flow stress evolution for arbitrary paths, a radial return algorithm can be used (Simo and Taylor, 1986; Simo and Hughes, 1998). This requires hardening modulus and updated internal variables for each time increment. In the proposed model, $\sigma_y = \sigma_y(\bar{\varepsilon}^p, \rho_i, c_v)$ where ρ_i and c_v are described by a coupled set of differential equations. These internal variables can be written in vector form as $\mathbf{q}^T = [q_1, q_2] = [\rho_i, c_v]$. An implicit iterative procedure is used in every time increment to calculate its evolution. Assuming a constant $\dot{\bar{\varepsilon}}^p$ during the increment, the change in state variables can be computed as

$$\mathbf{H}^T = [H_1, H_2] = 0 \tag{32}$$

$$H_1 = \Delta q_1 - \left[\frac{m}{b\Lambda} \Delta\bar{\varepsilon}^p - \Omega q_1 \Delta\bar{\varepsilon}^p - 2c_\gamma \left(\frac{D_v^*}{c_v^{eq}} q_2 + \frac{n_a^p}{N_a^T} q_1 \right) \frac{Gb^3}{kT} \left(q_1^2 - \rho_{eq}^2 \right) \rho_{i0} \Delta t - \psi X_g \left(q_1 - \rho_{eq} \right) \right] \tag{33}$$

$$H_2 = \Delta q_2 - \left[\chi \frac{\Omega_0 m\alpha Gb}{Q_{vf}} \sqrt{q_1} \Delta\bar{\varepsilon}^p + \zeta \frac{c_j \Omega_0}{4b^3} \Delta\bar{\varepsilon}^p - D_{vm} \left[\frac{1}{s^2} + \frac{1}{g^2} \right] (q_2 - c_v^{eq}) \Delta t + c_v^{eq} \left(\frac{Q_{vf}}{kT^2} \right) \Delta T \right] \tag{34}$$

The iterative change in $\mathbf{q}$ can be written as

$$d\mathbf{q} = -\left[\frac{\partial \mathbf{H}_{(i)}}{\partial \mathbf{q}} \right]^{-1} \mathbf{H}_{(i)} \tag{35}$$

where, i is the iteration counter. The value of the state variables can be updated as

$$\mathbf{q}_{(i+1)} = \mathbf{q}_{(i)} + d\mathbf{q} \tag{36}$$

The hardening modulus needed in the radial return algorithm is

$$H' = \frac{d\sigma_y(\mathbf{q})}{d\bar{\varepsilon}^p} = \frac{\partial \sigma_y}{\partial \mathbf{q}} \frac{\partial \mathbf{q}}{\partial \bar{\varepsilon}^p} = \frac{\partial \sigma_G}{\partial \rho_i} \left[\frac{\partial \rho_i}{\partial \bar{\varepsilon}^p} + \frac{\partial \rho_i}{\partial c_v} \frac{\partial c_v}{\partial \bar{\varepsilon}^p} \right] + \frac{\partial \sigma^*}{\partial \bar{\varepsilon}^p} \tag{37}$$

The model for grain growth given in Eq. (13) can be written in incremental form as

$$g_{i+1} = \sqrt[n]{g_i^n + K\Delta t} \tag{38}$$

5. Experiments

Compression tests performed at the nominal temperatures 20, 100, 200, 300, 400, 500, 600, 700, 800, 900, 950, 1000 1050 and 1100 °C and strain rates from 0.001 s⁻¹ to 1.0 s⁻¹ were used to calibrate the model. The length (L≈8 mm) and diameter (D) of the specimens are varied ($1.2 \leqslant \frac{L}{D} \leqslant 1.4$) for each temperature to receive a measurable force response from the Gleeble® thermo-mechanical simulator and to prevent buckling. In order to reduce the friction between the specimen and anvil, Tantalum films were placed between the two. In-spite of this, some specimens exhibited barreling, which is evidence of significant friction. The specimens are heated to test temperature at a rate of 10 °Cs⁻¹. It is held for 30 s to achieve an even temperature distribution followed by compression at a given strain rate.

During compression, strain rate and temperature are controlled using a closed loop control system and force is measured from the load cells attached to the anvils. Temperature is increased to the predefined value by using resistance electrical heating. However, due to the additional deformation heating, the temperature of the specimen increases (<50 °C for $\dot{\bar{\varepsilon}} = 1$ s⁻¹ and <5 °C for $\dot{\bar{\varepsilon}} = 0.001$ s⁻¹) during deformation. This is recorded with the thermocouple welded to the specimen

and used in the model calibration. Diametrical change of the specimen is measured during the tests. This data combined with the force measurement from the load cell is used to compute the stress. The data obtained from measurement is smoothed to remove the noise generated by the dynamics of the machine operation. Corrections are made to compensate for the compliance of the anvil and lubricant film. Owing to the strong affinity of the alloy to oxygen at high temperatures, the experiments were performed in an evacuated chamber.

6. Optimization of the model

The parameters for the model are obtained by calibration using an in-house Matlab®-based toolbox. This toolbox uses Matlab®'s constrained minimization routine and can handle multiple experiments for optimization (Domkin et al., 2003).
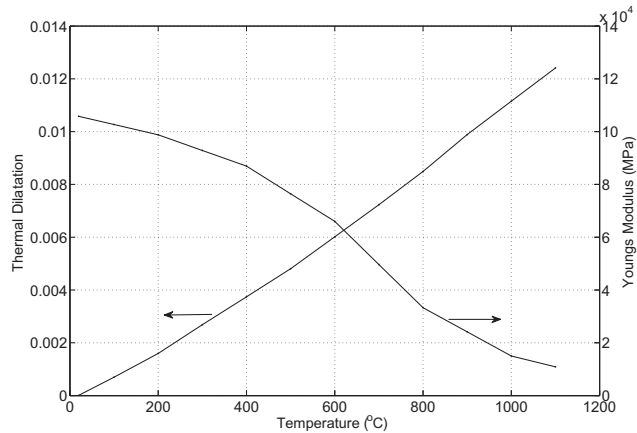
Fig. 1. Thermal dilatation (ε_{th}) and Young's modulus.

Table 3
Constant parameters for the model.

Parameter	Dimension	Value	Reference
T_{melt}	°C	1600	f
$T_{\beta-transus}$	°C	890	f
k	JK^{-1}	$1.38 \cdot 10^{-23}$	f
b	m	$2.95 \cdot 10^{-10}$	a
$D_{\alpha 0}$	$m^2 s^{-1}$	$5 \cdot 10^{-6}$	d
$D_{\beta 0}$	$m^2 s^{-1}$	$3 \cdot 10^{-7}$	d
Q_{vf}	J	$1.9 \cdot 10^{-19}$	b
Q_{vm}	J	$2.49 \cdot 10^{-19}$	a
Q_{β}	J	$2.5 \cdot 10^{-19}$	d
Q_p	J	$1.61 \cdot 10^{-19}$	a
n_a^p	–	2	f
n_ρ	–	ρ_i	f
Ω_0	m^3	$1.76 \cdot 10^{-29}$	a
g_0	m	$2 \cdot 10^{-6}$	f
K	$m^3 hr$	$5 \cdot 10^{-18}$	e
n	–	3	e
$\dot{\varepsilon}_{ref}$	s^{-1}	10^6	a
ΔS_{vm}	JK^{-1}	$1.38 \cdot 10^{-23}$	g

[a]Frost and Ashby (1982).
[b]Novikov et al. (1980).
[c]Conrad (1981).
[d]Mishin and Herzig (2000).
[e]Sargent et al. (2008).
[f]Calculated or measured value.
[g]Hernan et al. (2005).

Fig. 2. Self diffusion.

Table 4
Calibrated parameters of the model.

Parameter	Dimension	Value
D_{p0}	$m^2 s^{-1}$	10^{-8}
N_a^l	–	10^{19}
p	–	0.3
q	–	1.8
Ω	–	38
ρ_{eq}	m^{-2}	10^{10}

Table 5
Calibrated temperature-dependant parameters of the model.

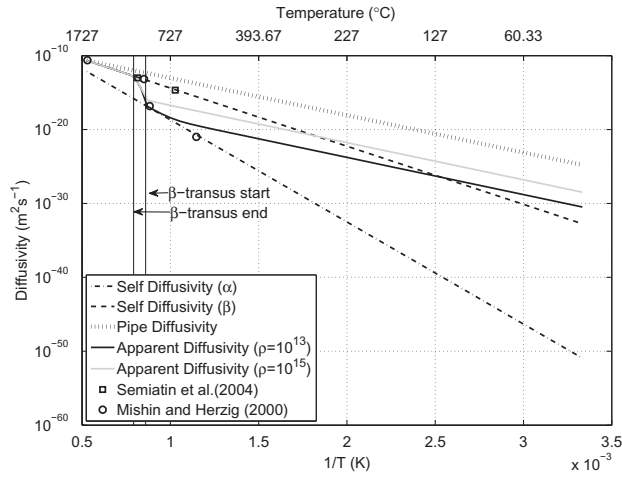| T [°C]	25	100	200	300	400	500	600	700	800	900	1000	1100
α	2.30	1.92	1.90	1.90	2.10	2.15	1.70	0.80	1.00	1.15	1.20	1.10
C_γ [10^{-1}]	0.00	0.00	0.00	0.00	0.00	3.00	4.00	5.00	5.00	0.50	1.00	2.00
K_c [10^2]	0.40	0.40	0.40	0.40	0.40	0.40	0.40	0.80	1.20	1.20	1.20	1.20
τ_0 [10^{-1}]	0.10	0.20	0.20	0.20	0.20	0.40	1.20	1.50	3.50	3.00	1.00	0.50
Δf_0	0.50	0.50	0.50	0.50	0.50	0.60	0.80	1.70	1.70	1.55	1.30	0.90
ρ_i^{init} [10^{14}]	1.00	1.00	1.00	1.00	1.00	1.00	0.70	0.10	0.10	0.10	0.01	0.01
ρ_i^{crit} [10^{14}]	5.00	5.00	5.00	5.00	2.24	2.00	1.50	0.20	0.20	0.20	0.10	0.10
B	1.00	1.00	1.00	1.00	0.50	0.50	0.50	0.60	0.50	0.10	0.01	0.01
k	2.00	2.00	2.00	2.00	2.00	2.00	1.00	1.50	2.00	2.00	2.00	2.00
M [10^2]	0.00	0.00	0.00	0.00	0.00	1.00	6.00	6.00	1.00	1.00	1.00	1.00
ψ	0.00	0.00	0.00	0.00	0.05	0.05	0.60	2.00	8.00	1.00	1.00	1.00
K [10^{-1}]	0.00	0.00	0.00	0.00	0.00	0.05	0.25	6.50	8.00	8.00	8.00	8.00

The shear modulus is computed according to equation (3) using the temperature-dependent Young's modulus given in Fig. 1. These values are obtained from isothermal tension tests using 0.2% offset. The Poisson ratio is assumed to be 0.33 for all temperatures (Cai et al., 2011). Strain has contributions from mechanical and thermal loads. Fig. 1 shows the thermal strain measured using a differential expansion dilatometer. According to Hernan et al. (2005), the entropy of vacancy migration for HCP metals lies in the range (0.9–1.6) k. Here, ΔS_{vm} is assumed to be equal to k. The activation energy of vacancy formation
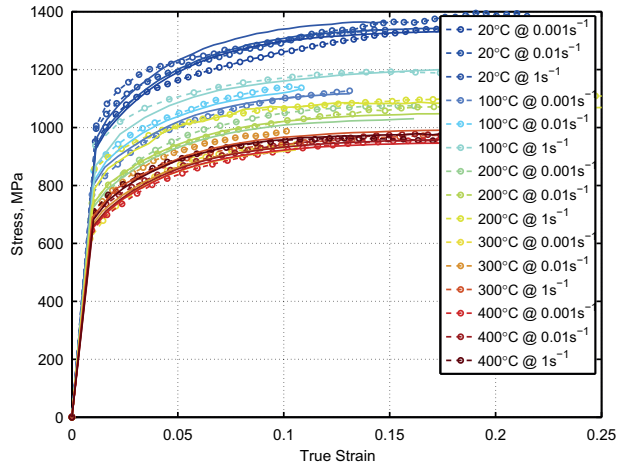
Fig. 3. Measured and computed stress–strain curve for 20 °C to 400 °C.
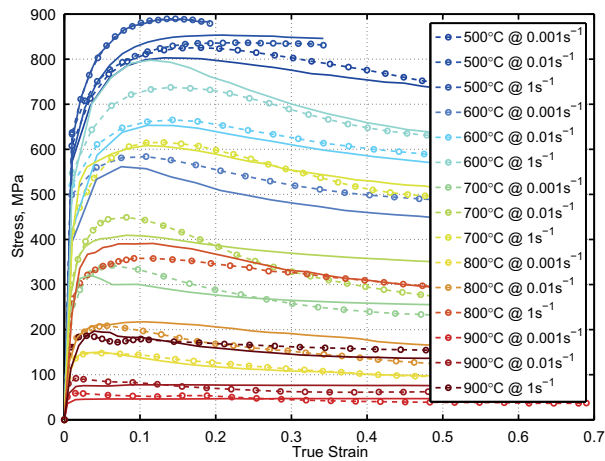
Fig. 4. Measured and computed stress–strain curve for 500 °C to 900 °C.

(Q_{vf}) measured by Novikov et al. (1980) for pure Ti is used in this work. Table 3 lists the various material constants obtained from measurements and literature.

Conrad, 1981 measured the dislocation density of undeformed Ti alloy with (0.1–1.0) at.% O_{eq} to be of the order of 10^{13} m^{-2}. Picu and Majorell (2002) used $\rho_{init} = 10^{12}$ m^{-2} based on calibration. Following a similar approach, varying values of ρ_i^{init} between ($10^{14} - 10^{12}$ m^{-2}) for increasing temperature are used here.

Fig. 2 shows diffusivities needed to compute the apparent diffusivity of Ti-6Al-4V for different values of dislocation density which correspond to annealed and deformed material. Enhanced diffusivity due to pipe diffusion has a significant effect at low temperature ($< 0.5 T_{melt}$). At high temperature, it is the lattice diffusivity which has significance. The measurements of Mishin and Herzig (2000) show the self diffusion of Ti in α and β phases, whereas the measurement of Semiatin et al. (2003) show diffusion of Al in β phase of Ti-6Al-4V. The activity factor of pipe diffusion (D_{p0}) is assumed to be of the same order as that of lattice diffusion.
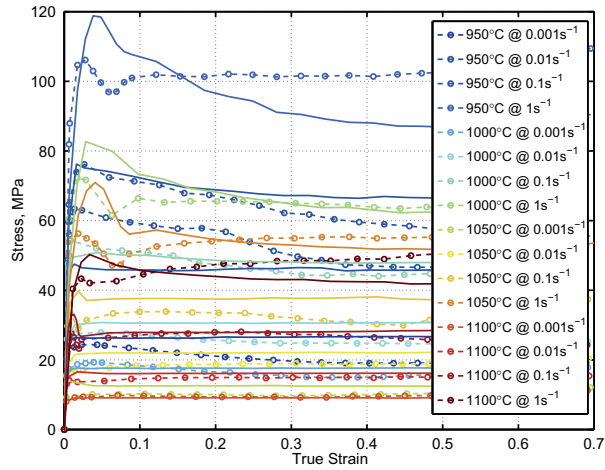
Fig. 5. Measured and computed stress–strain curve for 950 °C to 1100 °C.
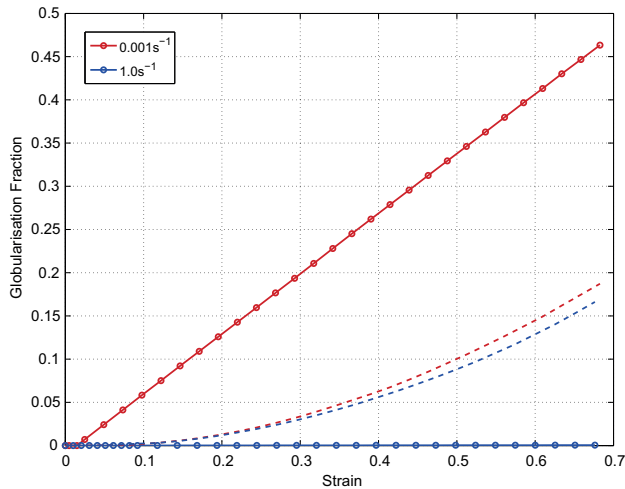
Fig. 6. Globularization during deformation at 800 °C.

The different parameters of the model obtained after calibration using σ-ε measurements are shown in Tables 4 and 5.

7. Comparison of model and experiments

Measured and computed stress–strain curves are plotted in Figs. 3–5. The dotted lines with markers denote measurements and continuous lines denote simulations. Compression tests performed at 20 °C to 400 °C showed very little rate dependence and resulted in hardening followed by fracture. Here, dislocation glide is the dominant deformation mechanism. Tests performed between 500 °C to 900 °C resulted in flow softening after the initial hardening. Sargent et al. (2008) observed that grain coarsening is enhanced approximately one order of magnitude during deformation as compared to static
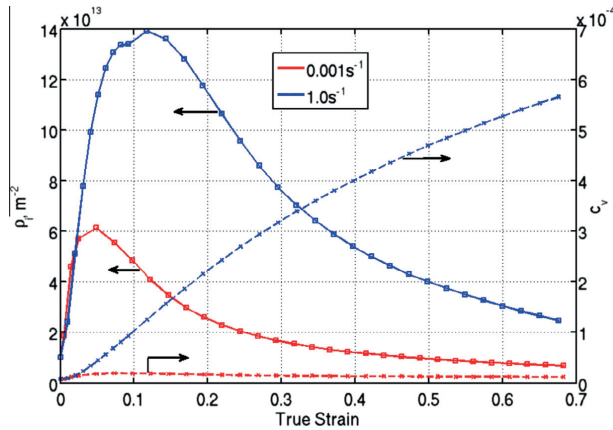
Fig. 7. Evolution of dislocation density and excess vacancy concentration during deformation at 800 °C.
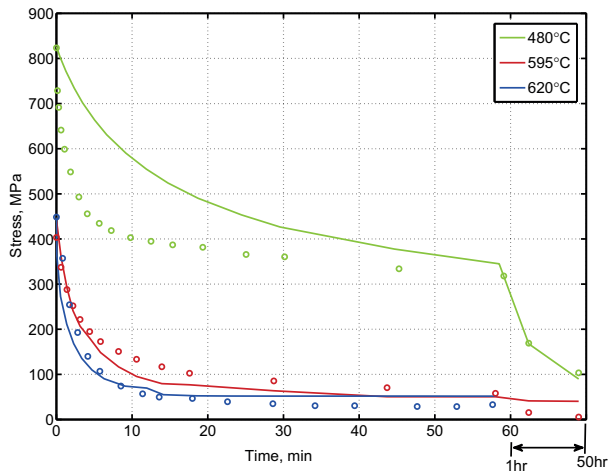
Fig. 8. Measured and computed stress relaxation at 480 °C, 595 °C and 620 °C.

conditions. Dynamic globularization leads to flow softening at elevated temperatures (Yeom et al., 2007). In addition, dislocation glide and climb are also dominant during this temperature range. Comparing the theoretical and experimental results in Figs. 3–5 shows that the model can reproduce the dominant phenomena observed during the plastic deformation of Ti-6Al-4V. Fig. 6 shows the globularization kinetics during deformation at 800 °C with dotted lines showing dynamic component and continuous lines showing static component. Red lines[1] denote deformation at 0.001 s^{-1} and blue at 1 s^{-1}. Dislocation density and excess vacancy concentration for the same tests are given in Fig. 7.

The tests from 950 °C to 1100 °C showed elastic-perfectly-plastic behavior, since the strain hardening and restoration processes are in balance.

Comparison of stress relaxation measurements done by Donachie (1988) and the model predictions are given in Fig. 8. However, the exact initial loading in the experiments and the composition of the alloy are not known. This comparison demonstrates the capacity of the model to compute the decay of stress with time.

---

[1] For interpretation of color in Figs. 6, the reader is referred to the web version of this article.

8. Discussions and conclusions

Banerjee and Williams (2013) identified a lack of physically based models for globularization of Titanium alloys. In this article, a constitutive model for Ti-6Al-4V including globularization and its effect on flow softening and stress relaxation has been developed. This model is capable of describing the plastic flow of the alloy in a wide range of temperature and strain rates by including all the dominant deformation mechanisms. Compared to the model for β-recrystallization by Fan and Yang (2011) which assumes constant strain rate sensitivity and is applicable only at high temperature, the current model can better reproduce plastic flow and softening behavior at a range of temperatures. This is crucial in the simulation of manufacturing processes. The model has already been used for simulations of a chain of manufacturing processes including forming, welding, metal deposition and heat treatment (Tersing et al., 2012; Babu and Lundbäck, 2009). Some of the parameters used in the model are available from measurements outside the domain of classical mechanical testing. Since some of these parameters are not available for this specific alloy, the data for pure Ti has been used here. The flow stress model used here follows a clear physical framework; therefore, new deformation mechanisms can be added when needed. This model assumes that the $\alpha - \beta$ phase composition of the alloy is in equilibrium at all temperatures which is sound only for low heating or cooling rates. Work to extend this model with the effects of non-equilibrium phase transformation is already in progress.

Acknowledgment

References

Arsenlis, A., Parks, D.M., Becker, R., Bulatov, V.V., 2004. On the evolution of crystallographic dislocation density in non-homogeneously deforming crystals. Journal of the Mechanics and Physics of Solids 52, 1213–1246.
Babu, B., Lundbäck, A., 2009. Physically based constitutive model for Ti-6Al-4V used in the simulation of manufacturing chain. In: Onate, E., Owen, D., Suarez, B. (Eds.), Computational Plasticity X: fundamentals and applications, International Center for Numerical Methods in Engineering.
Bai, Q., Lin, J., Dean, T., Balint, D., Gao, T., Zhang, Z., 2012. Modeling of dominant softening mechanisms for Ti-6Al-4V in steady state hot forming conditions. Materials Science and Engineering: A.
Banerjee, D., Williams, J., 2013. Perspectives on titanium science and technology. Acta Materialia 61, 844–879.
Barlat, F., Gracio, J.J., Lee, M.G., Rauch, E.F., Vincze, G., 2011. An alternative to kinematic hardening in classical plasticity. International Journal of Plasticity 27, 1309–1327.
Bergström, Y., 1969. Dislocation model for the stress-strain behaviour of polycrystalline alpha-iron with special emphasis on the variation of the densities of mobile and immobile dislocations. Materials Science & Engineering 5, 193–200.
Bergström, Y., 1970. A dislocation model for the stress-strain behaviour of polycrystalline [alpha]-Fe with special emphasis on the variation of the densities of mobile and immobile dislocations. Materials Science and Engineering 5, 193–200.
Bergström, Y., 1983. The plastic deformation of metals – A dislocation model and its applicability. Reviews on Powder Metallurgy and Physical Ceramics, 79–265.
Bergström, Y., Roberts, W., 1973. The dynamical strain ageing of [alpha]-iron: effects of strain rate and nitrogen content in the Jerky-flow region. Acta Metallurgica 21, 741–745.
Beyerlein, I., Tomé, C., 2008. A dislocation-based constitutive law for pure Zr including temperature effects. International Journal of Plasticity 24, 867–895.
Busso, E.P., McClintock, F.A., 1996. A dislocation mechanics-based crystallographic model of a B2-type intermetallic alloy. International Journal of Plasticity 12, 1–28.
Cahn, R.W., Peter, H., 1996, . Physical Metallurgy, 4 ed., 1. North-Holland Publishers, Amsterdam, NL.
Cai, J., Li, F., Liu, T., Chen, B., 2011. Investigation of mechanical behavior of quenched Ti-6Al-4V alloy by microindentation. Materials Characterization 62, 287–293.
Cheong, K., Busso, E., Arsenlis, A., 2005. A study of microstructural length scale effects on the behaviour of FCC polycrystals using strain gradient concepts. International Journal of Plasticity 21, 1797–1814.
Conrad, H., 1981. Effect of interstitial solutes on the strength and ductility of titanium 26, 123.
Domkin, K., Lindgren, L.E., Segle, P., 2003. Dislocation density based models of plastic hardening and parameter identification. In: The 7th International Conference on Computational Plasticity.
Donachie, J.M.J., 1988. Titanium – A Technical Guide. ASM International.
Estrin, Y., Tóth, L., Molinari, A., Bréchet, Y., 1998. A dislocation-based model for all hardening stages in large strain deformation. Acta Materialia 46, 5509–5522.
Fan, X., Yang, H., 2011. Internal-state-variable based self-consistent constitutive modeling for hot working of two-phase titanium alloys coupling microstructure evolution. International Journal of Plasticity 27, 1833–1852.
Feaugas, X., 1999. On the origin of the tensile flow stress in the stainless steel AISI 316L at 300 K: back stress and effective stress. Acta Materialia 47, 3617–3632.
Feaugas, X., Gaudin, C., 2001. Different levels of plastic strain incompatibility during cyclic loading: in terms of dislocation density and distribution. Materials Science and Engineering: A, 382–385.
Fisk, M., 2011. Modeling of induction heat treatment in a manufacturing chain. Ph.D. thesis, Luleå University of Technology, Luleå, Sweden.
Friedel, J., 1964. Dislocations. International Series of Monographs on Solid State Physics, 3. Pergamon Press.
Frost, H.J., Ashby, M.F., 1982. Deformation-Mechanism Maps: The Plasticity and Creep of Metals and Ceramics (Paperback).
Gao, C., Zhang, L., Yan, H., 2011. A new constitutive model for HCP metals. Materials Science and Engineering: A 528, 4445–4452.
Hernan, R.D., Maria, G.L., Maria, M.A., 2005. Self-diffusion in the hexagonal structure of Zirconium and Hafnium: computer simulation studies. Materials Research 8, 431–434.
Holt, D.L., 1970. Dislocation cell formation in metals. Journal of Applied Physics 41, 3197.
Horstemeyer, M.F., Bammann, D.J., 2010. Historical review of internal state variable theory for inelasticity. International Journal of Plasticity 26, 1310–1334.
James, C.W., Lutjering, G., 2003. Titanium. Springer- Verlag.

Jessell, M.W., Kostenko, O., Jamtveit, B., 2003. The preservation potential of microstructures during static grain growth. Journal of Metamorphic Geology 21, 481–491.

Chaboche, J.L., 2008. A review of some plasticity and viscoplasticity constitutive theories. International Journal of Plasticity 24, 1642–1693.

Johnson, C.H., Richter, S.K., Hamilton, C.H., Hoyt, J.J., 1998. Static grain growth in a microduplex Ti-6Al-4V alloy. Acta Materialia 47, 23–29.

Kailas, S.V., Prasad, Y.V.R.K., Biswas, S.K., 1994. Flow Instabilities and Fracture in Ti-6Al-4V Deformed in Compression at 298-673K. Metallurgical and Materials Transactions A 25A, 2173–2179.

Karpat, Y., 2011. Temperature dependent flow softening of titanium alloy Ti6Al4V: an investigation using finite element simulation of machining. Journal of Materials Processing Technology 211, 737–749.

Khan, A.S., Yu, S., 2012. Deformation induced anisotropic responses of Ti-6Al-4V alloy. Part I: Experiments. International Journal of Plasticity 38, 1–13.

Khan, A.S., Yu, S., Liu, H., 2012. Deformation induced anisotropic responses of Ti-6Al-4V alloy. Part II: a strain rate and temperature dependent anisotropic yield criterion. International Journal of Plasticity 38, 14–26.

Kocks, U., 1976. Laws for work-hardening and low-temperature creep. Journal of Engineering Materials and Technology, Transactions of the ASME, Ser H 98, 76–85.

Kocks, U.F., 1966. A statistical theory of flow stress and work-hardening. Philosophical Magazine 13, 541–566.

Kocks, U.F., Argon, A.S., Ashby, M.F., 1975. Thermodynamics and Kinetics of Slip. Progress in Material Science, 19. Pergamon Press.

Lindgren, L.E., Domkin, K., Sofia, H., 2008. Dislocations, vacancies and solute diffusion in physical based plasticity model for AISI 316L. Mechanics of Materials 40, 907–919.

Liu, Z., Welsch, G., 1988. Literature survey on diffusivities of oxygen, aluminum, and vanadium in alpha titanium, beta titanium, and in rutile. Metallurgical and Materials Transactions A 19, 1121–1125.

Majorell, A., Srivatsa, S., Picu, R.C., 2002. Mechanical behavior of Ti-6Al-4V at high and moderate temperatures–Part I: experimental results. Materials Science and Engineering A 326, 297–305.

Mecking, H., Estrin, Y., 1980. The effect of vacancy generation on plastic deformation. Scripta Metallurgica 14, 815.

Mecking, H., Kocks, U., 1981. Kinetics of flow and strain-hardening. Acta Metallurgica 29, 1865–1875.

Militzer, M., Sun, W.P., Jonas, J.J., 1994. Modeling the effect of deformation-induced vacancies on segregation and precipitation. Acta Metallurgica et Materialia 42, 133.

Mishin, Y., Herzig, C., 2000. Diffusion in the Ti-Al system. Acta Materialia 48, 589–623.

Montheillet, F., Jonas, J.J., 2009. Fundamentals of modeling for metals processing. ASM Handbook, 22A. ASM International, Materials Park, Ohio 44073-0002, pp. 220–231.

Nemat-Nasser, S., Guo, W.G., Cheng, J.Y., 1999. Mechanical properties and deformation mechanisms of a commercially pure titanium. Acta Materialia 47, 3705.

Nembach, E., Neite, G., 1985. Precipitation hardening of superalloys by ordered Gamma prime-particles. Progress in Materials Science 29, 177–319.

Novikov, I.I., Roshchupkin, V.V., Semashko, N.A., Fordeeva, L.K., 1980. Experimental investigation of vacancy effects in pure metals. Journal of Engineering Physics and Thermophysics V39, 1316.

Orowan, E., 1948. In: Symposium on Internal Stresses in Metals and Alloys, Institute of Metals, pp. 451.

Park, C.H., Ko, Y.G., Park, J.W., Ko, Y.G., 2008a. Enhanced Superplasticity Utilizing Dynamic Globularization of Ti-6Al-4V Alloy. Materials Science and Engineering: A.

Park, C.H., Park, K.T., Shin, D.H., Lee, C.S., 2008b. Microstructural Mechanisms during Dynamic Globularization of Ti-6Al-4V Alloy. Materials Transactions 49, 2196–2200.

Peeters, B., Seefeldt, M., Teodosiu, C., Kalidindi, S., Houtte, P.V., Aernoudt, E., 2001. Work-hardening/softening behaviour of b.c.c. polycrystals during changing strain paths: I. an integrated model based on substructure and texture evolution, and its prediction of the stress–strain behaviour of an IF steel during two-stage strain paths. Acta Materialia 49, 1607–1619.

Picu, R.C., Majorell, A., 2002. Mechanical behavior of Ti-6Al-4V at high and moderate temperatures–Part II: constitutive modeling. Materials Science and Engineering A 326, 306–316.

Pietrzyk, M., Jedrzejewski, J., 2001. Identification of parameters in the history dependent constitutive model for steels. CIRP Annals – Manufacturing Technology 50, 161–164.

Porter, D.A., Easterling, K.E., 1992. Phase Transformations in Metals and Alloys, second ed. CRC Press.

Prinz, F., Argon, A.S., Moffatt, W.C., 1982. Recovery of dislocation structures in plastically deformed copper and nickel single crystals. Acta Metallurgica 30, 821–830.

Przybyla, C.P., McDowell, D.L., 2011. Simulated microstructure-sensitive extreme value probabilities for high cycle fatigue of duplex Ti-6Al-4V. International Journal of Plasticity 27, 1871–1895.

Reed-Hill, R.E., Abbaschian, R., 1991. Physical Metallurgy Principles, third ed. PWS Publishing Company.

Roberts, W., Bergström, Y., 1973. The stress-strain behaviour of single crystals and polycrystals of face-centered cubic metals–a new dislocation treatment. Acta Metallurgica 21, 457–469.

Salem, A., Semiatin, S., 2009. Anisotropy of the hot plastic deformation of Ti-6Al-4V single-colony samples. Materials Science and Engineering: A 508, 114–120.

Sandstrom, R., Lagneborg, R., 1975. A model for hot working occurring by recrystallization. Acta Metallurgica 23, 387.

Sargent, G., Zane, A., Fagin, P., Ghosh, A., Semiatin, S., 2008. Low-Temperature coarsening and plastic flow behavior of an alpha/beta titanium billet material with an ultrafine microstructure. Metallurgical and Materials Transactions A 39, 2949–2964.

Seeger, A., 1956. The mechanism of Glide and Work Hardening in FCC and HCP Metals. In: Fisher, J., Johnston, W.G., Thomson, R., Vreeland, T.J. (Eds.), Dislocations and Mechanical Properties of Crystals, pp. 243–329.

Semiatin, S., Knisley, S., Fagin, P., Barker, D., Zhang, F., 2003. Microstructure evolution during alpha-beta heat treatment of Ti-6Al-4V. Metallurgical and Materials Transactions A 34, 2377–2386.

Semiatin, S.L., Stefansson, N., Doherty, R.D., 2005. Prediction of the Kinetics of Static Globularization of Ti-6Al-4V. Metallurgical and Materials Transactions 36A, 1372–1376.

Seshacharyulu, T., Medeiros, S.C., Frazier, W.G., Prasad, Y.V.R.K., 2002. Microstructural mechanisms during hot working of commercial grade Ti-6Al-4V with lamellar starting structure, vol. 325, pp. 112.

Shafaat, M.A., Omidvar, H., Fallah, B., 2011. Prediction of hot compression flow curves of Ti-6Al-4V alloy in $\alpha + \beta$ phase region. Materials & Design 32, 4689–4695.

Shewmon, P.G., 1963. Diffusion in solids. McGraw-Hill Series in Materials Science and Engineering. McGraw-Hill.

Simo, J., Hughes, T.J.R., 1998. Computational Inelasticity, . Interdisciplinary Applied Mathematics, first ed., 7. Springer.

Simo, J.C., Taylor, R.L., 1986. A return mapping algorithm for plane stress elastoplasticity. International Journal for Numerical Methods in Engineering 22, 649–670.

Stefansson, N., Semiatin, S.L., 2003. Mechanisms of globularization of Ti-6Al-4V during static heat treatment. Metallurgical and Materials Transactions 34A, 691–698.

Tersing, H., Lorentzon, J., Francois, A., Lundbäck, A., Babu, B., Barboza, J., Bäcker, V., Lindgren, L.E., 2012. Simulation of manufacturing chain of a titanium aerospace component with experimental validation. Finite Elements in Analysis and Design 51, 10–21.

Thomas, J.P., Semiatin, S.L., 2006. Mesoscale Modeling of the Recrystallization of Waspaloy and Application to the Simulation of the Ingot-Cogging Process. Technical Report AFRL-ML-WP-TP-2006-483. Materials and Manufacturing Directorate. Air Force Research Laboratory, Air Force Materiel Command, Wright-Patterson AFB, OH 45433–7750.

Tiley, J.S., 2002. Modeling of Microstructure Property Relationships in Ti-6Al-4V. Ph.D. thesis, Ohio State University.
Yeom, J.T., Kim, J.H., Kim, N.Y., Park, N.K., Lee, C.S., 2007. Characterization of dynamic globularization behavior during hot working of Ti-6Al-4V alloy. Advanced Materials Research 26–28, 1033–1036.
Zhao, W.J., Ding, H., Song, D., Cao, F., Hou, H.L., 2007. The Effect of Grain Size on Superplastic Deformation of Ti-6Al-4V Alloy. In: Zhang, K. (Ed.), Materials Science Forum, pp. 387–392.

Physically-based constitutive model of Ti-6Al-4V for arbitrary phase composition

Authors:
Bijish Babu, Corinne Charles Murgau, Lars-Erik Lindgren.

Physically-based constitutive model of Ti-6Al-4V for arbitrary phase composition

Bijish Babu

Swerim AB, Box 812, SE-971 25 Luleå, Sweden

Corinne Charles Murgau

Department of Industrial Production, Högskolan Väst, SE-461 86, Trollhättan, Sweden

Lars-Erik Lindgren

Mechanics of Sold Materials, Luleå University of Technology, SE-971 87, Luleå, Sweden

Abstract

The principal challenge in producing aerospace components using Ti-6Al-4V alloy is to employ the optimum process window of deformation rate and temperature to achieve desired material properties. Qualitatively understanding the microstructure-property relationship is not enough to accomplish this goal. Developing advanced material models to be used in manufacturing process simulation is the key to compute and optimize the process iteratively. The focus in this work is on physically based flow stress models coupled with microstructure evolution models. Such a model can be used to simulate processes involving complex and cyclic thermo-mechanical loading.

Keywords: Ti-6Al-4V, Flow-Stress, Dislocation density, Vacancy concentration, Phase Evolution, Alpha, Beta, Finite Element Method (FEM)

1. Introduction

The most widely used titanium alloy, Ti-6Al-4V, has an α(HCP) $+\beta$(BCC) phase composition. This allotropic property of titanium allows it to possess diverse microstructures/morphologies thereby giving a large variation of thermo-mechanical properties. This paper features a physically based thermo-mechanical-microstructural model for plastic flow of Ti-6Al-4V for arbitrary phase composition. It is an enhancement of an earlier model (Babu and Lindgren, 2013) that has been improved with respect to handling non-equilibrium phase compositions. Such a model can be used in the simulation of manufacturing processes involving a wide range of temperatures and strain rates.

Simulation of the manufacturing process using FEM employing advanced material models can give a deeper understanding as well as be used in process optimization. This allows us to predict and control local microstructure and properties within components thereby meeting complex design specifications demanded by the aerospace industry. Such a strategy has facilitated rapid advancement in technology related to the manufacturing process as well as alloy design (Committee on Integrated Computational Materials Engineering, 2008; Backman et al., 2006).

The model described here can be used in coupled thermo-mechanical-microstructural simulations and can predict the material state for arbitrary thermo-mechanical loading. Owing to its wide range of applicability, this model can be used to simulate processes involving complex histories.

---

2. State of the art in models for Ti-6Al-4V

Several different approaches were followed by researchers to model the constitutive behavior of Ti-6Al-4V. Shafaat et al. (2011) proposed an empirical flow stress model for Ti-6Al-4V by combining the Cingara model during hardening up to the peak stress and a softening model by a sigmoidal equation thereafter. A similar approach was followed by Karpat (2011) by mixing a modified Johnson-Cook model for hardening and a hyperbolic model for softening which is used during the machining simulation of Ti-6Al-4V. Porntadawit et al. (2014) incorporated the Cingara model for hardening and the Shafiei-Ebrahimi model for softening by dynamic recrystallization. Calamaz et al. (2011) proposed a model including the strain softening and thermal softening to be used in the simulation of machining. A modified Zerilli-Armstrong model together with a failure model was proposed by Liu et al. (2013). A microstructure simulation of Ti-6Al-4V using Representative Volume Element (RVE) has been employed by Przybyla and McDowell (2011) to generate probabilistic data and developed a model for fatigue crack formation. Anisotropic flow rule for Ti-6Al-4V based on the Khan-Huang-Liang model was developed by Khan and Yu (2012); Khan et al. (2012). Dislocation density based models have been used by Nemat-Nasser et al. (1999) for commercially pure titanium and Picu and Majorell (2002) & Gao et al. (2011) for Ti-6Al-4V. Tabei et al. (2017) proposed a microstructure-based flow stress model for Ti-6Al-4V at a wide range of temperature and strain rates. A model utilizing dislocation density and vacancy concentration as Internal State Variables (ISV) was developed by Babu and Lindgren (2013) that included globularization which is assumed to be responsible for flow-softening and stress relaxation.

There are relatively few published papers about microstructure models for Ti-6Al-4V. Using resistivity measurements and Differential Scanning Calorimetry (DSC), Malinov et al. (2001a,b) quantified the $\beta \rightarrow \alpha$ isothermal transformation of the alloy and modeled the phenomenon. Katzarov et al. (2002) using FEM, modeled the morphology changes of the alloy during transformation. Kelly (2004); Kelly et al. (2005) developed a FEM based themo-microstructural model for the metal deposition process. This was later extended to thermo-mechanical-microstructural domains by Crespo et al. (2009); Longuet et al. (2009). Charles Murgau et al. (2012) compared many available models and evaluated their applicability in the simulation of metal deposition. Lately, Mi et al. (2014) developed a fully coupled thermo-microstructural FE model for welding of Ti-6Al-4V using the JMAK formulation for phase transformation.

Modeling the microstructure-property relationship has been attempted by a few. Yu et al. (2010) used a fuzzy neural network based logic to predict the bulk properties of Ti-6Al-4V. A similar method was also used by Sun et al. (2011). But these studies were unable to predict the flow stress curves. Hayes et al. (2017) prepared samples with varying microstructure using additive manufacturing and developed a hybrid model based on neural network and genetic algorithm to define the microstructure-property relationship along with a flow stress model. A similar microstructure sensitive model is also developed by Baykasoglu et al. (2018) that can describe the room temperature flow stress curves of Ti-6Al-4V with varying microstructures.

In the current work, the constitutive model by Babu and Lindgren (2013) and the microstructure model by Charles Murgau et al. (2012) are combined to provide a model for arbitrary temperature and mechanical loading. An internal state variable approach is adopted to represent the microstructure evolution. This microstructure model uses a combination of models for formation and dissolution of various phases applied in a sequential logic in order to handle general temperature histories. Klusemann and Bambach (2018) evaluated the capacity of this microstructure model to simulate three complex cases of additive manufacturing and found the methodology appropriate. Compared to the previous work (Babu and Lindgren, 2013), the current flow stress model has a wider window of applicability since the non-equilibrium phase compositions is now included. The model parameters in Babu and Lindgren (2013) were a function of temperature and they were obtained by calibration using tests with constant equilibrium phase composition for each temperature. In the current work, a separate set of parameters of the flow stress model for each phase is calibrated. This is combined with the microstructure model and a mixture rule to include any arbitrary microstructure.

3. Thermo-mechanical-microstructural coupling

A staggered approach is typically used to compute the thermo-mechanical-metallurgical problems. For each time step and material point, the microstructure model computes the phase composition (X_α, X_β) using explicit formulation after receiving the temperature (T) from the thermal pass which is followed by the

mechanical pass that is based on X_α, X_β and T. Phase change can be exo/endothermic. This is included in the current model using temperature-dependent specific heat in the thermal field.

4. A dislocation density based flow stress model

An incompressible von Mises model is used here with the assumption of isotropic plasticity. The flow stress is split in to two parts (Babu and Lindgren, 2013),

$$\sigma_y = \sigma_G + \sigma^* \tag{1}$$

where, σ_G is the athermal stress contribution from the long-range interactions of the dislocation substructure. The second term σ^*, is the friction stress needed to move dislocations through the lattice and to pass short-range obstacles. Thermal vibrations can assist dislocations to overcome these obstacles. This formulation is very much in accordance to the material behavior demonstrated by Conrad (1981).

4.1. Long range stress component:

The long-range term from equation (1) is derived by Seeger (1956) as,

$$\sigma_G = m\alpha G b \sqrt{\rho_i} \tag{2}$$

where m is the Taylor orientation factor translating the effect of the resolved shear stress in different slip systems into effective stress and strain quantities. Furthermore, α is a proportionality factor to be calibrated, b is the magnitude of Burger's vector, G is the temperature dependent shear modulus and ρ_i is the immobile dislocation density.

4.2. Short range stress component:

The strain rate dependent part of the yield stress from equation (1) can be derived according to the Kocks-Mecking formulation (Mecking and Kocks, 1981) as,

$$\sigma^* = \tau_0 G \left[1 - \left[\frac{kT}{\Delta f_0 G b^3} \ln\left(\frac{\dot{\varepsilon}^{ref}}{\dot{\varepsilon}^p} \right) \right]^{1/q} \right]^{1/p} \tag{3}$$

Here, $\tau_0 G$ is the shear strength in the absence of thermal energy and $\Delta f_0 G b^3$ is the activation energy necessary to overcome lattice resistance. Some guidelines for selection of Δf_0 and τ_0 are given in (Frost and Ashby, 1982). The shape of the obstacle barrier for dislocation motion is defined by p and q. Further, k is the Boltzmann constant, T is the temperature in kelvin and ($\dot{\varepsilon}^{ref}$ and $\dot{\varepsilon}^p$) are the reference and plastic strain rates.

4.3. Evolution of immobile dislocation density

The basic components for the yield stress in equation (1) are obtained from equations (2) and (3). However, the evolution of ρ_i in equation (2) needs to be computed. The model for the evolution of the immobile dislocation density has two parts; hardening and restoration.

$$\dot{\rho}_i = \dot{\rho}_i^{(+)} - \dot{\rho}_i^{(-)} \tag{4}$$

4.3.1. Hardening process

It is assumed that mobile dislocations move, on average, a distance Λ (mean free path), before they are immobilized or annihilated. According to the Orowan equation, the density of mobile dislocations and their average velocity are proportional to the plastic strain rate. Then the immobilization is assumed to be proportional to the amount of mobile dislocation which is taken here as proportional to plastic strain rate. It is inversely proportional to the mean free path Λ.

$$\dot{\rho}_i^{(+)} = \frac{m}{b} \frac{1}{\Lambda} \dot{\varepsilon}^p \tag{5}$$

3

The mean free path can be computed from the grain size (g) and dislocation subcell or subgrain diameter (s) as,

$$\frac{1}{\Lambda} = \left(\frac{1}{g} + \frac{1}{s} \right) \tag{6}$$

The formation and evolution of subcells have been modeled using a relation proposed by Holt (1970).

$$s = K_c \frac{1}{\sqrt{\rho_i}} \tag{7}$$

4.3.2. Restoration processes

The motion of vacancies is related to the recovery of dislocations. This usually occurs at elevated temperatures and therefore is a thermally activated reorganization process. Creation of vacancy increases entropy but consumes energy and its concentration increases with temperature and deformation. In high stacking fault materials, recovery process might balance the effects of strain hardening leading to a constant flow stress. The primary mechanisms of restoration are dislocation glide, dislocation climb, and globularization.

$$\dot{\rho}_i{}^{(-)} = \dot{\rho}_i{}^{(glide)} + \dot{\rho}_i{}^{(climb)} + \dot{\rho}_i{}^{(globularization)} \tag{8}$$

The model for recovery by glide can be written based on the formulation by Bergström (1983)as,

$$\dot{\rho}_i{}^{(glide)} = \Omega \rho_i \dot{\bar{\varepsilon}}^p \tag{9}$$

where Ω is a function dependent on temperature.

Militzer et al. (1994) proposed a model for dislocation climb. With a modification of the diffusivity according to Babu and Lindgren (2013), the model can be written as,

$$\dot{\rho}_i{}^{(climb)} = 2c_\gamma D_{app} \frac{Gb^3}{kT} \left(\rho_i^2 - \rho_{eq}^2 \right) \tag{10}$$

where, c_γ is a material coefficient and ρ_{eq} is the equilibrium value of the dislocation density. Here D_{app} is the apparent diffusivity which includes the diffusivity of $\alpha - \beta$ phases weighted by their fractions in addition to pipe diffusion, as well as effects of vacancy concentration c_v.

A model for the evolution of dislocation density during globularization is proposed in Babu and Lindgren (2013). According to this model, the effect of grain growth on the reduction of flow stress is included only when the stored deformation energy is above a critical value.

$$\text{if} \quad \rho_i \geq \rho_{cr}$$
$$\dot{\rho}_i{}^{(globularization)} = \psi \dot{X}_g \left(\rho_i - \rho_{eq} \right); \ \text{until } \rho_i \leq \rho_{eq} \tag{11}$$
$$\text{else}$$
$$\dot{\rho}_i{}^{(globularization)} = 0 \tag{12}$$

Here, ρ_{cr} is the critical dislocation density above which globularization is initiated, ρ_{eq} is the equilibrium value of dislocation density, $\dot{X}_g$ is the globularization rate and ψ is a calibration constant.

4.4. Evolution of excess vacancy concentration

Militzer et al. (1994) proposed a model for excess vacancy concentration with generation and annihilation components. Assuming that only long range stress contributes to vacancy formation and introducing a component for temperature change, the Militzer model can be rewritten as,

$$\dot{c_v}^{ex} = \left[\chi \frac{m\alpha Gb^2 \sqrt{\rho_i}}{Q_{vf}} + \zeta \frac{c_j}{4b^2} \right] \frac{\Omega_0}{b} \dot{\bar{\varepsilon}} - D_{vm} \left[\frac{1}{s^2} + \frac{1}{g^2} \right] (c_v - c_v^{eq})$$
$$+ c_v^{eq} \left(\frac{Q_{vf}}{kT^2} \right) \dot{T} \tag{13}$$

Here, $\chi = 0.1$ is the fraction of mechanical energy spent on vacancy generation, Ω_0 is the atomic volume and ζ is the neutralization effect by vacancy emitting and absorbing jogs. The concentration of jogs (c_j) and D_{vm}, the diffusivity of vacancy are given in Babu and Lindgren (2013). Additionally, Q_{vf} is the activation energy of vacancy formation.

4

5. Model for phase evolution

The liquid–solid phase changes are not modeled in detail. Instead, a simplified model for the transition between the liquid and solid state is implemented to take care of temperatures above the melting temperature T_{melt} . In the liquid state, each of the solid phases is consequently set to zero. In the solid state, the Ti–6Al–4V microstructure is composed of two main phases; the high-temperature stable β-phase and the lower temperature stable α-phase. Depending on the formation conditions, a variety of α/β textures can be obtained by heat treatment giving varying mechanical properties. Lütjering (1998); Williams and Lütjering (2003) explored the relationship between processing, microstructure, and mechanical properties. Based on the literature (Semiatin et al., 1999b,a; Seetharaman and Semiatin, 2002; Thomas et al., 2005) few microstructural features have been identified to be relevant with respect to the mechanical properties. The three separate α-phase fractions; Widmanstatten (X_{α_w}), grain boundary ($X_{\alpha_{gb}}$), acicular and massive Martensite (X_{α_m}) and the β-phase fraction (X_β) are included in the current model. Though in the current flow stress model, the individual α-phase fractions are not included separately, it is possible to incorporate them when more details about their respective strengthening mechanisms are known.

5.1. Phase transformations

Depending on the temperature, heating/cooling rates, Ti-6Al-4V undergoes an allotropic transformation. The mathematical model for transformation is described schematically in figure 1. The transformations denoted by F1, F2, and F3 represent formation of α_{gb}, α_w and α_m phases respectively and D3, D2, and D1 shows the dissolution of the same phases. If the current volume fraction of β phase is more than β_{eq}, the excess β phase transforms to α phase. Here α_{gb} formation which occurs in high temperature is most preferred followed by the α_w. The remaining excess β fraction is transformed to α_m if the temperature is lower than T_m, the martinsite start temperature. Conversely, if the current volume fraction of β is lower than β_{eq}, the excess α phase is converted to β. Primary, the α_m phase dissolves to β and α_w

Figure 1: The Mechanism of phase change.

phases in the same proportion as the α_{eq} and β_{eq}. The remaining excess α_w and α_{gb} transform to β in that order.
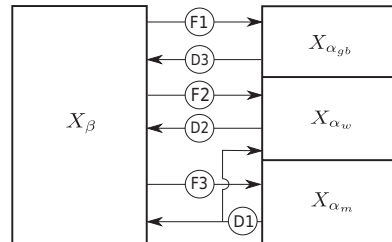
5.2. Adaptation of JMAK model for diffusional transformation

The JMAK model (Johnson and Mehl, 1939; Avrami, 1939; Kolmogorov, 1937) originally formulated for nucleation and growth during isothermal situations can be adapted to model any diffusional transformations. Employing the additivity principle, and using sufficiently small time steps ensures that any arbitrary temperature changes be computed. JMAK model assumes that a single phase X_1 which is 100% in volume from the start will transform to 100% of second phase X_2 in infinite time. However, in the case of Ti-6Al-4V, this is not the case as it is a $\alpha - \beta$ dual phase alloy below β-transus temperature. Hence, in order to accommodate incomplete transformation, the product fraction is normalized with the equilibrium volume. Conversely, the starting volume of a phase can also be less than 100% which is circumvented by assuming that the available phase volume is the total phase fraction. Another complication is the existence of simultaneous transformation of various α phases (α_w, α_{gb}, α_m) to β phase and back. This can be modeled by calculating each transformation in a sequential fashion within the time increment as shown in figure 1.

5.3. Equilibrium phase fraction

Charles Murgau et al. (2012) compared various measurements for equilibrium phase fraction of β^{eq}-phase ($X_{\beta^{eq}}$) available in the literature and identified that the data showed scatter. Compared to the measurements of phase fractions during cooling by Malinov et al. (2001a), the literature data showed an opposite trend.

5

Therefore, in this work, $X_{\beta^{eq}}$ is computed by calibrating the model given by the equation 14 and figure 7, were T is the temperature in degree Celsius.

$$
\begin{aligned}
X_\beta^{eq} &= 1 - 0.89\, e^{-\left(\frac{T^*+1.82}{1.73}\right)^2} + 0.28\, e^{-\left(\frac{T^*+0.59}{0.67}\right)^2} \\
T^* &= (T - 927)/24
\end{aligned}
\tag{14}
$$

5.4. Formation of α phase

During cooling from β-phase, α_{gb} and α_w phases are formed by a diffusional transformation. According to the incremental formulation of JMAK model described by Charles Murgau et al. (2012), the formation of α_{gb} and α_w can be modeled by the set of equations in rows F1 and F2 respectively of table 1. Martensite phase is formed at cooling rates above 410℃/s by a diffusion-less transformation. While cooling at rates above 20°C/s and upto 410℃/s, the massive α transformation has been observed to occur simultaneously with the martensite formation (Lu et al., 2016). Owing to the similitude in crystal structure between massive-α and martensite-α, they are not differentitated here except that above 410℃/s, 100% α_m is allowed to form. An incremental formulation of Koistinen-Marburger equation described by Charles Murgau et al. (2012) is used here (see equation set in row F3 of table 1).
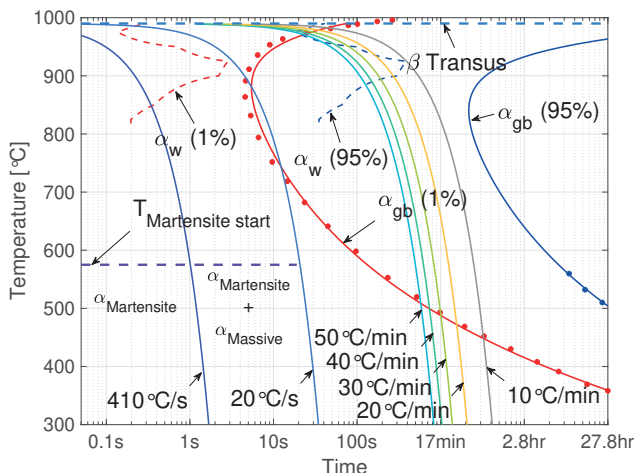

Figure 2: TTT Diagram.

The start(1%) shown in red and end(95%) shown in blue of phase transformation described in the table 1 is given in figure 2. The dots for α_{gb} are data taken from JMatPro software (Saunders et al., 2003). The martensite formation zone below the start temperature and above 410℃/s as well as the martensite and the massive α mixed zone between 20°C/s - 410°C/s are also shown in figure 2. The α_w start and end curves are obtained after calibrating the model with data for the total fraction of alpha from Malinov et al. (2001a).

5.5. Dissolution of α phase

The α_m phase formed by instantaneous transformation is unstable and therefore undergoes a diffusional transformation to α_w and β phases based on its current equilibrium composition. The incremental formulation of classical JMAK model by Charles Murgau et al. (2012) and its parameters are given in row D1 of table 2. During heating or reaching non-equilibrium phase composition, α_w and α_{gb} can transform to β-phase controlled by the diffusion of vanadium at the $\alpha - \beta$ interface. A parabolic equation developed by Kelly (2004); Kelly et al. (2005) derived in its incremental form by Charles Murgau et al. (2012) is used here (see rows D2 and D3 of table 2).

6

F1	$^{n+1}X_{\alpha_{gb}}=\left(1-e^{-k_{gb}\left(t_{gb}^*+\Delta t\right)^{N_{gb}}}\right)\left(^nX_\beta+{}^nX_{\alpha_w}+{}^nX_{\alpha_{gb}}\right)^{n+1}X_\alpha^{eq}-{}^nX_{\alpha_w}$ $t_{gb}^*=\sqrt[N_{gb}]{-ln\left(1-\dfrac{\left(^nX_{\alpha_w}+{}^nX_{\alpha_{gb}}\right)/^{n+1}X_\alpha^{eq}}{^nX_\beta+{}^nX_{\alpha_w}+{}^nX_{\alpha_{gb}}}\right)\bigg/k_{gb}}$ $t_{gb}^{1\%}=61.5e^{(-3.97e^{-3}T)}+10^{-13}e^{(2.43e^{-2}T)}$ $t_{gb}^{95\%}=t_{gb}^{1\%}+2.20$ $N_{gb}=\log_{10}\left(\dfrac{\ln(1-0.01)}{\ln(1-0.95)}\right)\bigg/\log_{10}\left(\dfrac{t_{gb}^{1\%}}{t_{gb}^{95\%}}\right)$ $k_{gb}=-\dfrac{\ln(1-0.01)}{(t_{gb}^{1\%})^{N_{gb}}}$

F2:

$$^{n+1}X_{\alpha_w}=\left(1-e^{-k_w(t_w^*+\Delta t)^{N_w}}\right)\left(^nX_\beta+{}^nX_{\alpha_w}+{}^nX_{\alpha_{gb}}\right)^{n+1}X_\alpha^{eq}-{}^nX_{\alpha_{gb}}$$

$$t_w^*=\sqrt[N_w]{-ln\left(1-\frac{\left(^nX_{\alpha_w}+{}^nX_{\alpha_{gb}}\right)/^{n+1}X_\alpha^{eq}}{^nX_\beta+{}^nX_{\alpha_w}+{}^nX_{\alpha_{gb}}}\right)\bigg/k_w}$$

T[°C]	0	825	850	875	900	925	950	975	1000	1900
N_w	1.10	1.10	1.10	1.13	1.16	1.16	1.16	1.16	1.16	1.16
$k_w\ [10^{-2}]$	6.00	6.00	3.00	1.70	0.40	0.30	0.15	10.0	0.00	0.00

F3:

$$^{n+1}X_{\alpha_m}=\begin{cases}\left(1-e^{-b_{km}(T_{ms}-T)}\right)\left(^nX_\beta+{}^nX_{\alpha_m}\right); & if\ (\dot T>410°C/s)\\[4pt]\left(1-e^{-b_{km}(T_{ms}-T)}\right)\left(^nX_\beta+{}^nX_{\alpha_m}-{}^{n+1}X_\alpha^{eq}\right); & if\ (20°C/s>\dot T>410°C/s)\end{cases}$$
$$b_{km}=5.0e^{-3};\ T_{ms}=851.0°C$$

Table 1: Models and parameters for α-phase formation.

D1:

$$^{n+1}X_{\alpha_m}=\left(^{n+1}X_{\alpha_m}^{eq}-e^{-k_m(t_m^*+\Delta t)^{N_m}}\right)\left(^nX_\beta+{}^nX_{\alpha_m}-{}^{n+1}X_{\alpha_m}^{eq}\right)$$

$$t_m^*=\sqrt[N_m]{-ln\left(\frac{\left(^nX_\alpha-{}^{n+1}X_{\alpha_m}^{eq}\right)}{^nX_\beta+{}^nX_{\alpha_m}-{}^{n+1}X_{\alpha_m}^{eq}}\right)/k_m}$$

$$^{n+1}X_{\alpha_w}={}^nX_{\alpha_w}+\Delta^nX_{\alpha_m}(1-{}^{n+1}X_\beta^{eq})$$
$$^{n+1}X_\beta={}^nX_\beta+\Delta^nX_{\alpha_m}\,{}^{n+1}X_\beta^{eq}$$

T [°C]	0	400	500	700	800	1900
N_m	1.019	1.019	1.015	1.025	1.031	1.031
k_m	0.667	0.667	1.106	1.252	1.326	1.326

D2 / D3:

$$^{n+1}(X_{\alpha_w}+X_{\alpha_{gb}})=\begin{cases}^{n+1}X_\alpha^{eq}f_{diss}(T)\sqrt{\Delta t+t^*}; & if\ (0<(\Delta t+t^*)<t_{crit})\\[4pt]^{n+1}X_\alpha^{eq}; & if\ (\Delta t+t^*>t_{crit})\end{cases}$$

$$t^*=\left(\frac{^nX_\beta}{^{n+1}X_\beta^{eq}f_{diss}(T)}\right)^2$$

$$f_{diss}(T)=2.2e^{-31}T^{9.89}$$
$$t_{crit}=\sqrt{f_{diss}(T)}$$

Table 2: Models and parameters for α-phase dissolution.

6. Coupling of phase and flow stress models

The Young's modulus can be written according to Fan (1993); Lee and Welsch (1990) as a linear rule of mixtures (ROM). However, since the elastic modulus of the individual phases is not available at elevated temperatures, the effective modulus is used here. The results of measurement and data from Fukuhara and Sanpei (1993) are plotted in figure 3 along with the model by Wachtman et al. (1961) fitted to the measurement. Based on the Wachtman model, Young's Modulus can be written as,

$$E = E_0 - B(T + 273.15)e^{(-T_0/(T+273.15))} \tag{15}$$

where T is the temperature in degree Celsius, $E_0 = 107GPa$ is the modulus of elasticity at $0K$, $B = 0.2$ is the calibration parameter and $T_0 = 1300K$ is the temperature at which $E - T$ relationship becomes linear.

Drawing from the fact that data for individual phases are not available, the Poisson's ratio is assumed to be constant for both phases. The measurement by Fukuhara and Sanpei (1993) and a linear model fitted to it are shown in figure 3. The model for Poisson's ratio can be written as,

$$\mu = 0.34 + 6.34 \cdot 10^{-5}T \tag{16}$$

where T is the temperature in degree Celsius.

Swarnakar et al. (2011) using X-Ray diffraction measured the volumetric expansion of unit cells of α and β phases during heating (see figure 4). Based on this, the average coefficient of thermal expansion (CTE)
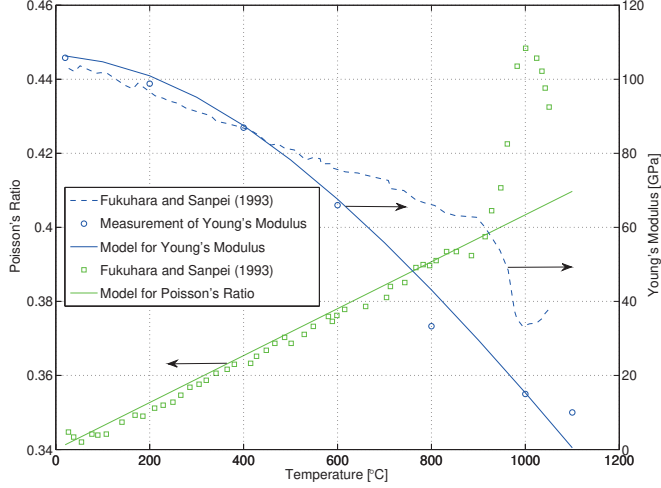
Figure 3: Youngs Modulus and Poisson's Ratio.

of the phase mixture can be calculated using the ROM as in equation 17, where α_α and α_β gives the CTE of α and β phases respectively. However, since the elastic properties of the α and β phases differ, a linear ROM is not suitable here (Ho and Taylor, 1998). There exist many models based on the elastic properties of the individual components applicable in this situation. However, this data is not available for the two phases at elevated temperatures. Hence, a modification of thermal strain, which is a calibration parameter as a function of temperature is introduced here. The linear thermal strain can be computed using equation 18 which is plotted in figure 4 and is compared with measurement data from Babu and Lindgren (2013).

$$\alpha_{avg} = X_\alpha \alpha_\alpha + X_\beta \alpha_\beta \tag{17}$$
$$\varepsilon^{th} = \alpha_{avg}\Delta T - \varepsilon^{adj} \tag{18}$$
$$\varepsilon^{adj} = 1.0e^{-8}T^2 - 8.4e^{-6}T + 3.0e^{-4} \tag{19}$$

Since the strengthening contributions of these individual alpha phases are not known, a linear ROM for the total alpha-beta composition is developed. The yield strength of the phase mixture can be written as,

$$\sigma_y = X_\alpha \sigma_y^\alpha + X_\beta \sigma_y^\beta \tag{20}$$

Assuming the ad-hoc iso-work principle, the distribution of plastic strain between the phases can be obtained. According to Bouaziz and Buessler (2004), this can be written as,

$$\sigma_y^\alpha \dot{\bar{\varepsilon}}_\alpha = \sigma_y^\beta \dot{\bar{\varepsilon}}_\beta \tag{21}$$
$$\dot{\bar{\varepsilon}}^p = X_\alpha \dot{\bar{\varepsilon}}_\alpha + X_\beta \dot{\bar{\varepsilon}}_\beta \tag{22}$$

8
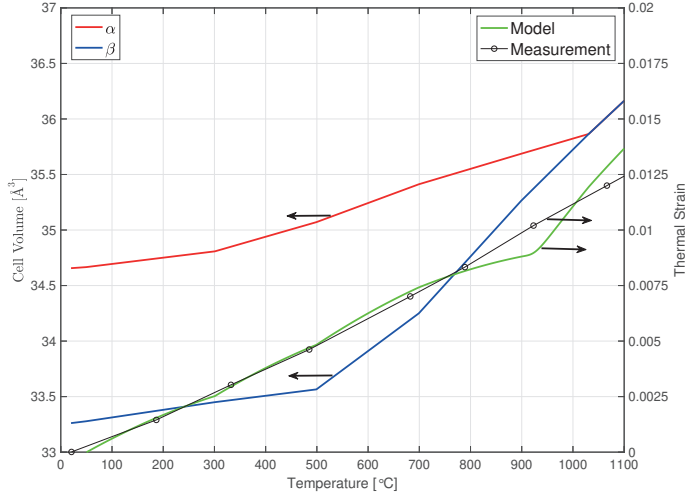
Figure 4: Thermal Expansion and Strain.

This ensures that the β phase with lower yield strength will get a larger share of plastic strain as compared to the stronger α phase

7. Calibration of constitutive models

The suitable parameters of the model are found by performing a calibration which poses a challenge. This is attributed to the fact that some of the parameters are temperature dependent which increases the number of parameters drastically for the model. An in-house Matlab™ based toolbox using constrained minimization routine for optimization is developed for this task. It enables calibration of multiple experiments and easy interaction with the optimization process. This is done by using a gradient-based algorithm which systematically chooses parameter values from between the given set. The cost function to be minimized is formulated as the weighted sum of the difference between computed and experimental stress. This assures equal significance to all the data points of an experiment. Additionally, this tool allows the user to specify a custom weight for different parts of the curve. Compression tests performed at the nominal temperatures between 20 and 1100℃ and strain rates from $0.001s^{-1}$ to $1.0s^{-1}$ were used to calibrate the model. These data is already published in Babu and Lindgren (2013). The different parameters of the model obtained after calibration using σ-ε measurements are shown in Tables 4, 6 and 5. The predicted flow stress curves along with measurements are given in Babu and Lindgren (2013) and is not repeated here because of negligible difference.

8. Demonstration of the model

A set of numerical tests was performed in order to compute the behavior of the microstructure model during cyclic heating and cooling. Figure 5 shows the computed total $\alpha-$phase fraction (X_α) during cyclic heating from 600℃ to 1050℃ followed by cooling and heating at rates varying between (1 to 100)℃/s The stress-strain relationship predicted by the model for varying strain rates and temperature are given in figure 6.

Parameter	Dimension	Value	Reference
T_{melt}	℃	1600	f
$T_{\beta-transus}$	℃	890	f
k	JK^{-1}	$1.38 \cdot 10^{-23}$	f
b	m	$2.95 \cdot 10^{-10}$	a
$D_{\alpha 0}$	m^2s^{-1}	$5 \cdot 10^{-6}$	d
$D_{\beta 0}$	m^2s^{-1}	$3 \cdot 10^{-7}$	d
Q_{vf}	J	$1.9 \cdot 10^{-19}$	b
Q_{vm}	J	$2.49 \cdot 10^{-19}$	a
Q_{β}	J	$2.5 \cdot 10^{-19}$	d
Q_p	J	$1.61 \cdot 10^{-19}$	a
n_a^p	–	2	f
n_ρ	–	ρ_i	f
Ω_0	m^3	$1.76 \cdot 10^{-29}$	a
g_0	m	$2 \cdot 10^{-6}$	f
n	–	3	e
$\dot{\varepsilon}_{ref}$	s^{-1}	10^6	a
ΔS_{vm}	JK^{-1}	$1.38 \cdot 10^{-23}$	g

[a]Frost and Ashby (1982)
[b]Novikov et al. (1980)
[c]Conrad (1981)
[d]Mishin and Herzig (2000)
[e]Sargent et al. (2008)
[f]Calculated or Measured Value
[g]Hernan et al. (2005)

Table 3: Parameters for the model from literature.

Parameter	Dimension	Value
D_{p0}	m^2s^{-1}	10^{-8}
N_a^l	–	10^{19}
p	–	0.3
q	–	1.8
Ω	–	38
ρ_{eq}	m^{-2}	10^{10}

Table 4: Calibrated parameters of the model.

α	C_γ $[10^{-1}]$	K_c $[10^2]$	τ_0 $[10^{-1}]$	Δf_0	ρ_i^{init} $[10^{12}]$
1.15	1.00	1.20	3.00	1.30	1.00

Table 5: Calibrated temperature-dependent parameters of the β-phase model.

T [℃]	25	100	200	300	400	500	600	700	800	900	1000	1100
α	2.30	1.92	1.90	1.90	2.10	2.15	1.70	0.80	1.00	1.15	1.20	1.10
C_γ $[10^{-1}]$	0.00	0.00	0.00	0.00	0.00	3.00	4.00	5.00	5.00	0.50	1.00	2.00
K_c $[10^2]$	0.40	0.40	0.40	0.40	0.40	0.40	0.40	0.80	1.20	1.20	1.20	1.20
τ_0 $[10^{-1}]$	0.10	0.20	0.20	0.20	0.20	0.40	1.20	1.50	3.50	3.00	1.00	0.50
Δf_0	0.50	0.50	0.50	0.50	0.50	0.60	0.80	1.70	1.70	1.55	1.30	0.90
ρ_i^{init} $[10^{14}]$	1.00	1.00	1.00	1.00	1.00	1.00	0.70	0.10	0.10	0.10	0.01	0.01
ρ_i^{crit} $[10^{14}]$	5.00	5.00	5.00	5.00	2.24	2.00	1.50	0.20	0.20	0.20	0.10	0.10
B	1.00	1.00	1.00	1.00	1.00	0.50	0.50	0.50	0.60	0.50	0.10	0.01
k	2.00	2.00	2.00	2.00	2.00	2.00	1.00	1.50	2.00	2.00	2.00	2.00
M $[10^2]$	0.00	0.00	0.00	0.00	0.00	1.00	6.00	6.00	6.00	6.00	6.00	6.00
ψ	0.00	0.00	0.00	0.00	0.05	0.05	0.60	2.00	8.00	1.00	1.00	1.00
K $[10^{-19}]$	0.00	0.00	0.00	0.00	0.00	0.05	0.25	6.50	8.00	8.00	8.00	8.00

Table 6: Calibrated temperature-dependent parameters of the α-phase model.

9. Validation of the constitutive model

Experiments were performed to evaluate the validity of the model. Using the Gleeble-3800 machine, compression tests at varying rates were performed on cylindrical specimens which were subjected to continuous cooling from 1000℃ at rates varying between 50℃/min to 10℃/min. See figure 8 where dotted lines indicate applied strain and continuous lines the controlled temperature. Malinov et al. (2001a) performed a DSC study on Ti-6Al-4V at the same cooling rates and measured the phase fractions. Their data together with the computed phase fraction from the model is given in figure 7 where dots denote measurement and lines, the model. During the compression test, stress and strain values are recorded and is plotted along with computed values in figure 9 and stress vs time in figure 10 with dots denoting measurement and lines, the computed model.
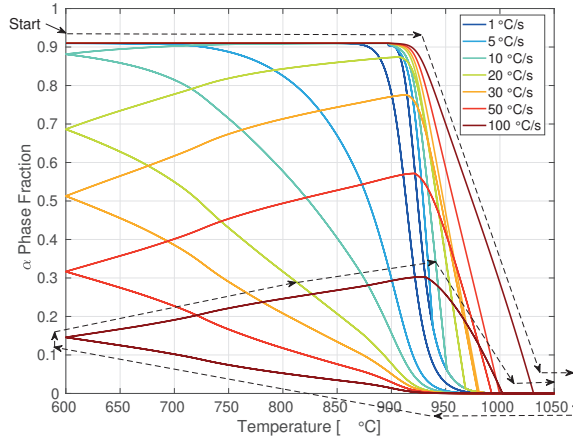
Figure 5: Computed phase transformation during cyclic Heating-Cooling-Heating.

$\dot{\bar{\varepsilon}} = 0.001 s^{-1}$

$\dot{\bar{\varepsilon}} = 0.01 s^{-1}$

$\dot{\bar{\varepsilon}} = 0.1 s^{-1}$
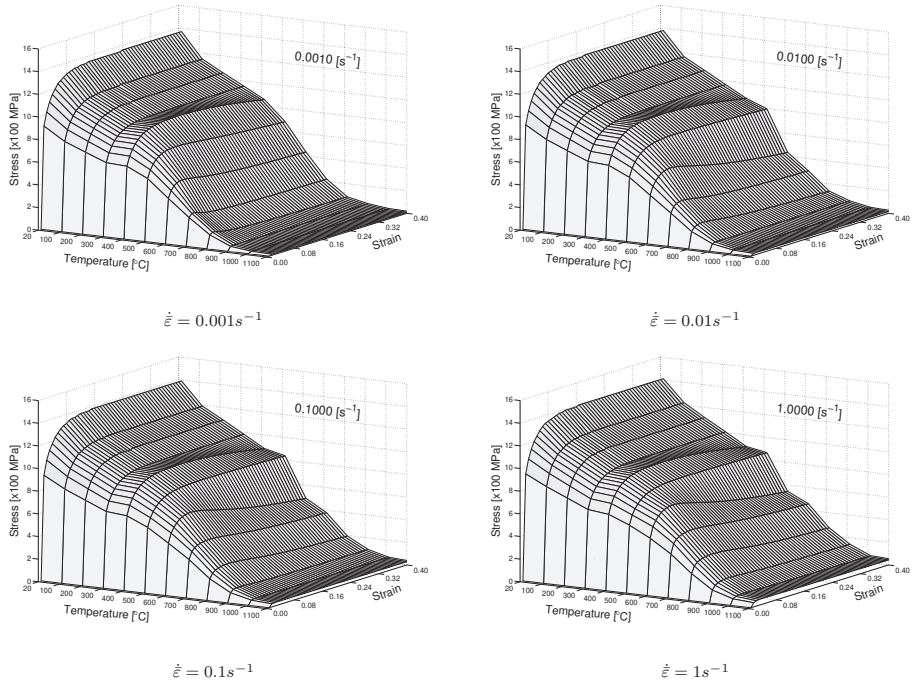

$\dot{\bar{\varepsilon}} = 1 s^{-1}$

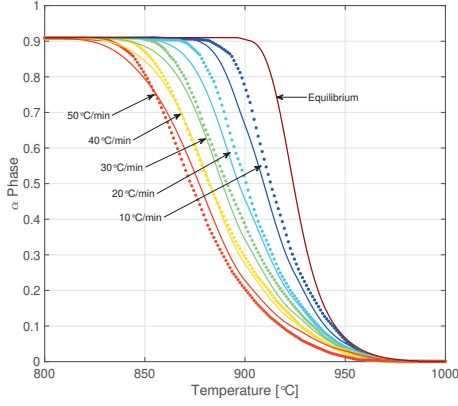Figure 6: Stress-strain-temperature relationship.

Figure 7: Phase Transformation.
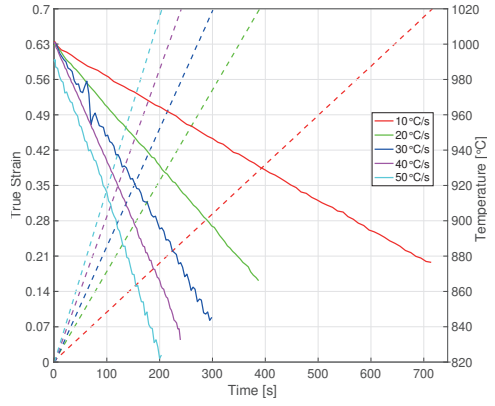
Figure 8: Deformation (points-strain; lines-temperature).
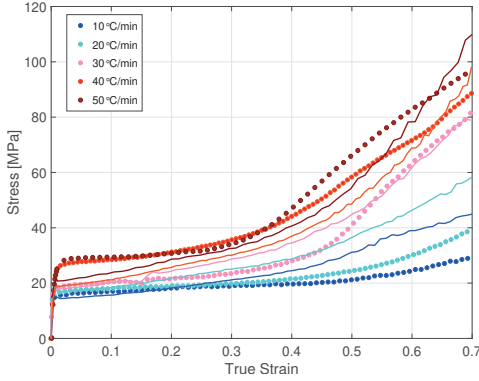
Figure 9: Measured and computed stress-strain curves.
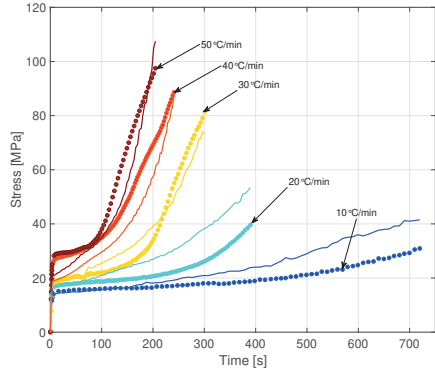
Figure 10: Measured and computed stress-time curves.

10. Discussions and conclusions

The model predictions for stress-strain (figure 9) and stress-time (figure 10) behavior during faster cooling rates (50-30℃/min) follows the measurements much better than the slower cooling rates (10-20℃/min). One reason for this behavior could be because of the prolonged exposure to oxygen, (an α stabilizer) altering the phase transformation kinetics as well as the mechanical response (Khan et al., 2007) which is not included in the model. The force recorded by Gleeble thermo-mechanical simulator during the initial part of the deformation is at about the limit of the equipment. Therefore, the authors did not attempt to use a non-linear ROM with calibration parameters to improve the accuracy of the predictions. Another uncertainty is that during cooling, though is feedback controlled by a thermocouple at the middle of the specimen, the thermal gradient along its length is ignored.

This article presents a calibrated thermo-mechanical-microstructural model for the Ti-6Al-4V alloy to be used in simulations involving arbitrary thermo-mechanical loading. Compared to the earlier work by Babu and Lindgren (2013) for equilibrium phase compositions, the non-equilibrium phase evolution model coupled with flow stress model developed in the current work allows us to simulate complex transient and cyclic loading situations that emerge during manufacturing processes like welding, additive manufacturing etc.

References

Avrami, M., 1939. Kinetics of Phase Change. I General Theory. The Journal of Chemical Physics 7 (12), 1103–1112.

Babu, B., Lindgren, L.-E., 2013. Dislocation density based model for plastic deformation and globularization of Ti-6Al-4V. International Journal of Plasticity 50 (0), 94–108.

Backman, D., Wei, D., Whitis, D., Buczek, M., Finnigan, P., Gao, D., 2006. ICME at GE: Accelerating the insertion of new materials and processes. JOM 58 (11), 36–41.

Baykasoglu, C., Akyildiz, O., Candemir, D., Yang, Q., To, A. C., 2018. Predicting microstructure evolution during directed energy deposition additive manufacturing of ti-6al-4v. Journal of Manufacturing Science and Engineering 140 (5), 051003.

Bergström, Y., 1983. The plastic deformation of metals - A dislocation model and its applicability. Reviews on Powder Metallurgy and Physical Ceramics (2/3), 79–265.

Bouaziz, O., Buessler, P., 2004. Iso-work Increment Assumption for Heterogeneous Material Behaviour Modelling. Advanced Engineering Materials 6 (1-2), 79–83.

Calamaz, M., Coupard, D., Nouari, M., Girot, F., 2011. Numerical analysis of chip formation and shear localisation processes in machining the Ti-6Al-4V titanium alloy. The International Journal of Advanced Manufacturing Technology 52 (9-12), 887–895.

Charles Murgau, C., Pederson, R., Lindgren, L., 2012. A model for Ti–6Al–4V microstructure evolution for arbitrary temperature changes. Modelling and Simulation in Materials Science and Engineering 20 (5), 055006.

Committee on Integrated Computational Materials Engineering, N. R. C., 2008. Integrated Computational Materials Engineering: A Transformational Discipline for Improved Competitiveness and National Security. The National Academies Press.

Conrad, H., 1981. Effect of interstitial solutes on the strength and ductility of titanium. Progress in Materials Science 26 (2-4), 123–403.

Crespo, A., Deus, A., Vilar, R., 2009. Modeling of phase transformations and internal stresses in laser powder deposition. In: XVII International Symposium on Gas Flow, Chemical Lasers, and High-Power Lasers. Vol. 7131. International Society for Optics and Photonics, p. 713120.

Fan, Z., 1993. On the young's moduli of Ti-6Al-4V alloys. Scripta Metallurgica et Materialia 29 (11), 1427–1432.

Frost, H. J., Ashby, M. F., 1982. Deformation-Mechanism Maps: The Plasticity and Creep of Metals and Ceramics. Paperback.

Fukuhara, M., Sanpei, A., 1993. Elastic moduli and internal frictions of Inconel 718 and Ti-6Al-4V as a function of temperature. Journal of Materials Science Letters 12, 1122–1124.

Gao, C., Zhang, L., Yan, H., 2011. A new constitutive model for HCP metals. Materials Science and Engineering: A 528 (13-14), 4445–4452.

Hayes, B. J., Martin, B. W., Welk, B., Kuhr, S. J., Ales, T. K., Brice, D. A., Ghamarian, I., Baker, A. H., Haden, C. V., Harlow, D. G., et al., 2017. Predicting tensile properties of ti-6al-4v produced via directed energy deposition. Acta Materialia 133, 120–133.

Hernan, R. D., Maria, G. L., Maria, M. A., 12 2005. Self-diffusion in the hexagonal structure of Zirconium and Hafnium: computer simulation studies. Materials Research 8, 431–434.

Ho, C. Y., Taylor, R. E., 1998. Thermal expansion of solids. ASM International, Materials Park, OH.

Holt, D. L., 1970. Dislocation cell formation in metals. Journal of applied physics 41 (8), 3197.

Johnson, W., Mehl, R., 1939. Reaction Kinetics in Processes of Nucleation and Growth. Trans. Soc. Pet. Eng. 135, 416.

Karpat, Y., 2011. Temperature dependent flow softening of titanium alloy Ti6Al4V: An investigation using finite element simulation of machining. Journal of Materials Processing Technology 211 (4), 737–749.

Katzarov, I., Malinov, S., Sha, W., 2002. Finite element modeling of the morphology of (beta) to (alpha) phase transformation in Ti-6AI-4V alloy. Metallurgical and Materials Transactions A 33A (4), 1027.

Kelly, S. M., 2004. Thermal and Microstructure Modeling of Metal Deposition Processes with Application to Ti-6Al-4V. Phd thesis, Virginia Polytechnic Institute and State University.

Kelly, S. M., Babu, S. S., David, S. A., Zacharia, T., Kampe, S. L., 2005. A microstructure model for laser processing of Ti-6Al-4V. In: 24th International Congress on Applications of Lasers and Electro-Optics, ICALEO 2005. 24th International Congress on Applications of Lasers and Electro-Optics, ICALEO 2005 - Congress Proceedings. Laser Institute of America, Orlando, FL 32826, United States, Miami, FL, United States, pp. 489–496.

Khan, A. S., Kazmi, R., Farrokh, B., Zupan, M., 2007. Effect of oxygen content and microstructure on the thermo-mechanical response of three Ti-6Al-4V alloys: Experiments and modeling over a wide range of strain-rates and temperatures. nternational Journal of Plasticity 23 (7), 1105–1125.

Khan, A. S., Yu, S., 2012. Deformation induced anisotropic responses of Ti-6Al-4V alloy. Part I: Experiments. International Journal of Plasticity 38 (0), 1–13.

Khan, A. S., Yu, S., Liu, H., 2012. Deformation induced anisotropic responses of Ti-6Al-4V alloy Part II: A strain rate and temperature dependent anisotropic yield criterion. International Journal of Plasticity 38 (0), 14–26.

Klusemann, B., Bambach, M., 2018. Stability of phase transformation models for ti-6al-4v under cyclic thermal loading imposed during laser metal deposition. In: AIP Conference Proceedings. Vol. 1960. AIP Publishing, p. 140012.

Kolmogorov, A., 1937. A statistical theory for the recrystallisation of metals, Akad Nauk SSSR, Izv. Izv. Akad. Nauk. SSSR 3.

Lee, Y., Welsch, G., 1990. Young's modulus and damping of Ti6Al4V alloy as a function of heat treatment and oxygen concentration. Materials Science and Engineering A 128 (1), 77–89.

Liu, R., Melkote, S., Pucha, R., Morehouse, J., Man, X., Marusich, T., 2013. An enhanced constitutive material model for machining of Ti–6Al–4V alloy. Journal of Materials Processing Technology 213 (12), 2238–2246.

Longuet, A., Robert, Y., Aeby-Gautier, E., Appolaire, B., Mariage, J., Colin, C., Cailletaud, G., 2009. A multiphase mechanical model for ti–6al–4v: Application to the modeling of laser assisted processing. Computational Materials Science 46 (3), 761–766.

Lu, S., Qian, M., Tang, H., Yan, M., Wang, J., StJohn, D., 2016. Massive transformation in ti–6al–4v additively manufactured by selective electron beam melting. Acta Materialia 104, 303–311.

Lütjering, G., 1998. Influence of processing on microstructure and mechanical properties of $(\alpha + \beta)$ titanium alloys. Materials Science and Engineering: A 243 (1–2), 32–45.

Malinov, S., Guo, Z. X., Sha, W., Wilson, A., 2001a. Differential scanning calorimetry study and computer modeling of beta to alpha phase transformation in a Ti-6AI-4V alloy. Metallurgical and Materials Transactions: A 32A (4), 879.

Malinov, S., Markovsky, P. E., Sha, W., Guo, Z. X., 2001b. Resistivity study and computer modelling of the isothermal transformation kinetics of Ti-6Al-4V and Ti-6Al-2Sn-4Zr-2Mo-0.08Si alloys. Journal of Alloys and Compounds 314 (1-2), 181.

Mecking, H., Kocks, U., 1981. Kinetics of flow and strain-hardening. Acta Metallurgica 29 (11), 1865–1875.

Mi, G., Wei, Y., Zhan, X., Gu, C., Yu, F., 2014. A coupled thermal and metallurgical model for welding simulation of Ti–6Al–4V alloy. Journal of Materials Processing Technology 214 (11), 2434–2443.

Militzer, M., Sun, W. P., Jonas, J. J., 1994. Modelling the effect of deformation-induced vacancies on segregation and precipitation. Acta Metallurgica et Materialia 42 (1), 133.

Mishin, Y., Herzig, C., Feb. 2000. Diffusion in the Ti-Al system. Acta Materialia 48 (3), 589–623.

Nemat-Nasser, S., Guo, W.-G., Cheng, J. Y., 1999. Mechanical properties and deformation mechanisms of a commercially pure titanium. Acta Materialia 47 (13), 3705.

Novikov, I. I., Roshchupkin, V. V., Semashko, N. A., Fordeeva, L. K., 1980. Experimental investigation of vacancy effects in pure metals. Journal of Engineering Physics and Thermophysics V39 (6), 1316.

Picu, R. C., Majorell, A., 2002. Mechanical behavior of Ti-6Al-4V at high and moderate temperatures–Part II: constitutive modeling. Materials Science and Engineering A 326 (2), 306–316.

Porntadawit, J., Uthaisangsuk, V., Choungthong, P., 2014. Modeling of flow behavior of Ti–6Al–4V alloy at elevated temperatures. Materials Science and Engineering: A 599 (0), 212–222.

Przybyla, C. P., McDowell, D. L., 2011. Simulated microstructure-sensitive extreme value probabilities for high cycle fatigue of duplex Ti–6Al–4V. International Journal of Plasticity 27 (12), 1871–1895.

Sargent, G., Zane, A., Fagin, P., Ghosh, A., Semiatin, S., 2008. Low-Temperature Coarsening and Plastic Flow Behavior of an Alpha/Beta Titanium Billet Material with an Ultrafine Microstructure. Metallurgical and Materials Transactions A 39, 2949–2964.

Saunders, N., Guo, U., Li, X., Miodownik, A., Schillé, J.-P., 2003. Using JMatPro to model materials properties and behavior. Jom 55 (12), 60–65.

Seeger, A., 1956. The mechanism of Glide and Work Hardening in FCC and HCP Metals. In: Fisher, J., Johnston, W. G., Thomson, R., Vreeland, T. J. (Eds.), Dislocations and Mechanical Properties of Crystals. pp. 243–329.

Seetharaman, V., Semiatin, S. L., 2002. Effect of the lamellar grain size on plastic flow behavior and microstructure evolution during hot working of a gamma titanium aluminide alloy. Metallurgical and Materials Transactions A 33A (12), 3817.

Semiatin, S. L., Seetharaman, V., Ghosh, A. K., 1999a. Plastic flow, microstructure evolution, and defect formation during primary hot working of titanium and titanium aluminide alloys with lamellar colony microstructures. Philosophical Transactions: Mathematical, Physical and Engineering Sciences 357, 1487 – 1512.

Semiatin, S. L., Seetharaman, V., Weiss, I., 1999b. Flow behavior and globularization kinetics during hot working of Ti-6Al-4V with a colony alpha microstructure. Materials Science and Engineering A 263 (2), 257.

Shafaat, M. A., Omidvar, H., Fallah, B., 2011. Prediction of hot compression flow curves of Ti–6Al–4V alloy in $\alpha + \beta$ phase region. Materials & Design 32 (10), 4689–4695.

Sun, Y., Zeng, W., Han, Y., Zhao, Y., Wang, G., Dargusch, M. S., Guo, P., 2011. Modeling the correlation between microstructure and the properties of the ti–6al–4v alloy based on an artificial neural network. Materials Science and Engineering: A 528 (29-30), 8757–8764.

Swarnakar, A. K., der Biest, O. V., Baufeld, B., 2011. Thermal expansion and lattice parameters of shaped metal deposited Ti–6Al–4V. Journal of Alloys and Compounds 509 (6), 2723–2728.

Tabei, A., Abed, F., Voyiadjis, G., Garmestani, H., 2017. Constitutive modeling of ti-6al-4v at a wide range of temperatures and strain rates. European Journal of Mechanics-A/Solids 63, 128–135.

Thomas, R. B., Nicolaou, P. D., Semiatin, S. L., 2005. An Experimental and Theoretical Investigation of the Effect of Local Colony Orientations and Misorientation on Cavitation during Hot Working of Ti-6Al-4V. Metallurgical and Materials Transactions A 36A (1), 129.

Wachtman, J. B., Tefft, W. E., Lam, D. G., Apstein, C. S., Jun 1961. Exponential Temperature Dependence of Young's Modulus for Several Oxides. Phys. Rev. 122, 1754–1759.

Williams, J. C., Lütjering, G., 2003. Titanium. Springer - Verlag.

Yu, W., Li, M., Luo, J., Su, S., Li, C., 2010. Prediction of the mechanical properties of the post-forged ti–6al–4v alloy using fuzzy neural network. Materials & Design 31 (7), 3282–3288.

Dislocation density based plasticity model applied to high strain rate deformation of Ti-6Al-4V

Authors:
Bijish Babu, Ales Svoboda, Ehsan Ghassemali, Lars-Erik Lindgren.

Paper to be submitted.

Dislocation density based flow stress model extended to high strain rate deformation of Ti-6Al-4V

Bijish Babu

Swerim AB, Box 812, SE-971 25, Luleå, Sweden

Ales Svoboda

Mechanics of Sold Materials, Luleå University of Technology, SE-971 87, Luleå, Sweden

Ehsan Ghassemali

School of Engineering, Jönköping University, P.O. Box 1026, SE-551 11, Jönköping, Sweden

Lars-Erik Lindgren

Mechanics of Solid Materials, Luleå University of Technology, SE-971 87, Luleå, Sweden

Abstract

One of the main challenges in the simulation of machining is accurately describing the material behavior during severe plastic deformation at strain rates ranging six orders of magnitude and temperature between $T_{room} - 0.9 T_{melt}$. High strain rate measurements are performed using Split-Hopkinson Pressure Bar (SHPB) technique at a range of temperatures. The temperature change during deformation is included by computing the plastic work converted to heat energy. A physics-based material model published earlier (Babu and Lindgren, 2013) is extended in this paper to include the high strain rate mechanisms of phonon and electron drag. Characterization of the microstructure is performed using Electron Backscatter Diffraction (EBSD) and a novel method to quantify the extent of globularization is also proposed which is compared with model predictions.

Keywords: Dislocation density, Vacancy concentration, Ti-6Al-4V, Phonon-drag, Electron-drag, Finite Element (FE), Split-Hopkinson Pressure Bar (SHPB), Electron Backscatter Diffraction (EBSD)

1. Introduction

Titanium alloys have remarkable properties such as high specific mechanical properties (viz. stiffness, strength, toughness, fatigue resistance), corrosion resistance and bio-compatibility (Leyens and Peters, 2003). These properties make them attractive for applications in aerospace, chemical industry, energy production, surgical implants, etc. Many of these applications have to satisfy high requirements on mechanical properties, which are directly affected by the microstructure (Williams and Lütjering, 2003). Therefore, it is important to understand and to model the microstructure evolution during manufacturing as well as in-service. Ti-6Al-4V was used in the present study with the specific task to improve the description of the material behavior within the context of machining simulations.

Machining involves high strain rate deformation in localized primary and secondary shear zones while the rest of the work-piece deforms at low strain rates. The deformation zones formed during orthogonal cutting is shown schematically in figure 1. The primary shear zone is where the significant shearing of the work-piece material occurs. The secondary shear zone lies adjacent to the tool-chip interface where shearing due to contact conditions takes place (Wedberg et al., 2012). The heat generation due to plastic work in the shear

---

zones does not have sufficient time to diffuse away leading to a temperature increase. The poor thermal diffusivity of Ti-6Al-4V aggravates this problem. During machining, the workpiece is subjected to extremely large strains (1-10), temperatures up to to $0.9T_{melt}$ and strain rates in the range $(10^3$ - $10^6)\text{s}^{-1}$(Guo, 2003). The relatively high flow strength at elevated temperature and enhanced work-hardenability of Ti-6Al-4V at high strain rates result in an immense tool force (Pramanik, 2014). This, combined with low elastic modulus gives a large workpiece deflection, (Olofson et al., 1965) which increases the demands on the machining system. Lindgren et al. (2016) reviewed the challenges involved in performing machining simulations. They have identified that describing the plastic behavior of the material realistically as a central pillar to achieve accuracy.

Various empirical approaches have been employed to model the deformation behavior of Ti-6Al-4V. The commonly used model by Johnson and Cook (1985) (JC), is of a curve-fitting nature and has a limited descriptive capability as it consists of multiplicative functions of strain, strain rate, and temperature. Meyer and Kleponis (2001) compared the JC and Zerilli and Armstrong (1987) (ZA) models for Ti-6Al-4V and concluded that ZA model gives a better correlation with measurements. A modified version of the JC model has been proposed by Seo et al. (2005) for high strain rate behavior of Ti-6Al-4V. A microstructure-based probabilistic framework was used by Przybyla and McDowell (2011) for Ti-6Al-4V to model fatigue crack formation. Khan and Yu (2012); Khan et al. (2012) developed an anisotropic yield criterion for Ti-6Al-4V.

Figure 1: The deformation zones.

However, models based on the physics of plastic deformation is assumed to have a better descriptive capability. Explicit dislocation dynamics based models are not practically feasible for manufacturing process simulations and therefore the concept of dislocation density, ρ (length of dislocations per unit volume) developed by (Kocks, 1966; Bergström, 1970; Bergström and Roberts, 1973; Roberts and Bergström, 1973; Kocks et al., 1975; Mecking and Estrin, 1980) is followed here. Bergström (1983) later classified ρ as ρ_{mobile} and $\rho_{immobile}$. This approach provides a representation of the average behavior of a large number of dislocations, grains, etc. Hence, the microstructure is not represented explicitly, but in an average sense. Estrin (1998) developed a unified elastic-viscoplastic constitutive model, based on dislocation density which was implemented in an FE software. Dislocation density based models for commercially pure Titanium were presented in Nemat-Nasser et al. (1999). Meyers et al. (2002) presented a review of physically based models for plasticity by dislocation glide as well as twinning. They also included the 'Hall-Petch' relationship and discussed high strain rate phenomena applicable for Ti-6Al-4V. Picu and Majorell (2002); Gao et al. (2011) have also developed variants of physics-based models specifically for Ti-6Al-4V.

In the current work, an existing physics-based material model (Babu and Lindgren, 2013) is extended to include the high strain rate mechanisms of phonon and electron drag. This viscous drag component will give additional flow strength to the material at strain rates above 10^3s^{-1}. Machining, the collision of vehicles, containment of turbine blades, etc, are examples of high strain rate processes where viscous drag effects becomes dominant. The proposed model includes dislocation density and excess vacancy concentration as internal state variables (ISV) which provides a bridge between various small-scale mechanisms and macro scale continuum mechanics. This model developed here can be implemented in any standard FE software that provides appropriate user interfaces. A novel method for quantitative estimation of the globularization fraction is developed in this work which is compared with predictions based on the model developed earlier (Babu and Lindgren, 2013).

2. Material and related deformation mechanisms

Ti-6Al-4V is a two-phase alloy consisting of 6 wt% Al that stabilizes the (α) phase; hexagonal closed packed (HCP) structure, and of 4 wt% V that stabilizes the (β) phase; body centric cubic (BCC) structure. The microstructure consists of roughly 91% (α) phase and remaining retained (β) phase at room temperature. The (α) phase transforms to (β) at approximately 990°C upon heating, depending on the precise composition of Al and V and other (α, β) stabilizing elements. The material used in this work was Grade 5 which is certified
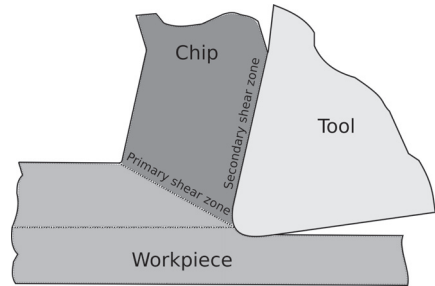
for the aerospace applications. The material was supplied as 8mm rolled rods by Harald Pihl AB. It has been checked for defects and has undergone annealing heat treatment for 1.5h at 700℃ followed by air cooling. The chemical composition is shown in Table 1.

Table 1: Chemical composition given in wt%. Remaining is Ti.

Al	V	O	Fe	C	H	N
6.02	4.07	0.152	0.0015	0.003	0.0012	0.01

The inelastic deformations of metals and alloys are mainly related to the motion of dislocation. Dislocations, vacancies, solutes, and precipitates are material defects that influence the motion of dislocations. The influence of those various factors on the strength and ductility of titanium alloys was studied by Conrad (1981). He identified dislocation glide and climb, which is assisted by diffusion, as mechanisms governing plastic flow. The dislocations, which are emitted from $\alpha - \beta$ phase interface, glide in basal planes rather than on prismatic planes because of its compatibility with the (HCP)-(BCC) interface (Castany et al., 2007; Salem and Semiatin, 2009). The α phase exhibits greater strength but lower ductility, compared to β phase. Many authors report globularization of the Ti-6Al-4V alloy at elevated temperature (Stefansson and Semiatin, 2003; Semiatin et al., 2005; Yeom et al., 2007; Zhao et al., 2007; Sargent et al., 2008; Park et al., 2008; Mironov et al., 2009). Bai et al. (2012), based on experimental evidence, demonstrated the mechanism of globularization and how it leads to flow softening. Babu and Lindgren (2013) have developed a model for globularization which is used here. The strain rate sensitivity of Ti-6Al-4V has an extra increase when the rates exceed approximately $10^3 s^{-1}$ (Lesuer et al., 2001). Phonon and electron drag was reported in several papers as a dominant deformation mechanism during the high strain rate response of materials; see (Frost and Ashby, 1982; Regazzoni et al., 1987).

Twinning is a deformation mechanism in HCP materials with its response depending on the fraction of twins formed. However, Ti alloyed with 6% Al (α phase) does not twin even at a low temperature such as -173℃; Paton et al. (1976). Under high strain rate loading ($5000s^{-1}$) at room temperature, twins have been observed to form preferentially in the large α grains in Ti-6Al-4V, (Follansbee and Gray, 1989). Increasing temperature above 200℃ inhibited twinning at all investigated strain rates. EBSD scans of specimens analyzed in the current work did not show any evidence of twin boundaries and therefore the constitutive model presented here does not account for twinning.

3. Experimental procedures

In most high strain rate manufacturing processes, high strain rate deformation is concentrated in narrow shear bands while the rest of the material deforms at low strain rates. Therefore, the model has to work with both low and high strain rates at varying temperatures. The Gleeble™ thermo-mechanical simulator was used for low strain rates compression tests. Within the range between 0.001s^{-1} and 1.0 s^{-1}, compression tests were performed at the initial temperatures of 20 to 1100°C. Detailed description of the experimental program and tests results are presented in Babu and Lindgren (2013). In the present study, this test program is extended by including high strain rate testing with a total range of validity between (0.001 - 9000)s^{-1}.

3.1. Mechanical characterization

The Split-Hopkinson Pressure Bar (SHPB) method is commonly used when determining the inelastic response of materials at high strain rates. SHPB testing is based on longitudinal elastic stress wave propagation through bars where a mechanical impact initiates stress waves. Characteristics of SHPB testing are that the impact velocity of the striker and the length of specimens affect both strain and strain rates.

In the presented work, the testing was performed over a broad range of strain rates and temperatures on cylindrical specimens with 8mm diameter and 4mm height . The tested strain rates were approximately 2000, 5000, and 9000s^{-1}. The initial temperature for each strain rate level were 20, 200, 400, 600, 800, 850, 900 and 950℃. Tests at elevated initial temperature were performed using a moving arm loaded with the specimen. The arm was pushed into a stand-alone furnace. After the desired temperature was reached, the specimen was placed between the incident and the transmitting bars, but still without any contact to prevent thermal gradients in the specimen. Just before the stress wave reached the interface between the incident bar and the specimen, the transmitting bar was pushed towards the specimen establishing contact. During deformation, the temperature of the specimen was further increased due to dissipative work. A detailed description of the equipment used in this work is given in Apostol et al. (2003).

3.2. Microstructural characterization

The cylindrical/disk samples were cut into half along the specimen's axis. Microstructural analysis was carried out at the middle of the cross section for all samples. This location was selected based on the assumption that the amount of deformation was comparable between test specimens and is homogeneous. The cross sections were mounted and ground using SiC paper followed by polishing using fine colloidal silica suspension. In order to reduce the subsurface deformation during sample preparation, in the last polishing step, 20% of H_2O_2 was added to the polishing suspension.

A field emission SEM (JSM7001F), equipped with an EBSD detector combined with the TSL (OIMA, v. 8.0) analysis software was used for microstructural investigations. A small beam diameter was aligned and selected in the SEM, which is accelerated at 15kV to resolve small features even at highly deformed areas. A high-speed Hikari camera was used for pattern acquisition at binning of 4x4, which provided a proper successful indexing rate and indexing speed. Data were recorded at $0.09\mu m$ step size. The Hough transform parameters were optimized to achieve the best angular resolution. Only one clean-up procedure was done on the EBSD data and pixels with CI$\geq$0.1 are presented.

4. Formulation of the constitutive model

Basic equations of the model are shown in the next section. Details of the model including experimental procedures and parameter optimization are to be found in Lindgren et al. (2008) for low strain rate applications, and modeling of high strain phenomena is presented in Wedberg and Lindgren (2015) for AISI 316L. A dislocation density model for plastic deformation and globularization of Ti-6Al-4V was developed by Babu and Lindgren (2013) and is the basis for the current extension.

4.1. Flow stress model

An in-compressible von Mises model is used here with the assumption of isotropic plasticity. The flow stress is split into three parts (Seeger, 1956; Bergström, 1969; Kocks, 1976; Babu and Lindgren, 2013),

$$\sigma_y = \sigma_G + \sigma^* + \sigma_{drag} \tag{1}$$

where, σ_G is the a-thermal stress contribution from the long-range interactions of the dislocation substructure. The second term σ^*, is the stress needed to move dislocations through the lattice and to pass short-range obstacles. This formulation is very much in accordance with the material behavior demonstrated by Conrad (1981). At very high strain rates ($> 10^3 s^{-1}$), deformation rate of Ti-6Al-4V is controlled by the phonon and electron drag on moving dislocations (Lesuer, 2000). The viscous drag component of stress σ_{drag} can be computed based on a formulation proposed by Ferguson et al. (1967) and later developed by Frost and Ashby (1982).

4.1.1. Long range contribution:

The long-range term from equation (1) is derived by Seeger (1956) as,

$$\sigma_G = m\alpha Gb\sqrt{\rho_i} \tag{2}$$

where m is the Taylor orientation factor translating the effect of the resolved shear stress in different slip systems into effective stress and strain quantities. Furthermore, α is a proportionality factor, b is the magnitude of Burgers vector, G is the temperature dependent shear modulus and ρ_i is the immobile dislocation density.

4.1.2. Short range contribution:

The strength of obstacles, which a dislocation encounters during its motion determines the dependence of flow strength on applied strain rate. The dislocation velocity is related to the plastic strain rate via the Orowan equation (Orowan, 1948)

$$\dot{\varepsilon}^p = \frac{\rho_m b\bar{\nu}}{m} \tag{3}$$

where $\bar{\nu}$ is the average velocity of mobile dislocations (ρ_m). This velocity is related to the time taken for a dislocation to pass an obstacle. It is assumed that the time to travel between two obstacles is negligible compared with the waiting time at the obstacle. This waiting time is related to the probability ($e^{-\Delta G/kT}$) that the thermal vibrations assist the dislocation in overcoming the obstacle. Here, ΔG is the activation energy, k

4

is the Boltzmann constant and T is the temperature in kelvin. The velocity of dislocation motion is written according to Frost and Ashby (1982) as,

$$\bar{\nu} = \Lambda \nu_a e^{-\Delta G/kT} \tag{4}$$

where Λ is the mean free path and ν_a is the attempt frequency. The Orowan equation can be rewritten as,

$$\dot{\bar{\varepsilon}}^p = f e^{-\Delta G/kT} \tag{5}$$

The form of the function f and ΔG depends on the applied stress, the strength of obstacles etc. The stress available to move a dislocation past an obstacle is the difference between applied stress and the long-range flow stress component. Here ΔG is the free energy of activation which can be written according to Kocks et al. (1975) as

$$\Delta G = \Delta F \left[1 - \left(\frac{\sigma^*}{\sigma_{ath}} \right)^p \right]^q \tag{6}$$
$$0 \le p \le 1$$
$$1 \le q \le 2$$

Here, $\Delta F = \Delta f_0 G b^3$ is the activation energy necessary to overcome lattice resistance in the absence of any external force and $\sigma_{ath} = \tau_0 G$ is the shear strength in the absence of thermal energy. The parameters p and q determine the shape of the barrier which can be either sinusoidal, hyperbolic, or somewhere in between. Some guidelines for selection of Δf_0 and τ_0 are given in (Frost and Ashby, 1982).

The strain rate dependent part of the yield stress from equation 1 can be derived according to the Kocks-Mecking formulation (Kocks et al., 1975; Mecking and Kocks, 1981) as

$$\sigma^* = \tau_0 G \left[1 - \left[\frac{kT}{\Delta f_0 G b^3} \ln \left(\frac{\dot{\varepsilon}^{ref}}{\dot{\bar{\varepsilon}}^p} \right) \right]^{1/q} \right]^{1/p} \tag{7}$$

Here $\dot{\varepsilon}^{ref}$ is a reference strain rate.

4.1.3. Phonon and electron drag contribution:

At strain rates greater than $1e^3 s^{-1}$, the interaction of moving dislocations with phonons and electrons can limit dislocation velocity. The strength of interaction is measured by the drag coefficient B with $\frac{Ns}{m^2}$ as its unit. As the temperature increases, phonon density rises and B increases linearly with temperature.

$$B = B_e + B_p \frac{T}{300} \tag{8}$$

where B_e is the electron drag coefficient and B_p is the phonon drag coefficient at temperature $300K$; (Frost and Ashby, 1982). Average dislocation velocity can be defined as

$$v = \frac{\sigma_{drag} b}{B} \tag{9}$$

Introducing the Orowan equation and combining with equation 9, (Frost and Ashby, 1982) proposed a rate equation where the drag coefficients characterize the opposing forces.

$$\dot{\bar{\varepsilon}} = \frac{\rho_m b^2 G \frac{1}{B_p}}{\frac{B_e}{B_p} + \frac{T}{300}} \left(\frac{\sigma_{drag}}{G} \right) \tag{10}$$

Rewriting equation 10, stress component σ_{drag} accounting for electron and phonon drag is derived as,

$$\sigma_{drag} = G \left(\frac{\frac{B_e}{B_p} + \frac{T}{300}}{C_{drag}} \right) \dot{\bar{\varepsilon}}^p \tag{11}$$

where C_{drag} and $\frac{Be}{Bp}$ are calibration parameters.

4.2. Evolution of immobile dislocation density

The basic components of the yield stress in equation 1 are obtained from equations 2, 7 and 11. However, the evolution of ρ_i in equation 2 needs to be computed. The model for the evolution of the immobile dislocation density has two parts; hardening and restoration.

$$\dot{\rho}_i = \dot{\rho}_i^{(+)} - \dot{\rho}_i^{(-)} \tag{12}$$

4.2.1. Hardening process

It is assumed that mobile dislocations move, on average, a distance Λ (mean free path), before they are immobilized or annihilated. According to the Orowan equation, the density of mobile dislocations and their average velocity are proportional to the plastic strain rate. It is reasonable to assume that an increase in immobile dislocation density also follows the same relation. Thus the pile-up of immobile dislocation density can be written as,

$$\dot{\rho}_i^{(+)} = \frac{m}{b}\frac{1}{\Lambda}\dot{\bar{\varepsilon}}^p \tag{13}$$

The mean free path can be computed from the grain size (g) and dislocation sub-cell or sub-grain diameter (s) as,

$$\frac{1}{\Lambda} = \left(\frac{1}{g} + \frac{1}{s}\right) \tag{14}$$

The formation and evolution of sub-cells have been modeled using a relation proposed by Holt (1970).

$$s = K_c\frac{1}{\sqrt{\rho_i}} \tag{15}$$

The current grain size g in equation 14 is calculated using grain growth model written in incremental form as,

$$g^{i+1} = g^i + \dot{g}^i\Delta t \quad \text{where} \quad \dot{g}^i = \frac{K}{ng^{i(n-1)}} \tag{16}$$

where, $g^{i=1} = g_0$, the initial grain size, K and n are material parameters, Δt is the time step size, and i is the increment number.

4.2.2. Restoration processes

The motion of vacancies is related to the recovery of dislocations. Recovery usually occurs at elevated temperatures and therefore is a thermally activated reorganization process. The creation of vacancies increases entropy but requires energy and its concentration increases with temperature and deformation. In high stacking fault materials, recovery process might balance the effects of strain hardening leading to constant flow stress. The primary mechanisms of restoration are dislocation glide, dislocation climb, and globularization.

$$\dot{\rho}_i^{(-)} = \dot{\rho}_i^{(glide)} + \dot{\rho}_i^{(climb)} + \dot{\rho}_i^{(globularization)} \tag{17}$$

The model for recovery by glide can be written based on the formulation by Bergström (1983) as,

$$\dot{\rho}_i^{(glide)} = \Omega\rho_i\dot{\bar{\varepsilon}}^p \tag{18}$$

where Ω is a function dependent on temperature. Militzer et al. (1994) proposed a model for dislocation climb based on Sandstrom and Lagneborg (1975) and Mecking and Estrin (1980). With a modification of the diffusivity according to Babu and Lindgren (2013), the model can be written as,

$$\dot{\rho}_i^{(climb)} = 2c_\gamma D_{app}\frac{Gb^3}{kT}\left(\rho_i^2 - \rho_{eq}^2\right) \tag{19}$$

where, c_γ is a material coefficient and ρ_{eq} is the equilibrium value of the dislocation density.

Here, D_{app} is the apparent diffusivity which includes the diffusivity of $\alpha-\beta$ phases weighted by their fractions X_α and X_β in addition to pipe diffusion D_p, as well as effects of vacancy concentration c_v. Lattice diffusivity can be written as

$$D_l = \frac{c_v}{c_v^{eq}}\left[D_\alpha \cdot X_\alpha + D_\beta \cdot X_\beta\right] \tag{20}$$

Diffusion through dislocation pipes can be written as,

$$D_p = D_{p0} e^{-\frac{Q_p}{kT}} \tag{21}$$

where, D_{p0} is the frequency factor and Q_p is the activation energy. The total diffusive flux in the material is enhanced by the short circuit diffusion, which is dependent on the relative cross-sectional area of pipe and matrix, (parameter N in equation 22). According to the model proposed by Porter and Easterling (1992); Militzer et al. (1994), the apparent diffusivity can be written as

$$
\begin{aligned}
D_{app} &= D_l + N D_p \\
N &= \frac{n_a^p n_\rho}{N_a^l}
\end{aligned}
\tag{22}
$$

where, n_a^p is the number of atoms that can fill the cross-sectional area of a dislocation, n_ρ is the number of dislocations intersecting a unit area $(= \rho_i)$ and N_a^l is the number of atoms per unit area of the lattice.

A model for the evolution of dislocation density during globularization is proposed in Babu and Lindgren (2013). According to this model, the effect of grain growth on the reduction of flow stress is included only when the stored deformation energy is above a critical value.

$$
\begin{aligned}
\text{if} \quad & \rho_i \geq \rho_{cr} \\
& \dot{\rho}_i{}^{(globularization)} = \psi \dot{X}_g \left(\rho_i - \rho_{eq} \right); \quad \text{until } \rho_i \leq \rho_{eq} \\
\text{else} \quad & \\
& \dot{\rho}_i{}^{(globularization)} = 0
\end{aligned}
\tag{23}
$$

Here, ρ_{cr} is the critical dislocation density above which globularization is initiated, ρ_{eq} is the equilibrium value of dislocation density, $\dot{X}_g$ is the globularization rate and ψ is a calibration constant. The mechanism of globularization can be modeled as a two-stage process of dynamic and static recrystallization described by Thomas and Semiatin (2006).

$$X_g = X_d + (1 - X_d) X_s \tag{24}$$

Here, the volume fractions X_g, X_d and X_s denote total globularized, its dynamic component and the static component, respectively. Assuming that grain growth and static recrystallization have the same driving force, the static globularization rate can be written as (Pietrzyk and Jedrzejewski, 2001; Montheillet and Jonas, 2009),

$$\dot{X}_s = M \frac{\dot{g}}{g} \tag{25}$$

where, M is a material parameter. The rate of dynamic globularization is modeled based on Thomas and Semiatin (2006) as,

$$\dot{X}_d = \frac{B k_p \dot{\bar{\varepsilon}}_p}{\bar{\varepsilon}_p{}^{1-k_p} e^{B \bar{\varepsilon}_p^{k_p}}} \tag{26}$$

where, B and k_p are material parameters.

4.3. Evolution of excess vacancy concentration

Militzer et al. (1994) proposed a model for excess vacancy concentration with generation and annihilation components. Assuming that only long-range stress contributes to vacancy formation and introducing a component for temperature change, the Militzer model can be rewritten as,

$$
\begin{aligned}
\dot{c_v}^{ex} = \quad & \left[\chi \frac{m \alpha G b^2 \sqrt{\rho_i}}{Q_{vf}} + \zeta \frac{c_j}{4b^2} \right] \frac{\Omega_0}{b} \dot{\bar{\varepsilon}} - D_{vm} \left[\frac{1}{s^2} + \frac{1}{g^2} \right] (c_v - c_v^{eq}) \\
& + c_v^{eq} \left(\frac{Q_{vf}}{kT^2} \right) \dot{T}
\end{aligned}
\tag{27}
$$

Here, $\chi = 0.1$ is the fraction of mechanical energy spent on vacancy generation, Ω_0 is the atomic volume and ζ is the neutralization effect by vacancy emitting and absorbing jogs. The concentration of jogs (c_j) and D_{vm}, the diffusivity of vacancy are given in Babu and Lindgren (2013). Additionally, Q_{vf} is the activation energy of vacancy formation.

Parameter	Dimension	Value	Reference
T_{melt}	℃	1600	[6]
$T_{\beta-transus}$	℃	890	[6]
k	JK^{-1}	$1.38 \cdot 10^{-23}$	[6]
b	m	$2.95 \cdot 10^{-10}$	[1]
$D_{\alpha 0}$	m^2s^{-1}	$5 \cdot 10^{-6}$	[4]
$D_{\beta 0}$	m^2s^{-1}	$3 \cdot 10^{-7}$	[4]
Q_{vf}	J	$1.9 \cdot 10^{-19}$	[2]
Q_{vm}	J	$2.49 \cdot 10^{-19}$	[1]
Q_{β}	J	$2.5 \cdot 10^{-19}$	[4]
Q_p	J	$1.61 \cdot 10^{-19}$	[1]
n_a^p	–	2	[6]
n_{ρ}	–	ρ_i	[6]
Ω_0	m^3	$1.76 \cdot 10^{-29}$	[1]
g_0	m	$2 \cdot 10^{-6}$	[6]
n	–	3	[5]
$\dot{\varepsilon}_{ref}$	s^{-1}	10^6	[1]
ΔS_{vm}	JK^{-1}	$1.38 \cdot 10^{-23}$	[7]

[a]Frost and Ashby (1982)
[b]Novikov et al. (1980)
[c]Conrad (1981)
[d]Mishin and Herzig (2000)
[e]Sargent et al. (2008)
[f]Calculated or Measured Value
[g]Hernan et al. (2005)

Table 2: Parameters for the model from literature.

T [℃]	20	200	400	600	800	900	1000
α	2.30	1.90	2.10	1.70	1.00	1.15	1.20
Ω [10]	3.80	4.00	4.70	4.00	4.00	4.00	3.60
C_{γ} $[10^{-1}]$	0.00	0.00	0.00	4.00	5.00	0.50	1.00
K_c $[10^2]$	0.40	0.40	0.40	0.40	1.20	1.20	1.20
τ_0 $[10^{-1}]$	0.19	0.21	0.20	0.75	2.13	1.54	1.34
Δf_0	0.44	0.38	0.45	0.59	1.36	1.93	1.90
ρ_i^{init} $[10^{14}]$	1.00	1.00	1.00	0.70	0.10	0.10	0.01
ρ_i^{crit} $[10^{14}]$	5.00	5.00	2.20	1.50	0.20	0.20	0.10
B	1.00	1.00	0.50	0.50	0.50	0.10	0.01
k_p	2.00	2.00	2.00	1.00	2.00	2.00	2.00
M $[10^2]$	0.00	0.00	0.00	6.00	6.00	6.00	6.00
ψ	0.00	0.00	0.05	0.60	8.00	1.00	1.00
K $[10^{-1}]$	0.00	0.00	0.00	0.25	8.00	8.00	8.00

Table 3: Calibrated temperature-dependent parameters of the model.

Parameter	Dimension	Value
D_{p0}	m^2s^{-1}	10^{-8}
N_a^l	–	10^{19}
p	–	0.3
q	–	1.8
ρ_{eq}	m^{-2}	10^{10}
C_{drag}	–	$1.16 \cdot 10^7$
$\frac{B_e}{B_p}$	–	0.19

Table 4: Calibrated parameters of the model.

5. Calibration of model

Calibration using an in-house Matlab™ based software obtained the parameters for the model. This software uses constrained minimization routine in Matlab™ and can handle multiple experiments for optimization. The model is calibrated using data from high strain rate tests at $(2000 - 9000)s^{-1}$ All parameters for dislocation model presented in Babu and Lindgren (2013), were used as initial values. In the first step, the parameters of high strain rate model B_e, B_p and C_{drag}, were optimized by keeping initial values fixed. Constant parameters for the model are presented in Table 2, calibrated temperature dependent parameters of the model are shown in Table 3 and finally calibrated temperature independent parameters are presented in Table 4. Four parameters, Ω, τ_0, Δf_0, and M highlighted in grey in table 3 were modified with respect to the original model in Babu and Lindgren (2013).

6. Results from microstructural characterization

Specimens deformed at $2000s^{-1}$ are selected for microscopic characterization. Attempts to repeat the tests for higher strain rates gave only limited success owing to the visible localization of the deformation. High strain rate tests also resulted in higher total deformation which increases the localization as compared to $2000s^{-1}$. Kernel average misorientation (KAM) maps show the localized plastic strain (dislocation density) present in the microstructure qualitatively. The blue regions in the KAM maps (5a), represent areas with the lowest dislocation density/plastic strain and white regions are non-indexed areas. With deformation, the density of these blue regions decreased, implying the increased density of dislocations in the microstructure (figure 2). Inverse pole figure maps and texture analysis did not show any particular texture due to deformation at the observed regions.

6.1. Quantification of globularization

During deformation, the lamellar microstructure is fragmented by the formation of kinks (Park et al., 2008; Mironov et al., 2009). Globularization occurs at these kinked alpha plates where some grains grow and become
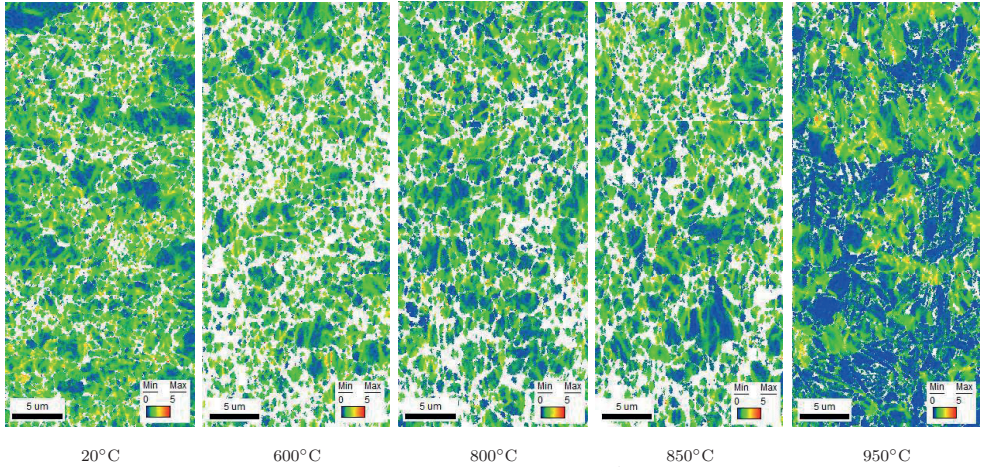
Figure 2: KAM maps ($\dot{\varepsilon} = 2000s^{-1}$).

globular subsequently reducing the aspect ratios. These phenomena are shown in the schematic diagram described in figure 3. Quantification of globularization has been attempted by many authors (Shell and Semiatin, 1999; Semiatin et al., 1999; Poths et al., 2004; Kedia et al., 2018). These works have been based on analysing the images using ImageJ software (Schneider et al., 2012) and estimating the globularization by measuring the aspect ratios of the lamellae. Grains with aspect ratios less than 2.0 are accounted as fully globularized. However, the drawback with this technique is that it requires manual intervention in sample etching, and image enhancement and therefore is qualitative. In the current work, a numerical algorithm is created based on the results from EBSD to quantify the extent of globularization. Applying the high angle grain boundary (HAGB)
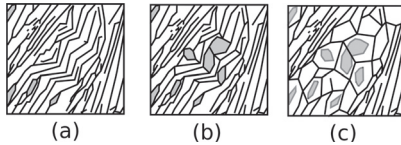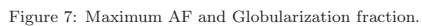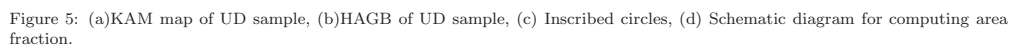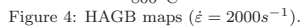

Figure 3: Schematic diagram of globularization: (a) Lamella kinking (b) Fragmentation (c) Grain growth.

misorientation threshold of 15˚, grain boundaries are identified as shown in figures 4 and 5b. Circles are inscribed within the grain starting from the largest diameter and progressively reducing diameter in steps (See figure 5c). Area fraction (AF) is the ratio of total area covered by circles to the total area of the analyzed region as shown in figure 5d and equation 28.

$$AF = \frac{0.25\pi}{x \cdot y} \sum_{i=1}^{n} D_i^2 \tag{28}$$

The size distribution of circles inscribed in a 2D slice is not the same as the size distribution of spheres in 3D. Their relationship can be computed with knowing or assuming the shape of the distribution of the spheres in 3D. However, in the current case, the attempt is only made to compare different test cases and not to measure the absolute grain sizes. The cumulative area fractions starting from high to low diameter of the specimens deformed at $2000s^{-1}$ are shown in figure 6. Figure 5a shows the KAM map of the un-deformed (UD) sample and the overwhelmingly blue-green regions show that the specimen is fully annealed. The maximum value of the cumulative area fraction (MAF) from figure 6 is used to estimate the globularization fraction shown in figure 7. We assumed that the sample deformed at 20℃ has undergone no globularization and the undeformed sample which has undergone mill-anneal heat treatment is fully globularized. A relative globularization fraction is estimated and is shown in figure 7. The predictions of globularization fraction for both $2000s^{-1}$ and $9000s^{-1}$ are also given in figure 7.

9

Figure 4: HAGB maps ($\dot{\varepsilon} = 2000s^{-1}$).

Figure 5: (a)KAM map of UD sample, (b)HAGB of UD sample, (c) Inscribed circles, (d) Schematic diagram for computing area fraction.

Figure 6: Inscribed Circle AF ($\dot{\varepsilon} = 2000s^{-1}$).

Figure 7: Maximum AF and Globularization fraction.

7. Results for calibrated flow stress model

The comparison of experiments and model showing the σ-ε curves at different temperature and strain-rates are shown in figures 8a - 8f. Here, figures 8a - 8c show the comparison of the current model with tests performed at low strain rates in Babu and Lindgren (2013).
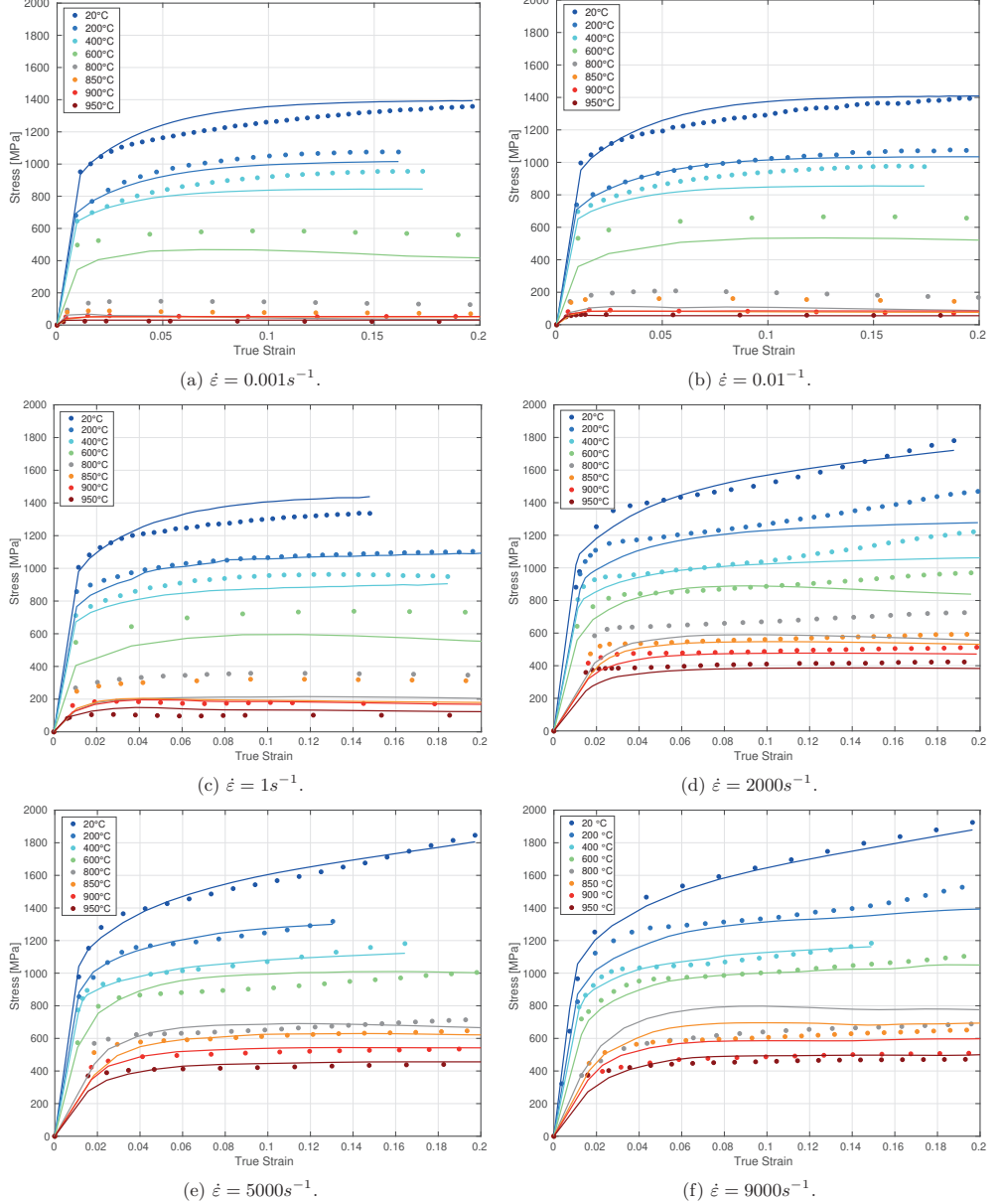

(a) $\dot{\varepsilon} = 0.001 s^{-1}$.

(b) $\dot{\varepsilon} = 0.01^{-1}$.

(c) $\dot{\varepsilon} = 1 s^{-1}$.

(d) $\dot{\varepsilon} = 2000 s^{-1}$.

(e) $\dot{\varepsilon} = 5000 s^{-1}$.

(f) $\dot{\varepsilon} = 9000 s^{-1}$.

Figure 8: Stress vs Strain curves.

8. Discussions and conclusions

This article presents a calibrated thermo-mechanical model for the high strain-rate behavior of Ti-6Al-4V alloy to be used in simulations of machining or other high strain rate processes. This work builds on and extends the earlier article by Babu and Lindgren (2013) for low strain-rate behavior. Owing to the clear physics-based framework, the inclusion of an additional mechanism for dislocation drag was relatively easy. Though the low strain rates tests were performed using Ti-6Al-4V with very similar composition, it was heat treated at 790℃ for 6h resulting in a different starting microstructure when compared with the material for high strain rate testing. This can be attributed to the need for re-calibrating certain parameters and the sub-optimal fit between 600℃ - 850℃ at low strain rates. A novel method based on EBSD to quantify the extent of globularization is developed here. The measured globularization fraction and the model predictions are in good agreement. Although, this model has only been calibrated below the $\alpha - \beta$ transition temperature (≈ 980℃), it can be extended to include arbitrary phase composition. The flow stress model is formulated in a way that it can be implemented in any standard finite element software that allows implementing user-defined yield surface.

9. Acknowledgments

References

Apostol, M., Vuoristo, T., Kuokkala, V.T., 2003. High temperature high strain rate testing with a compressive SHPB, in: Journal de Physique IV (Proceedings), EDP sciences. pp. 459–464.

Babu, B., Lindgren, L.E., 2013. Dislocation density based model for plastic deformation and globularization of Ti-6Al-4V. International Journal of Plasticity 50, 94–108.

Bai, Q., Lin, J., Dean, T., Balint, D., Gao, T., Zhang, Z., 2012. Modelling of dominant softening mechanisms for Ti-6Al-4V in steady state hot forming conditions. Materials Science and Engineering: A , 352–358.

Bergström, Y., 1969. Dislocation model for the stress-strain behaviour of polycrystalline alpha-iron with special emphasis on the variation of the densities of mobile and immobile dislocations. Materials Science & Engineering 5, 193–200.

Bergström, Y., 1970. A dislocation model for the stress-strain behaviour of polycrystalline [alpha]-Fe with special emphasis on the variation of the densities of mobile and immobile dislocations. Materials Science and Engineering 5, 193–200.

Bergström, Y., 1983. The plastic deformation of metals - A dislocation model and its applicability. Reviews on Powder Metallurgy and Physical Ceramics , 79–265.

Bergström, Y., Roberts, W., 1973. The dynamical strain ageing of [alpha]-iron: Effects of strain rate and nitrogen content in the jerky-flow region. Acta Metallurgica 21, 741–745.

Castany, P., Pettinari-Sturmel, F., Crestou, J., Douin, J., Coujou, A., 2007. Experimental study of dislocation mobility in a Ti-6Al-4V alloy. Acta Materialia 55, 6284–6291.

Conrad, H., 1981. Effect of interstitial solutes on the strength and ductility of titanium. Progress in Materials Science 26, 123–403.

Estrin, Y., 1998. Dislocation theory based constitutive modelling: foundations and applications. Journal of Materials Processing Technology 80-81, 33.

Ferguson, W., Kumar, A., Dorn, J., 1967. Dislocation damping in aluminum at high strain rates. Journal of Applied Physics 38, 1863–1869.

Follansbee, P.S., Gray, G.T., 1989. An analysis of the low temperature, low and high strain rate deformation of Ti-6Al-4V. Metallurgical Transactions A 20, 863–874.

Frost, H.J., Ashby, M.F., 1982. Deformation-Mechanism Maps: The Plasticity and Creep of Metals and Ceramics. Paperback.

Gao, C., Zhang, L., Yan, H., 2011. A new constitutive model for HCP metals. Materials Science and Engineering: A 528, 4445–4452.

Guo, Y., 2003. An integral method to determine the mechanical behavior of materials in metal cutting. Journal of Materials Processing Technology 142, 72–81.

Hernan, R.D., Maria, G.L., Maria, M.A., 2005. Self-diffusion in the hexagonal structure of Zirconium and Hafnium: computer simulation studies. Materials Research 8, 431–434.

Holt, D.L., 1970. Dislocation cell formation in metals. Journal of applied physics 41, 3197.

Johnson, G.R., Cook, W.H., 1985. Fracture characteristics of three metals subjected to various strains, strain rates, temperatures and pressures. Engineering Fracture Mechanics 21, 31–48.

Kedia, B., Balasundar, I., Raghu, T., 2018. Globularisation of α lamellae in titanium alloy: Effect of strain, strain path and starting microstructure. Transactions of the Indian Institute of Metals 71, 1791–1801.

Khan, A.S., Yu, S., 2012. Deformation induced anisotropic responses of Ti-6Al-4V alloy. Part I: Experiments. International Journal of Plasticity 38, 1–13.

Khan, A.S., Yu, S., Liu, H., 2012. Deformation induced anisotropic responses of Ti-6Al-4V alloy Part II: A strain rate and temperature dependent anisotropic yield criterion. International Journal of Plasticity 38, 14–26.

Kocks, U., 1976. Laws for Work-Hardening and Low-Temperature Creep. Journal of Engineering Materials and Technology, Transactions of the ASME 98 Ser H, 76–85.

Kocks, U.F., 1966. A statistical theory of flow stress and work-hardening. Philosophical Magazine 13, 541–566.

Kocks, U.F., Argon, A.S., Ashby, M.F., 1975. Thermodynamics and Kinetics of Slip. volume 19 of *Progress in Material Science*. Pergamon Press.

Lesuer, D.R., 2000. Experimental Investigations of Material Models for Ti-6Al-4V Titanium and 2024-T3 Aluminum.

Lesuer, D.R., Kay, G., LeBlanc, M., 2001. Modeling large-strain, high-rate deformation in metals. Technical Report. Lawrence Livermore National Lab., CA (US).

Leyens, C., Peters, M., 2003. Titanium and titanium alloys: fundamentals and applications. John Wiley & Sons.

Lindgren, L.E., Domkin, K., Sofia, H., 2008. Dislocations, vacancies and solute diffusion in physical based plasticity model for AISI 316L. Mechanics of Materials 40, 907–919.

Lindgren, L.E., Svoboda, A., Wedberg, D., Lundblad, M., 2016. Towards predictive simulations of machining. Comptes Rendus Mécanique 344, 284–295. Computational simulation of manufacturing processes.

Mecking, H., Estrin, Y., 1980. The effect of vacancy generation on plastic deformation. Scripta Metallurgica 14, 815.

Mecking, H., Kocks, U., 1981. Kinetics of flow and strain-hardening. Acta Metallurgica 29, 1865–1875.

Meyer, J.H.W., Kleponis, D.S., 2001. Modeling the high strain rate behavior of titanium undergoing ballistic impact and penetration. International Journal of Impact Engineering 26, 509–521.

Meyers, M.A., Benson, D., Vöhringer, O., Kad, Q.X.B., Fu, H.H., 2002. Constitutive description of dynamic deformation: physically-based mechanisms. Materials Science and Engineering A 322, 194–216.

Militzer, M., Sun, W.P., Jonas, J.J., 1994. Modelling the effect of deformation-induced vacancies on segregation and precipitation. Acta Metallurgica et Materialia 42, 133.

Mironov, S., Murzinova, M., Zherebtsov, S., Salishchev, G., Semiatin, S., 2009. Microstructure evolution during warm working of Ti-6Al-4V with a colony-alpha microstructure. Acta Materialia 57, 2470–2481.

Mishin, Y., Herzig, C., 2000. Diffusion in the Ti-Al system. Acta Materialia 48, 589–623.

Montheillet, F., Jonas, J.J., 2009. Fundamentals of Modeling for Metals Processing. ASM International, Materials Park, Ohio 44073-0002. volume 22A of *ASM Handbook*. chapter 17: Models of Recrystallization. pp. 220–231.

Nemat-Nasser, S., Guo, W.G., Cheng, J.Y., 1999. Mechanical properties and deformation mechanisms of a commercially pure titanium. Acta Materialia 47, 3705.

Novikov, I.I., Roshchupkin, V.V., Semashko, N.A., Fordeeva, L.K., 1980. Experimental investigation of vacancy effects in pure metals. Journal of Engineering Physics and Thermophysics V39, 1316.

Olofson, C., Gerds, A., Boulger, F., Gurklis, J., 1965. Machining of Titanium Alloys. DMIC memorandum, Battelle Memorial Institute, Defense Metals Information Center.

Orowan, E., 1948. in: Symposium on Internal Stresses in Metals and Alloys, Institute of Metals. p. 451.

Park, C.H., Park, K.T., Shin, D.H., Lee, C.S., 2008. Microstructural Mechanisms during Dynamic Globularization of Ti-6Al-4V Alloy. Materials Transactions 49, 2196–2200.

Paton, N., Baggerly, R., Williams, J., 1976. Deformation and Solid Solution Strengthening of Titanium-Aluminum Single Crystals. Technical Report. Rockwell International Thousand Oaks California Science Center.

Picu, R.C., Majorell, A., 2002. Mechanical behavior of Ti-6Al-4V at high and moderate temperatures–Part II: constitutive modeling. Materials Science and Engineering A 326, 306–316.

Pietrzyk, M., Jedrzejewski, J., 2001. Identification of Parameters in the History Dependent Constitutive Model for Steels. CIRP Annals - Manufacturing Technology 50, 161–164.

Porter, D.A., Easterling, K.E., 1992. Phase Transformations in Metals and Alloys. CRC Press. 2 edition.

Poths, R.M., Wynne, B., Rainforth, W., Beynon, J., Angella, G., Semiatin, S., 2004. Effect of strain reversal on the dynamic spheroidization of ti-6al-4v during hot deformation. Metallurgical and Materials Transactions A 35, 2993–3001.

Pramanik, A., 2014. Problems and solutions in machining of titanium alloys. The International Journal of Advanced Manufacturing Technology 70, 919–928.

Przybyla, C.P., McDowell, D.L., 2011. Simulated microstructure-sensitive extreme value probabilities for high cycle fatigue of duplex Ti–6Al–4V. International Journal of Plasticity 27, 1871–1895.

Regazzoni, G., Johnston, J., Follansbee, P., 1987. Theoretical study of the dynamic tensile test. Journal of Applied Mechanics, Transactions ASME 53, 519–528.

Roberts, W., Bergström, Y., 1973. The stress-strain behaviour of single crystals and polycrystals of face-centered cubic metals–a new dislocation treatment. Acta Metallurgica 21, 457–469.

Salem, A., Semiatin, S., 2009. Anisotropy of the hot plastic deformation of Ti-6Al-4V single-colony samples. Materials Science and Engineering: A 508, 114–120.

Sandstrom, R., Lagneborg, R., 1975. A model for hot working occurring by recrystallization. Acta Metallurgica 23, 387.

Sargent, G., Zane, A., Fagin, P., Ghosh, A., Semiatin, S., 2008. Low-Temperature Coarsening and Plastic Flow Behavior of an Alpha/Beta Titanium Billet Material with an Ultrafine Microstructure. Metallurgical and Materials Transactions A 39, 2949–2964.

Schneider, C.A., Rasband, W.S., Eliceiri, K.W., 2012. Nih image to imagej: 25 years of image analysis. Nature methods 9, 671.

Seeger, A., 1956. The mechanism of Glide and Work Hardening in FCC and HCP Metals, in: Fisher, J., Johnston, W.G., Thomson, R., Vreeland, T.J. (Eds.), Dislocations and Mechanical Properties of Crystals, pp. 243–329.

Semiatin, S.L., Seetharaman, V., Weiss, I., 1999. Flow behavior and globularization kinetics during hot working of Ti-6Al-4V with a colony alpha microstructure. Materials Science and Engineering A 263, 257.

Semiatin, S.L., Stefansson, N., Doherty, R.D., 2005. Prediction of the Kinetics of Static Globularization of Ti-6Al-4V. Metallurgical and Materials Transactions 36A, 1372–1376.

Seo, S., Min, O., Yang, H., 2005. Constitutive equation for Ti-6Al-4V at high temperatures measured using the SHPB technique 31, 735.

Shell, E., Semiatin, S.L., 1999. Effect of initial microstructure on plastic flow and dynamic globularization during hot working of Ti-6Al-4V. Metallurgical and Materials Transactions A 30, 3219–3229.

Stefansson, N., Semiatin, S.L., 2003. Mechanisms of globularization of Ti-6Al-4V during static heat treatment. Metallurgical and Materials Transactions 34A, 691–698.

Thomas, J.P., Semiatin, S.L., 2006. Mesoscale Modeling of the Recrystallization of Waspaloy and Application to the Simulation of the Ingot-Cogging Process. Technical Report AFRL-ML-WP-TP-2006-483. Materials and Manufacturing Directorate. Air Force Research Laboratory, Air Force Materiel Command, Wright-Patterson AFB, OH 45433-7750.

Wedberg, D., Lindgren, L.E., 2015. Modelling flow stress of AISI 316L at high strain rates. Mechanics of Materials 91, 194–207.

Wedberg, D., Svoboda, A., Lindgren, L.E., 2012. Modelling high strain rate phenomena in metal cutting simulation. Modelling and Simulation in Materials Science and Engineering 20.

Williams, J.C., Lütjering, G., 2003. Titanium. Springer - Verlag.

Yeom, J.T., Kim, J.H., Kim, N.Y., Park, N.K., Lee, C.S., 2007. Characterization of Dynamic Globularization Behavior during Hot Working of Ti-6Al-4V Alloy. Advanced Materials Research 26-28, 1033–1036.

Zerilli, F.J., Armstrong, R.W., 1987. Dislocation-mechanics-based constitutive relations for material dynamics calculations. Journal of Applied Physics 61, 1816.

Zhao, W.J., Ding, H., Song, D., Cao, F., Hou, H.L., 2007. The Effect of Grain Size on Superplastic Deformation of Ti-6Al-4V Alloy, in: Zhang, K. (Ed.), Materials Science Forum, pp. 387–392.

Simulation of additive manufacturing of Ti-6Al-4V using a coupled physically-based flow stress and metallurgical model

Authors:
Bijish Babu, Andreas Lundbäack, Lars-Erik Lindgren.

Simulation of additive manufacturing of Ti-6Al-4V using a coupled physically-based flow stress and metallurgical model

Bijish Babu

Swerim AB, Box 812, SE-971 25 Luleå, Sweden

Andreas Lundbäck

Mechanics of Sold Materials, Luleå University of Technology, SE-971 87, Luleå, Sweden

Lars-Erik Lindgren

Mechanics of Solid Materials, Luleå University of Technology, SE-971 87, Luleå, Sweden

Abstract

Simulating the additive manufacturing process of Ti-6Al-4V is very complex owing to the microstructural changes and allotropic transformation occurring during its thermo-mechanical processing. The α-phase with a hexagonal close pack structure is present in three different forms; Widmanstatten, grain boundary, and Martensite. A metallurgical model that computes the formation and dissolution of each of these phases is used here. Furthermore, a physically based flow-stress model coupled with the metallurgical model is applied in the simulation of an additive manufacturing case using directed energy deposition method.

Key words: Dislocation density, Vacancy concentration, Ti-6Al-4V, Additive Manufacturing, Directed Energy Deposition

1. Introduction

Directed energy deposition (DED) additive manufacturing (AM) can be considered as computer numerically controlled multi-pass welding with progressive weldments made on a substrate to create free-form structures. The added metals can be either in powder or wire form and the heat source be laser or electron beam. One of the challenges involved in the AM process is the residual deformation and stresses due to the thermal dilatation of the substrate and added structure. The final properties of the AM structure is strongly influenced by the microstructure which is dependent on the thermo-mechanical processing history of the component.

A material model combining a metallurgical and flow stress model described in Babu et al. (2018) is used here. This model which works for arbitrary phase composition is an improved version of Babu and Lindgren (2013). AM process involves cyclic heating and cooling resulting in non-equilibrium phase evolution which can be addressed with this model.

2. A physically-based flow stress model

An in-compressible von Mises model is used here with the assumption of isotropic plasticity. The flow stress is split into two parts (Seeger, 1956; Bergström, 1969; Kocks, 1976; Babu and Lindgren, 2013),

$$\sigma_y = \sigma_G + \sigma^* \tag{1}$$

where, σ_G is the athermal stress contribution from the long-range interactions of the dislocation substructure. The second term σ^*, is the stress needed to move dislocations through the lattice and to pass short-range obstacles. This formulation is very much in accordance with the material behavior demonstrated by Conrad (1981).

Email addresses: `bijish.babu@swerim.se` (Bijish Babu), `andreas.lundback@ltu.se` (Andreas Lundbäck), `lars-erik.lindgren@ltu.se` (Lars-Erik Lindgren)
URL: `https://www.swerim.se` (Bijish Babu)

2.1. Long range stress component:

The long-range term from equation (1) is derived by Seeger (1956) as,

$$\sigma_G = m\alpha G b \sqrt{\rho_i} \tag{2}$$

where m is the Taylor orientation factor translating the effect of the resolved shear stress in different slip systems into effective stress and strain quantities. Furthermore, α is a proportionality factor, b is the magnitude of Burgers vector, G is the temperature dependent shear modulus and ρ_i is the immobile dislocation density.

2.2. Short range stress component:

The strain rate dependent part of the yield stress from equation (1) can be derived according to the Kocks-Mecking formulation (Kocks et al., 1975; Mecking and Kocks, 1981) as,

$$\sigma^* = \tau_0 G \left[1 - \left[\frac{kT}{\Delta f_0 G b^3} \ln \left(\frac{\dot{\varepsilon}^{ref}}{\dot{\bar{\varepsilon}}^p} \right) \right]^{1/q} \right]^{1/p} \tag{3}$$

Here, $\tau_0 G$ is the shear strength in the absence of thermal energy and $\Delta f_0 G b^3$ is the activation energy necessary to overcome lattice resistance. Some guidelines for selection of Δf_0 and τ_0 are given in (Frost and Ashby, 1982). The parameters p and q define the shape of the obstacle barrier for dislocation motion. Further, k is the Boltzmann constant, T is the temperature in kelvin and ($\dot{\varepsilon}^{ref}$ and $\dot{\varepsilon}^p$) are the reference and plastic strain rates respectively.

2.3. Evolution of immobile dislocation density

The components of the yield stress in equation (1) are obtained from equations (2)and (3). However, the evolution of ρ_i in equation (2) needs to be computed. The model for the evolution of the immobile dislocation density has two parts; hardening and restoration.

$$\dot{\rho}_i = \dot{\rho}_i^{(+)} - \dot{\rho}_i^{(-)} \tag{4}$$

2.3.1. Hardening process

It is assumed that mobile dislocations move, on average, a distance Λ (mean free path), before they are immobilized or annihilated. According to the Orowan equation, the density of mobile dislocations and their average velocity are proportional to the plastic strain rate. It is assumed that immobile dislocation density also follows the same relation. This leads to,

$$\dot{\rho}_i^{(+)} = \frac{m}{b} \frac{1}{\Lambda} \dot{\bar{\varepsilon}}^p \tag{5}$$

The mean free path can be computed from the grain size (g) and dislocation subcell or subgrain diameter (s) as,

$$\frac{1}{\Lambda} = \left(\frac{1}{g} + \frac{1}{s} \right) \tag{6}$$

The formation and evolution of subcells have been modeled using a relation proposed by Holt (1970).

$$s = K_c \frac{1}{\sqrt{\rho_i}} \tag{7}$$

2.3.2. Restoration processes

The motion of vacancies is related to the recovery of dislocations. Recovery usually occur at elevated temperatures and therefore is a thermally activated reorganization process. Creation of vacancies increases entropy but requires energy and its concentration increases with temperature and deformation. In high stacking fault materials, recovery process might balance the effects of strain hardening leading to constant flow stress. The primary mechanisms of restoration are dislocation glide, dislocation climb, and globularization.

$$\dot{\rho}_i^{(-)} = \dot{\rho}_i^{(glide)} + \dot{\rho}_i^{(climb)} + \dot{\rho}_i^{(globularization)} \tag{8}$$

2

The model for recovery by glide can be written based on the formulation by Bergström (1983)as,

$$\dot{\rho_i}^{(glide)} = \Omega \rho_i \dot{\bar{\varepsilon}}^p \tag{9}$$

where Ω is a function dependent on temperature.

Militzer et al. (1994) proposed a model for dislocation climb based on Sandstrom and Lagneborg (1975) and Mecking and Estrin (1980). With a modification of the diffusivity according to Babu and Lindgren (2013), the model can be written as,

$$\dot{\rho_i}^{(climb)} = 2c_\gamma D_{app} \frac{Gb^3}{kT} \left(\rho_i^2 - \rho_{eq}^2 \right) \tag{10}$$

where, c_γ is a material coefficient and ρ_{eq} is the equilibrium value of the dislocation density. Here, D_{app} is the apparent diffusivity which includes the diffusivity of $\alpha - \beta$ phases weighted by their fractions X_α and X_β, pipe diffusion D_p, as well as effects of excess vacancy concentration c_v.

Babu and Lindgren (2013) proposed a model for the evolution of dislocation density during globularization. According to this model, the effect of grain growth on the reduction of flow stress is included only when the stored deformation energy is above a critical value.

$$\text{if} \quad \rho_i \geq \rho_{cr}$$
$$\dot{\rho_i}^{(globularization)} = \psi \dot{X}_g \left(\rho_i - \rho_{eq} \right); \quad \text{until } \rho_i \leq \rho_{eq} \tag{11}$$
$$\text{else}$$
$$\dot{\rho_i}^{(globularization)} = 0 \tag{12}$$

Here, ρ_{cr} is the critical dislocation density above which globularization is initiated, ρ_{eq} is the equilibrium value of dislocation density, $\dot{X}_g$ is the globularization rate and ψ is a calibration constant.

The mechanism of globularization can be modeled as a two-stage process of dynamic and static recrystallization described by Thomas and Semiatin (2006).

$$X_g = X_d + (1 - X_d) X_s \tag{13}$$

Here, the volume fractions X_g, X_d and X_s denote total globularized, its dynamic component and the static component, respectively. Assuming that grain growth and static recrystallization have the same driving force, the static globularization rate can be written as (Pietrzyk and Jedrzejewski, 2001; Montheillet and Jonas, 2009),

$$\dot{X}_s = M \frac{\dot{g}}{g} \tag{14}$$

where, M is a material parameter. The rate of dynamic globularization is modeled based on Thomas and Semiatin (2006) as,

$$\dot{X}_d = \frac{Bk_p \dot{\bar{\varepsilon}}_p}{\bar{\varepsilon}_p^{1-k_p} e^{B\bar{\varepsilon}_p^{k_p}}} \tag{15}$$

where, B and k_p are material parameters.

2.4. Evolution of excess vacancy concentration

Militzer et al. (1994) proposed a model for excess vacancy concentration with generation and annihilation components. Assuming that only long range stress contributes to vacancy formation and introducing a component for temperature change, the Militzer model can be rewritten as,

$$\dot{c_v}^{ex} = \left[\chi \frac{m\alpha Gb^2 \sqrt{\rho_i}}{Q_{vf}} + \zeta \frac{c_j}{4b^2} \right] \frac{\Omega_0}{b} \dot{\bar{\varepsilon}} - D_{vm} \left[\frac{1}{s^2} + \frac{1}{g^2} \right] (c_v - c_v^{eq})$$
$$+ c_v^{eq} \left(\frac{Q_{vf}}{kT^2} \right) \dot{T} \tag{16}$$

Here, $\chi = 0.1$ is the fraction of mechanical energy spent on vacancy generation, Ω_0 is the atomic volume and ζ is the neutralization effect by vacancy emitting and absorbing jogs. The concentration of jogs (c_j) and D_{vm}, the diffusivity of vacancy are given in Babu and Lindgren (2013). Additionally, Q_{vf} is the activation energy of vacancy formation.

3

3. Model for phase evolution

The liquid-solid phase changes are not modeled in detail. Instead, a simplified model for the transition between the liquid and solid state is implemented to take care of temperatures above the melting temperature (T_{melt}) . In the liquid state, each of the solid phases is consequently set to zero. In the solid state, the Ti-6Al-4V microstructure is composed of two main phases; the high-temperature stable β-phase and the lower temperature stable α-phase. Depending on the formation conditions, a variety of α/β textures can be obtained by heat treatment giving different mechanical properties. Lütjering (1998); Williams and Lütjering (2003) explored the relationship between processing, microstructure, and mechanical properties. Based on the literature (Semiatin et al., 1999b,a; Seetharaman and Semiatin, 2002; Thomas et al., 2005) few microstructural features have been identified to be relevant concerning the mechanical properties. The three separate α-phase fractions; Widmanstatten (X_{α_w}), grain boundary ($X_{\alpha_{gb}}$), acicualr and massive Martensite (X_{α_m}) and the β-phase fraction (X_β) are included in the current model. Though in the current flow stress model, the individual α-phase fractions are not included separately, it is possible to incorporate them when more details about their respective strengthening mechanisms are known.

3.1. Phase transformations

Depending on the temperature, heating/cooling rates, Ti-6Al-4V undergoes an allotropic transformation. The mathematical model for transformation is described schematically in figure 1. The transformations denoted by F1, F2, and F3 represent the formation of α_{gb}, α_w and α_m phases respectively, and D3, D2, and D1 shows the dissolution of the same phases. If the current volume fraction of β phase is more than β_{eq}, the excess β phase transforms to α phase. Here α_{gb} formation which occurs in high temperature is most preferred followed by the α_w. The remaining excess β fraction is transformed to α_m if the temperature is lower than T_m, (martensite start temperature) and cooling rate is above 20°C/s. Conversely, if the current volume fraction of β is lower than β_{eq}, the excess α phase is converted to β. Primary, the α_m phase dissolves to β and α_w phases in the same proportion as the α_{eq} and β_{eq}. The remaining excess α_w and α_{gb} transform to β in that order. The equilibrium fraction of β phase (see figure 2) is computed by the equation 17 where T is the temperature in degree Celsius.
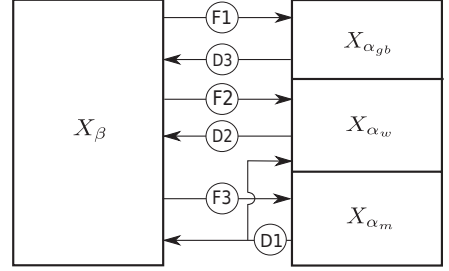

Figure 1: The Mechanism of phase change.

$$
\begin{aligned}
X_\beta^{eq} &= 1 - 0.89\, e^{-\left(\frac{T^*+1.82}{1.73}\right)^2} + 0.28\, e^{-\left(\frac{T^*+0.59}{0.67}\right)^2} \\
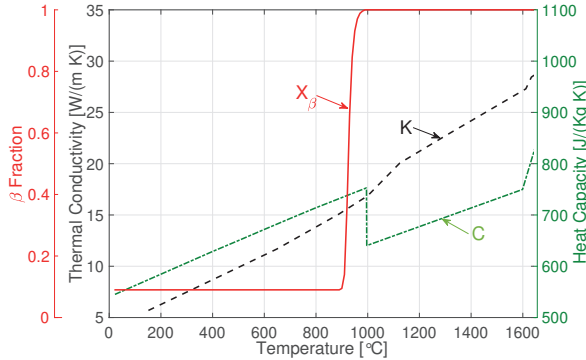T^* &= (T - 927)/24
\end{aligned}
\tag{17}
$$

Figure 2: Thermal conductivity (K), Specific heat capacity (C) & Equilibrium phase fraction (X_β).

4

3.2. Adaptation of the JMAK model for diffusional transformation

The JMAK model (Johnson and Mehl, 1939; Avrami, 1939; Kolmogorov, 1937) originally formulated for nucleation and growth during isothermal situations can be adapted to model any diffusional transformations. Employing the additivity principle, and using sufficiently small time steps ensures that any arbitrary temperature changes can be computed. JMAK model assumes that a single phase X_1 which is 100% in volume from the start will transform to 100% of second phase X_2 in infinite time. However in the case of Ti-6Al-4V, this is not the case as it is a $\alpha - \beta$ dual phase alloy below β-transus temperature. Hence, in order to accommodate incomplete transformation, the product fraction is normalized with the equilibrium volume. Conversely, the starting volume of a phase can also be less than 100% which is circumvented by assuming that the available phase volume is the total phase fraction. Another complication is the existence of simultaneous transformation of various α phases (α_w, α_{gb}, α_m) to β phase and back. This can be modeled by sequentially calculating each transformation within the time increment (Charles Murgau et al., 2012).

3.3. Formation of α phase

During cooling from β-phase, α_{gb} and α_w phases are formed by a diffusional transformation. According to the incremental formulation of JMAK model described by Charles Murgau et al. (2012), the formation of α_{gb} and α_w can be modeled by the set of equations in rows F1 and F2 respectively of table1. Martensite phase is formed at cooling rates above 410°C/s by a diffusion-less transformation. While cooling at rates above 20°C/s and upto 410°C/s, the massive α transformation has been observed to co-occur with the martensite formation (Ahmed and Rack, 1998; Lu et al., 2016). Owing to the similitude in crystal structure between massive-α and martensite-α, they are not differentiated here except that above 410°C/s, 100% α_m is allowed to form. An incremental formulation of Koistinen-Marburger equation described by Charles Murgau et al. (2012) is used here (see equation set in row F3 of table 1).

F1	$^{n+1}X_{\alpha_{gb}} = \left(1 - e^{-k_{gb}\left(t_{gb}^* + \Delta t\right)^{N_{gb}}}\right)\left(^nX_\beta + {}^nX_{\alpha w} + {}^nX_{\alpha_{gb}}\right)^{n+1}X_\alpha^{eq} - {}^nX_{\alpha w}$ $t_{gb}^* = \sqrt[N_{gb}]{-ln\left(1 - \dfrac{\left(^nX_{\alpha w} + {}^nX_{\alpha_{gb}}\right)/^{n+1}X_\alpha^{eq}}{^nX_\beta + {}^nX_{\alpha w} + {}^nX_{\alpha_{gb}}}\right)/k_{gb}}$
F2	$^{n+1}X_{\alpha w} = \left(1 - e^{-k_w\left(t_w^* + \Delta t\right)^{N_w}}\right)\left(^nX_\beta + {}^nX_{\alpha w} + {}^nX_{\alpha_{gb}}\right)^{n+1}X_\alpha^{eq} - {}^nX_{\alpha_{gb}}$ $t_w^* = \sqrt[N_w]{-ln\left(1 - \dfrac{\left(^nX_{\alpha w} + {}^nX_{\alpha_{gb}}\right)/^{n+1}X_\alpha^{eq}}{^nX_\beta + {}^nX_{\alpha w} + {}^nX_{\alpha_{gb}}}\right)/k_w}$
F3	$^{n+1}X_{\alpha_m} = \begin{cases} \left(1 - e^{-b_{km}\left(T_{ms} - T\right)}\right)\left(^nX_\beta + {}^nX_{\alpha_m}\right); & if\ (\dot{T} > 410°C/s) \\ \left(1 - e^{-b_{km}\left(T_{ms} - T\right)}\right)\left(^nX_\beta + {}^nX_{\alpha_m} - {}^{n+1}X_\alpha^{eq}\right); & if\ (20°C/s > \dot{T} > 410°C/s) \end{cases}$

Table 1: Models for α-phase formation.

3.4. Dissolution of α phase

The α_m phase formed by instantaneous transformation is unstable and therefore undergoes a diffusional transformation to α_w and β phases based on its current equilibrium composition. The incremental formulation of classical JMAK model by Charles Murgau et al. (2012) and its parameters are given in row D1 of table 2. During heating or reaching non-equilibrium phase composition, α_w and α_{gb} can transform to β-phase controlled by the diffusion of vanadium at the $\alpha - \beta$ interface. A parabolic equation developed by Kelly (2004); Kelly et al. (2005) derived in its incremental form by Charles Murgau et al. (2012) is used here (see rows D2 and D3 of table 2).

D1	$^{n+1}X_{\alpha_m} = \left(^{n+1}X_{\alpha_m}^{eq} - e^{-k_m\left(t_m^* + \Delta t\right)^{N_m}}\right)\left(^nX_\beta + {}^nX_{\alpha_m} - {}^{n+1}X_{\alpha_m}^{eq}\right)$ $t_m^* = \sqrt[N_m]{-ln\left(\dfrac{\left(^nX_\alpha - {}^{n+1}X_{\alpha_m}^{eq}\right)}{^nX_\beta + {}^nX_{\alpha_m} - {}^{n+1}X_{\alpha_m}^{eq}}\right)/k_m}$
D2	$^{n+1}(X_{\alpha w} + X_{\alpha_{gb}}) = \begin{cases} ^{n+1}X_\alpha^{eq} f_{diss}(T)\sqrt{\Delta t + t^*}; & if\ (0 < (\Delta t + t^*) < t_{crit}) \\ ^{n+1}X_\alpha^{eq}; & if\ (\Delta t + t^* > t_{crit}) \end{cases}$
D3	$t^* = \left(\dfrac{^nX_\beta}{^{n+1}X_\beta^{eq} f_{diss}(T)}\right)^2$

Table 2: Models for α-phase dissolution.

4. Coupling of phase and flow stress models

Young's modulus and Poisson's ratio are assumed to be identical for both phases. The Wachtman et al. (1961) model for Young's modulus (E) is calibrated using measurements from Babu and Lindgren (2013) is written as

$$E = 107 - 0.2\ (T + 273)\ e^{-(1300/T+273)} \tag{18}$$

where T is the temperature in degree Celsius applied with a cut-off at T=1050°C (see figure 3). A linear model for Poisson's ratio (μ) after fitting to measurements by Fukuhara and Sanpei (1993) as

$$\mu \quad = \quad 0.34 + 6.34\ e^{-5}\ T \tag{19}$$

$$\tag{20}$$

where T is the temperature in degree Celsius (see figure 3).
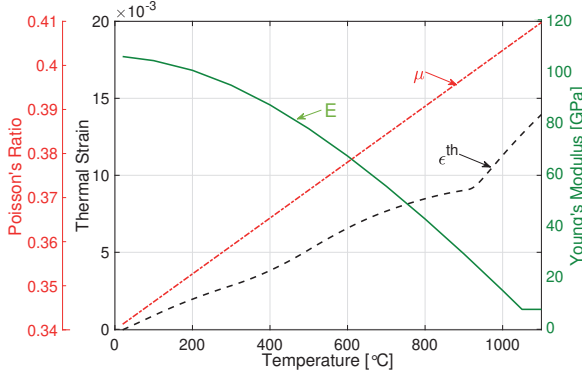
Figure 3: Poisson's Ratio (μ), Thermal Strain (ϵ^{th}) & Youngs Modulus (E).

Using X-Ray diffraction, Swarnakar et al. (2011) measured the volumetric expansion of unit cells of α and β phases during heating. Based on this, the average Coefficient of Thermal Expansion (CTE) of the phase mixture can be calculated using the rule of mixtures (ROM) as in equation 21, where α_α and α_β gives the CTE of α and β phases respectively. The linear thermal strain can be computed using equation 22 is plotted in figure 3. Here, the ε^{adj} makes the ROM (equation 21) non-linear.

$$\alpha_{avg} \quad = \quad X_\alpha \alpha_\alpha + X_\beta \alpha_\beta \tag{21}$$

$$\varepsilon^{th} \quad = \quad \alpha_{avg}\Delta T - \varepsilon^{adj} \tag{22}$$

$$\varepsilon^{adj} \quad = \quad 1.0e^{-8}T^2 - 8.4e^{-6}T + 3.0e^{-4} \tag{23}$$

The thermal conductivity and specific heat capacity of the alloy taken from Boivineau et al. (2006) and Mills (2002) respectively are given in figure 2. The latent heat of phase transformation ($\alpha \rightarrow \beta$) and the latent heat of fusion are measured to be 64kJ/Kg and (290 ± 5)kJ/Kg respectively (Boivineau et al., 2006).

The yield strength of the phase mixture can be written according to the linear rule of mixtures as,

$$\sigma_y = X_\alpha \sigma_y^\alpha + X_\beta \sigma_y^\beta \tag{24}$$

The distribution of plastic strain can be obtained assuming iso-work principle. According to Bouaziz and Buessler (2004), this can be written as,

$$\sigma_y^\alpha \dot{\bar{\varepsilon}}_\alpha \quad = \quad \sigma_y^\beta \dot{\bar{\varepsilon}}_\beta \tag{25}$$

$$\dot{\bar{\varepsilon}}^p \quad = \quad X_\alpha \dot{\bar{\varepsilon}}_\alpha + X_\beta \dot{\bar{\varepsilon}}_\beta \tag{26}$$

The above formulation ensures that the β phase with lower yield strength will get a more significant share of plastic strain as compared to the stronger α phase. For temperatures above 1100°C, ($\sigma_y^{>1100°C} = \sigma_y^{1100°C}$). The stress-strain relationship predicted by the model for varying strain rates and temperature are given in figure 4. The rate dependence and flow-softening demonstrated by the model is visible here. A detailed comparison of model predictions and measurements along with model parameters are given in Babu and Lindgren (2013); Babu et al. (2018).
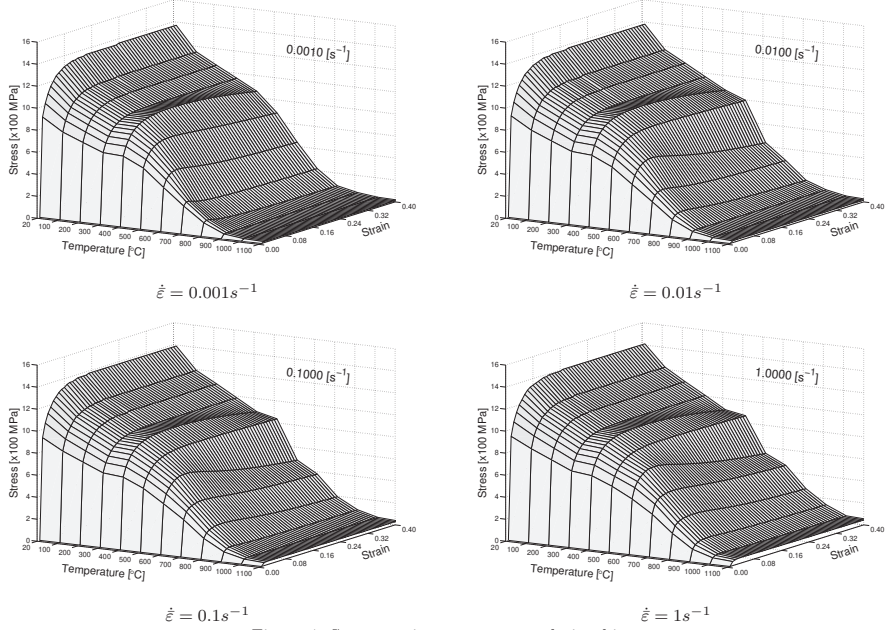
6

$$\dot{\bar{\varepsilon}} = 0.001 s^{-1}$$

$$\dot{\bar{\varepsilon}} = 0.01 s^{-1}$$

$$\dot{\bar{\varepsilon}} = 0.1 s^{-1}$$

$$\dot{\bar{\varepsilon}} = 1 s^{-1}$$

Figure 4: Stress-strain-temperature relationship.

5. Additive manufacturing

In the AM process, powder or wire is used for the addition of material with a heat source such as laser, electron beam or electric arc. The deposition path is generated from a CAD geometry and is pre-programmed in a CNC machine which makes the process very flexible and suitable for low volume production eliminating the need for tooling and dies. This also enables the production of complicated geometries that are traditionally difficult to produce with the conventional manufacturing processes.
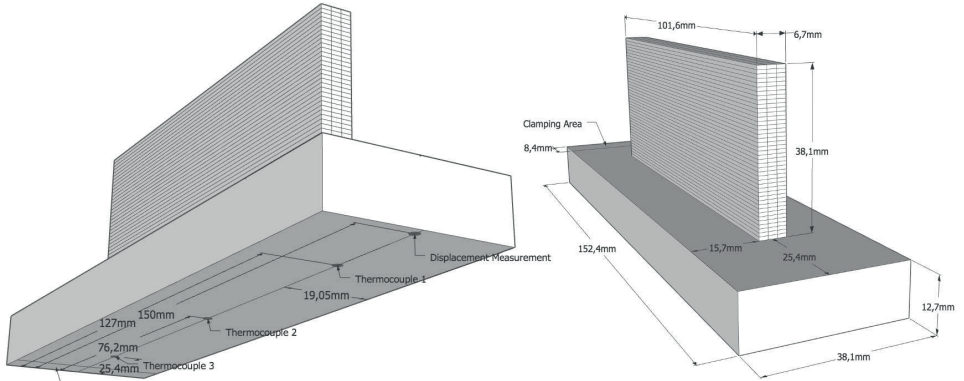
Figure 5: Dimensions of the AM Component.

Powder Bed Fusion (PBF) is the technique of building a thin layer over layer by melting the fine metal powder. DED, on the other hand, is used usually for building features on large existing parts as well as for repairing damaged ones. PBF typically adds layers that are thinner than DED and therefore can create high-resolution structures whereas DED produces components at a higher built rate. The primary challenge of DED is that the higher energy input from the heat source may lead to substantial distortion and higher residual stresses. In this article, a DED process described in Denlinger et al. (2015) is simulated

7

using the general purpose Finite Element (FE) software MSC.Marc. A set of subroutines for modeling of AM process is implemented in MSC.Marc which is explained in Lundbäck and Lindgren (2011). A coupled thermo-mechanical-metallurgical model described in previous sections is also implemented as subroutines within MSC.Marc.

The dimensions of the substrate (152.4 x 38.1 x 12.7)mm and AM component are given in figure 5. One end of the fixture is held in position by a clamping fixture (see the notations in figure 5). Three
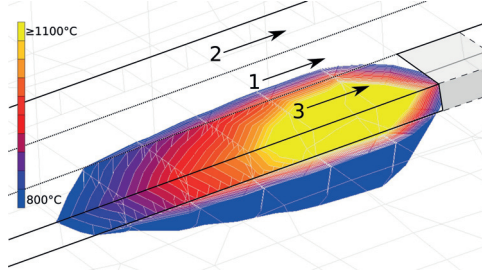

Figure 6: Temperature contours in the weld pool.

beads are added per layer with a total width of 6.7mm and a height of 38.1mm. 42 discrete layers and its respective beads are also shown in figure 5. Figure 6 shows the order of deposition starting with the middle bead followed by one on each side. Odd layers are deposited in the direction away from the clamping followed by even layers in the opposite direction. Figure 6 also shows the temperature contours and direction of deposition of bead three of the first layer. After each layer, a dwell time (DT) of 0, 20, and 40s were applied for studying the effect of varying cooling rates.

6. Modeling of additive manufacturing

In the current work, the scope of the model is to predict the evolution of microstructure, the overall distortion of the component, and the residual stresses. This requires a solution where thermo-mechanical-metallurgical models are coupled using a staggered approach. Figure 7 shows the coupling of different domains using a staggered approach. The thermal field is solved using the FE implicit iterative scheme by computing the heat input and heat losses by conduction, convection, and radiation. Based on the computed temperature in the increment, the metallurgical model computes the phase evolution for each Gauss point. The computed temperature and phase fractions are input to solve the mechanical field equations. A large deformation FE implicit iterative scheme is used here where mechanical and physical properties are strongly dependent on the temperature and phase composition. Latent heat & volume change due to phase evolution and deformation energy converted to heat are included here.
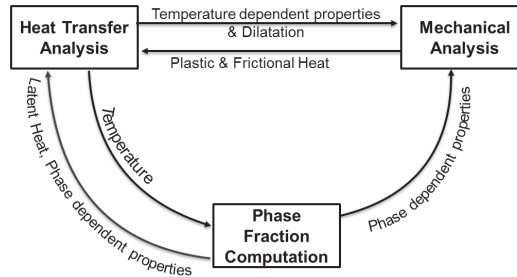

Figure 7: Coupling of Thermo-mechanical-microstructural fields.

6.1. Heat source

Modeling of weld pool phenomena requires high resolution discretization and at least one other physics domain, fluid flow. This would require an impractical amount of resources for solving the problem and can be avoided considering the scope of current work. The heat input can be modeled using volume heat flux in a geometric region representing the weld pool and is calibrated using measured temperatures.

8

Goldak's (Goldak et al., 1984) double ellipsoidal heat input model is implemented in the current work with the efficiency calibrated to be 0.29. The parameters of the heat source are given in figure 8. See Lundbäck and Lindgren (2011) for details of the implementation of this model.
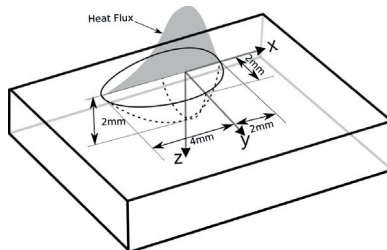

Figure 8: Gaussian distribution of density and double ellipsoid shape in xy-plane.

6.2. Modeling of material addition

The inactive element approach is used here where all the elements representing the added metal are de-activated before the start of the simulation and is activated only after meeting certain criteria. In each increment, the set of elements that overlaps and the geometric region represented by the current weld-pool position is activated thermally whereas mechanical activation occurs only when the thermally active elements cool below the solidus temperature. Before thermal activation, the elements may have to be moved to accommodate for the distortion of the substrate and the already activated elements during the process. The moving elements will maintain connectivity with the activated elements, and their volume matches the material added during that time step (Lundbäck and Lindgren, 2011).

6.3. Boundary conditions

In DED, much of the heat input in the initially deposited layers will be absorbed by the substrate. To balance the heat input, losses by free and forced convection, conduction to fixtures as well as radiation are to be included in the model. A lumped convective coefficient of 18 $W/m^2/℃$ is applied to model the natural and forced convection from shielding gas. Both convective and radiative boundary conditions are applied on the outer surface of all thermally active elements. A surface emissivity of 0.25 is used here. In the current model, heat loses due to cooling by the fixture is achieved by using convective heat transfer with a high coefficient of 250 $W/m^2/℃$.
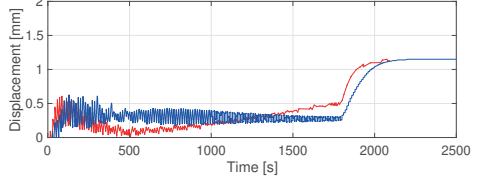
7. Comparison of measurements and simulations

In situ measurement of temperature and distortion is performed during the AM process. Three thermocouples were attached to the bottom of the substrate at positions shown in the left part of figure 5. Dwell times (DT) allow the component to cool down considerably during the process. In figure 9a, 9c, and 9e, the dots denote the thermocouple measurements and lines, the predictions from model. The thermocouple attached in the middle of the component (TC2) registered the highest temperature as the other two are closer to the ends which are subjected to higher convective cooling. The thermocouple attached close to the clamping (TC3) has the lowest temperature since the fixture acts as a heat sink. The raising of dwell times by 20s increased the cooling and thereby reducing the peaks. As the height of the wall increases, this effect is less detectable as this thermocouple is beneath the substrate.

The distortion of the component is measured at the free end using a laser displacement sensor. In figures 9b, 9d, and 9f, the red lines denote the measured values and blue lines, the predictions from the model. Addition of each layer makes the component to bend downwards due to the thermal gradient between the top and bottom of the substrate which is diminished during cooling producing oscillations. In order to compare the measurements and simulation results, these oscillations are smoothed out using Savitzky and Golay (1964) filter and are plotted in figure 10. Here, the dotted lines denote the measurements and continuous lines denote the model predictions. The start and end of the linear region, its slope, and the detection of the first peak are deduced from figure 10 and is shown in table 3. The peak to peak amplitude of the oscillations at the first peak and also at the start & end of the linear region are given in table 3. The measured final bending of the build plate at the outer edge increase by 0.4mm for
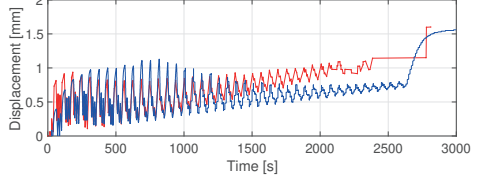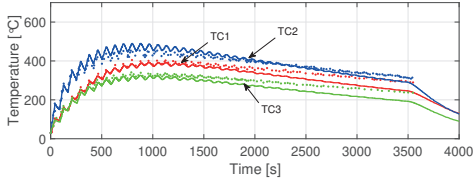
9
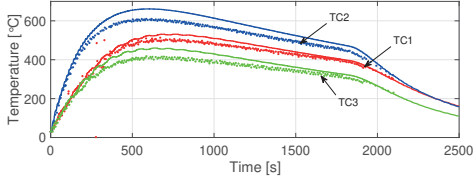
(a) Temperature (DT=0s)
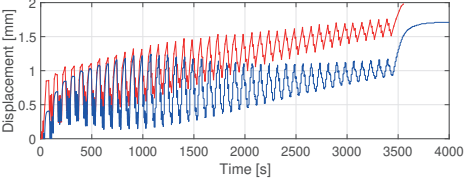
(b) Distortion (DT=0s)
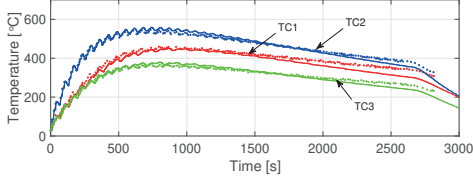
(c) Temperature (DT=20s)

(d) Distortion (DT=20s)

(e) Temperature (DT=40s)

(f) Distortion (DT=40s)

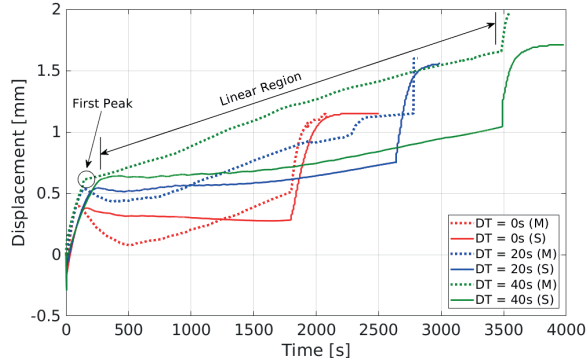Figure 9: Comparison of measurements and simulations.

Figure 10: Comparison of distortions.

	0s (comp)	20s (comp)	40s (comp)
Final displacement [mm]	1.2 (1.2)	1.6 (1.6)	2.0 (1.7)
Slope of linear region $[10^{-4}\text{mm/s}]$	3.4 (-0.2)	3.7 (1.1)	3.2 (1.4)
Time at 1st Peak [s]	110 (140)	170 (230)	150 (300)
Amplitude at 1st Peak $[10^{-1}\text{mm}]$	3.5 (3.8)	7.6 (7.0)	6.4 (6.9)
Amplitude at start of linear region $[10^{-1}\text{mm}]$	1.0 (0.9)	6.2 (8.4)	6.6 (6.1)
Amplitude at end of linear region $[10^{-1}\text{mm}]$	0.1 (0.4)	1.1 (0.8)	2.4 (2.1)

Table 3: Comparison of distortion (computed values given in brackets).

each 20s increase in dwell time. The simulations also gave a similar result. The results from simulations are given in table 3 within brackets.

10

Figure 11 shows the residual stress in the welding direction along with its spread measured by Denlinger et al. (2015) using hole drilling. The location of the testing was in the middle of the specimen at the bottom of the substrate. The results show that for the case with dwell times 0s and 20s, simulation results are close to measurements or within the margin of error, and for 40s, it is slightly below the margin. The residual stress distribution after cooling to room temperature in the welding direction and the von Mises effective stress for the case with dwell time 0s are plotted in the figure 12. The predicted temperature for the case with dwell time 0s at the top surface of the substrate above the location of TC2 is given in figure 13. The computed α-phase fraction is also provided here. The addition of each bead is denoted as B1-3 and the grey areas in between is the cooling time. In total, 5 layers are shown in figure 13.
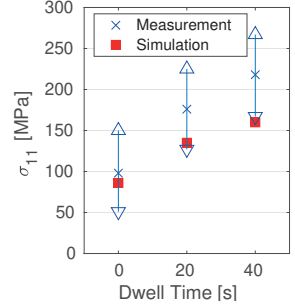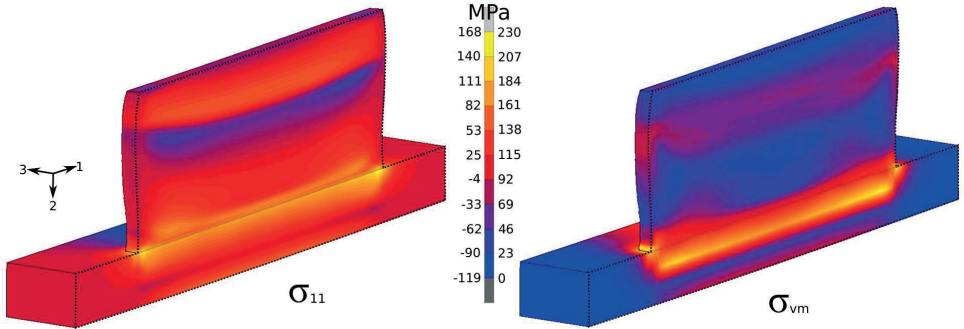

Figure 11: Residual stress.

Figure 12: Residual stress for 0s dwell time (model clipped longitudinally in the mid-plane).
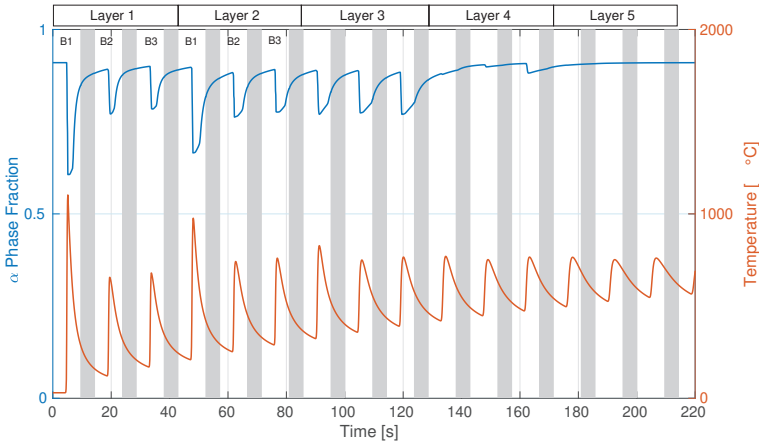

Figure 13: Prediction of phase fraction and temperature.

8. Discussions and conclusions

The advanced material model described here combining the metallurgical model and flow stress model has proven to be suitable for the simulation of AM. Diffusional and instantaneous transformations are included in the metallurgical model. This model is formulated in a way that it can be implemented in any standard finite element software. The temperature measurements and results from simulations

11

demonstrated good overall fit. This model predicts the final distortion of the component with good accuracy except for the case with 40s dwell time. This trend is also evident in the residual stress measurements. The comparison of distortion before the onset of cooling shows a larger difference between the model and measurements. This might be because the stress-relaxation behavior is less accurately described by the model. The computed phase fraction in figure 13 shows that after the addition of the fourth layer, the substrate undergoes no significant phase evolution. Denlinger and Michaleris (2016) performed the simulation of all the three cases described here. They have used an approach where the plastic strain is reset to zero at a temperature of 690℃ which is a parameter calibrated for the AM case. This transformation strain parameter made it possible for Denlinger and Michaleris (2016) to include the effects of dwell time whereas, in the current work, mechanisms of dislocation climb and globularization results in restoration of the lattice.

References

Ahmed, T., Rack, H. J., 1998. Phase transformations during cooling in [alpha]+[beta] titanium alloys. Materials Science and Engineering A 243 (1-2), 206–211.

Avrami, M., 1939. Kinetics of Phase Change. I General Theory. The Journal of Chemical Physics 7 (12), 1103–1112.

Babu, B., Charles, C., Lindgren, L.-E., 2018. Physically Based Constitutive Model of Ti-6Al-4V for Arbitrary Phase Composition. Submitted to Modelling and Simulation in Materials Science and Engineering 0 (0), 0–11.

Babu, B., Lindgren, L.-E., 2013. Dislocation density based model for plastic deformation and globularization of Ti-6Al-4V. International Journal of Plasticity 50 (0), 94–108.

Bergström, Y., 1969. Dislocation model for the stress-strain behaviour of polycrystalline alpha-iron with special emphasis on the variation of the densities of mobile and immobile dislocations. Materials Science & Engineering 5, 193–200.

Bergström, Y., 1983. The plastic deformation of metals - A dislocation model and its applicability. Reviews on Powder Metallurgy and Physical Ceramics (2/3), 79–265.

Boivineau, M., Cagran, C., Doytier, D., Eyraud, V., Nadal, M., Wilthan, B., Pottlacher, G., 2006. Thermophysical Properties of Solid and Liquid Ti-6Al-4V (TA6V) Alloy. International Journal of Thermophysics 27, 507–529.

Bouaziz, O., Buessler, P., 2004. Iso-work Increment Assumption for Heterogeneous Material Behaviour Modelling. Advanced Engineering Materials 6 (1-2), 79–83.

Charles Murgau, C., Pederson, R., Lindgren, L., 2012. A model for Ti–6Al–4V microstructure evolution for arbitrary temperature changes. Modelling and Simulation in Materials Science and Engineering 20 (5), 055006.

Conrad, H., 1981. Effect of interstitial solutes on the strength and ductility of titanium. Progress in Materials Science 26 (2-4), 123–403.

Denlinger, E. R., Heigel, J. C., Michaleris, P., Palmer, T., 2015. Effect of inter-layer dwell time on distortion and residual stress in additive manufacturing of titanium and nickel alloys. Journal of Materials Processing Technology 215, 123–131.

Denlinger, E. R., Michaleris, P., 2016. Effect of stress relaxation on distortion in additive manufacturing process modeling. Additive Manufacturing 12, 51–59.

Frost, H. J., Ashby, M. F., 1982. Deformation-Mechanism Maps: The Plasticity and Creep of Metals and Ceramics. Paperback.

Fukuhara, M., Sanpei, A., 1993. Elastic moduli and internal frictions of Inconel 718 and Ti-6Al-4V as a function of temperature. Journal of Materials Science Letters 12, 1122–1124.

Goldak, J., Chakravarti, A., Bibby, M., Jun 1984. A new finite element model for welding heat sources. Metallurgical Transactions B 15 (2), 299–305.

Holt, D. L., 1970. Dislocation cell formation in metals. Journal of applied physics 41 (8), 3197.

Johnson, W., Mehl, R., 1939. Reaction Kinetics in Processes of Nucleation and Growth. Trans. Soc. Pet. Eng. 135, 416.

Kelly, S. M., 2004. Thermal and Microstructure Modeling of Metal Deposition Processes with Application to Ti-6Al-4V. Phd thesis, Virginia Polytechnic Institute and State University.

Kelly, S. M., Babu, S. S., David, S. A., Zacharia, T., Kampe, S. L., 2005. A microstructure model for laser processing of Ti-6Al-4V. In: 24th International Congress on Applications of Lasers and Electro-Optics, ICALEO 2005. 24th International Congress on Applications of Lasers and Electro-Optics, ICALEO 2005 - Congress Proceedings. Laser Institute of America, Orlando, FL 32826, United States, Miami, FL, United States, pp. 489–496.

Kocks, U., 1976. Laws for Work-Hardening and Low-Temperature Creep. Journal of Engineering Materials and Technology, Transactions of the ASME 98 Ser H (1), 76–85.

Kocks, U. F., Argon, A. S., Ashby, M. F., 1975. Thermodynamics and Kinetics of Slip. Vol. 19 of Progress in Material Science. Pergamon Press.

Kolmogorov, A., 1937. A statistical theory for the recrystallisation of metals, Akad Nauk SSSR, Izv. Izv. Akad. Nauk. SSSR 3.

Lu, S., Qian, M., Tang, H., Yan, M., Wang, J., StJohn, D., 2016. Massive transformation in ti6al4v additively manufactured by selective electron beam melting. Acta Materialia 104, 303311.

Lundbäck, A., Lindgren, L.-E., 2011. Modelling of metal deposition. Finite Elements in Analysis and Design 47 (10), 1169–1177.

Lütjering, G., 1998. Influence of processing on microstructure and mechanical properties of $(\alpha+\beta)$ titanium alloys. Materials Science and Engineering: A 243 (1–2), 32–45.

Mecking, H., Estrin, Y., 1980. The effect of vacancy generation on plastic deformation. Scripta Metallurgica 14 (7), 815.

Mecking, H., Kocks, U., 1981. Kinetics of flow and strain-hardening. Acta Metallurgica 29 (11), 1865–1875.

Militzer, M., Sun, W. P., Jonas, J. J., 1994. Modelling the effect of deformation-induced vacancies on segregation and precipitation. Acta Metallurgica et Materialia 42 (1), 133.

Mills, K. C., 2002. Recommended Values of Thermophysical Properties for Selected Commercial Alloys. Woodhead Publishing.

Montheillet, F., Jonas, J. J., 2009. Fundamentals of Modeling for Metals Processing. Vol. 22A of ASM Handbook. ASM International, Materials Park, Ohio 44073-0002, Ch. 17: Models of Recrystallization, pp. 220–231.

Pietrzyk, M., Jedrzejewski, J., 2001. Identification of Parameters in the History Dependent Constitutive Model for Steels. CIRP Annals - Manufacturing Technology 50 (1), 161–164.

Sandstrom, R., Lagneborg, R., 1975. A model for hot working occurring by recrystallization. Acta Metallurgica 23 (3), 387.

Savitzky, A., Golay, M. J. E., 1964. Smoothing and differentiation of data by simplified least squares procedures. Analytical Chemistry 36 (8), 16271639.

Seeger, A., 1956. The mechanism of Glide and Work Hardening in FCC and HCP Metals. In: Fisher, J., Johnston, W. G., Thomson, R., Vreeland, T. J. (Eds.), Dislocations and Mechanical Properties of Crystals. pp. 243–329.

Seetharaman, V., Semiatin, S. L., 2002. Effect of the lamellar grain size on plastic flow behavior and microstructure evolution during hot working of a gamma titanium aluminide alloy. Metallurgical and Materials Transactions A 33A (12), 3817.

Semiatin, S. L., Seetharaman, V., Ghosh, A. K., 1999a. Plastic flow, microstructure evolution, and defect formation during primary hot working of titanium and titanium aluminide alloys with lamellar colony microstructures. Philosophical Transactions: Mathematical, Physical and Engineering Sciences 357, 1487 – 1512.

Semiatin, S. L., Seetharaman, V., Weiss, I., 1999b. Flow behavior and globularization kinetics during hot working of Ti-6Al-4V with a colony alpha microstructure. Materials Science and Engineering A 263 (2), 257.

Swarnakar, A. K., der Biest, O. V., Baufeld, B., 2011. Thermal expansion and lattice parameters of shaped metal deposited Ti–6Al–4V. Journal of Alloys and Compounds 509 (6), 2723–2728.

Thomas, J.-P., Semiatin, S. L., September 2006. Mesoscale Modeling of the Recrystallization of Waspaloy and Application to the Simulation of the Ingot-Cogging Process. Tech. Rep. AFRL-ML-WP-TP-2006-483, Materials and Manufacturing Directorate, Air Force Research Laboratory, Air Force Materiel Command, Wright-Patterson AFB, OH 45433-7750.

Thomas, R. B., Nicolaou, P. D., Semiatin, S. L., 2005. An Experimental and Theoretical Investigation of the Effect of Local Colony Orientations and Misorientation on Cavitation during Hot Working of Ti-6Al-4V. Metallurgical and Materials Transactions A 36A (1), 129.

Wachtman, J. B., Tefft, W. E., Lam, D. G., Apstein, C. S., Jun 1961. Exponential Temperature Dependence of Young's Modulus for Several Oxides. Phys. Rev. 122, 1754–1759.

Williams, J. C., Lütjering, G., 2003. Titanium. Springer - Verlag.